Crestal fault reactivation on rising salt diapirs: An integrated analysis from large to small scales of observation

Ze Tao

Submitted in partial fulfilment of the requirements for the degree of Ph.D.

School of Earth and Ocean Sciences
Cardiff University
September 2018

Crestal fault reactivation on rising salt diapirs: An integrated analysis from large to small scales of observation

Ze Tao

DECLARATION

This work has not been submitted in substance for any other degree or award at this or any other university or place of learning, nor is being submitted concurrently in candidature for any degree or other award.

Signed ………………………… (candidate)   Date …………………..……

STATEMENT 1

This thesis is being submitted in partial fulfilment of the requirements for the degree of PhD

Signed ………………………… (candidate)   Date …………………..……

STATEMENT 2

This thesis is the result of my own independent work/investigation, except where otherwise stated, and the thesis has not been edited by a third party beyond what is permitted by Cardiff University's Policy on the Use of Third Party Editors by Research Degree Students. Other sources are acknowledged by explicit references. The views expressed are my own.

Signed ………………………… (candidate)   Date …………………..……

STATEMENT 3

I hereby give consent for my thesis, if accepted, to be available online in the University's Open Access repository and for inter-library loan, and for the title and summary to be made available to outside organisations.

Signed ………………………… (candidate)   Date …………………..……

STATEMENT 4: PREVIOUSLY APPROVED BAR ON ACCESS

I hereby give consent for my thesis, if accepted, to be available online in the University's Open Access repository and for inter-library loans after expiry of a bar on access previously approved by the Academic Standards & Quality Committee.

Signed ………………………… (candidate)   Date ………………….

Author's note and status of publications

The Chapters presented in this thesis are published or under review as scientific journal articles. The status of publications at the time of submission are as follows:

Chapter 4 has been published as Ze, T. and T. M. Alves (2016). The role of gravitational collapse in controlling the evolution of crestal fault systems (Espírito Santo Basin, SE Brazil), Journal of Structural Geology, v. 92, p. 79-98.

Chapter 5 is under review in AAPG Bulletin as Ze, T. and T. M. Alves, Localized tier-bound domino faulting offshore Espírito Santo Basin (SE Brazil): the case for sudden release of fluid in salt-withdrawal basins.

Chapter 6 is under review in Tectonophysics as Ze, T., and T. M. Alves, Data sampling and its effects on the interpretation of normal faults' propagation and linkage.

Chapter 7, section 7.2 has been published as Ze, T., and T. M. Alves, 2017, The role of gravitational collapse in controlling the evolution of crestal fault systems (Espírito Santo Basin, SE Brazil)–Reply, Journal of Structural Geology, v. 98, p. 12-14.

Chapter 7, section 7.3 is under review in Terra Nova as Ze, T., and T. M. Alves, Seal failure and fluid flow through a salt giant (Espírito Santo Basin, SE Brazil).

Acknowledgments

You were extremely valuable for me when adjusting to the stressful final stages of the thesis.

My grandma, father, mother and sister are thanked for all the love and support. WE ARE FAMILY.

Abstract

The modes in which faults can propagate and grow through subsurface rocks and strata are key to the establishment of fluid paths in sedimentary basins; faults are potential conduits for fluid in some regions, at the same time they are associated with fault-related traps in others. The classical fault propagation models addressed in the published literature have so-far considered isolated, linkage (lateral-tip linkage and dip-linkage), constant-length, and coherent models. However, the propagation histories of faults in regions dominated by salt tectonics are scarcely documented; rather, the existing fault propagation models lack critical thinking when applied to crestal faults, particularly due to the limited resolution of imaged strata in most publications, and the relatively small size of crestal faults (length < 2.3 km, maximum throw < 50 m). With the increasing use of high-resolution seismic data in recent decades, it is now possible to undertake research into the evolution of both crestal faults and fluid flow paths in regions dominated by salt tectonics. In parallel, the uniqueness of crestal faults in terms of their scales has brought up important questions about how data resolution and scale variance influence many a fault analysis, and the current fault propagation models, when based on seismic and outcrop information.

This research uses high resolution seismic data from the Espírito Santo Basin, offshore SE Brazil, to investigate the growth histories of crestal faults, fluid flow in an area of significant salt tectonics, and how crestal faults are associated with traps in supra-salt successions. To answer the question, in a second stage, of how scale variance can influence the analysis of faults' propagation histories, data from Somerset (Bristol Channel) and the Ierapetra Basin (Crete) were collected in the field to broaden the database in this thesis from the larger, rift-basin scale to the seismic and sub-seismic scales.

Segment linkage is predominant in areas where crestal faults grow. Interpreted crestal faults in SE Brazil propagated vertically and horizontally. Horizontal propagation was often hindered by natural barriers such as an accommodation zone (Chapter 4), or oblique transfer zones (Chapter 5), onto which faults terminate. Vertical propagation stopped when the fault meets the sea floor or when vertical propagation was accommodated by blind faults or larger (adjacent) faults showing relatively large

displacements. Hence, this thesis shows that the propagation of crestal faults does not follow a 'coherent growth model'. Rather, the geometry and history of propagation of discrete faults segments are not comparable. In SE Brazil, large fault segments propagated to link with non-reactivated small fault segments on the crest of the salt ridge, and can show later 'blind' propagation towards the surface.

In terms of how scale variance can potentially (negatively) influence fault growth models interpreted on seismic data and in the field, a new quantitative method and two new parameters (sampling interval and module error) are introduced in this thesis for faults of multiple scales - from a few meters to 10s of kilometers. Sampling interval has a significant influence on the interpretation of fault growth histories. By changing one's sampling interval: 1) the interpretation of fault geometries is significantly changed; 2) maximum fault throw values are underestimated; 3) fault segments are underrepresented; 4) the geometry of fault linkage zones is changed; 5) the width of fault linkage zones is underestimated; 6) fault interaction zones are lost. Using the SE Brazil seismic data, the accuracy of Throw-Distance plots was shown to be quantitatively lost when sampling intervals were larger than 37.5 m (every 3 shot-points) for the 'unique' crestal fault families in this thesis. However, this thesis demonstrates that sampling intervals adopted by interpreters should differ depending on the resolution of seismic data used, and the total length of investigated structures. A practical *sampling interval/fault length* ratio is therefore proposed in this work to address the caveats behind using variable (and indiscriminate) sampling intervals when analysing faults.

Supra-salt sequences capable of promoting episodic fluid flow in regions of salt tectonics are of vital economic importance. Following on the two latter themes (crestal faulting and fault scaling), the thesis addressed the episodic fluid flow documented in the Espírito Santo Basin in a third stage. The results of this section are proposed as a case study for supra-salt sequences. In detail, seal failure is systematically recorded in the study area, and is interpreted to have contributed to most of the supra-salt fluid flow events investigated in SE Brazil. Six types of traps are therefore widely identified in supra-salt successions of the Espírito Santo Basin – all forming examples of trapping geometries in sedimentary basins associated with salt tectonics.

Regardless of a thermogenic or diagenetic origin for fluid off Espírito Santo, the results in this thesis demonstrate important (and focused) fluid flow above salt giants when, at least, two critical conditions are observed: 1) a certain thickness of overburden

strata is deposited on top of the salt structures, 2) the generation of highly developed (i.e. large) crestal fault systems is observed over these same salt structures. It is therefore postulated that, if overburden strata is thinner than a certain value, or pressure imposed by growing salt increases significantly, active salt intrusion occurring together with fluid flow will replace more focused fluid flow features in salt giants.

Table of Contents

List of figures

Fig. 4-12 Expansion Indexes (EI) for major faults showing variation in strata thickness across their hanging-wall and footwall blocks. An EI of >1 implies thickening of strata in the hanging-wall section, whereas EI < 1 means thinning of hanging-wall strata relative

List of tables

List of equations

Chapter 1

Introduction

1.1 Thesis layout

This thesis comprises four principal sections and eight chapters. Part 1 includes Chapters 1 to 3, which introduce the main themes addressed in this thesis. Chapter 1 presents the aims of the research and a literature review. Specifically, salt tectonics, faulting mechanisms, fault-growth models, fault-analysis techniques and fluid flow features typical of passive continental margins are summarised in Chapter 1. Chapter 2 describes the data and methods used to complete the thesis. Three-dimensional data interpretation and methods used in seismic interpretation and structural analyses are presented in this chapter, followed by a section specifying the new methods developed in Chapter 6. Chapter 3 focuses mainly on the geological setting of the Espírito Santo Basin, which comprises the main study area in this thesis. Seismic stratigraphic interpretation methods used in subsequent chapters (Chapters 4 to 6) are introduced in Chapter 3.

The second part of the thesis includes the main result chapters. Chapter 4 documents the reactivation histories of crestal faults in the Espírito Santo Basin. A new fault propagation model for crestal faults is proposed here, with wider applications to understand fault evolution in areas of important salt tectonics. Chapter 5 focus on a unique set of tier-bound domino faults (TBFs) associated with a significant episode of fluid release within supra-salt successions. Episodic fluid flow, and how crestal faults are associated with these fluid release events, are investigated in Chapter 5. Chapter 6 presents a new method to quality control (and thus validate or rebuke) the interpretation of fault segmentation and growth histories in multiple scales of analysis. Comprehensive criteria to guide future fault analyses, and consequences of failing to follow these same criteria, are proposed in Chapter 6.

Part 3 of this thesis includes Chapter 7, i.e., the main discussion chapter. Limitations and future research are briefly summarised in Part 3. The discussion chapter comprises three main themes that are closely related to the research questions in this work: 1) What are the effects of scale variations and techniques used to undertake fault analysis and to postulate fault growth histories; 2) What seal failure mechanisms dominate areas of important salt tectonics, often occurring in association with crestal fault reactivation and fluid readjustment in supra-salt successions; 3) What types of supra-salt traps are associated with fluid flow features in salt-rich sedimentary basins.

Chapter 8 summarises the main conclusions of this research.

1.2 Rationale and aim of the thesis

1.2.1   Rationale

Exploration in regions with significant salt tectonics is important for the oil and gas industry. The Gulf of Mexico, North Sea, the Brazilian and West Africa continental margins, comprising the majority of oil and gas fields in salt-rich basins (Hudec and Jackson, 2007), have a history of exploration that spans over a century. In the last two decades, new oil and gas discoveries offshore Brazil, and the conjugate West African margin, have led to further investment into these offshore areas with significant salt tectonics. However, the development of fault systems in regions dominated by salt are still poorly understood as: 1) acquiring new, state-of-the-art seismic data in such areas is expensive, especially as regions with important halokinesis extend into ultra-deep water regions (> 1500 m water depth); 2) the resolution of seismic data has been limited by the slow development of high-quality acquisition and processing methods, which only became available in the recent decade (post-2000); 3) the study of fault systems in areas dominated by salt tectonics is often complex as faulting is controlled by local processes, structures show relatively small scales, but show more complex evolution histories than their counterparts in salt-poor sedimentary basins (Alves et al., 2009; Mattos et al., 2016, Morley, 2007; Rowan et al., 1999; Ze and Alves, 2016). With increasing investment into ultra-deep water areas, and significant advances in 3D seismic technology, it became possible to unravel the structural evolution of salt-rich basins and how distinct fault systems relates to regional petroleum systems.

To investigate the mechanisms of fault formation and evolution comprises a fundamental tool for the assessment of potential hydrocarbon reservoirs. Complex fault growth and reactivation styles have been systematically recorded above thick evaporite deposits in sedimentary basins (Brun and Fort, 2011; Hudec and Jackson, 2007; Vendeville and Jackson, 1992a, Smit et al., 2008; Stewart, 2006). Halokinesis, which is often influenced by a complex interaction of regional tectonics and local processes such

as the deposition of mass-transport deposits (MTDs) or submarine-channel incision, has primary influence on the structural deformation of supra-salt successions. With modern structural techniques (displacement analyses, stress analyses, expansion index, isochron maps, etc.) being systematically applied in the analysis of faults at different scales of observation, scale variance becomes an important aspect affecting the quality of interpretations - for similar fault systems in the same region, different researchers will adopt different scales of observation and data collection, a caveat that can result in misunderstandings when interpreting fault growth models.

Finally, a key question under investigation in multiple sedimentary basins is the relationship between pre- and supra-salt fluid systems - one of the least understood aspects of petroleum systems in regions affected by salt tectonics. Salt layers are often viewed as impermeable structures that hinder fluid flow. However, salt rock samples indicate hydrocarbon residuals within salt intervals (Schoenherr et al., 2007) and relatively connected fracturing networks (Jackson et al., 2015; Davison, 2009), two characteristics that hint at important phases of seal failure through evaporite successions. Mechanisms of seal failure, and how they relate and/or influence supra-salt fluid flow and compartmentalisation, still remain an important research question in many a sedimentary basin in the world.

1.2.2   Aims of the thesis

Using high-resolution 3D seismic data provided by CGG®, this thesis addresses some of the least understood questions on fault systems in regions recording important salt tectonics. More specifically, this thesis aims at addressing the following hypotheses:

1) Crestal fault propagation history is closely associated with localised halokinesis. In this particular case, 'standard' fault propagation models will not apply to crestal fault propagation; rather, complex fault growth histories will be recorded as a result of the complexity of localised salt movements. If this hypothesis is not valid, crestal faults will show a simple geometry, likely dominated by isolated fault

segments with little interaction and linkage between them. In addition, Throw-Distance (T-D) and Throw-Depth (T-Z) data will show very simple profiles.

2) Crestal fault families breach seal units in areas with salt tectonics and are closely associated with fluid flow. If this is the case, one should observe fluid flow features associated with crestal faults and associated fault reactivation should be observed systematically in the study area(s). If this hypothesis is not valid, one should observe very scarce evidence of fluid flow, and most fluid migration will occur away, and below, developed salt structures.

3) Displacement analysis to postulate fault growth histories is closely associated with the interpreters' selection of sampling intervals. Improved geometric and sampling constraints are necessary. If this hypothesis is true, one will be able to record significant variations in interpreted fault growth models (and T-D and T-Z plots) when varying the sampling intervals of acquired data. If the hypothesis is not valid, coarse throw-sampling techniques will produce similar results when interpreting fault propagation models.

4) In sedimentary basins with significant salt tectonics, salt seal failure occurs often, which transfers fluid into supra-salt tectonics forming fluid compartments. With improved seismic data derived from the oil and gas industry, anomalies within salt structures are expected to be revealed in more detail so to understand mechanisms of salt-seal failure. If the hypothesis above is valid, interpreters should be able to identify varied styles of fluid migration in regions dominated by salt tectonics, if using high-resolution data as that used in this thesis. If the hypothesis is not valid, fluid flow thorough salt giants will be essentially of similar magnitude(s) as previously recorded on vintage 2D seismic data.

5) Trap geometries in supra-salt sequences are closely associated with the growth histories of crestal faults. If this is the case, traps associated with crestal faults should dominate in supra-salt successions. If this hypothesis is not valid, most fluid should be trapped in simpler, broader structures such as diapir-related anticlines with little influence of faults on fluid migration and entrapment.

The following sections will present a summary of the relevant literature on salt tectonics, fault propagation models, structural analyses and fluid flow in sedimentary basins, all themes directly related to this work.

1.3 Salt tectonics and halokinesis

Approximately 120 basins around the world record some degree of halokinesis (Fig. 1-1). Even though evaporites comprise only < 2% of the world's sediment rocks, 14 of the world's 25 largest oil fields and 9 of the world's 25 largest gas fields are located in regions of important halokinesis. Among these latter regions are included offshore and onshore prospects in the Gulf of Mexico, the North Sea Basin, and the conjugate continental margins of Brazil and West Africa (Hudec and Jackson, 2007), which present both sub- and supra-salt oil and gas fields (Hudec and Jackson, 2007; Yu et al., 2014).

Halokinesis – the subsurface movement of salt under certain loading and P-T conditions - occurs above a source salt layer capable of deforming its overburden strata to a great extent (Jackson et al., 1994). Salt systems often form genetically and kinematically linked groups of faulted intervals, diapirs, and welds connecting sub-salt and supra-salt strata (Rowan et al., 1999). Important halokinesis develops in salt-rich basins under three main geological settings: 1) inter-cratonic basins as represented by the Zechstein Supergroup of the North Sea (Cameron, 1992; Stewart and Coward, 1995); 2) syn-rift and post-rift passive margins such as those developed along East Brazil and its conjugate West African margin (Mohriak et al., 2008; Mohriak et al., 2012; Chang et al., 1992a, Petri, 1987); 3) continental collision zones and foreland basins such as the Tarim Basin in Northwest China (Yu et al., 2014).

Different classifications of salt basins have been proposed in the literature when considering the timings of salt deposition relative to rifting such as pre-rift, syn-rift, post-rift salt basins (Jackson and Vendeville, 1994) or pre-rift, syn-stretching, syn-thinning, and syn-exhumation salt basins (Rowan, 2014).

Fig. 1-1 Global distribution of sedimentary basins comprising salt structures (dark-grey areas), including oil and gas basins in the Gulf of Mexico (GC), the North Sea Basin, the Red Sea, Southeast Brazilian margin, Western African margin, the Mediterranean Sea and the Middle East (modified from Hudec et. al., 2007). The red box bounds the main study area in this thesis, which comprises widespread evidence for salt tectonics. AD South Adriatic; AG Agadir; AL Atlas; AM Amadeus; AN Appenines; AP Appalachian Plateau; AQ Aquitaine; AR Arabian; AT Atacama; AZ Amazon; BB Bohai Bay; BC Baltimore Canyon; BE Betic; BG Benguela Namibe; BL Balearic; BP Bonaparte; BR Berrechid; CA Carson; CB Cuban; CG Canning; CL Cicilia Latakia; CK Cankiri; CN Carnavon; CP Campos; CR Carpathian; CS Chu Sarysu; CT Cantabrian West Pyrenees; DD Dnepr Donetz; DK Danakil; DS Dead Sea; EA East Alpine; EB Ebro; EM Emirates; EN Eritrean; ER Essaouira; ES Espirito Santo; ET East Texas; FL Flinders; FP Flemish Pass; GB Guinea-Bissau; GC Gulf Coast; GE Georges Bank; GK Great Kavir–Garmsar Qom; GN Gabon; GQ Guadalquivir; HB Haltenbanken; HM Hadhramaut South Yemen; HP Haymana Polatli; HS Horseshoe; HT Haitian; IL Iljac Tabriz; IO Ionian; JA Jeanne d'Arc; JH Jianghan; JU Jura; KH Khorat; KL Kalut; KM North Kerman; KQ Kuqa; KT Katanga; KW Kuwait; KZ Kwanza; LC Lower Congo; LG Ligurian; LP La Popa; LU Lusitanian; LV Levantine; MA Maestrat; MD Mandawa; MJ Majunga; MK Mackenzie; MN Moesian; MO Moncton; MP Mississippi; MS Messinian; MT Mauritania; MZ Mozambique; NK Nordkapp; NL North Louisiana; OF Officer; OM Oman Fahud; OR Orpheus; OU Oriente Ucayali; PA Palmyra; PC Pricaspian; PI Parry Islands Central Ellesmere; PT Petenchiapas; PX Paradox; PY Pripyat; QD Qaidam; RF Rufiji; RH Rhodanian; RM Rio Muni; SA Sabinas; SB Sable; SC Sicilian; SE Senegal; SF Safi; SG Sergipe Alagoas; SI Saltville; SK Somal Kenya; SL Salina Sigsbee; SN Santos; SR Salt Range; SS Scotian Slope; ST South Texas; SU Suriname; SV Sverdrup; SW South Whale; SZ Suez; TD Tadjik; TF Tarfaya; TK Takutu; TM Timan; TR Tromsø; TV Transylvanian; TY Tyrrhenian; WH Whale; YE Yemeni; ZG Zagros; ZQ Zipaquira; ZS Zechstein.

1.3.1 Salt properties and flow mechanisms

1.3.1.1 Salt properties

Pure salt comprises a crystalline aggregate of halite (NaCl) (Jackson, 1997). Salt layers in sedimentary basins often include other (evaporite) minerals such as hydrite, anhydrite and carnallite, and interbedded carbonate and siliciclastic sediments (Warren, 2006). The unique physical and chemical properties of salt contribute to its viscous-plastic behaviour when buried beneath non-evaporite deposits, resulting in its complex overburden deformation. The inherent viscosity of salt makes it sensitive to relative

increases in temperature and pressure, and to stress variations imposed by an often-mobile and thickening overburden strata.

Sedimentary rocks lose effective porosity within the first 100-200 meters of burial, after which they will become less compressible. With salt, density will remain more or less constant, for example, 2160 kg/m3 in pure halite (Talbot and Jackson, 1987a, Talbot and Jackson, 1987b) (Fig. 1-2). This property differs from that of siliciclastic sediments, which progressively lose their porosity and permeability as a result of compaction (Hudec and Jackson, 2007).

Different responses of salt and its overburden strata with increasing burial depths result in important density inversions. When overburden units exceed a certain thickness (500-2000 meters according to 'ideal' compaction trends for different lithologies), salt layers will concentrate important buoyancy forces (Hudec and Jackson, 2007). The viscosity of rock salt is usually inferred from laboratory experiments, field observations and numerical models, typically falling between 1010 -to-1023 Pa s (Mukherjee et al., 2010). If one disregards known impurities within rock salt, the viscosity of rock salt depends on four main factors as water content, temperature, grain size and differential stress (Talbot and Rogers, 1980; Van Keken et al., 1993). Impurities and spatial variations in viscosity are important in evaporite sequences; though salt is viewed as an impermeable material that acts as a competent seal interval, saturated brine of different chemical compositions, and hydrocarbon residuals, are often observed in naturally deformed salt (Schoenherr et al., 2007).

1.3.1.2 Salt-flow mechanisms

Density inversion, which causes salt-rich basins to become gravitationally unstable, is postulated as the main mechanism for 'buoyant' salt rise to the surface. For salt to move due to density inversion, a minimum thickness of overburden strata between 1600 to 3000 m is necessary (Nelson and Fairchild, 1989) or 2000 to 4000 m (Jackson and Lewis, 2012).

Apart from buoyancy, which can potentially contribute to important halokinesis, unloading of overburden strata by erosional and mass-wasting processes, together with
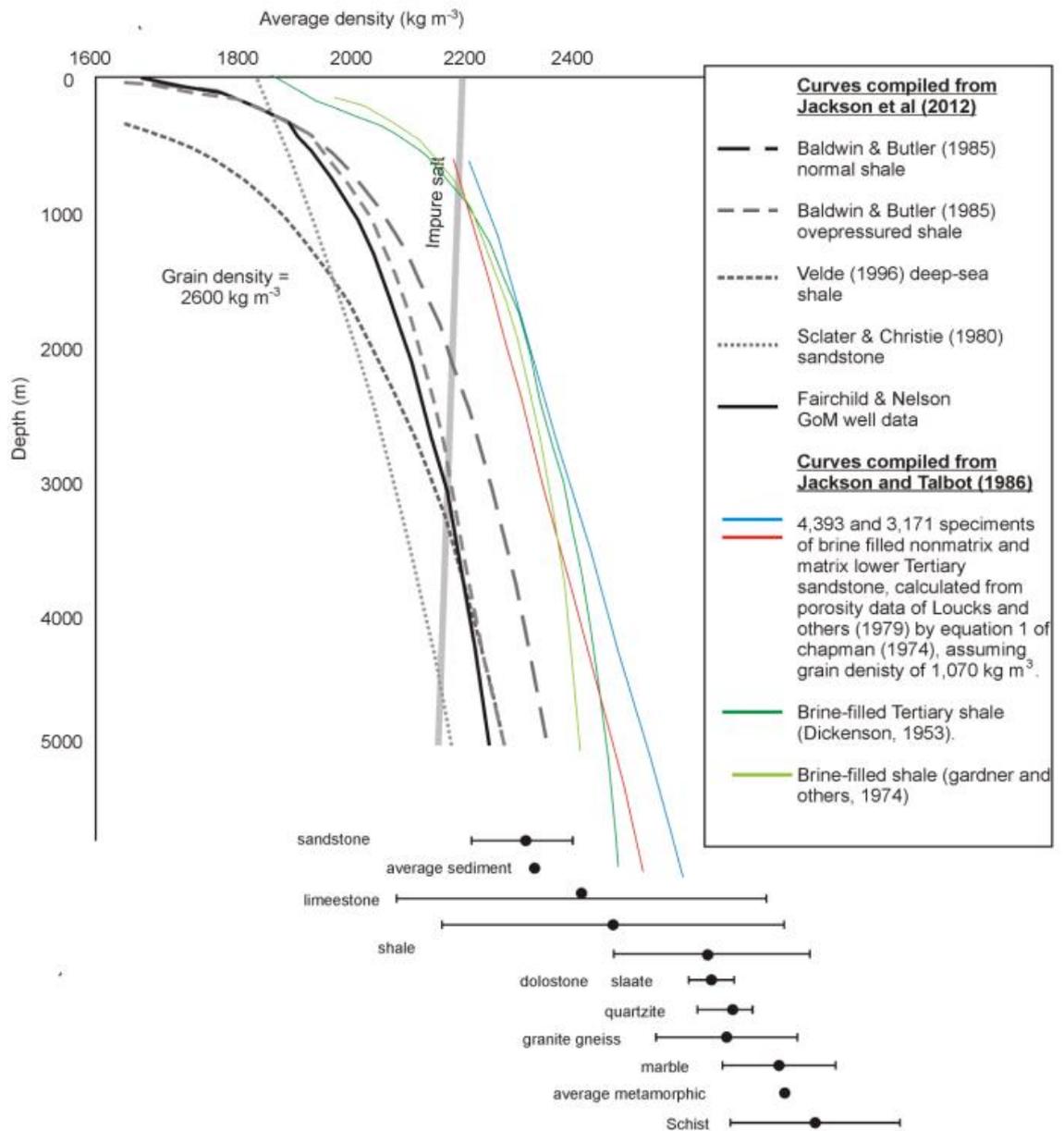
Fig. 1-2 Density-depth curves for halite and varied overburden lithologies. Figure from Carruthers (2012).

regional extensional and compressional stresses, can also promote salt movement in many a sedimentary basin (Stewart and Coward, 1995; Jackson and Vendeville, 1994; Evans et al., 2003). Conversely, important resisting forces retarding the flow of salt, such as the strength of overlying strata and friction between salt layers and surrounding sub- and

supra-salt strata, have also been proposed in the literature (Hudec and Jackson, 2007; Alves et al., 2017) (Fig. 1-3).Three driving forces are considered in the published literature as initiating and promoting salt flow on regional scales of analysis: gravitational loading, displacement loading and thermal loading (Kehle, 1988; Hudec and Jackson, 2007). Differential overburden loading is often regarded as the primary mechanism inducing salt movement from high- to low-pressure zones (Fig. 1-4). Gravitational loading results from the combined weight of the rocks overlying the salt and the gravitational body forced inside the salt. Displacement loading refers to the movement of sediment towards or away from the salt, a phenomenon usually related to regional tectonics such as regional extension or shortening. Thermal loading is postulated to have a significant influence on salt flow due to the high thermal conductivity of salt rock, with volume changes occurring whenever thermal conditions change.

The initial mechanism for salt flow varies in different salt basins (Rowan, 2014). Salt mobilisation and diapirism are suggested to be triggered by thick-skinned extension during the stretching stage in pre-rift salt basins. In syn-stretching salt basins, mobility begins as soon as the salt is deposited. In syn-exhumation salt basins, salt mobility is triggered by gravity gliding as the margin tilts oceanwards due to differential thermal subsidence (Rowan, 2014).
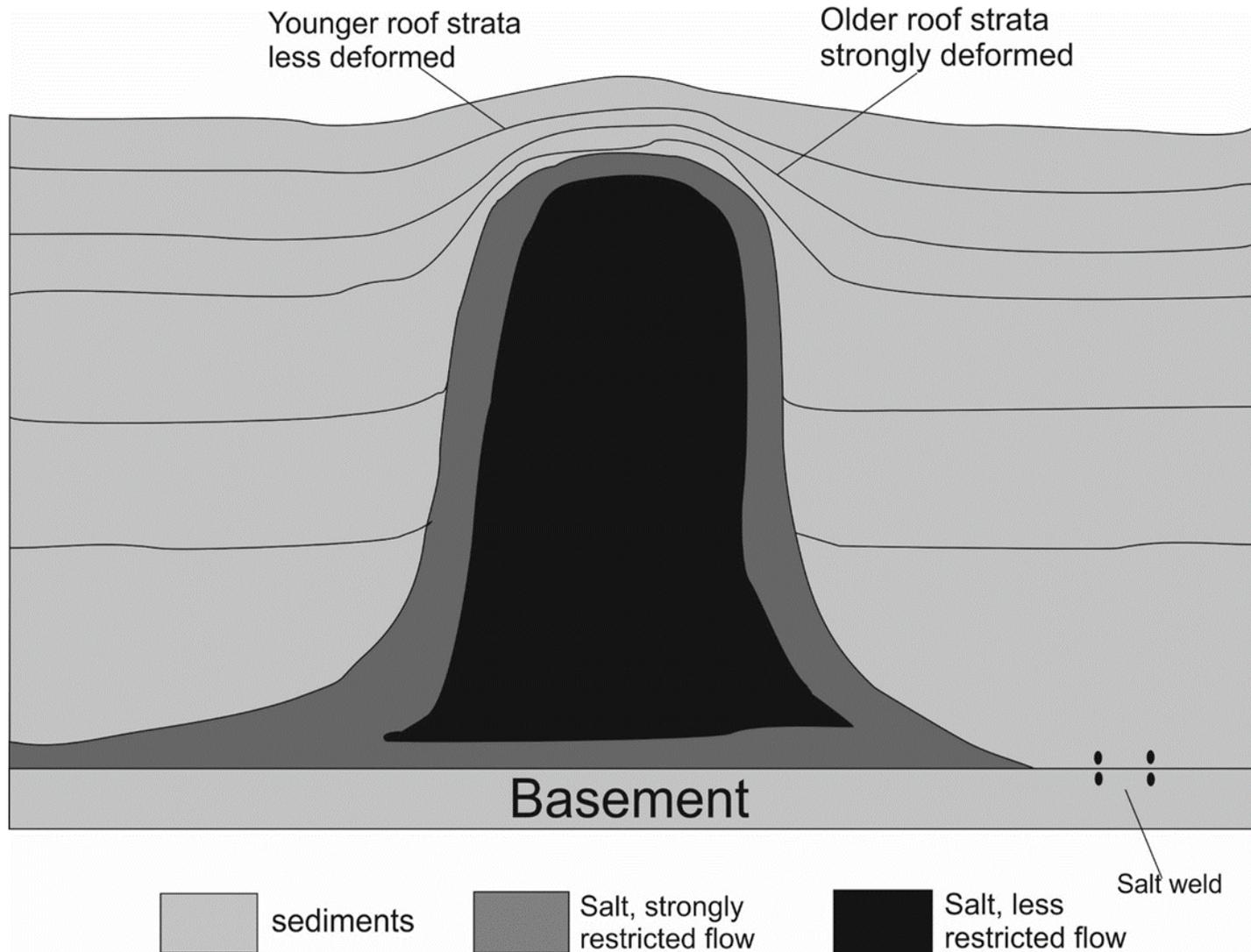
Fig. 1-3 Factors resisting salt flow. Salt deformation occurs if the roof is thin and weak, but becomes progressively more difficult as the roof thickens. Salt is strongly sheared near the edges of salt bodies during flow, a phenomenon causing resistance to deformation. Salt flow is inhibited when the salt layer becomes too thin. Modified after Hudec and Jackson (2007).

12
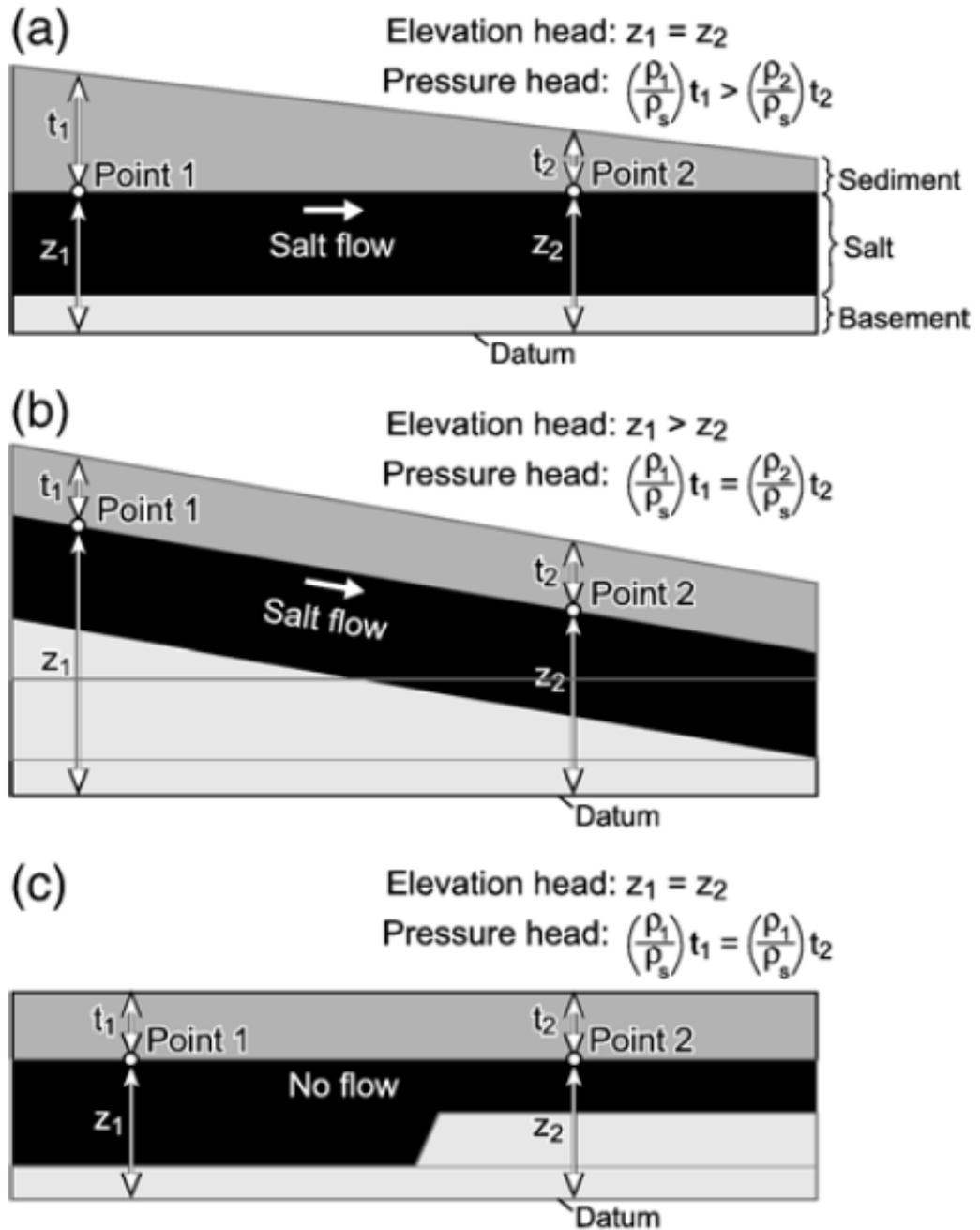
Fig. 1-4 Differential overburden loading is the main driving force behind halokinesis. (a) Salt will flow from Point 1 to Point 2 along a pressure head gradient. Variations in loading may be produced by sedimentation, deformation or erosion. (b) Salt will flow from Point 1 to Point 2 down the elevation head gradient. (c) A uniform overburden thickness above a flat-lying salt layer produces neither elevation nor head gradients. Salt remains at rest. Figure from Hudec and Jackson (2007).

13

1.3.2   Types of salt structures

The onset of salt flow (halokinesis) is recorded when driving forces exceed the resisting forces. Following the initiation of halokinesis, salt will buoyantly rise in a vertical or sub-vertical direction to form structures with different geometries (Fig. 1-5). According to the relationship between salt structures and its source locations, salt structures can be divided into two major categories: autochthonous and allochthonous (Mohr et al., 2007; Hudec and Jackson, 2007). "Allochthonous salt" refers to mobilised salt that overlies stratigraphically younger rocks, such as salt canopies and salt glaciers. 'Allochthonous salt' often connects with the feeders and shows arching roofs (e.g. salt anticlines) (Fig. 1-5). Salt structures, which often refer in the literature to diapiric salt structures or salt diapirs that are dependent from the mechanisms of salt intruding the overburden, are classified into different groups (see details from Jackson et al., 1994). Often, the more common cone-shaped diapirs, or those with circular planforms, are called salt stocks. Elongate salt structures are termed salt walls, and are common in the study areas of this thesis (Fig. 1-5).

1.3.3   Modes of salt diapirs

The flow of salt can be diapiric or non-diapiric. In parallel, overburden sediment must be removed or replaced so that a diapir can be formed. Modes of diapirism include reactive, thrust, active, ductile, erosional and passive piercement (Hudec and Jackson, 2007) (Fig. 1-6).

The generation of salt structures, as observed on seismic data, involves complex processes, and diapiric salt structures often form due to regional extension in an initial stage, e.g. diapirs on the Brazilian continental margin and in the Gulf of Mexico (Vendeville and Jackson, 1992). After salt flow is initiated, mechanisms for salt growth and halokinesis vary due to regional and local controls on salt structures (Cartwright et al., 2001; Rouby et al., 2003; Yu et al., 2014). It is noted that a salt structure has a multi-stage nature, and that salt-diapir growth does not involve simple inward flow and
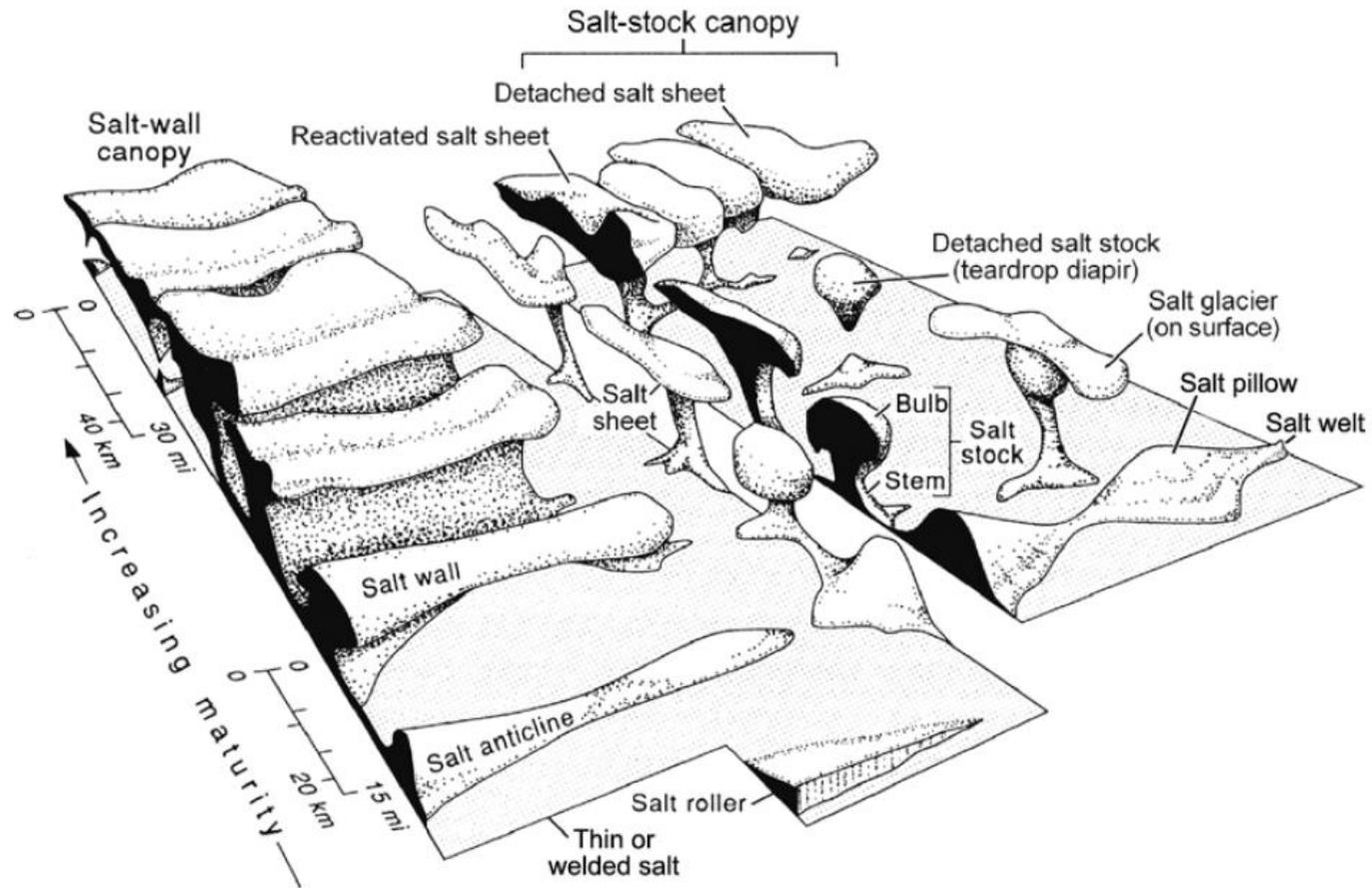
Fig. 1-5 Block diagram showing the principal shapes of salt structures relative to increasing structural maturity and size. In the upper slope domain, predominant salt structures include salt rollers, salt pillows and salt anticlines. In the transitional domain, salt walls predominate, whereas the lower slope domain is dominated by mature salt structures such as canopies. Figure from Hudec and Jackson (2007).

thickening of salt (Trusheim, 1960; Jackson et al., 2014; Ge et al., 1997). In fact, known mechanisms forming salt diapirs include reactive, active and passive diapirism (Fig. 1-7).

1.3.3.1 Reactive diapirism

Regional extension, which thins the overburden above salt intervals, accounts for reactive diapirism (Jackson and Vendeville, 1994; Vendeville and Jackson, 1992a, Vendeville and Jackson, 1992b). During this process, 'room' or accommodation space is created by the thinning overburden and, more frequently, by separating faulted blocks to create space for salt to intrude (Fig. 1-7). During reactive diapirism, salt diapirs will stop rising on the condition that sufficient overburden remains above the salt structures when regional extension stops, as salt diapirism is controlled by regional extension (Jackson and Vendeville, 1994). As the breaching of the resisting forces that retard salt diapirism will result in weakened salt roofs, one possible phenomenon to take into account is that of salt diapirs intruding the overburden strata up to the surface, a process involving both active and passive diapirism (Vendeville and Jackson, 1992a, Vendeville and Jackson, 1992b, Jackson and Vendeville, 1994; Hudec and Jackson, 2007).

1.3.3.2 Active diapirism

An active salt diapir often presents an arching roof (Schultz-Ela et al., 1993; Dooley et al., 2009). The main driving forces for active diapirism are either regional compressional forces or buoyancy, especially when a previously formed salt structure is present in the area where the diapir is ultimately formed (Davison et al., 1996). As salt is weaker than other lithologies in sedimentary basins, the overburden strata above salt diapirs is often shortened during regional compression in greater degree than adjacent areas with relatively little salt. Shortening forces adding to previously deformed salt structures often amplify any pre-existing structures, such as crestal faults above salt diapirs (Hudec and Jackson, 2007).

16

Buoyancy forces alone do not provide sufficient lift to form active diapirs in areas of thick overburden rocks (Dooley et al., 2009). A threshold of 260 m was suggested for buoyancy forces to raise the post-salt overburden (Davison et al., 1996). However, the validity of such a strict value can be argued due to the fact that the strength of salt's roofs, and the retarding forces generated both within salt bodies and between salt structures and their flanking siliciclastic, are known to vary in many a sedimentary basin. Jackson et al. (1994) suggested a 5:1 ratio between the thickness of strata flanking salt structures and the thickness of the overburden strata as a threshold for buoyancy to act as the main driver of diapirism. In fact, with an overburden thickness < 20% of the flanking strata thickness, active salt diapirism tends to occur without regional compressional forces.

1.3.3.3 Passive diapirism

Passive diapirism is often driven by differential loading between adjacent salt-withdrawal basins when diapirs are already exposed at the surface (Barton, 1933; Jackson et al., 1994), as in the case of the Persian Gulf. Here, large volumes of sediment deposited during the Lower Miocene led to greater subsidence of salt-withdrawal basins and promoted passive diapirism of the (Early Miocene) Fars salt, as well as further inflation of Hormuz salt into neighbouring structures (Alsouki et al., 2011). Passive diapirism often places the salt's roof on the depositional surface. However, the contrast between salt-supply and sedimentation rates often results in partially covered roofs in evolving salt structures. In any case, buoyancy is sufficient to drive further salt rise during passive diapirism (Rowan et al., 2003).
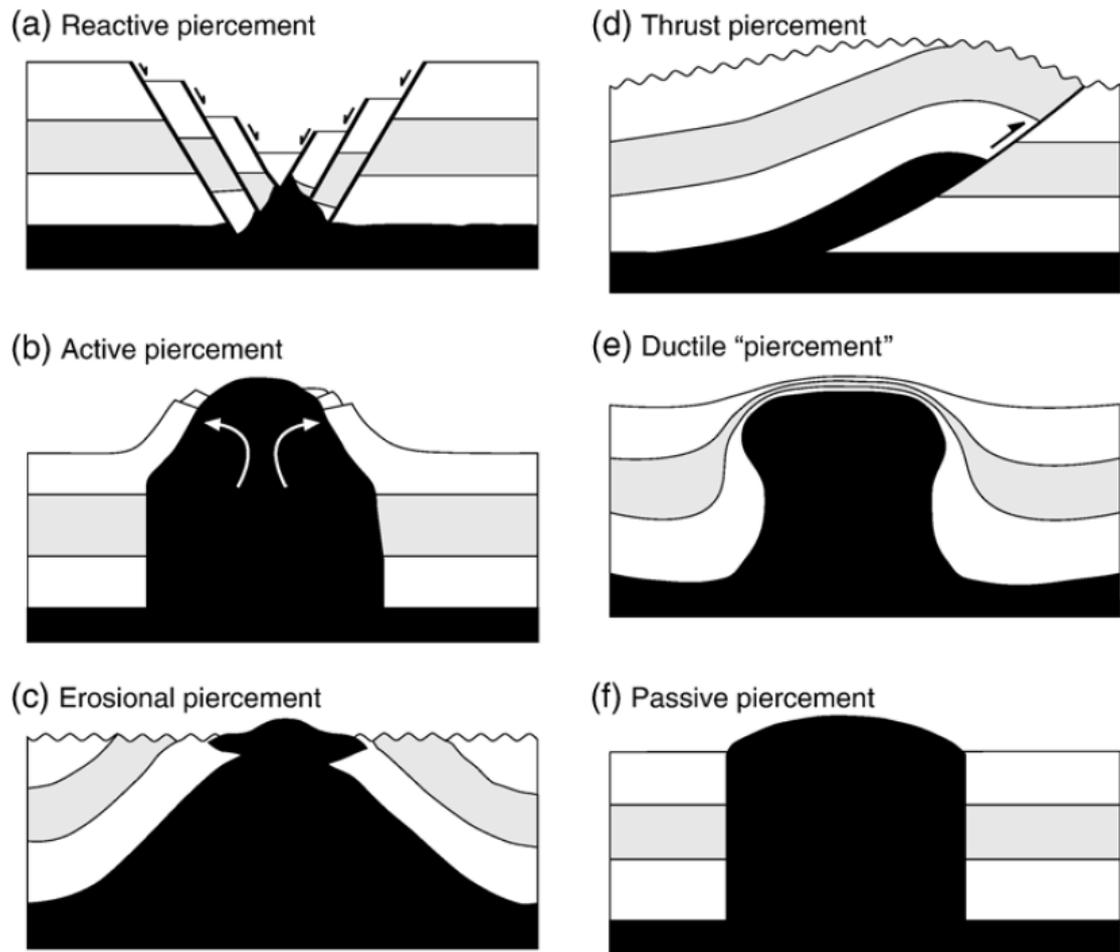
Fig. 1-6 Modes of diapir piercement shown in schematic cross sections. Figure from Hudec and Jackson (2007).

DESCRIPTION	REACTIVE SALT DIAPIR	PASSIVE SALT DIAPIR	ACTIVE SALT DIAPIR	SQUEEZED SALT DIAPIR	EXTRUDED SALT DIAPIR
DEFINITION	Diapir growth initiated by regional extension	Passive diapirs grow at the depositional surface as the surrounding sediments subside into the salt layer.	Active diapirs grow by forcefully intruding their overburden and raising it above the regional datum.	Active diapirs which grow by lateral shortening or regional compression are termed squeezed diapirs.	Diapirs are extruded at the surface when either salt supply far exceeds aggradation rate or by later erosion.
SCHEMATIC DIAGRAM					
SEISMIC EXAMPLE					
DIAGNOSTIC FEATURES	**Diapir geometry:** T-Pee/traingular shaped cross section. often elongate in plan-form parallel major faults, diapirs and stocks often sit at fault intersections. **Deformation:** Inward facing extensional faults, normal faults parallel regional trends (orthogonal to extension direction). **Stratigraphic architecture:** **Other:**	**Diapir geometry:** collumnular, conical, outward flaring (sometimes at more than one level around stem). **Deformation:** minor radial faulting around flanks, drag folds depending on composition of overburden. **Stratigraphic architecture:** rim-synclines, parallel onlap, minor erosional surfaces and facies changes, periodic onlap onto crest of diapir (often rotated during later active phases) **Other:**	**Diapir geometry:** Bulbous, conical **Deformation:** elevation of diapir head above regional datum, thick arched roof, radial faults in carapace and around flanks, concentric thrust faults **Stratigraphic architecture:** steeply dipping strata against salt diapir, thinning of strata toward diapir, convergent onlap, offlap. **Other:** Deflection of channels around structure, failure of material on flanks of structure.	**Diapir geometry:** Bulbous head, detached head, narrow stem or weld, salt pedestal at base of stem. **Deformation:** thick arched roof, radial faults in carapace, reverse concentric faults beneath bulbous head, inverted faults, rotated normal faults, box fold in carapace **Stratigraphic architecture:** overturned strata beneath bulbous head, elevation of carapace strata above regional datum, thinning if strata toward diapir, convergent onlap, offlap. **Other:** Deflection of channels around structure, failure of material on flanks of structure.	**Diapir geometry:** Mushroom shaped head which is much wider than the underlying stem. **Deformation:** Base overhang of salt diapir is parallel to younger, underlying overburden. thursting beneath and infront of extruded wing. **Stratigraphic architecture:** overturned strata beneath bulbous head, onlap onto extruded wing, parallel strata above the diapir head **Other:**

Fig. 1-7 Table summarising the different modes of salt diapir growth; reactive diapir (column 2), passive diapir (column 3), active diapir (column 4), squeezed diapir (column 5) and extruded diapir (column 6). Figure from Carruthers (2012).

19

1.3.4   Internal deformation and faulting of salt

Evaporites are thought to be the weakest lithology in sedimentary basins, and are viewed as a viscous material deforming by viscous or power-law flow, e.g., pressure solution, solid state diffusion, and dislocation creep (Davison, 2009). When physically modelling halokinesis, salt layers are often represented by viscous silicone in laboratory conditions (Dooley et al., 2015).

Systematic studies into internal deformation and faulting in salt only began in the last decade with advances in 3D seismic technology, whenever high-resolution seismic data was available (Jackson et al., 2014; Jackson et al., 2015; Strozyk et al., 2012). Salt structures often comprise thick volumes of evaporites (Hübscher et al., 2007), with acoustically transparent internal reflections on seismic data, and have been previously regarded as lithologically homogeneous (Schoenherr et al., 2007). With improved seismic data acquisition and processing, the internal character of salt giants that comprise significant volumes of salt has been progressively revealed in detail. Recent studies indicate that salt rock is impure (Warren, 2016; Davison, 2009; Schoenherr et al., 2007), and that hydrocarbon residuals exist in fractures inside 'impure' evaporite intervals (Schoenherr et al., 2007). New seismic data have also revealed, for the first time, seismically resolved strata and internal deformation within salt giants (Alsop et al., 2015; Jackson et al., 2014; Alves et al, 2017) (Fig. 1-8).

Brittle faulting of salt has rarely been modelled in laboratory conditions, or even observed at outcrop. However, localised brittle faulting of salt does occur when effective stresses within salt structures are extremely low, or fluid pressure within 'impure' salt structures reaching lithostatic conditions (Cristescu et al., 1998; Schléder et al., 2008; Schléder and Urai, 2007). High fluid pressures, high local stresses, and rapid strain rates are documented as the main mechanisms of brittle faulting of salt in multiple physical models (Schoenherr et al., 2007; Schléder and Urai, 2007; Ghanbarzadeh et al., 2015) (see Table 1-1 for examples from the published literature).
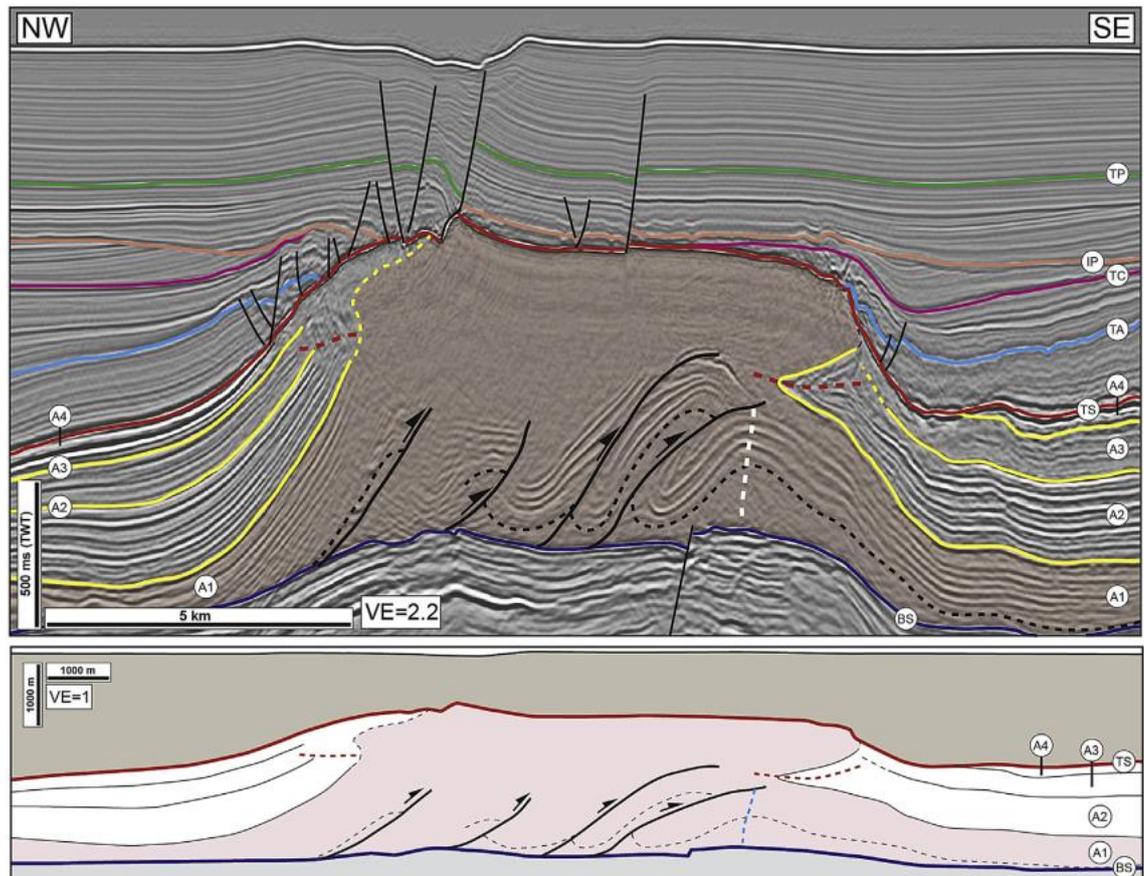
Fig. 1-8 Seismic section and line diagrams illustrating intra-salt deformation. Figure from Dooley (2015).

Basin	Evidence	References
Santos Basin	Folding, recumbent folds	C.A.L Jackson, 2014; 2015
Great Kavir, Iran		Jackson et al., 1990
Hanigsen - Wathlingen salt dome	Forced folding	Schachl, 1987
Sergipe - Alagoas Basin	Faulting	Carvalho et al. 1995; Machado & Szatmari, 2008; Davison, 2009
Santos basin	Faulting	Freitas, 2006
Pugwash salt diapir (Nova Scotia)	Faulting	Evans, 1965; Carter, 1990
Iranian salt	Faulting	Talbot & Aftabi 2004
Gorleben salt diapir, northern Germany	Faulting	Bornemann 1991; Zirngast 1996
Gulf Coast of Mexico salt domes	Faulting	Kupfer, 1962; 1976; 1990; Neal et al. 1993
Northern Red Sea	Faulting	W. Bosworth

Table 1-1 Internal deformation and faulting of salt as summarised from the published literature.

1.4 Fault propagation models and scaling laws

1.4.1   Terminology used in the thesis

The published literature has proposed a complex set of terms abridging multiple fault propagation models. The terminology used in this thesis is briefly summarised in Figure 1-9. Fault length comprises the along-strike dimension of fault planes along their lateral tips. Fault height is the longest dimension of the fault plane in a direction normal to the strike. These two dimensions are independent of the orientation of the slip vector and can be identified both on outcropping fault surfaces, and on faults interpreted on 3D seismic data (Kim and Sanderson, 2005). When fault characteristics are compared for different fault populations, fault dimensions can be expressed as their maximum values Lmax and Hmax. Fault displacement decreases to zero towards the lateral-tip loops of an ellipse (fault surface) and increases to a maximum (Dmax) close to the centre of the fault (Childs et al., 2003; Cowie and Scholz, 1992c, Kim and Sanderson, 2005; Walsh and Watterson, 1988).

1.4.2   Scaling laws

Fault growth models are based on the scaling of fault dimensions, i.e. they reflect distinct fault scaling laws, namely the relationship between fault displacement and length (D/L) (Walsh and Watterson, 1988; Cowie and Scholz, 1992c, Cartwright et al., 1995). Typical non-linear power-law and linear power-law relationship have been proposed in the published literature based on extensive data sets (Kim and Sanderson, 2005). The relationship between fault displacement and length is, therefore, expressed as:

$$D = c*L^n$$

Equation 1-1

23
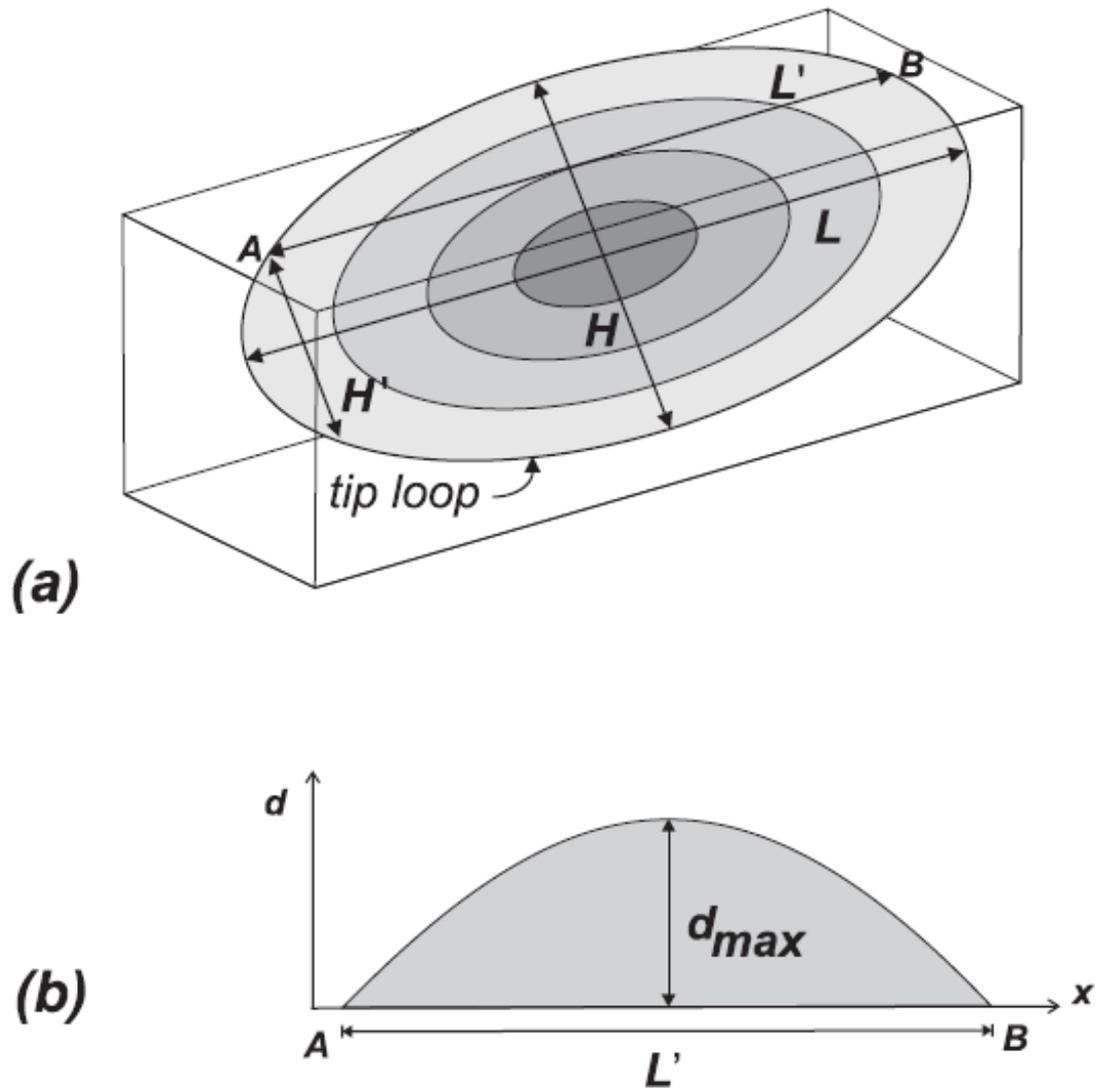
Fig. 1-9 (a) Diagram illustrating displacement distribution on an elliptical fault surface of length (L) and height (H). (b) Displacement (d)–distance (x) plot of fault trace along line A–B. Figure from Kim and Sanderson (2005).

where c is a constant parameter closely related to the lithology of the rocks intersected by the faults. The exponent n varies from 0.5 to 2 (Walsh and Watterson, 1988; Watterson, 1986; Marrett and Allmendinger, 1991; Gillespie et al., 1992; Cowie and Scholz, 1992c, Scholz et al., 1993; Dawers et al., 1993; Clark and Cox, 1996; Schlische et al., 1996; Fossen and Hesthammer, 1997) (Fig. 1-10). An exponent of 1 indicates a linear scaling law for fault dimensions, and $n \neq 1$ reflects a scale dependent fault geometry. This scale-dependent fault scale relationship often relates to distinct fault-slip events (Cowie and Scholz, 1992).

Significant data scattering is observed when discrete datasets are used and compared, often leading to misinterpretations of scale relationships between faults (Cowie and Scholz, 1992; Kim and Sanderson, 2005; Torabi and Berg, 2011). As noted by Kim and Sanderson (2005), data resolution, sampling effects, tectonic setting, history, and host lithology of interpreted faults can be different even for those formed under the same tectonic setting (Kim and Sanderson, 2005). According to data compiled by Kim and Sanderson (2005), which divided the data into groups of normal, strike-slip and thrust faults, D/L ratios for strike-slip faults are also slightly higher than for dip-slip faults (Fig. 1-10). The plot in Figure 1-10 indicates that D/L ratios may increase slightly with increasing fault length, which might be due to different fault growth mechanisms acting at different scales, with greater mechanical interaction and strain localisation acting on the larger faults when compared with their smaller counterparts (e.g., Cowie and Scholz, 1992c, Walsh et al., 2002a, Walsh et al., 2003; Willemse et al., 1996). Factors that can contribute to scattering in fault-scale relationships include:

1. Heterogeneous lithology in host rocks along the fault trace (Gudmundsson, 1992; Scholz et al., 1993; Cowie and Scholz, 1992a);

2. Incoherent sampling methods and measuring errors during fault growth analyses (Gillespie et al., 1992; Walsh and Watterson, 1988);

3. Lithological and mechanical barriers hindering fault growth (Bürgmann et al., 1994; Kim and Sanderson, 2005; Schultz and Fossen, 2002);

4. Fault segment-linkage and reactivation (Wojtal, 1994; Wojtal, 1996; Cartwright et al., 1995; Willemse et al., 1996; Peacock and Sanderson, 1991; Dawers and Anders, 1995; Kim and Sanderson, 2005; Kim et al., 2001);

5. Complex and variable earthquake rupture and slip/propagation histories of faults (Kim and Sanderson, 2005).

In addition to the factors mentioned above, interacting faults can also contribute to the scattering of scaling laws (Torabi and Berg, 2011). According to Torabi and Berg, (2011), a higher D/L ratio will occur for smaller faults that interact with larger faults, i.e. displacement-length ratios are expected to be larger in areas where faults overlap (Dawers and Anders, 1995; Peacock and Sanderson, 1991; Kim and Sanderson, 2005).

Research work has been carried out in the last few decades to investigate fault propagation, revealing marked increases in the length, displacement and area of a fault, from the initial locus of fracture nucleation towards fully developed fault segments (Segall and Pollard, 1983; Walsh and Watterson, 1987; Reches and Lockner, 1994). A number of fault growth models have been proposed by different authors, among which two end-members of fault growth models are predominantly accepted: 'isolated' and 'coherent' (Cartwright et al., 1995; Cowie and Scholz, 1992b, Morley et al., 2007; Cartwright et al., 2000; Jackson and Larsen, 2009; McLeod et al., 2000; Jackson and Rotevatn, 2013b, Yin and Groshong, 2007; Bose and Mitra, 2010).

An early fault growth model has also been proposed for ideal blind faults that propagate in a radial direction, recording minimum migration of maximum displacement location(s) (Barnett et al., 1987). Other researchers indicate that mature faults are often a result of fault-segment linkage (Lohr et al., 2008; Cowie et al., 2000; Cartwright et al., 1995; Stewart et al., 1997). As argued by Lohr (2008), faults grow most effectively by the coalescence of several smaller faults, whereas tip propagation is of only minor importance. Also, it is argued that the formation of a large fault is controlled by several small existing fault segments rather than a large fault created immediately (Sibson, 1985). In all these models, reactivation processes are thought to be an important parameter controlling fault growth (Walsh et al., 2002).
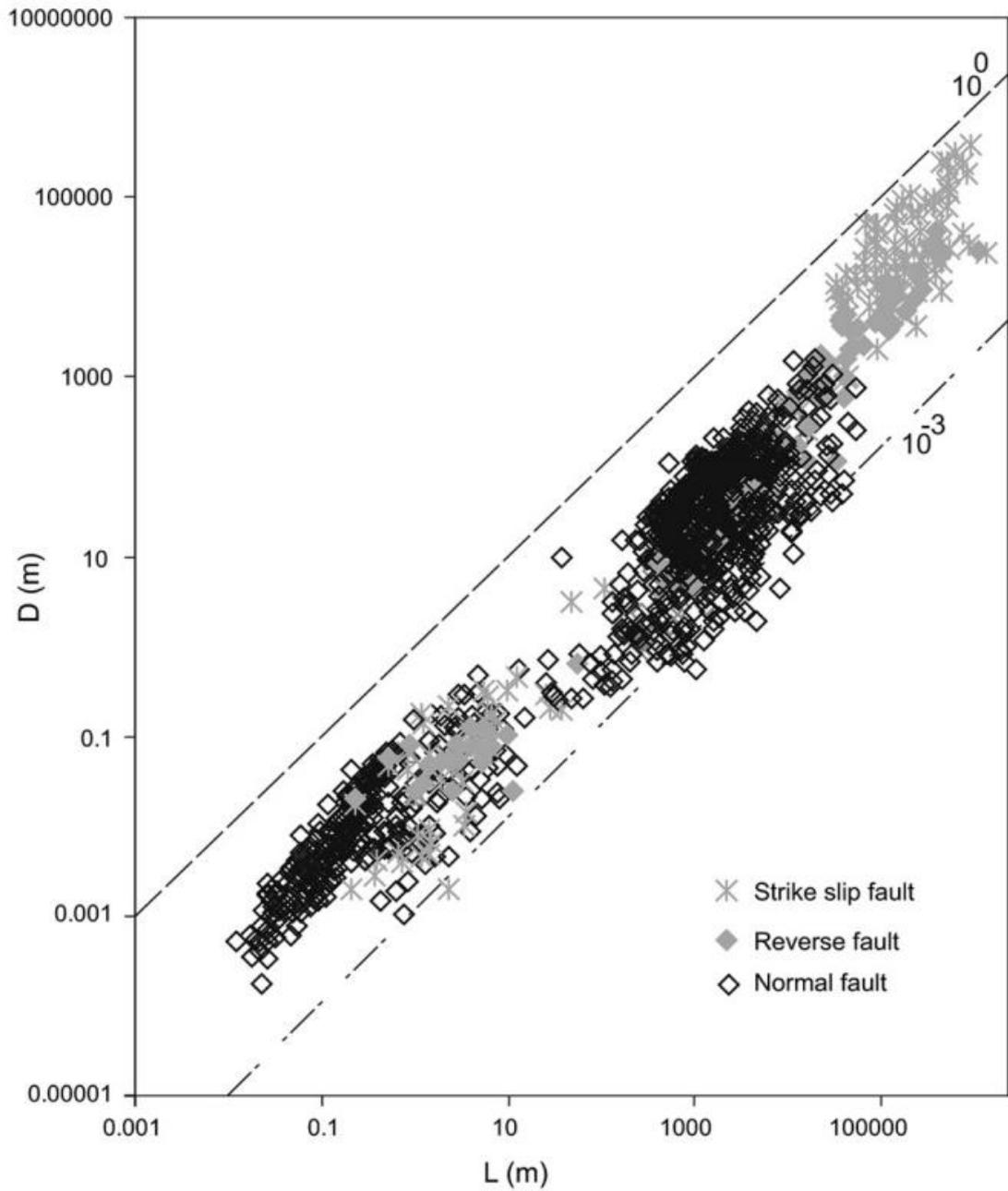
Fig. 1-10 Plots of maximum displacement (Dmax) against fault length (L) for normal, reverse and strike-slip faults. Figure from Torabi and Berg (2011).

1.4.3 Fault growth models

1.4.3.1 Fault growth by radial propagation

Fault propagation refers to an increase in fault length and displacement from their initial nucleation point (Segall et. al, 1983; Walsh et. al, 1987; Reches et. al, 1994; Peacock et. al, 1996). An ideal blind fault, not exposed to the surface, is often characterised by a maximum throw value at the centre of the fault plane, progressively diminishing towards the fault tips. The propagation of an idealised blind fault, developed in a mechanical homogeneous medium, often follows radial directions and presents an elliptical fault plane geometry (Barnett et al. 1987) (Fig. 1-11). The depth in which the maximum displacement values are recorded often indicate the initial point of fault nucleation.

1.4.3.2 Fault growth by segment linkage

Most of the Earth's upper crust comprises brittle rocks with multiple heterogeneities - complex faults resulting from the coalescence of distinct fault segments (Segall and Pollard, 1980; Gudmundsson, 1987; Walsh and Watterson, 1991; Mansfield and Cartwright, 1996). Faults developed in sedimentary basins often cover a wide range of scales from centimetres to tens of kilometres, even when formed under the same tectonic setting (Granier, 1985; Pollard and Aydin, 1984; Ze and Alves, 2016, see also Chapter 6 of the thesis). Segmented faults can result in a general scattering of displacement-length data, making any single scaling law hard to be applied in a specific area, or when comparing distinct regions (Mansfield and Cartwright, 1996; Bürgmann et al., 1994; Cartwright et al., 1995; Childs et al., 1995; Peacock and Sanderson, 1991; Willemse et al., 1996).
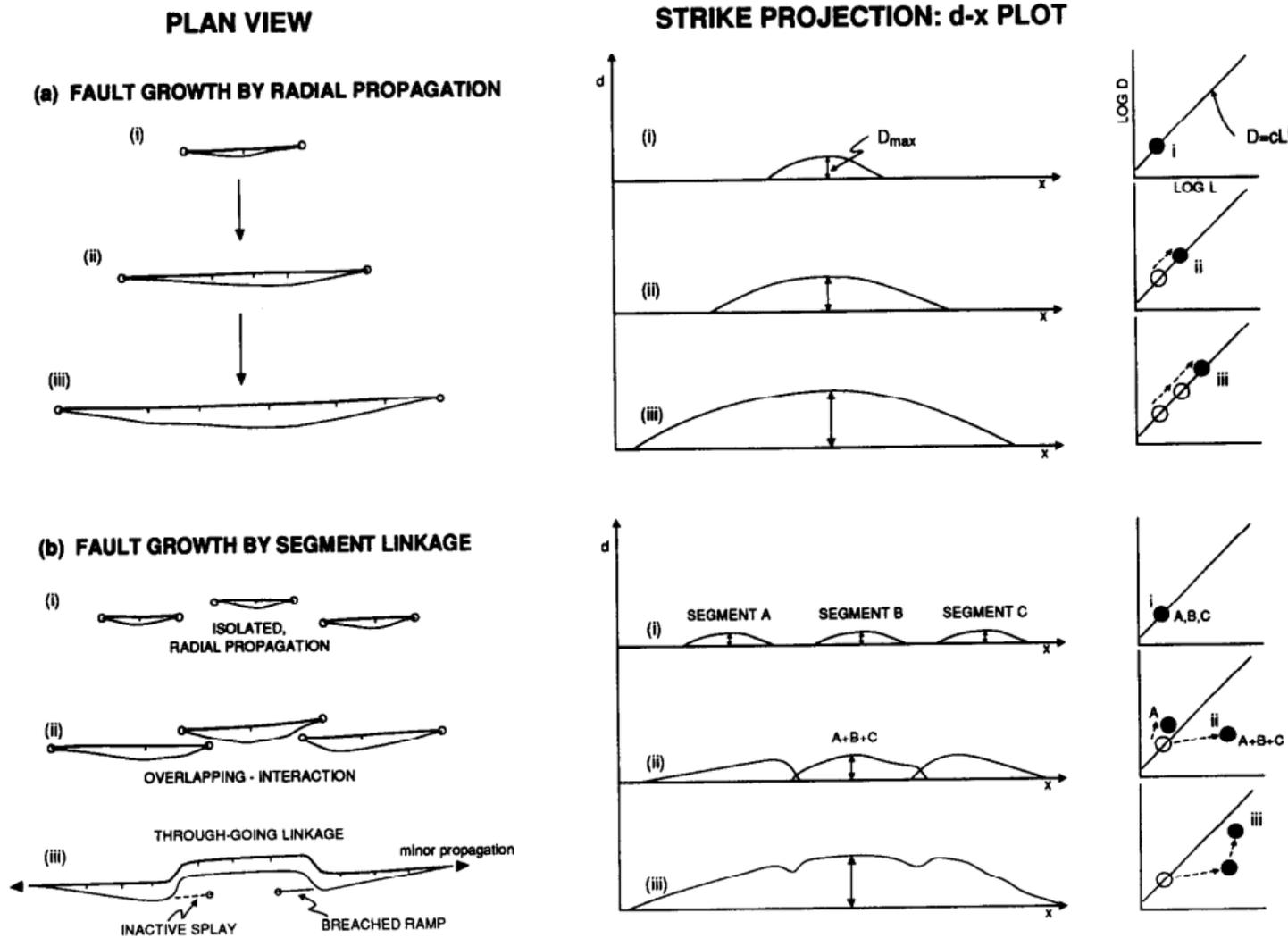
Fig. 1-11 Comparison between two distinct fault growth models: a) Fault growth by radial propagation, and b) Fault growth by segment linkage. Three distinct stages of fault growth are compared for both models in plan view, on a displacement-distance plot and on a log-log plot of maximum displacement (Dmax) against maximum length (L). The radially propagating fault follows a linear growth path, whereas the linked fault follows a step-like path. Figure from Cartwright et al. (1995).

29
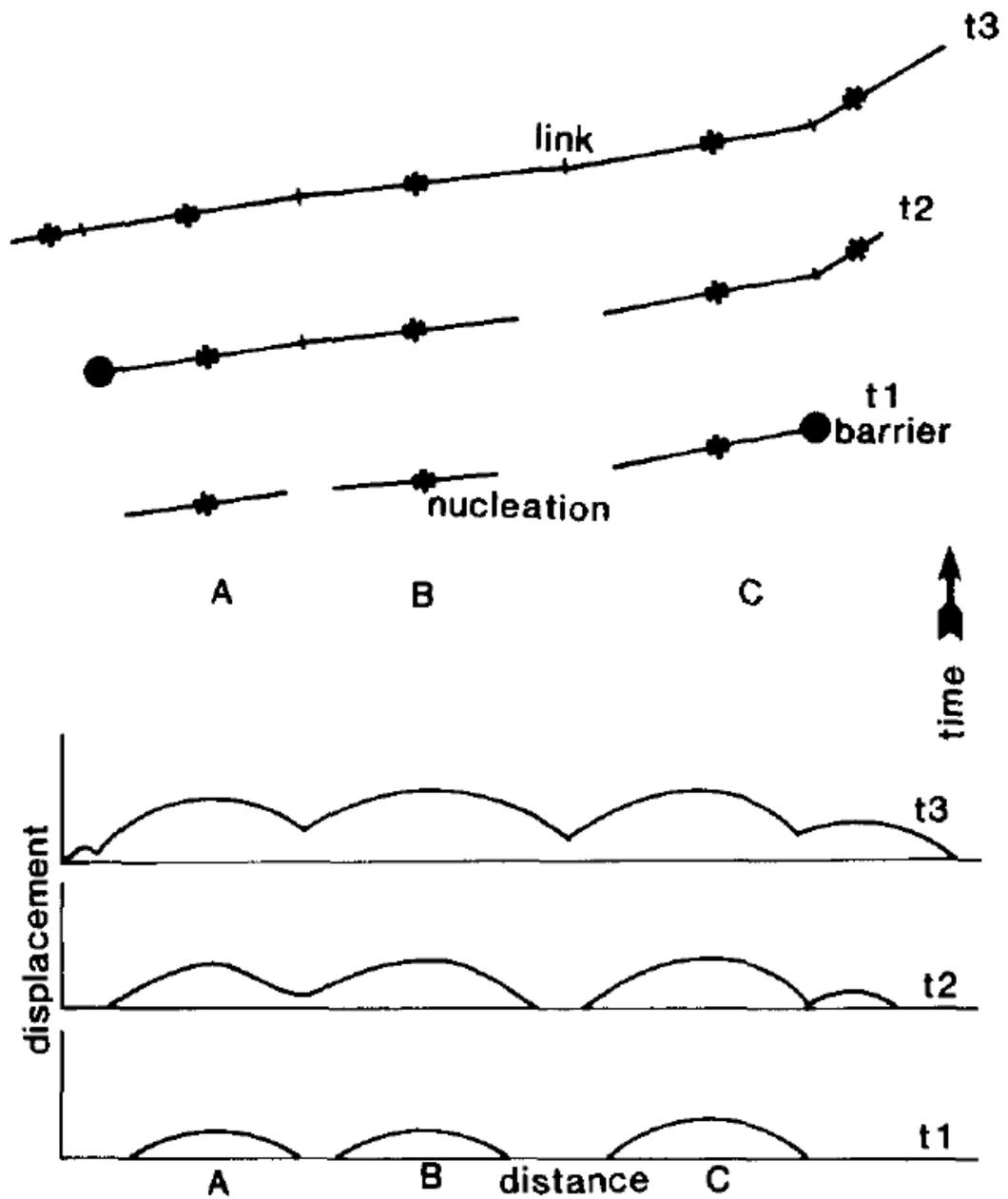
Fig. 1-12 Schematic representation of how large faults develop. Three initially independent faults, A, B and C, are formed in time t1. Further fault propagation occurs at t2. The fault propagation process continues to t3, which eventually results in the generation of a large, linked fault. Figure from Ellis and Dunlap (1988).

Fault growth by segment linkage can be classified into two modes according to the observed linkage directions: a) lateral tip linkage, and b) dip linkage (Baudon and Cartwright, 2008c, Baudon and Cartwright, 2008b). Faults linking at their lateral tips were initially observed in thrust faults, where the nucleation of fault segments can be recognised by displacement maxima and minima at the point of fault linkage (Ellis and Dunlap, 1988) (Fig. 1-12). Kinematic analyses for distinct normal fault zones revealing displacement variations due to segment linkage, suggest that faults show an approximately linear profile by initially developed isolated structures (Peacock and Sanderson, 1991). A three-stage model is often proposed to explain the growth of faults by lateral tip propagation and linkage (Peacock and Sanderson, 1991) (Fig. 1-11). The first stage witnesses the formation of distinct isolated faults, with a blind propagation mode leading to their coalescence towards each other (Stage 2). Eventually, lateral fault tips will interact with one another forming effective connections (hard-links) in breached relay zones (Stage 3), or showing no apparent connections between distinct fault segments (soft-linkages) (Kim and Sanderson, 2005) (Fig. 1-13). In faults that are hard-linked, the interaction zones (relay zones) will act as barriers for further fault propagation, a character often leading to the accumulation of displacement over a constant-length structure in the later stages of fault growth. This phenomenon usually results in high D/L ratios for hard-linked fault segments (Fig. 1-13).

Fault-dip linkage refers to the linkage of the upper tip of faults growing in lower stratigraphic levels, with the lower tips of shallower faults. This linkage zone is often characterised by relay structures that are sub-parallel to the strike of faults (Fig. 1-14) (Mansfield and Cartwright, 1996). As the linked faults propagate further as one single structure, a progressive destruction of the linkage zone (relay zone) will occur. Yet again, this latter phenomenon often results in high D/L ratios (Childs et al., 1996). With sufficient data resolution, fault displacement minima can be recognised to differentiate this mode of fault segment linkage (see the examples in Chapter 4).
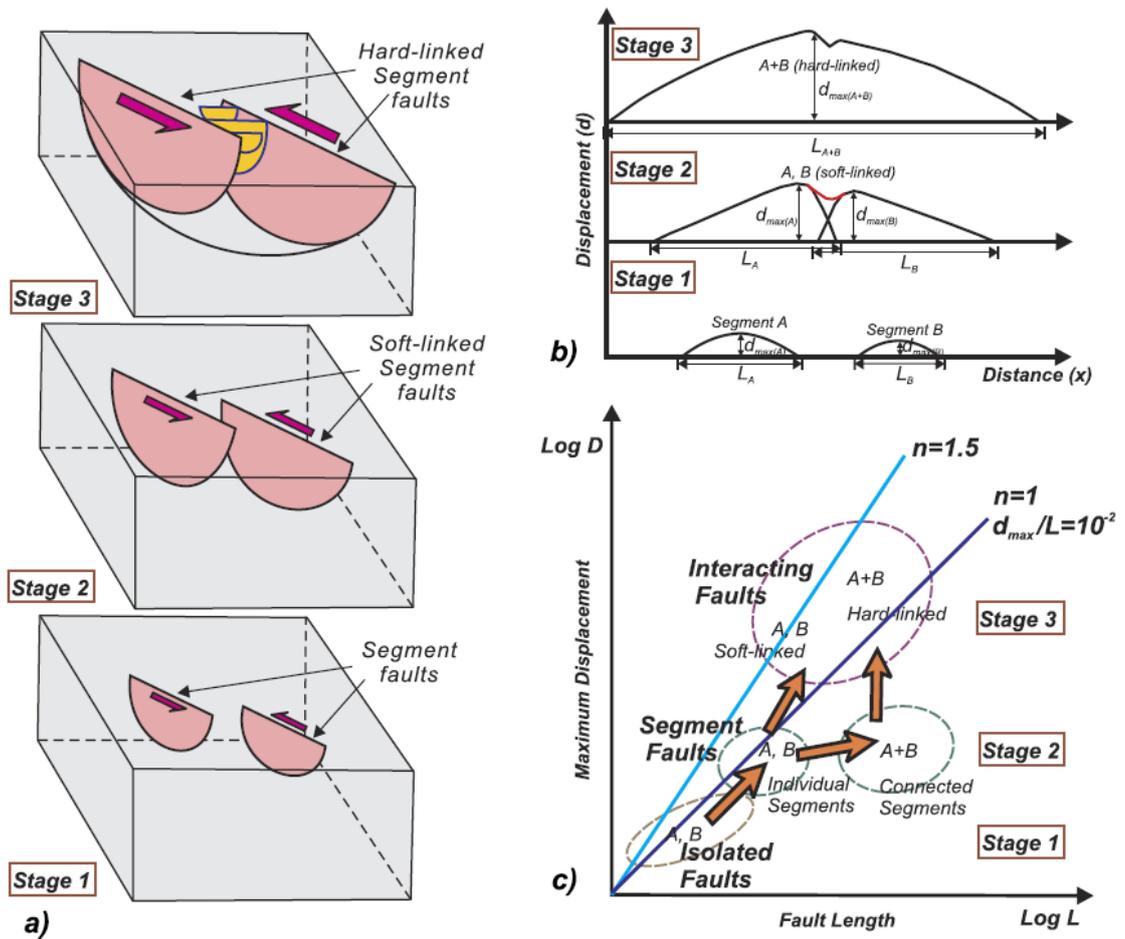
Fig. 1-13 Fault segmentation and linkage. Faults evolve from isolated faults to interacting faults via segment linkage. The ratio of Dmax/L increases at the same time faults interact, revealing a step-like evolution path. Fault lengths abruptly jump at the stage of segment linkage. Figure from Kim and Sanderson (2005).
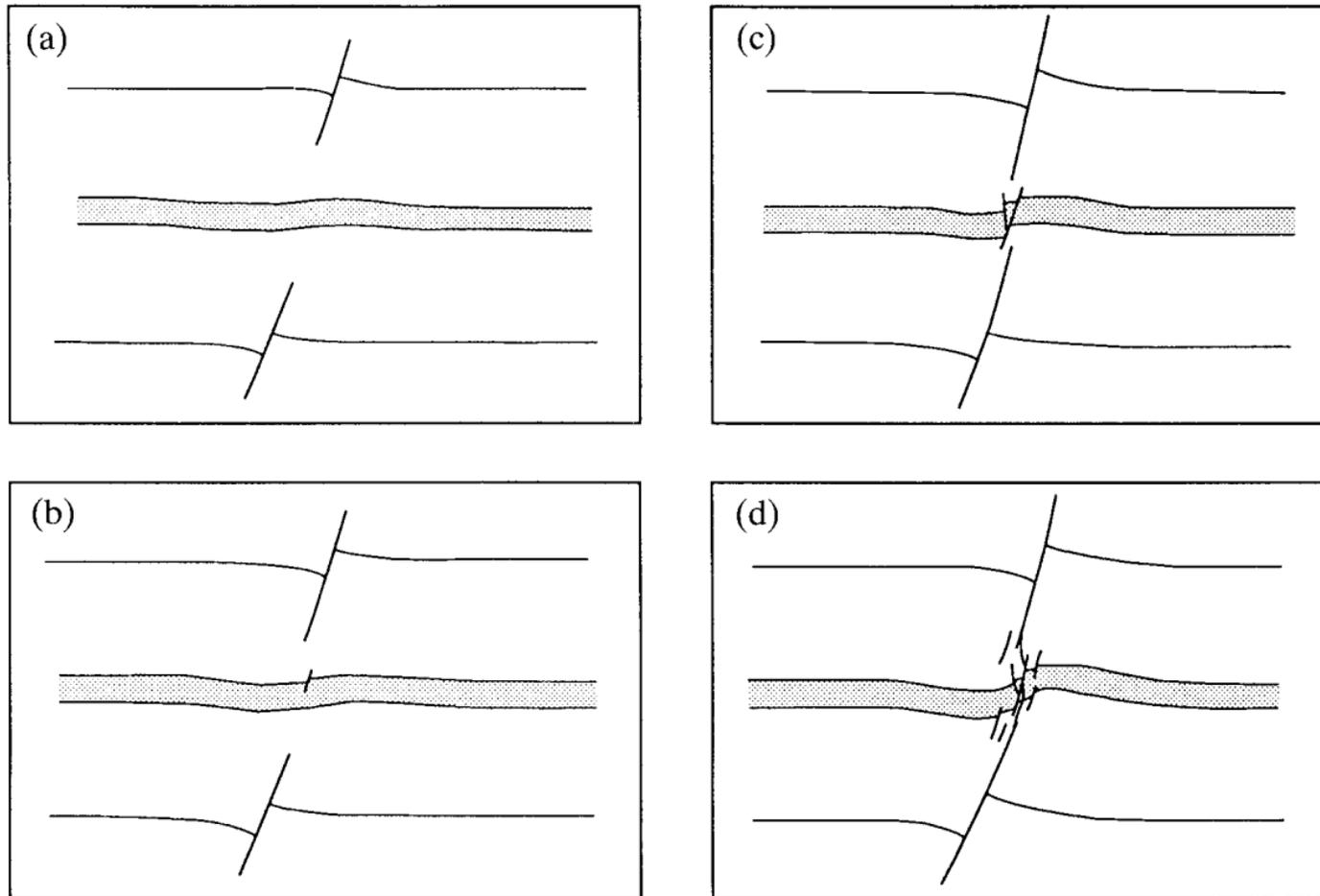
Fig. 1-14 Four-stage, schematic model depicting the progressive evolution of a normal fault dominated by linkage the dip direction between two initially isolated fault segments. Figure from Mansfield and Cartwright (1996)

1.4.3.3 Constant-length fault model

Faults generally indicate a longer near-final length during their propagation histories (Walsh and Watterson, 1988; Dawers et al., 1993; Schlische et al., 1996). However, a constant fault model has also been proposed in the literature based on the postulate that fault length is established rapidly, resulting in essentially constant lengths for much of the duration of faults. With further fault propagation, faults can only accumulate displacement in a vertical direction, returning high Dmax/L ratios (Fig. 1-15) (Walsh et al., 2002a). Examples are given in the literature, in both extensional and compressional settings, of faults reaching its near-final length when initiated by underlying structures. Another documented example is that of faults propagating rapidly to horizontal barriers (e.g. accommodation zones/transfer zones, salt diapirs), hindering further length accumulation (Meyer et al., 2002; Krueger and Grant, 2006; Mattos and Alves, 2018).

1.4.3.4 The coherent fault model

Overlapping, interacting and linking fault segments have been observed in many a study. Two end-members in the literature, differentiating fault growth histories according to whether fault segments are kinematic related or not, are the 'isolated' and 'coherent' fault models (Walsh et al., 2003). The isolated fault model is supported by multiple authors under the assumption that fault planes are self-contained (Cartwright et al., 1995; Dawers and Anders, 1995; Mansfield and Cartwright, 1996; Peacock and Sanderson, 1991). However, as high-resolution 3D seismic data becomes increasingly available, out-of-plane fault propagation models have been increasingly suggested as reflecting coherent fault models (Fig. 1-16). With the coherent fault model, fault segments initiate, propagate and develop as part of a spatially, kinematically and mechanically organised fault array (Walsh et al., 2003). The hard-linked or soft-linked processes can occur during fault propagation either by fault surface bifurcation or by stepping of initial fault segments (Walsh et al., 2003) (Fig. 1-16).

For 'Isolated fault model', faults propagation is not hindered by other faults,

a. Pre-existing underlying faults

b. Fault initiation and rapid propagation

nucleation point

segment linkage

c. Fault length established

'under-displaced' faults

tip interaction

d. Displacement accumulation no propagation
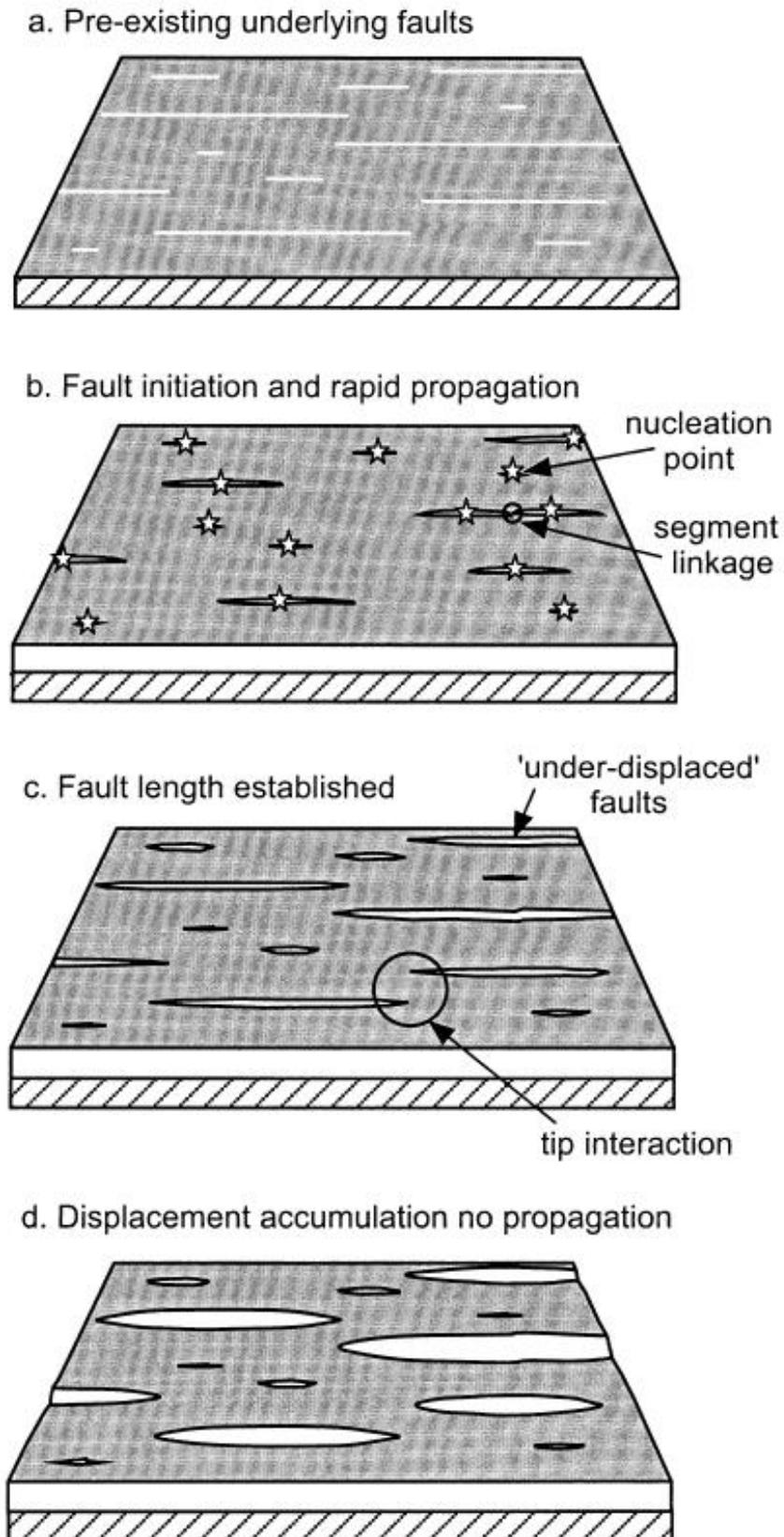
Fig. 1-15 Constant-length model suggested by Walsh et al. (2002), in which the fault length rapidly increases at an early stage of fault growth and then remains constant as displacement accumulates.
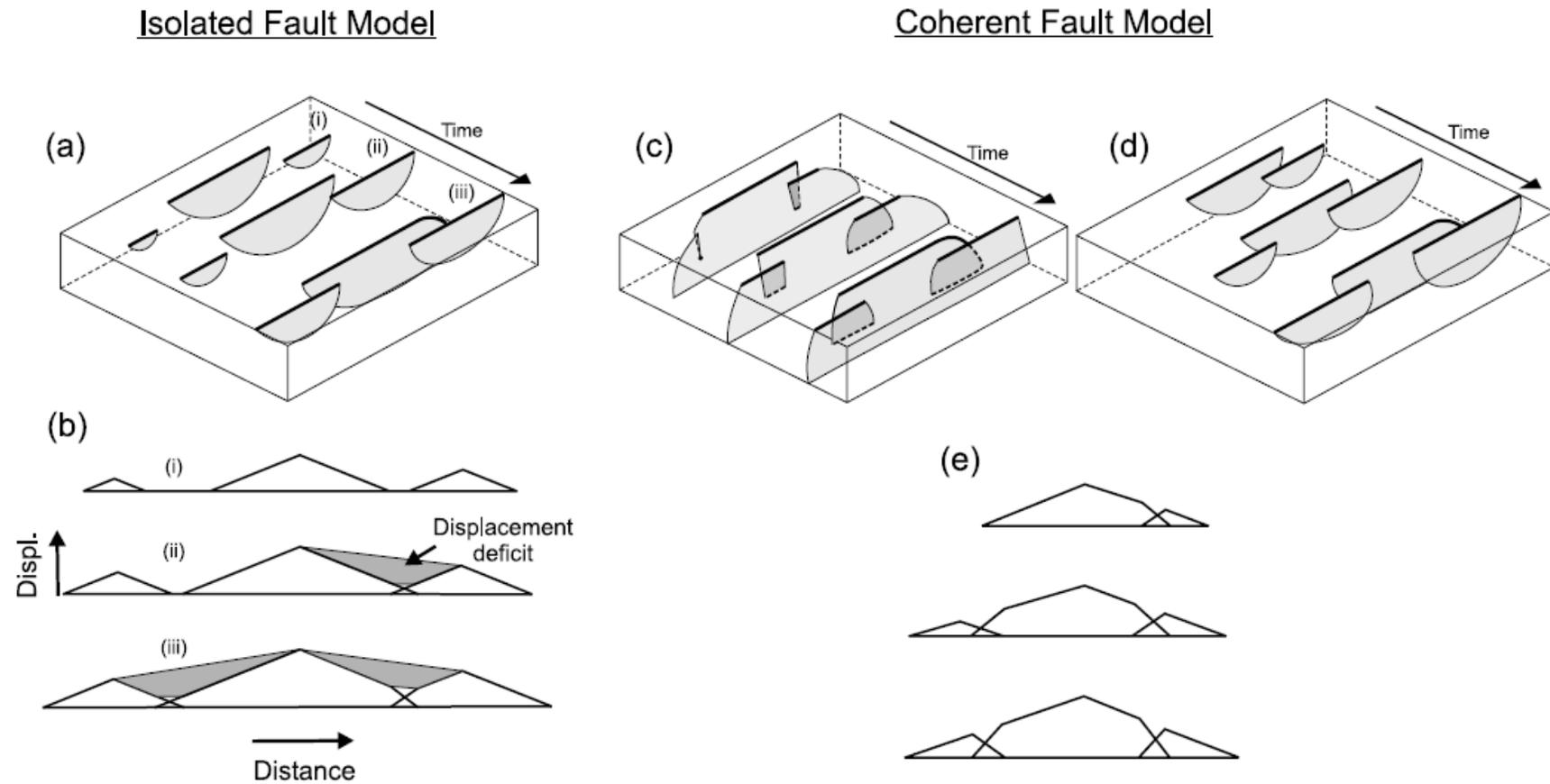
Fig. 1-16 Schematic comparison between the 'isolated fault' and the 'coherent fault' models. The block diagrams (a, c and d) show the growth stages of a segmented fault array (i–iii). The displacement-distance plots b and e are for fault traces on the upper surfaces of the block diagrams (bold lines). The coherent fault model is illustrated for hard-linked (c) and soft-linked (d) fault segments. Figure from Walsh et al. (2003).
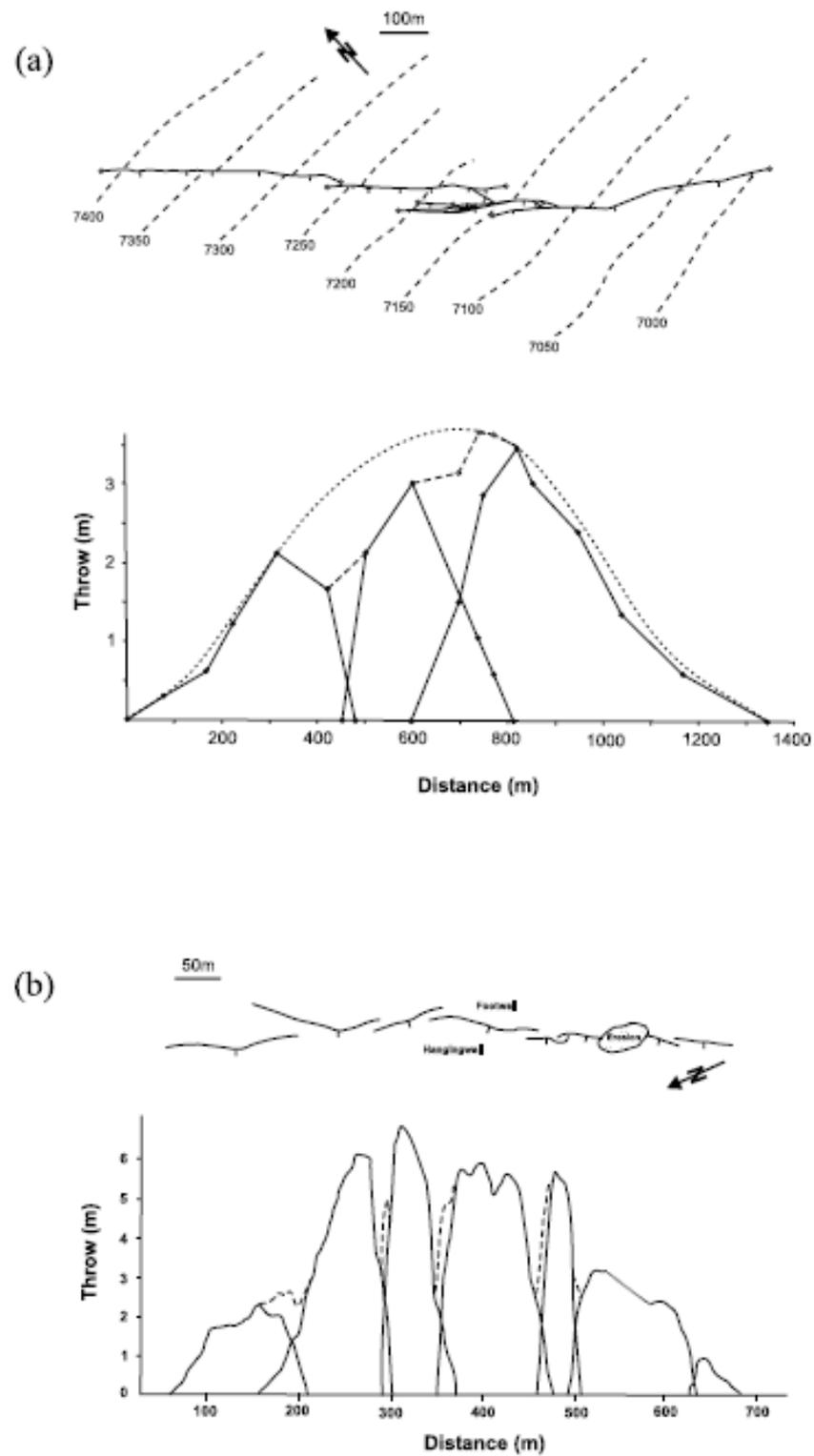
Fig. 1-17 (a) A segmented normal fault. The throw profile measured along the segmented fault array (solid lines) demonstrates that fault segments behave as one kinematically coherent structure as highlighted by the idealised envelope plotted through the summed up displacements (dashed line). (b) Segmented fault array showing a systematic distribution of throw along seven fault segments (solid lines), which may evolve as discrete structures. Figure from Walsh et al. (2003).

37

with a coherent fault growth model, fault propagation is closely associated with adjacent fault segments (Fig. 1-16). Furthermore, throw-distance profiles for coherent fault growth will show a coherent profile, which is often quite disrupted for an isolated fault growth model (Fig. 1-26). When identifying fault segmentation in a coherent model, sampling interval plays a key role in controlling the degree of accuracy of one's interpretation. When the sampling interval is coarse, throw-displacement profiles may indicate an isolated coherent fault rather than segmented fault displacement profiles (Fig. 1-17). This effect of data sampling on the interpretation of fault growth models is developed in more detail in this thesis.

1.4.4   Effects of scaling strategies

Sampling biases, namely truncation and censoring, have an important effect on the techniques applied to measure fault attributes and fault scaling laws (Nicol et al., 1996; Bonnet et al., 2001; Manzzochi et al., 2009) (Fig. 1-18).

Truncation will lead to an underestimation of the frequency of small faults due to resolution limitations of the sampling method utilised (Fig. 1-18). Apart from resolution limitations, 2D measurements through a 3D population of small faults, or a physically lower cut-off to the power-law size distribution of faults, also contribute to truncation effects (Torabi and Berg, 2011). Censoring will cause a systematic underestimation of the frequency of large faults due to subjective choices in data sampling (Fig. 1-18). This leads to underrepresentation and under-sampling of large faults (Bonnet et al., 2001), a caveat with significant influence on fault scaling laws and on the interpretation of fault propagation histories.

Published work in which throw-distance profiles are compiled to postulate fault growth histories, show sampling intervals on T-D and T-Z data ranging from 6 data points per fault to over 100 data points per fault, even for large tectonic faults that span several kilometres in length. This causes concerns as to the influence of sampling biases and censoring effects on fault analysis (Torabi and Berg, 2011) (Fig. 1-17).
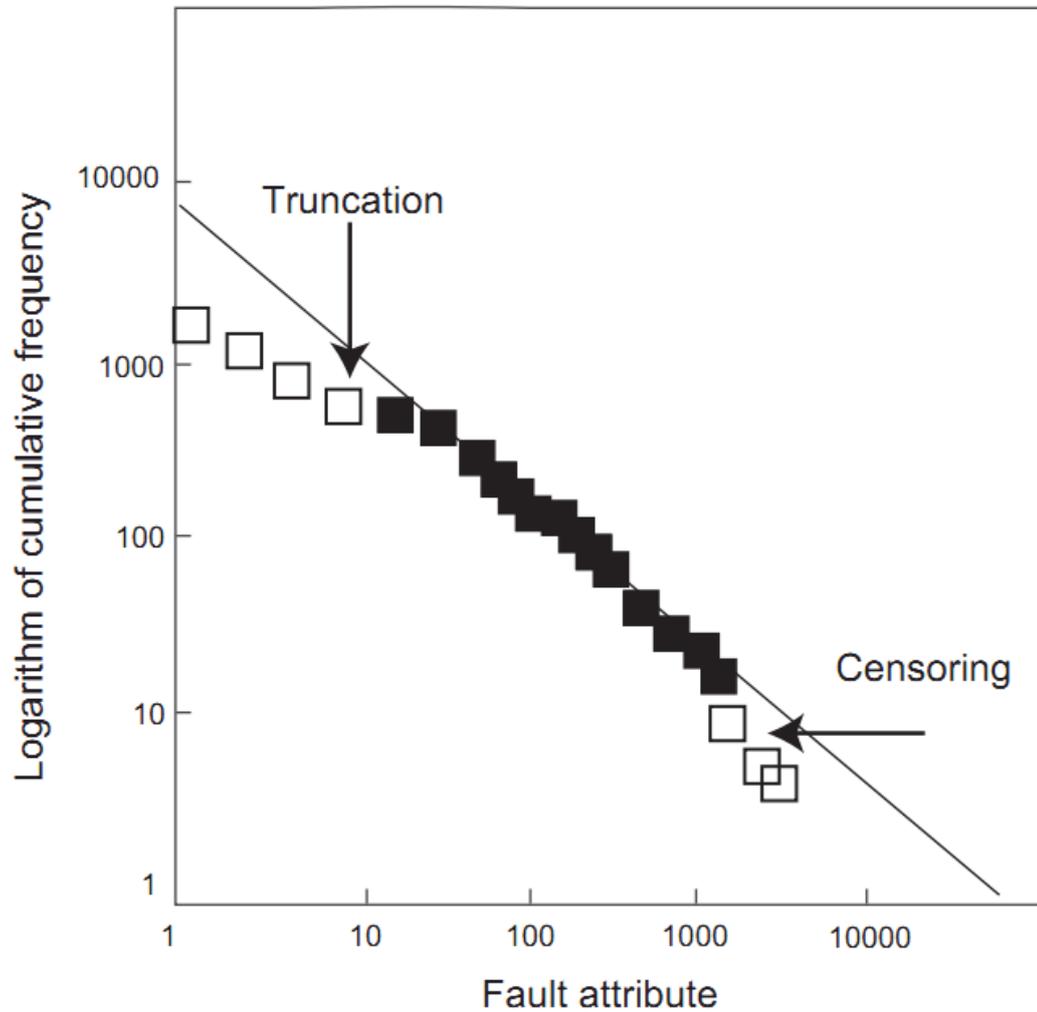
Fig. 1-18 Sampling biases (truncation and censoring) can potentially affect the distribution of fault attributes, e.g., the sampling biases can cause maximum displacement - fault length distribution being deviated from a straight line in log-log plots. Figure from Torabi and Berg (2011).

1.5   Techniques for fault analysis

Primary techniques for fault analysis include fault displacement analyses and stress inversions, as used in this thesis (e.g. Baudon and Cartwright, 2008c, Baudon and Cartwright, 2008b, Mansfield and Cartwright, 1996; Cartwright and Mansfield, 1998; Cartwright et al., 1998; Omosanya and Alves, 2014; Peacock and Sanderson, 1991; Mattos et al., 2016). Fault displacement analyses, namely displacement-distance and throw-depth plots plus expansion index and maximum displacement data, were completed in this work. Stress inversions completed in this work were used to obtain slip tendencies and leakage factors for selected faults.

Expansion index (EI) comprises a traditional method of addressing the propagation history of growth faults (Jackson and Rotevatn, 2013a, Bouroullec et al., 2004; Thorsen, 1963; Osagiede et al., 2014; Pochat et al., 2009; Ghalayini et al., 2017; Ze and Alves, 2016; Mohammedyasin et al., 2016) (Fig. 1-19). EI represents the thickness ratio between strata deposited on hanging-wall and footwall blocks (Lewis et al., 2013; Mansfield and Cartwright, 1996). EI < 1 is associated with thinning of sediments on the hanging-wall of discrete faults, whereas EI > 1 represent thickening hanging-wall strata (Thorsen, 1963; Pochat et al., 2009). This method has been widely adopted in the published literature to address fault growth episodes. However, seismic data resolution, accuracy of measurements and the lack of accurate stratigraphic correlations between hanging-wall and footwall blocks all contribute to a relative inaccurate EIs (Lopez, 1990; Osagiede et al., 2014). Assumptions are often made when using EI such as: 1) thickness variations are directly the result of variations in fault displacement rates, 2) erosion on footwall blocks is not significant. To avoid these caveats, other fault analysis techniques are often used to constrain the interpretation resulting from EI (Ze and Alves, 2016; Mohammedyasin et al., 2016).

The analysis of maximum throw vs. depth is an efficient way to identify the depth faults first nucleate (Alves, 2012). However, this method is based on the assumption that space is available for faults to propagate upwards and downwards. Such a method loses its practical meaning when faults sole into a basal detachment surface. In this latter case, faults are most likely to propagate upwards, with maximum throws developing only in an upward direction (Alves, 2012). To avoid this caveat, blind faults that are kinematically

and mechanically developed within a fault group are often selected to fulfil the 'free propagation' condition (Ze and Alves, 2016).

Throw vs. depth (T-Z) plots and throw vs. distance (T-D) plots are used to analyse the growth history of discrete faults (Baudon and Cartwright, 2008c, Baudon and Cartwright, 2008b, Durogbitan, 2016b). Non-reactivated faults are generally characterised by M-type or C-type throw-depth profiles, with throws tipping out towards the lower tip of faults without a clear detachment (Baudon and Cartwright, 2008c) (Fig. 1-20). Reactivated faults exhibit stepped vertical throw-depth profiles (e.g. double-C throw profiles with one episode of reactivation) and their lower parts show a similar throw profile to non-reactivated faults. In parallel, throw-distance profiles are often used to address fault segmentation. Faults that show only one fault segment often present a maximum throw value at their centre, diminishing towards both tips (Lohr et al., 2008; Mansfield and Cartwright, 2001). Faults that are formed by lateral linkage of different segments often present several peak values in throw, with lower throw values at the linkage area (Walsh et al., 2003) (Fig. 1-21).

Details of how these techniques were applied to conduct the analysis in this thesis are described in Chapter 2. The following section will briefly introduce displacement-distance relationships for normal faults, and the basic principles behind stress inversions.

1.5.1   Displacement-distance relationships

Displacement-length, displacement-height and displacement-width measurements comprise three ways of investigating displacement-distance relationships in faults, at the same time providing insights into fault (and fault zone) formation and development (Williams and Chapman, 1983; Cowie and Scholz, 1992a, Cowie and Scholz, 1992b, Cowie and Scholz, 1992c, Chapman and Williams, 1984; Rippon, 1984; Walsh and Watterson, 1988). Measurements of displacement vs. distance can be obtained from fault surfaces (or traces) on seismic cross-sections, geological outcrops and topographic surfaces (Kim and Sanderson, 2005).
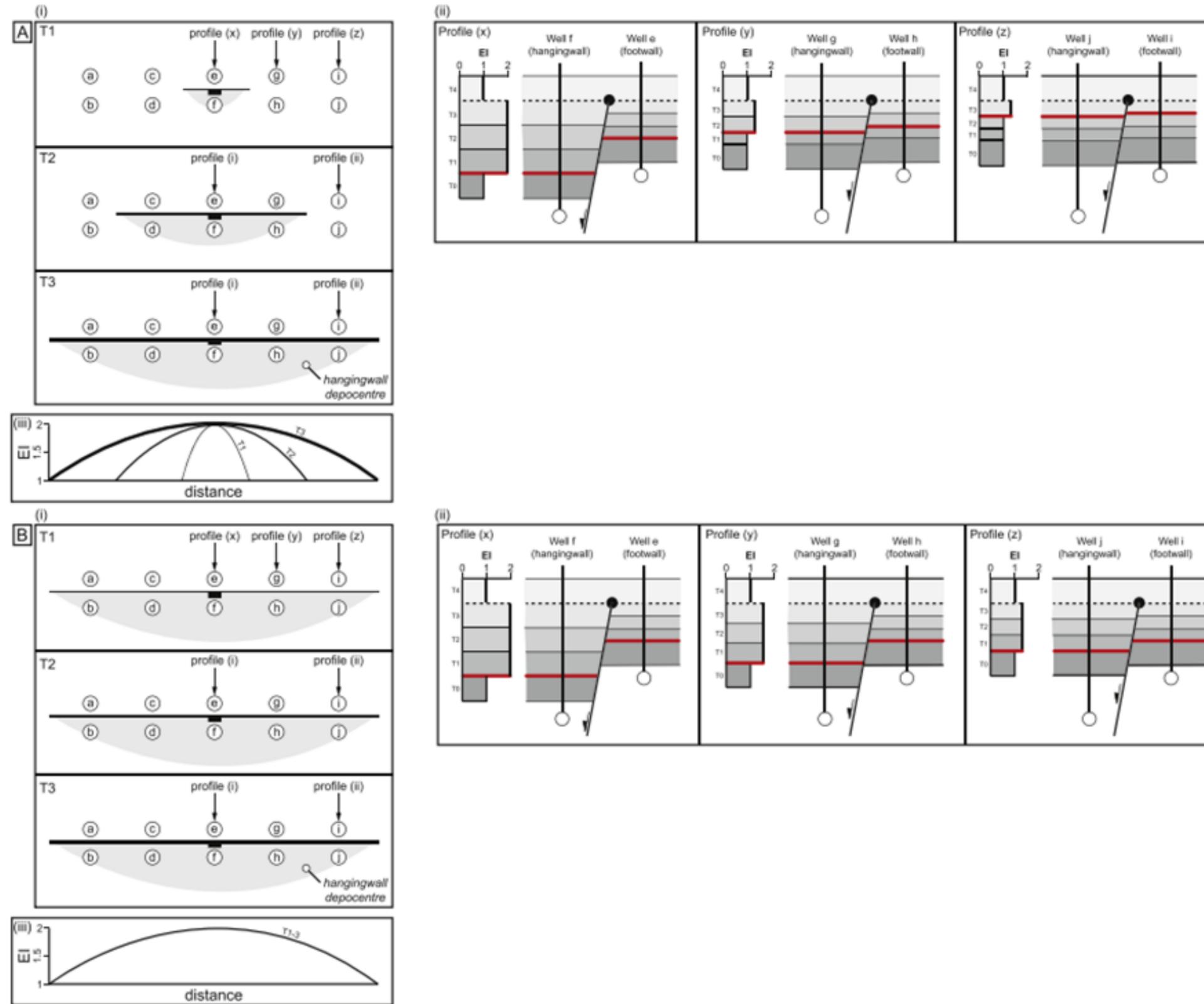
Fig. 1-19 Schematic diagrams illustrating how sequential expansion index (EI) plots are used to interpret fault growth histories. Figure from Jackson et. al. (2017).
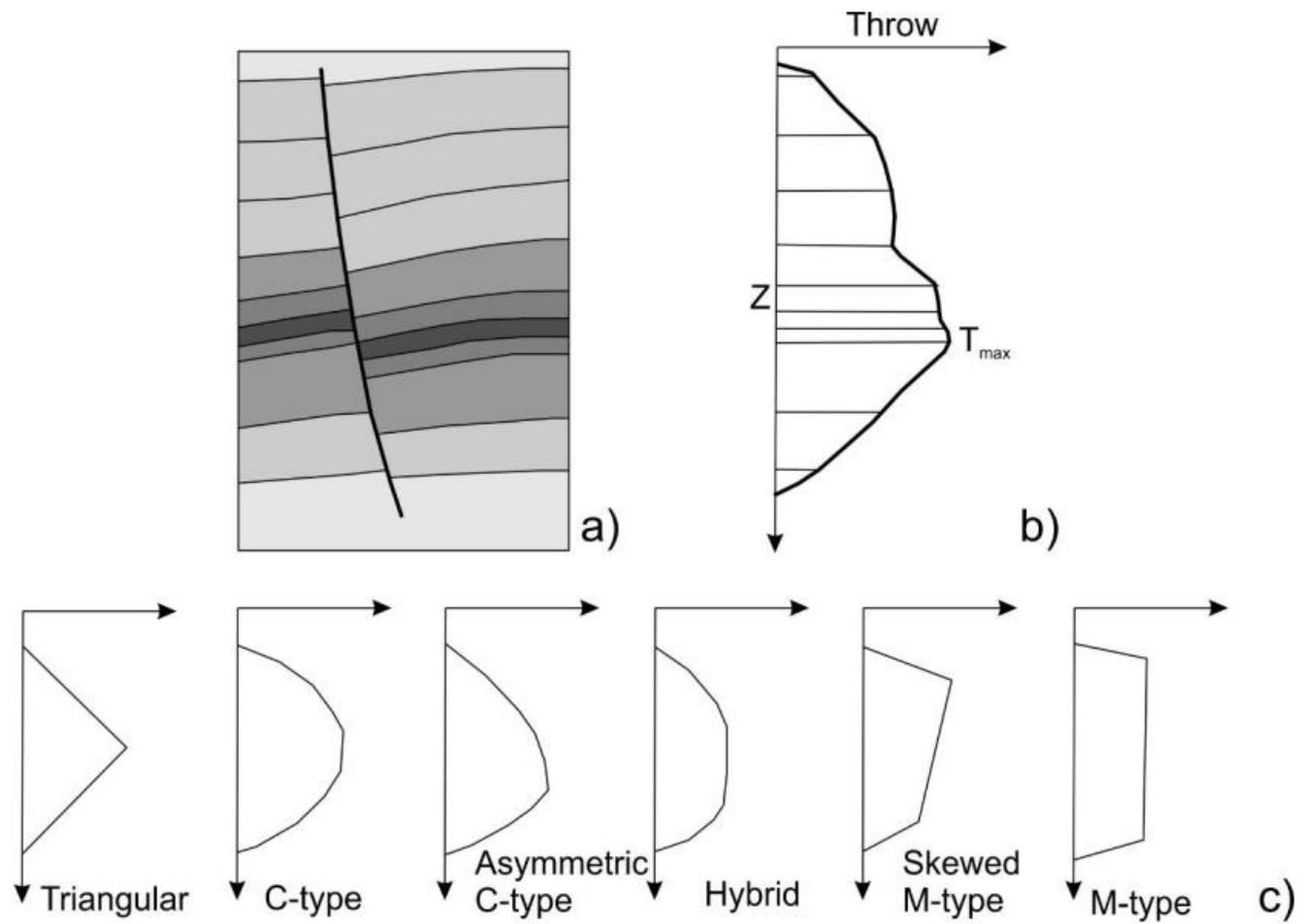
Fig. 1-20 Typical throw-depth profiles for non-reactivated faults. Figure from Baudon and Cartwright (2008).
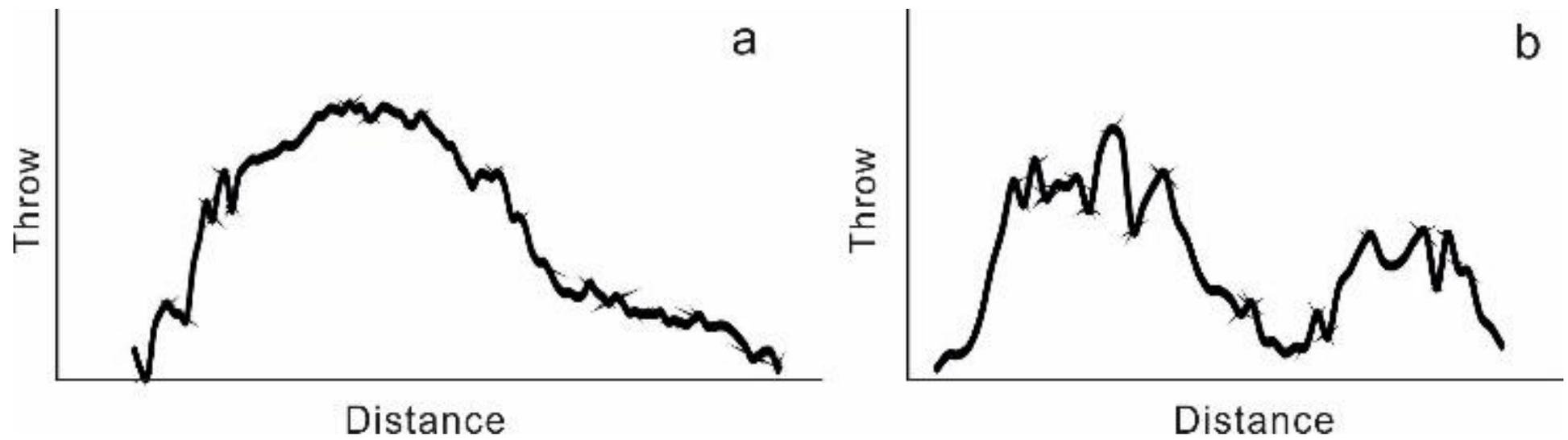
Fig. 1-21 Examples of throw-distance profiles showing an isolated fault segment (a) and a fault that is segmented (b)

Systematic correlations between the width of fault zones and maximum displacement have been identified in the literature as following a linear trend relationship on logarithmic displacement-width plots (Aviles et al., 1987; Power et al., 1987; Hull, 1988). However, some authors also indicate a minimum correlation between fault zone thickness and displacement along discrete faults (Jamison and Stearns, 1982; Blenkinsop and Rutter, 1986; Evans, 1990). Better constraints on these displacement-width relationships were suggested by Evans (1990) as a way to obtain more accurate results.

Displacement-height measurements refer to the vertical displacement distribution along a fault trace. This measurement can reveal the true dip-slip values for normal faults, thrust faults, thrust-fold zones and linked fault systems (Ellis and Dunlap, 1988; Muraoka and Kamata, 1983; Williams and Chapman, 1983; Chapman and Williams, 1984).

Displacement-length measurements can offer a full view of fault geometry in three dimensions (Cowie and Scholz, 1992a, Cowie and Scholz, 1992c), enabling rough estimates of total strain in a faulted rock. The most significant use of displacement-length plots is to provide insights into the mechanism of initiation and growth of faults through time, which ties closely with the distinct fault propagation models previously mentioned (Figs. 1-17, 1-20 and 1-21).

1.5.2   Stress inversions

The characterisation of in situ rock stresses is important in reservoir analyses, so as to estimate hydrocarbon retention within a reservoir interval and to assess borehole stability (Fejerskov and Lindholm, 2000; Lindholm et al., 1995). Common methods used to estimate stress include fault inversions based on Anderson's fault theory (Anderson, 1942), the Wallace and Bott hypothesis (Bott, 1959; Wallace, 1951), the Numeric Dynamic Analysis (Sperner et al., 1993), or Direct Stress Inversions (Angelier, 1990; Hippolyte et al., 1994). The World Stress Map (WSP) is an outstanding public database documenting global in situ stresses estimated from earthquake focal mechanisms, borehole breakouts and drilling-induced fractures (Heidbach et al., 2008).

Three principal stresses termed $\sigma 1$, $\sigma 2$ and $\sigma 3$ are used to describe the stress conditions at depth (Zoback, 2007). In Anderson's faulting theory, SHmax, SHmin, and

Sv are proposed to describe the relative stress magnitude and faulting regimes in a specific volume of rock, of which SHmax represents the maximum horizontal stress, Shmin represents the minimum horizontal stress and Sv represents the vertical stress. In this classification scheme, a specific horizontal stress (with respect to vertical stress) is defined for different faulting regimes (Anderson, 1942) (Table 1-2). Limitations of Anderson (1942) theory include details such: 1) the precise value of each stress magnitude cannot be determined by this method, 2) the theory is valid for relatively new structures with pure dip-slip or pure strike-slip movement, i.e. where slip occurs along a pre-existing discontinuity faulting processes might not correlate with current stress state, and Anderson's theory cannot be applied (Zoback, 2010).

Regime	Stress		
	S_1	S_2	S_3
Normal	S_v	S_{Hmax}	S_{hmin}
Strike-slip	S_{Hmax}	S_v	S_{hmin}
Reverse	S_{Hmax}	S_{hmin}	S_v

Table 1-2 Anderson's classification of relative stress magnitude and fault regimes. S_1, S_2 and S_3 represent the principle normal stresses. In normal faulting regime, Sv>SHmax>Shmin; in strike slip fault regime, SHmax>Sv>Shmin; in reverse fault regime, SHmax>Shmin>Sv.

The Wallace and Bott Hypothesis uses field indicators, including fault orientations and slip directions inferred from slickensides, to infer palaeostresses (Bott, 1959; Wallace, 1951). The Hypothesis assumes that incremental slip on faults occurs in the direction of the maximum resolved shear stress on the fault plane. This assumption is made in relation to the theoretical prediction of the kinematics of newly formed faults (Anderson, 1951; Wallace, 1951) and as well as to reactivated movements on pre-existing planes of weakness (Bott, 1959) from given stress states, which is fundamental to inverse methods that have been devised to estimate geological palaeostresses from data consisting of the

orientations of fault surfaces and of associated lineations indicating the direction of fault slip.

The Direct Stress Inversion (DSI) method (Angelier, 1990) allows for the calculation of the shear stress on a fault when the slip direction is known. The stress tensor is calculated using a least square algorithm that minimises the sum of the angles between the slip vectors and the calculated shear stress for all faults. Limitations of this method arise from the sensitivity of the method to heterogeneities in the input data.

With the Numeric Dynamic Analysis (NDA) (Sperner et al., 1993; Spang, 1972), the orientations of compressional (P), tensional (T) and neutral (B) axes for each fault are established together with the failure angle (Θ), which represents the angle between the P-axis and the fault surface.

1.5.2.1 Stress inversion in this thesis

A more reliable stress inversion method was proposed by authors focusing on sets of faults that are kinematically and dynamically related (Morris et al., 1996; McFarland et al., 2012; Sippel et al., 2010; Žalohar and Vrabec, 2007). The method is integrated with commercially developed software such as 3D Move® - Midland Valley. With the proposed method, based on the relationship between slip tendency values and the displacement measured for a set of faults, a fault is likely to slip when the shear stress is equal or greater than the normal stress acting on its surface (Morris et al., 1996). Some key conditions are expected to validate this method: a) a positive relationship is expected between slip tendency and displacement, and b) small displacements with large slip tendencies are more plausible than large displacements with small slip tendencies (McFarland et al., 2012).

After integrating stress and fault data into 3D Move®, slip tendency and leakage factors can be estimated to critically assess the likelihood that a fault will slip and fluid transmissivity through the faults (Morris et al., 1996) (Fig. 1-22).

Slip tendency depends on the magnitude and orientation of stresses acting on a fault surface. A fault will slip if the resolved shear stress (τ) is equal or surpasses the frictional

resistance to sliding (F) (Equation 1-2). Values for slip tendency vary from 0 (no slip) to 1 (slip occurs) (Morris et al., 1996) (Figure 1-22).

$$F \leq \tau = \mu\sigma_n$$

Equation 1-2

The leakage factor (L), which is defined as the ratio of fluid pressure (P_f) to the difference between the effective normal stress (σ_n') and the tensile strength (T) of a fault zone (Midland Valley Move Application, 2015), is calculated as:

$$L = \frac{P_f}{(\sigma_n' - T)}$$

Equation 1-3

1.6   Salt-related faults and structures

A group of faults kinematically and dynamically related, and forming distinct fault arrays, is defined as a fault family (Rowan et al., 1999). With the initiation of salt flow, the supra-salt strata will deform to, ultimately, form a wide range of salt structures (Fig. 1-23). These same diapiric processes will lead to brittle faulting (or folding) of supra-salt strata as a consequence of arching or buckling of roof units. Faults that are developed on top of discrete salt structures are often kinematically and dynamically related; thus fault families are often used to describe structures that are developed in supra-salt strata (Rowan et al., 1999; Jackson et al., 1994).
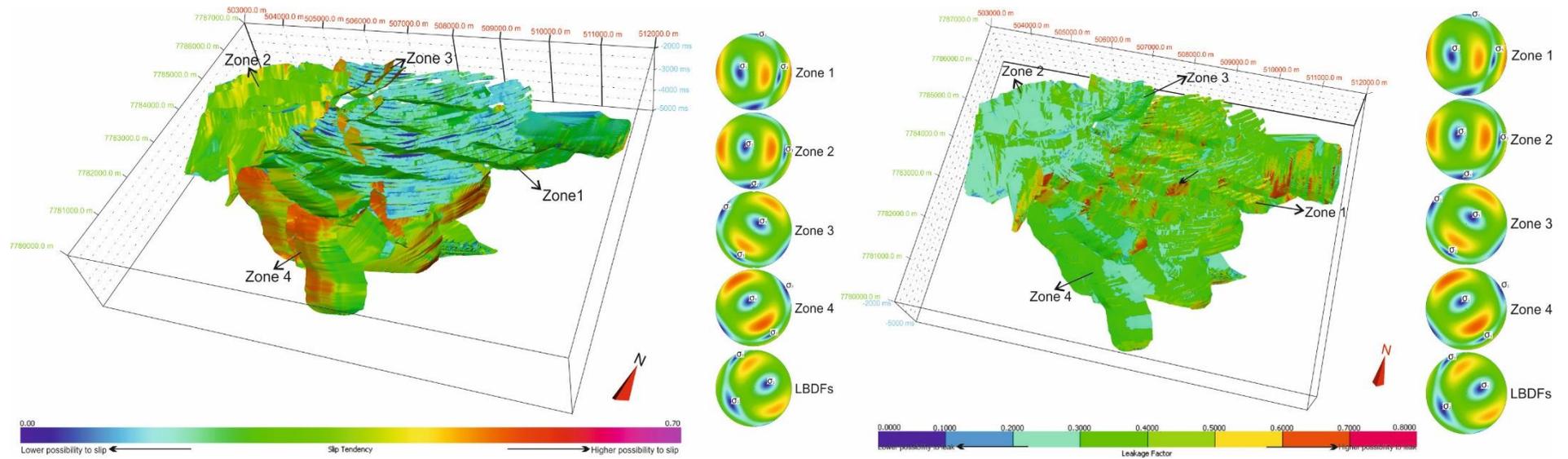
Fig. 1-22 Fig. 1-22 Examples of slip tendency and leakage factors resulting from stress inversion.

In contrast to salt-withdrawal basins, collapse structures predominate on top of salt diapiric structures (or salt domes/anticlines). Collapse structures are often controlled by underlying salt bodies, and are attributed to a range of tectonic and halokinetic processes causing localised extension or gravitational instability at the anticline crest. This section will briefly introduce fault families developed over (and adjacently) to salt structures, especially in extensional and compressional regimes (Fig. 1-23).

1.6.1   Fault families due to thin-skinned extension and gravitational gliding

On passive continental margins, salt movement is primarily driven by differential loading (Ge et al., 1997) and can be closely influenced by pre-salt slope topography (Cobbold and Szatmari, 1991). As sediment undergoes thin-skinned gliding due to its inherent gravitational instability, three domains are formed and separated by upslope extension, transitional and distal compression (Vendeville and Jackson, 1992a, Vendeville and Jackson, 1992b) (Fig. 1-23). Different fault families in these domains have been previous classified by Rowan et al. (1999) and shown in Figure 1-24.

Upper slope extensional domains are typically characterised by salt rollers and associated gravity-driven, seaward-dipping listric roller faults (McClay, 1995; Mauduit and Brun, 1998). Extensional (keystone) faults form in these domains to accommodate outer-arc extension on the crest of turtle anticlines and tectonic rafts (Woodcock, 1991; Rowan et al., 1999). The transitional domain is often dominated by salt diapirs, stocks and walls, whilst large allochthonous salt canopies and extruded diapirs dominate the base of the continental slope (Fig. 1-5). Faults in this region are usually contractional beneath the salt but are invariably extensional in strata deposited on top of allochthonous salt structures. Faults observed in the Espírito Santo Basin are classified as: roller faults, rollover faults, crestal faults, concentric faults, radial faults and reactivated rollover faults (Alves, 2012).
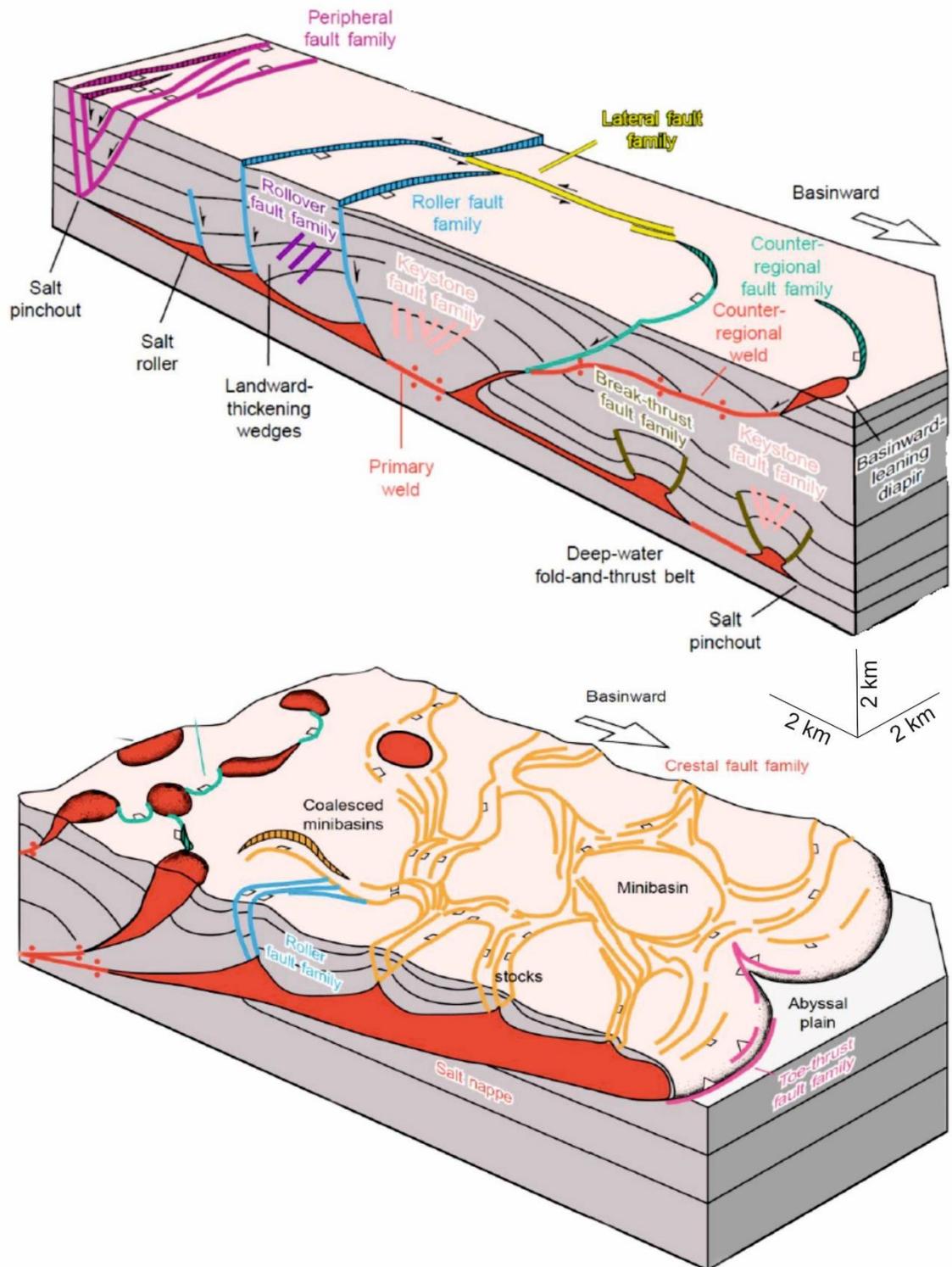
Fig. 1-23 3D cartoon showing the geometry of different fault families and associated structures. Modified from Rowan et al. (1999). Faults change basinwards from extensional roller faults to fault families related to salt canopies in the more distal, lower slope compressional domain.

51
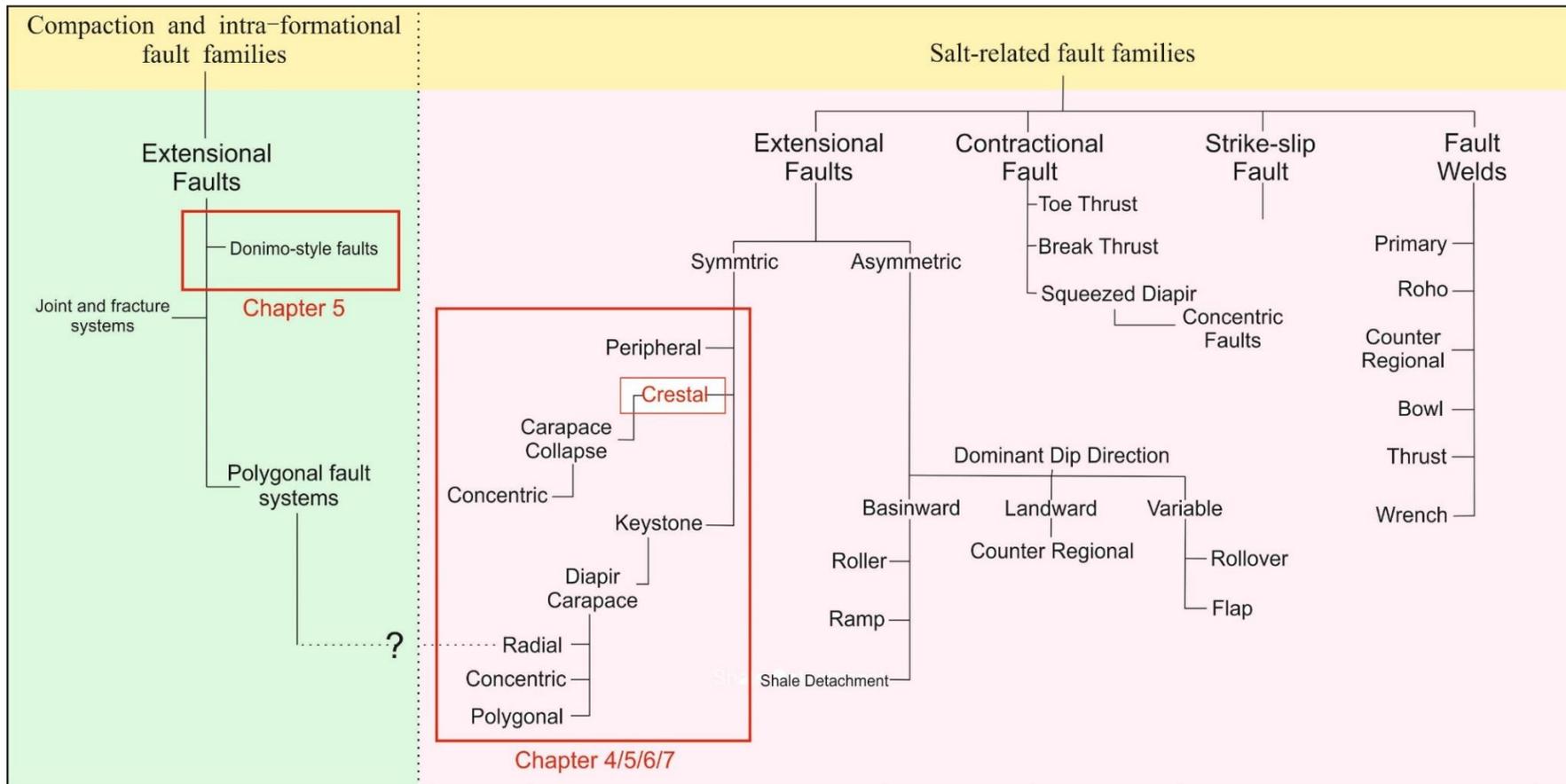
Fig. 1-24 Diagram summarising the main salt-related fault families observed in nature. Crestal faults and a set of domino-style faults are observed and studied in this thesis. Modified from Rowan et al. (1999).

1.6.1.1 Domino-style faults

The concept of 'domino faults' was first introduced by Mandl (1987), who described their formation as similar to a series of books (or domino pieces) toppling over a shelf. In practice, domino fault systems comprise a series of sub-parallel faults that rotate during extension (Buchanan and McClay, 1992) (Fig. 1-25). Physical experimental models indicate that this type of faults results from both bed and fault rotation (Axen, 1986), a geometry often requiring a certain amount of local extension above a basal detachment (Nur et al., 1986; Axen, 1988; Buchanan and McClay, 1992; Mandl, 1987; McClay, 1990a, Maloney et al., 2012). Analyses of domino-type faults are often based on large-scale structures, with fault displacements of several kilometres and fault lengths of hundreds of kilometres (Maloney et al., 2012). However, intra-formation domino-style faults can be found in sedimentary basins. Chapter 5 of the thesis presents examples of intra-formational domino-style faults associated with fluid flow in salt-withdrawal basins.

1.6.2   Fault families above salt diapiric structures

Fault families associated with diapiric structures, such as salt domes and elongated salt walls, are often classified according to their geometry with respect to these latter structures (Yin and Groshong, 2007; Alsop et al., 1996; Alsop et al., 2000; Davison et al., 2000b, Davison et al., 2000a, O'Brien and Lerche, 1988; Stewart, 2006). Radial faults, which comprise the most prevalent extensional faults around salt domes, result from the forceful intrusion of underlying salt diapirs (Schultz-Ela et al., 1993; Stewart, 2006; Vendeville and Jackson, 1992a, Vendeville and Jackson, 1992b, Yin and Groshong, 2007) (Fig. 1-26). Concentric faults are curved structural features formed in response to either the evacuation of subsurface sediment or by ensuing basin subsidence (Alsop et al., 1996; Bertoni and Cartwright, 2005; Ge and Jackson, 1998; Stewart et al., 1997; Stewart, 2006; Maione, 2001; Woodcock, 1991; Underhill, 2009) (Fig. 1-26). Growth histories of concentric faults involve both dip-linkage of fault segments from multiple phases of reactivation during inversion, and horizontal segment linkage via lateral propagation.
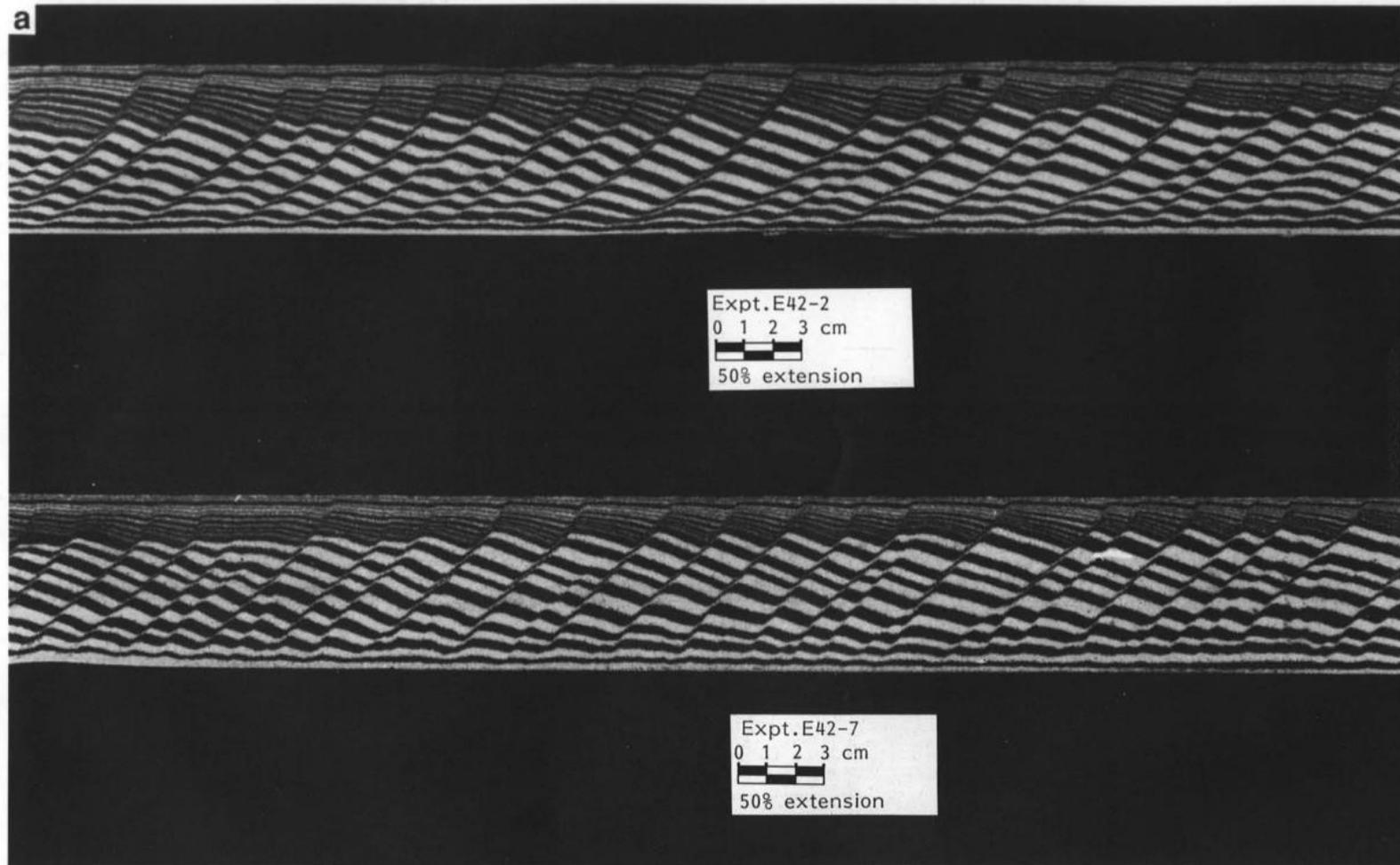
Fig. 1-25 Physical models of domino-style faults showing listric (a) and planar (b) fault geometries. Figure from McClay (1990).

1.6.2.1 Crestal faults

Crestal fault families are groups of planar growth faults that root into the crests of triangular diapirs, forming symmetrical grabens (Vendeville and Jackson, 1992a, Vendeville and Jackson, 1992b, Rowan et al., 1999; Jenyon, 1988). Main characteristics of crestal faults include their relatively small length (<2.3 km), and small throws (<50 ms TWT) (Morley, 2007; Alves, 2012). Detailed analyses into this fault families are scarce as: 1) very few outcrops of crestal faults exist in the world. Even when outcrops exist (Randles, 2012), it is only possible to study the main boundary faults of diapirs; 2) vintage seismic data is often of low resolution. Despite these limitations, research into this fault family is of great importance to understand local hydrocarbon accumulations as these faults: a) act as seals or conduits to migrating oil and gas. Even though it is hard to have reservoirs on crestal areas above salt, faults on the flanks of salt structures are potential conduits for oil and gas; b) can shape the seafloor morphology. Growth (and reactivation) of crestal faults leads to local movements on the sea floor, abruptly changing its morphology; c) can lead to the erosion of sediment feeding adjacent mini-basins. Collapse features are also prevalent on the crests of salt structures. The reactivation of faults can lead to local sediment failure, feeding sediment into adjacent salt-withdrawal basins, thus influencing local reservoir and seal-rock distribution (Gamboa et al., 2010; Omosanya and Alves, 2013).

1.6.3   Collapse structures on the crest of salt anticlines

Collapse structures are common features formed on the crests of salt structures, reflecting dissolution processes, regional extension, sub-surface salt redistribution or regional deformation of the overburden (Randles, 2014). Figure 1-27 presents three distinct collapse styles according to their triggering mechanisms; salt dissolution or halokinesis. Both ductile deformation and brittle-dominated deformation can occur in association with salt dissolution, with sag structures and folds reflecting predominant ductile deformation (Fig. 1-27), and half-graben systems and steep-sided grabens
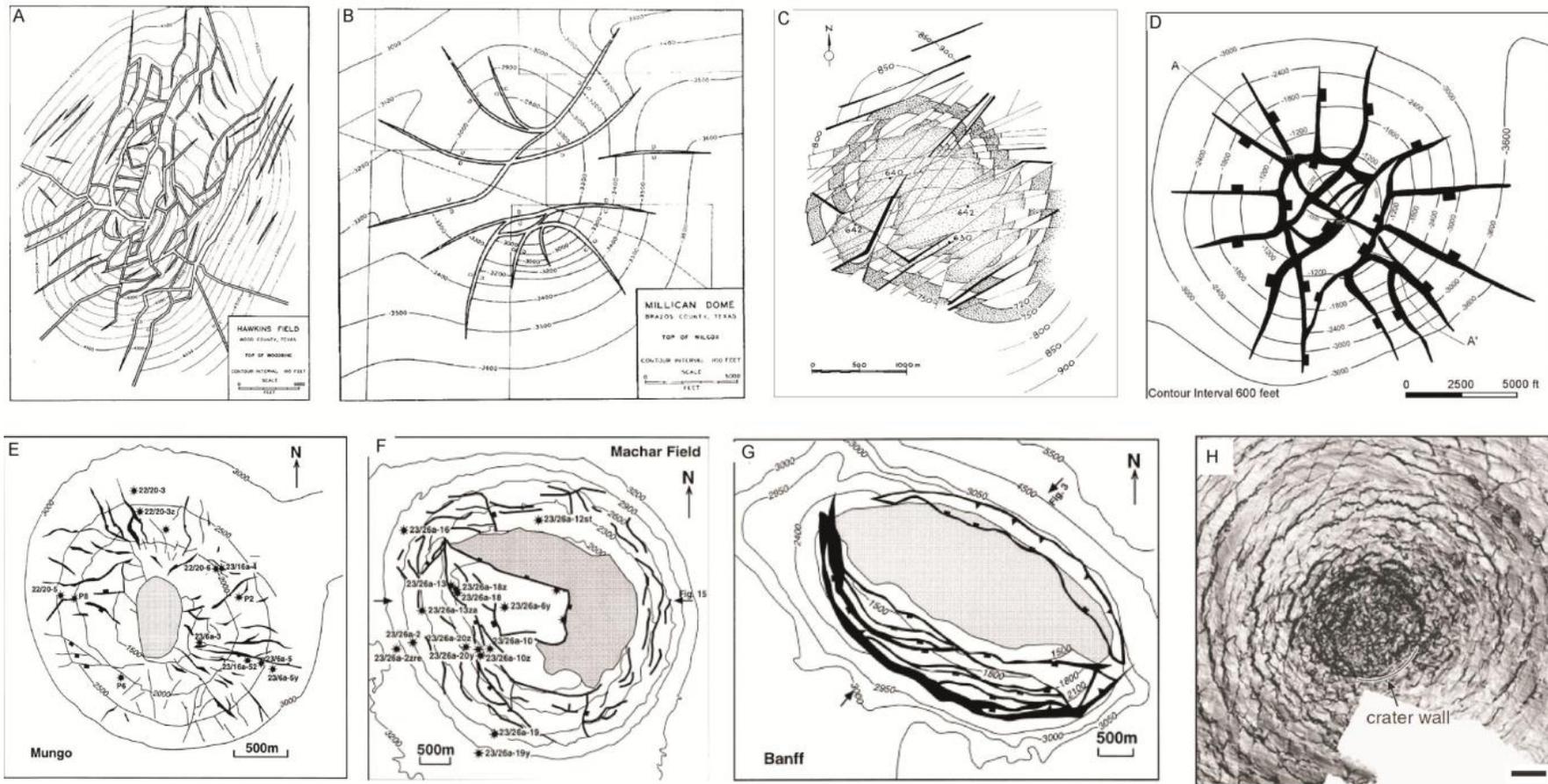
Fig. 1-26 Maps showing the principal fault patterns associated with salt domes. A-D) Carapace fault patterns showing radial faults around the flanks of the salt dome. E) Deep-seated radial faults around the stem of a salt diapir in the Central North Sea. F-G) Concentric faults around the Machar and Banff Salt Diapirs in the Central North Sea. H) Concentric faults above a collapse structure in the Southern North Sea. Figure from Carruthers (2012).
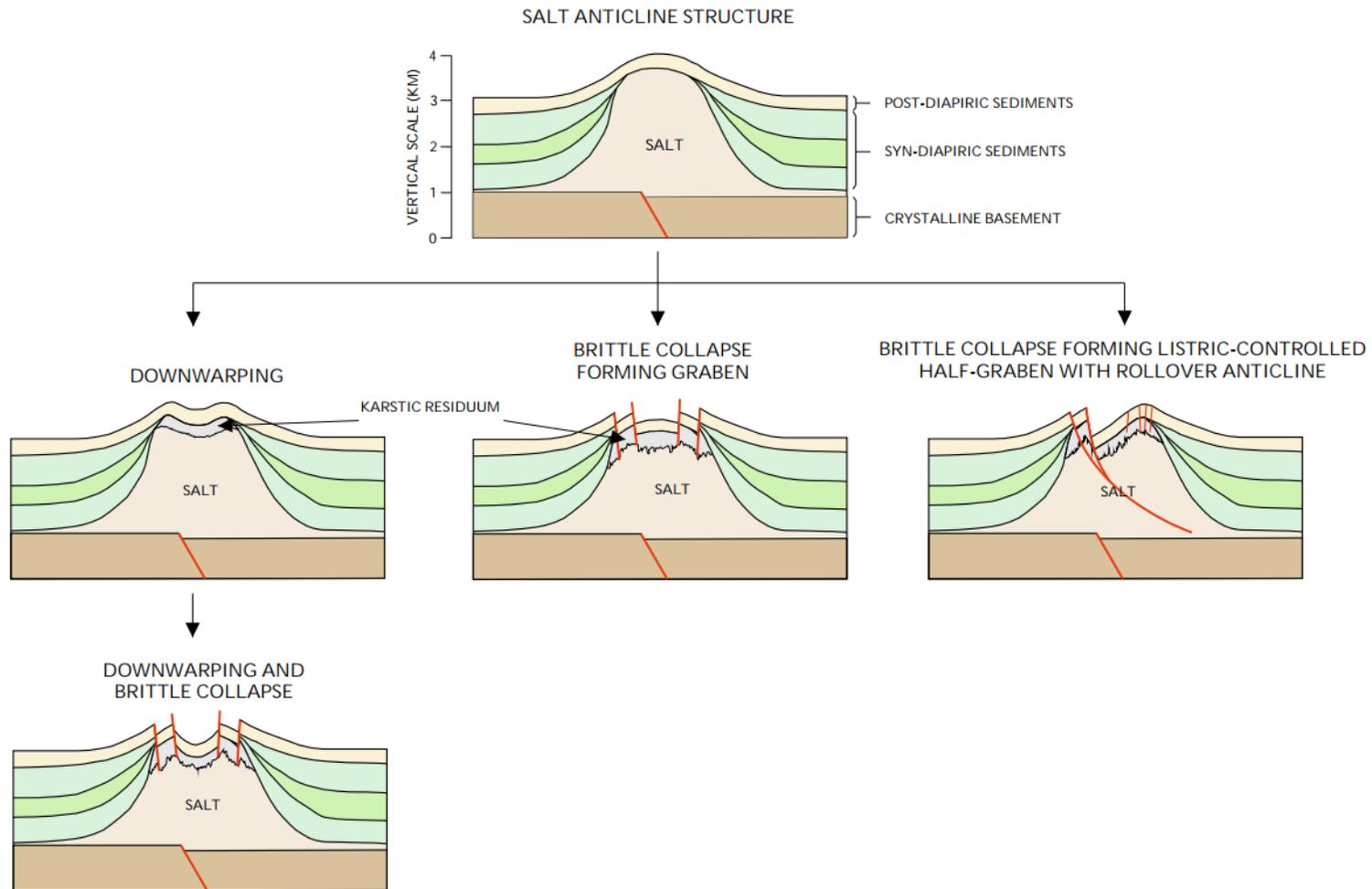
Fig. 1-27 Structural styles ranging from brittle graben and half-graben geometries to ductile sags and axial synforms in the Paradox Basin, Utah. Modified from Gutiérrez (2004).

reflecting brittle deformation (Randles, 2014) (Fig. 1-27). It has been suggested that the preferred style of dissolution-related collapse is related to the width of the salt anticline, with broader anticline crests being more susceptible to ductile deformation, and narrower crests typically showing brittle deformation (Cater and Craig, 1970). It is also important to note that ductile deformation will evolve to brittle structural styles whenever significant subsidence is recorded in crestal areas of salt structures (Fig. 1-27).

Apart from salt dissolution or salt withdrawal, which can lead to collapse structures on the crest of salt structures, regional tectonic stress is also significant, and is often related (together with salt-dissolution) to the formation of these same collapse structures (Ge et al., 1997; Ge and Jackson, 1998; Vendeville and Jackson, 1992a, Jackson and Vendeville, 1994). For example, extension is considered to be intrinsic in the development of graben and half-graben systems on the crests of salt structures (Vendeville and Jackson, 1992a).

1.6.3.1 Accommodation/transfer zones

Transfer zones are defined as discrete areas of strike-slip or oblique-slip faulting that trend parallel to the extension direction and facilitate the transfer of strain between extended domains arranged in *en echelon* patterns (Faulds and Varga, 1998). Accommodation zones are belts of overlapping fault terminations and can separate either system of uniformly dipping normal faults or adjacent domains of opposite-dipping normal faults (Faulds and Varga, 1998). Even though the definitions of transfer and accommodation zones is markedly different in the published literature, these two terms are used in an interchangeable manner as both of these structures indicate complex strain and stress regimes, often acting as zones adjusting the juxtaposition of regional and local stresses (Faulds and Varga, 1998).

Accommodation zones can be described as large rupture barriers (King, 1986) that impede the lateral propagation of normal fault systems (Fonseca, 1988; Thenhaus and Barnhard, 1989). They often occur in extensional domains. Key characteristics in transverse accommodation zones are an abrupt along-strike decrease in the displacement of major normal faults and reductions in fault-block tilting (Colletta et al., 1988). Figure

1-28 presents a classification scheme for accommodation zones, naming them as antithetic and synthetic (Faulds and Varga, 1998) (Fig. 1-28). Antithetic accommodation zones are characterised by antiform geometries between faults that converge with depth, and by synform geometries between faults diverging at depth. Synthetic accommodation zones are characterised by soft- and hard-linked relay ramp structures between en echelon arrangements of normal faults (Faulds and Varga, 1998) (Fig. 1-28).

Transfer zones or accommodation zones can influence the distribution of oil and gas fields by generating structural and stratigraphic traps, enhancing fluid flow and controlling syn-extensional sedimentary patterns, including the distribution of source and reservoir intervals (Faulds and Varga, 1998; Jacques, 2004; Paton et al., 2008; Liu et al., 2015). Accommodation zones can also form major drainage zones in related topographic lows, generating potential sources for sand-rich alluvial fans, fan deltas and turbidite deposits into adjacent basins (Faulds and Varga, 1998). A transverse accommodation zone and an oblique anticlinal transfer zone are studied in Chapters 4 and 5, respectively. The generation of accommodation zones, and their role as fluid migration paths are analysed.

1.7   Fluid flow in sedimentary basins

This section will briefly introduce mechanisms of excess fluid pressure (overpressure) in sedimentary basins, followed by an introduction of key fluid flow features on 3D seismic data. The last sub-section briefly explains the fault-seal mechanisms. Structural traps in supra-salt successions are often closely associated with densely developed fault families, which significantly control reservoir compartmentalisation.
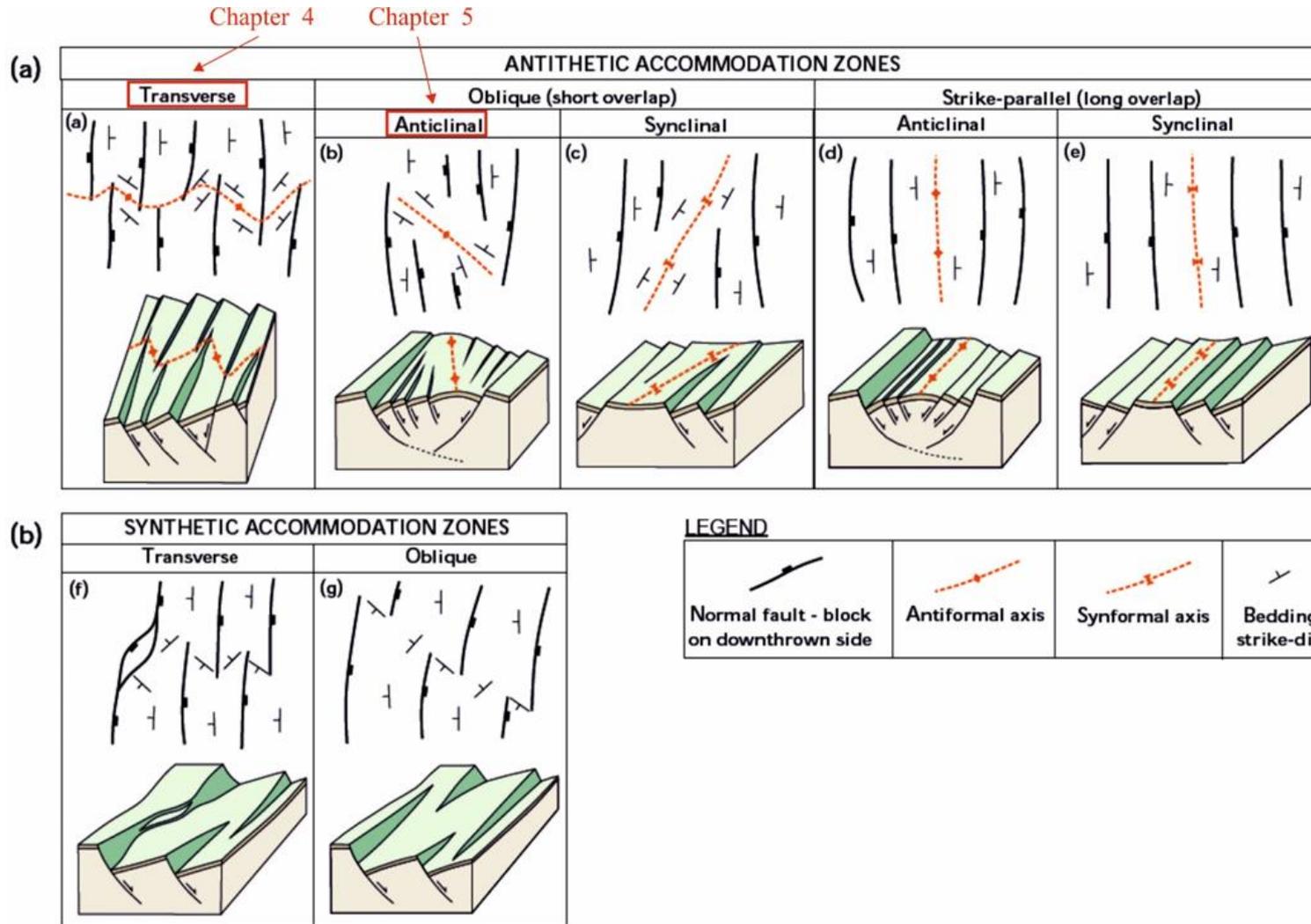
Fig. 1-28 Schematic map illustrating accommodation zones and their classsification. a) Antithetic accommodation zones are characterised by antiformal geometries between faults that converge with depth, and by synformal geometries between faults. Obliquity of the fold axes relative to fault strike is linked to the amount of overlap between fault tips. b) Synthetic accommodation zones are characterised by soft- and hard-linked relay ramp structures. Modified after Randles (2014).

1.7.1   Mechanisms of overpressure

Overpressure is a multi-disciplinary term applied both in and out of geosciences (Peacock et al., 2017). In this thesis, overpressure is defined as fluid pressure within a reservoir that exceeds hydrostatic fluid pressure, calculated as:

$$P_{ov} = P_f - P_h$$

Equation 1-4

in which equation, Pf represents fluid pressure within a reservoir interval. In the petroleum industry, fluid pressure is often measured by methods such as LWD (logging while drilling). P_h represents hydrostatic pressure, a parameter dependent on the depth of the targeting reservoir, and is calculated as:

$$P_h = \rho gh$$

Equation 1-5

ρ represents the density of pore water, which depends on its salinity and temperature. In practical terms, hydrostatic fluid pressure is often calculated using the following equation:

$$P_h = \rho_1 gh_1 + \rho_2 gh_2$$

Equation 1-6

ρ_1 represents the density of sea water, h_1 represents the height of water column from the free surface to the sea floor, and ρ_2 represents pore water density. The parameter h_2 represents the height between sea floor and the targeting depth.

Figure 1-29 illustrates the Terzaghi Principle, which was initially applied to soil mechanisms (Terzaghi, 1925). Fluid pressures which are located between ideal

hydrostatic and lithostatic trends are defined as overpressure (Fig. 1-29). In practice, reservoirs with fluid pressures exceeding 1.2 times the hydrostatic pressure are often defined as economically viable exploration targets in the petroleum industry.

Many of the worlds' largest oil and gas fields are often associated with overpressured reservoirs (Bethke, 1986; Hunt, 1990). However, overpressure in sedimentary basins comprises a major drilling hazard (Mouchet and Mitchell, 1989; Swarbrick and Osborne, 1998). The occurrence of overpressure can be as shallow as a few hundred meters below the surface, or occur at depths exceeding 6 or 7 km in strata ranging in age from the Pleistocene to the Precambrian (Vladimir and George, 1995). Numerous mechanisms for overpressure generation in sedimentary basins have been proposed, among which disequilibrium compaction and fluid expansion are often hypothesised as the main mechanisms (Sharp, 1976; Mark et al., 2009; Mouchet and Mitchell, 1989; Swarbrick and Osborne, 1998; Spencer, 1987; Bredehoeft et al., 1994) (Fig. 1-30).

Overpressure due to disequilibrium compaction will occur when pore-fluid expulsion is impeded during burial. When the rate of pore-fluid expulsion is slower than the rate of loading, the effectively sealed pore fluids will support some of the additional load and become overpressured as a result (Swarbrick and Osborne, 1998).

Overpressure due to fluid expansion is caused by an increase in fluid volume in an effectively sealed pore space, and includes mechanisms such as maturation of kerogen to gas (Spencer, 1987; Bredehoeft et al., 1994), dehydration reactions (e.g., smectite to illite) and expansion of fluids due to higher temperatures (Perry and Hower, 1972; Barker, 1990). Other mechanisms such as aquathermal and gas thermal expansion, buoyancy and load transfer are often thought to comprise minor factors contributing to overpressured intervals in sedimentary basins (Yardley and Swarbrick, 2000) (Fig. 1-30).

Overpressured intervals are inherently unstable and tend to return to hydrostatic equilibrium after they are initially generated (Borge, 2002). High magnitude overpressure is thus assumed to generate only within, or proximal to, their origins (Swarbrick and Osborne, 1998; Lee and Deming, 2002; Bowker, 2007). Examples include shale reservoirs in which oil and gas are generated and preserved within the same stratigraphy unit. However, significant reservoirs around the world often comprise oil and gas from various sources, hinting at an additional mechanism of overpressure within these same
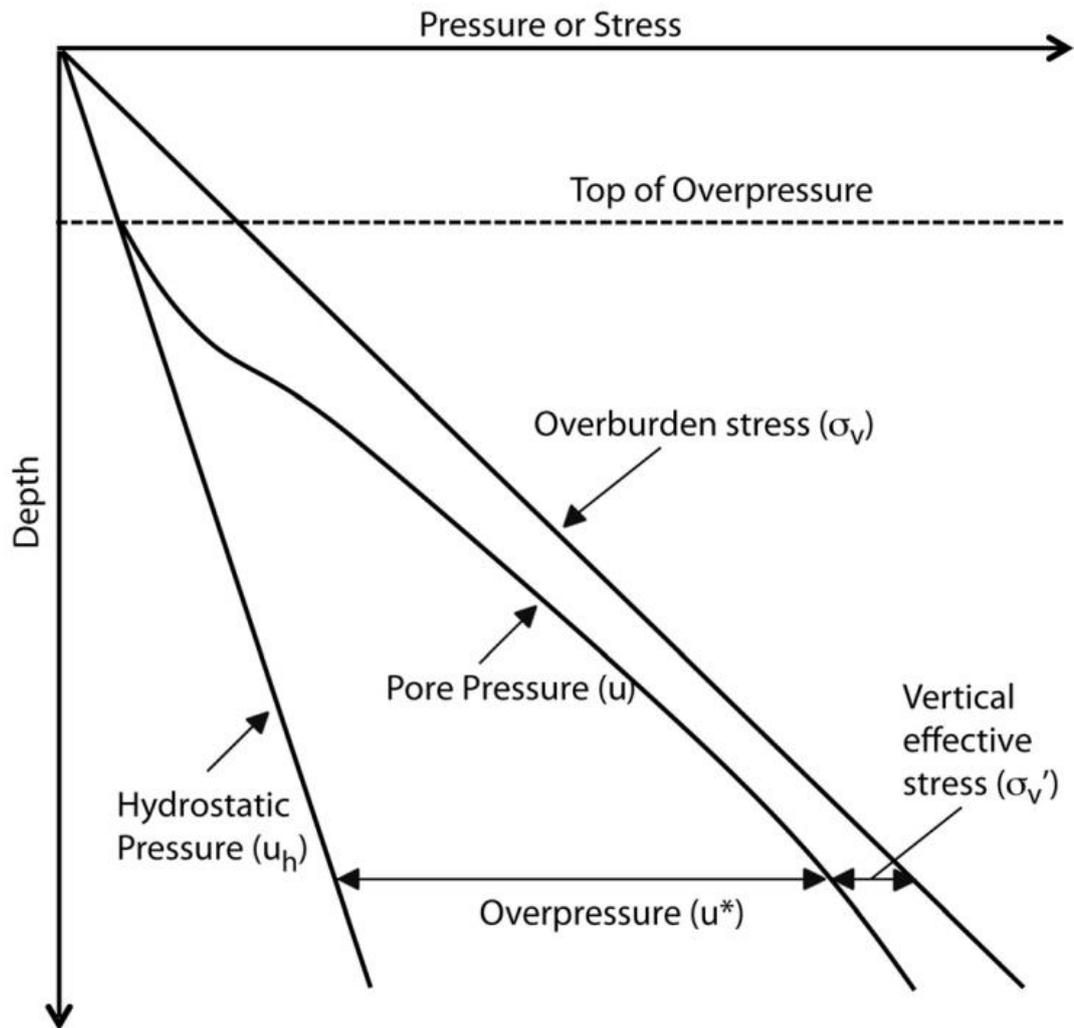
Fig. 1-29 Illustration of overpressure relative to hydrostatic pressure, pore pressure, overburden stress and effective vertical stress. Figure from Dugan (2012).
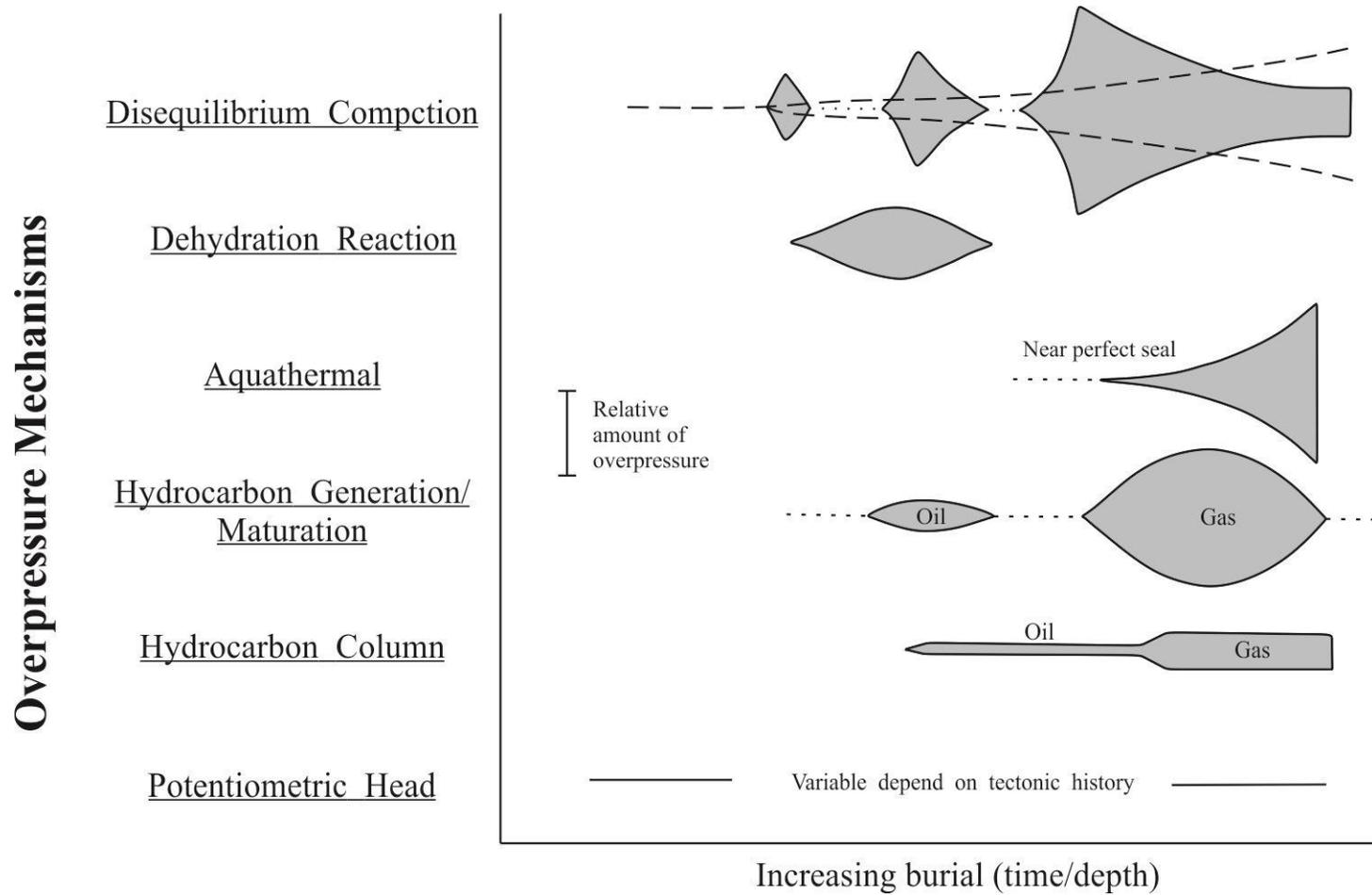
Fig. 1-30 Schematic representation of overpressure development through time during progressive burial for each of the principal mechanisms of overpressure generation. Modified from Swarbrick (1995).

reservoir intervals. Overpressure transfer, laterally or vertically, have thus been proposed to contribute to high-magnitude overpressure intervals (Tingay, 2007; Yardley, 2000). In detail, Yardley and Swarbrick (2000) demonstrated that overpressured intervals become redistributed within inclined, isolated reservoirs, resulting in "lateral transfer" of overpressure onto structural crests. Research work have also demonstrated vertically transferred overpressure through active faults and fractures, generating high-magnitude overpressure in tectonically inverted basins recently uplifted (Luo et al., 2003; Mark et al., 2007; 2009).

Distinct mechanisms are hypothesised as contributing to the generation of overpressure in sedimentary basins. However, no single mechanism accounts for the generation of overpressure. As indicated by Guo et Al. (2010), oil generation is rarely the predominant mechanism for overpressure in Cenozoic basins (Guo et. al, 2010). In this thesis, multiple stages of overpressure build-up and destruction within the same stratigraphic unit were identified, revealing important stages of fluid migration and trapping in supra-salt sediments.

1.7.2   Seismic fluid flow features

Fluid transfer may, or may not, necessarily generate overpressured intervals in sedimentary basins, i.e. subsurface fluids can end up being released into the surface or atmosphere. Fluid flow features represent anomalies generated during the subsurface flow of fluids (oil, gas, brine, groundwater and magmatic fluids), from source to the surface, or into subsurface sedimentary units (Christian, 2005; Cartwright et al., 2007; Løseth et al., 2009; Andresen, 2012). Processes behind the release of fluid in sedimentary basins can be instantaneous and catastrophic, e.g. fluid flow associated with sediment mobilization lasting millions of years (Huuse, 2010; Andresen, 2012). Fluid flow in sedimentary basins attracts widespread research interest due to its close association with groundwater flow systems, petroleum migration, geothermal reservoirs, ore-forming and seabed ecosystems, all of which of vital economic importance (Dando et al. 1991; Hovland et al. 2002).

Fluid flow features are typically represented by amplitude anomalies on seismic data, together with a wide range of structures such as pockmarks, mud volcanoes, gas hydrates, chimneys, pipes, sediment injection, carbonate mounds, seeps and related diagenetic phenomena (Cartwright et al., 2007; Løseth et al., 2009; Huuse et al., 2010; Andresen, 2012). Fluid flow features can be classified according to their geometry, lithology, the type of impact on the hosting sediment, and causes for their formation (e.g. Cartwright et al., 2007; Løseth et al., 2009; Huuse et al., 2010; Andresen, 2012). Three main groups of seismic fluid flow features, divided according to their formation mechanisms, were summarised by Andresen (2012) as subsurface sediment remobilization, vertically focused fluid flow, and laterally extensive fluid flow (Fig. 1-31).

Sediment remobilisation events are often associated with subsurface fluid migration. In parallel, fluid flow often results from overpressure build-up, which facilitates fluid remobilisation from pore to basin scales (Cartwright et al., 2007; Andresen, 2012). Typical expressions of fluid flow events are represented by sand injection complexes (Huuse et al., 2005; Huuse et al., 2007; Jackson et al., 2011; Huuse et al., 2012) and mud volcano systems (Stewart and Davies, 2006; Roberts et al., 2010; Judd and Hovland, 2007) (Fig. 1-31). Seismic features of vertically focused fluid flow include pockmarks, chimneys, pipes, and other discrete seabed features such as methane-derived authigenic carbonates (Fig. 1-31). Pockmarks are typical expressions of vertical focused fluid flow recognised as circular to elliptical depressions at the (paleo) sea floor (Judd and Hovland, 2007). Gas chimneys or pipes are vertical extensive low- or high-amplitude anomalies on seismic data (Hustoft et al., 2010; Moss and Cartwright, 2010; Løseth et al., 2011). Methane-derived authigenic carbonates are often described together with other focused fluid flow features such as pockmarks (Andresen et al., 2008; Liu et al., 2008).

Laterally extensive fluid flow features are often recognised as high-amplitude anomalies on seismic data such as gas hydrates, free gas zones, bottom-simulating reflections (BSRs), hydrocarbon-related diagenetic zones (HRDZs) and diagenetic fronts (Berndt et al., 2004; Davies and Cartwright, 2007; Andresen et al., 2011) (Fig. 1-31). In this thesis, significant fluid flow features such as pockmarks, hydrocarbon-related

66
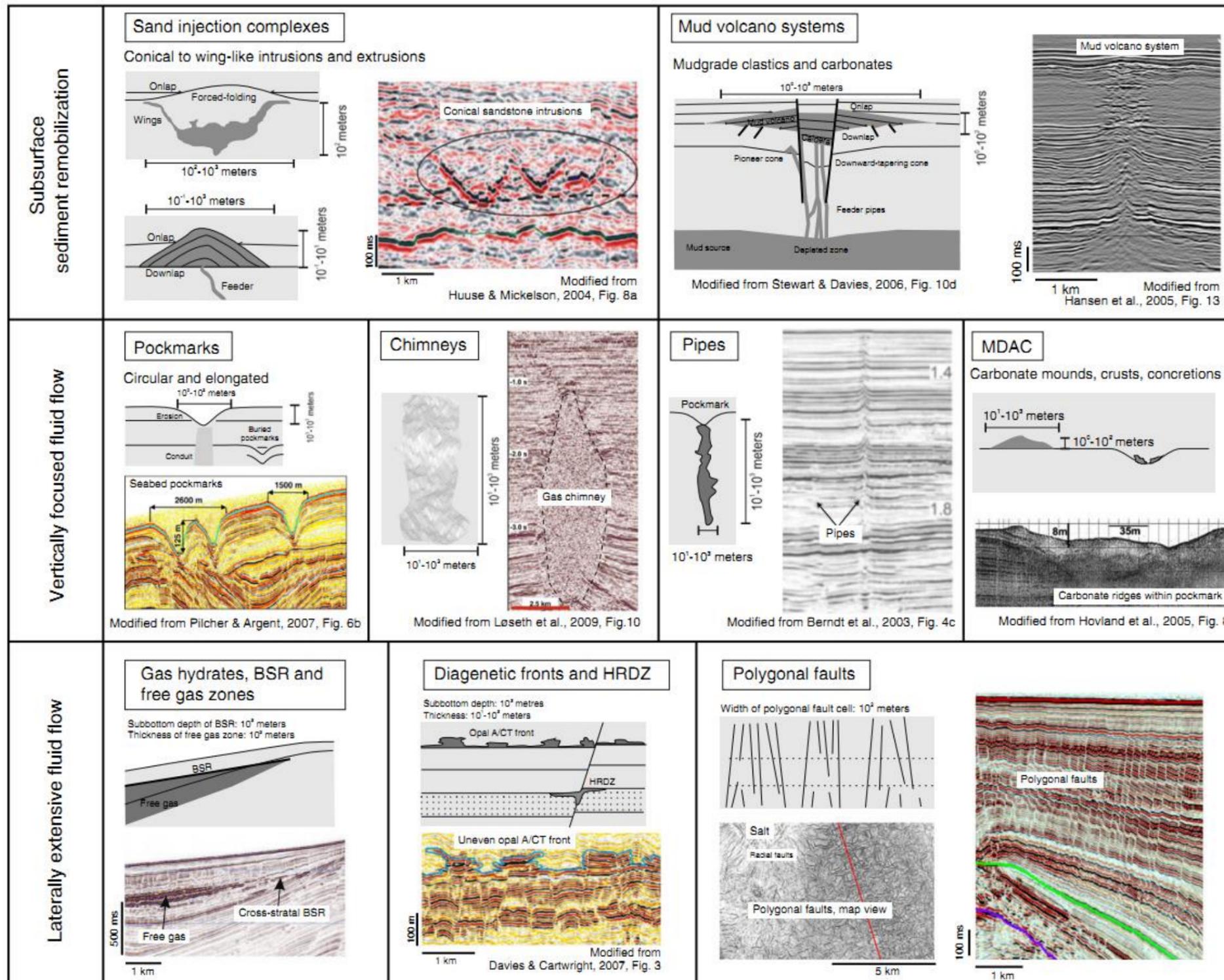
Fig. 1-31 Schematic illustrations and seismic examples of fluid flow features in sedimentary basins. Figure from Andresen (2012).

67

diagenetic zones, and free gas zones are analysed. The mechanisms behind these fluid flow events are discussed in detail.

1.7.3 Fault sealing behaviours

Faults represent the main pathways for fluid flow from deep reservoirs to the surface (see Faulkner, 2010), but can also act locally as impermeable barriers that restrict fluid flow (Frery et al., 2015). Whether faults are conduits or seals for fluid flow depends on their geometry, growth history, hydraulic properties and the nature of the displaced host stratigraphy (Yielding et al., 1997; Walsh et al., 1998; Ligtenberg, 2005; Cartwright et al., 2007; Andresen et al., 2009; Andresen, 2012; Magee, 2016). Fault seal behaviour may change through time, e.g. fault changing from seal to conduits due to fault reactivation in Chapter 4 (Wiprut, 2000; Wibberley, 2015). A number of mechanisms have been recognised in which fault planes can act as competent seals (Watts, 1987; Knipe, 1992) (Fig. 1-32):

- When different sediment units are juxtaposed along faults, e.g., reservoir sands are juxtaposed against a low-permeability unit (e.g., shale) with a high entry pressure.

- When clay smear/shale gouges (i.e., entrainment of clay or shale) occur in the fault plane, thereby giving the fault a high entry pressure *per se*.

- When cataclasis occurs on the fault plane, generating lithology-dependent damage zones with high capillary entry pressure.

- When diagenetic processes occur on fault planes, particularly if preferential cementation along an originally permeable fault plane may partially or completely remove porosity, ultimately creating a competent hydraulic seal.
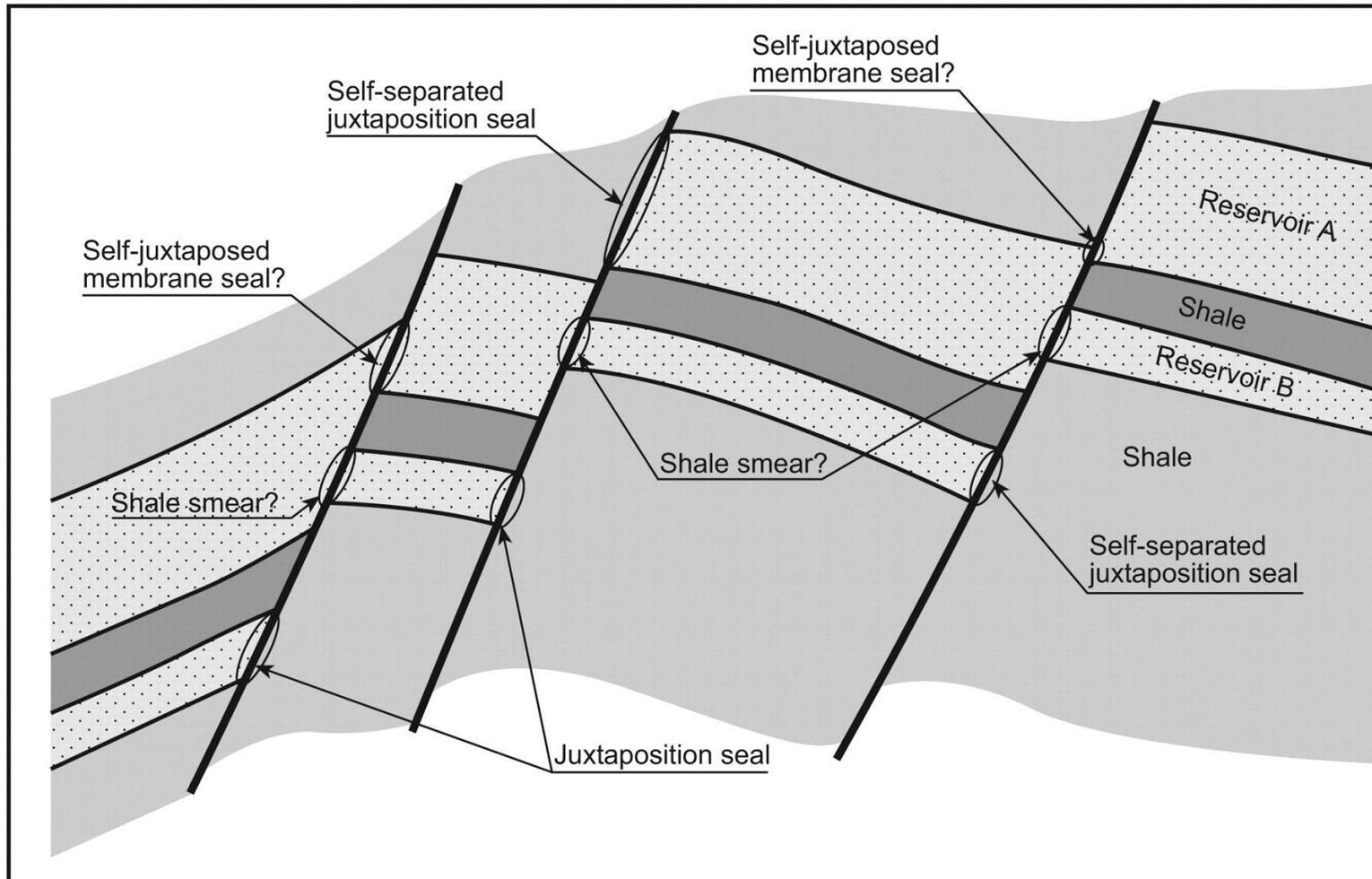
Fig. 1-32 Schematic illustration showing potential hydrocarbon traps resulting from normal faults that offset a sand–shale sequence. Figure from Ronald (2006).

Chapter 2

Datasets and methods

2.1 Introduction

Seismic data are widely used in the petroleum industry. The resolution of seismic data is constantly improving as a result of better processing algorithms, computer power and acquisition equipment. This chapter will briefly introduce the 3D seismic dataset used in the thesis. The readers will learn about the basics behind 3D seismic acquisition, processing, and interpretation in books such as 'seismic waves', '3D seismic interpretation' and Ph.D. theses such as D. Gamboa's (2014) and N. Mattos' (2017). The focus of this chapter will be on introducing the 3D seismic volume and field data analysed in this thesis, seismic interpretation and volume attributes utilised, key methods of structural and stress analysis, and other methods used in Chapter 6.

2.2 Study areas and data used in the thesis

The aims of the study are to understand crestal faults evolution and their association with fluid flow in sedimentary basins, and the limitations of current displacement analysis for fault growth histories. Due to the fact that crestal faults comprise a group of faults with limited scales (often with length < 3.5 km and displacement < 50 m), high resolution seismic data are essential to conduct research into the research of the thesis. High resolution seismic data offshore Espírito Santo Basin, SE Brazil is thus used in this research. To extend the understandings of how displacement analysis can potentially influence fault growth analysis, scales of faults are expanded from seismic scales to sub-seismic and rift scales, which are not available with the seismic volume offshore Espírito Santo Basin, SE Brazil.

The three-dimensional seismic volume used in this thesis covers an area of approximately 1800 km^2 of the Espírito Santo Basin, SE Brazil, at a minimum water depth of 1600 m (Fig. 2-1). The vertical sampling rate for the interpreted seismic volume is 2 ms, restacked at 4 ms after the application of an anti-aliasing filter. Its bin spacing is 12.5 m. With a dominant frequency of 40 Hz, the vertical resolution of the seismic data is estimated to be between 8-10 m near the sea floor and 20 m at the maximum depth of strata investigated in this work (Fig. 2-2). Field data includes throw profiles for thirteen
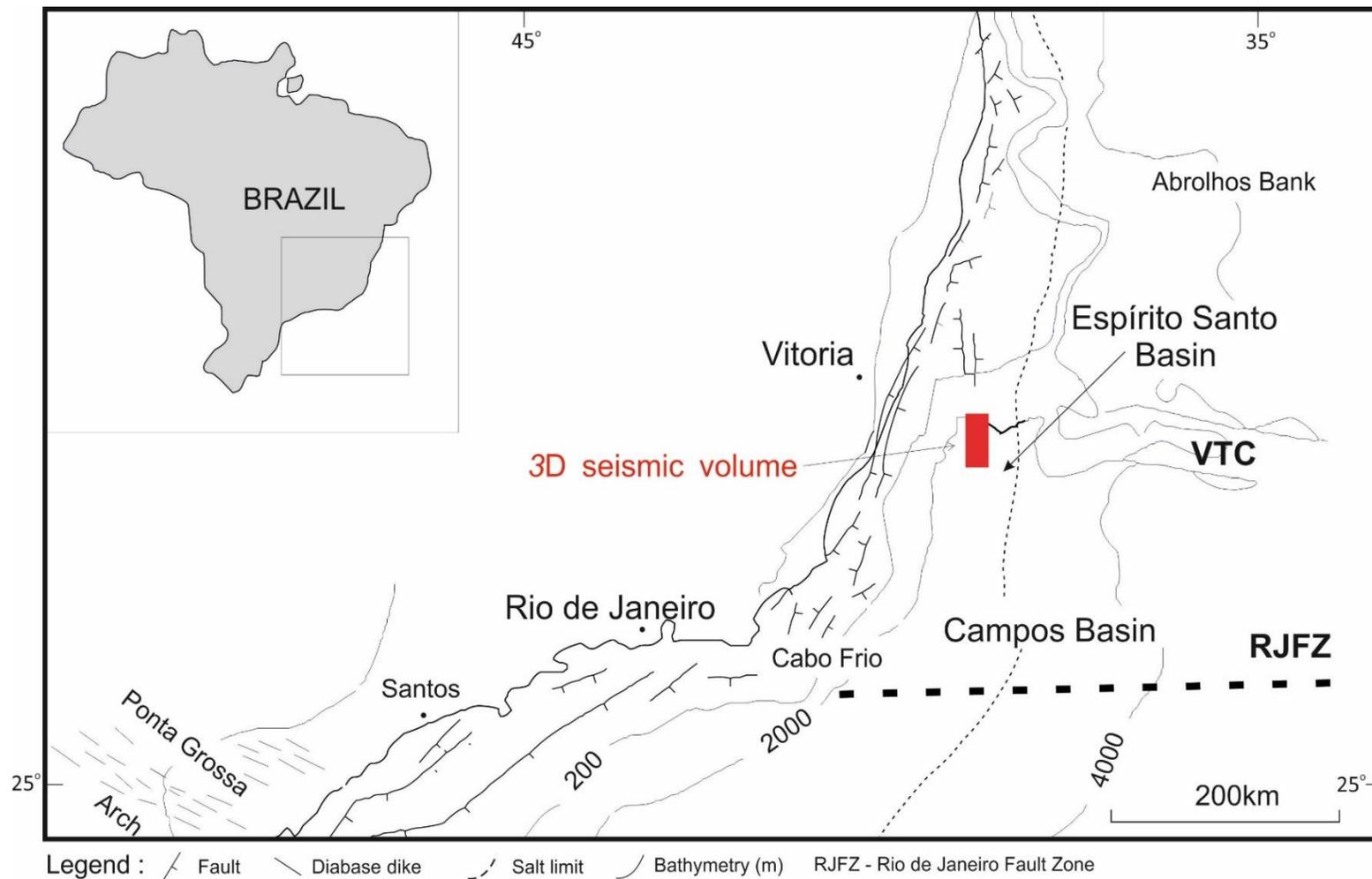
Fig. 2-1 Regional maps of the Southeast Brazilian margin showing the relative location of the South Atlantic and the location of the 3D seismic volume used in this thesis (red box).
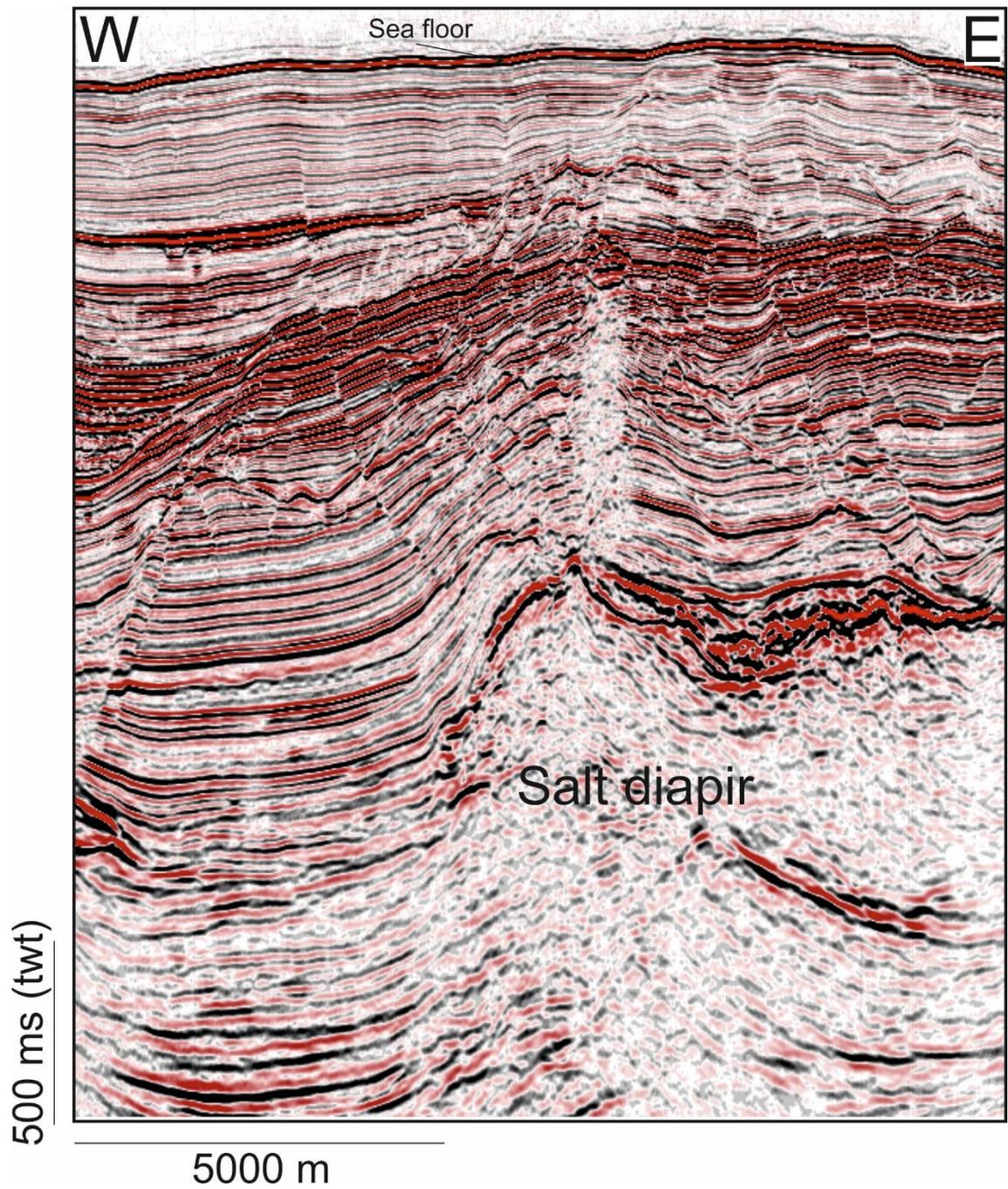
Fig. 2-2 Seismic section showing the high-resolution seismic volume used in the thesis. The maximum depth of the investigated supra-salt structures is approximately 2000 meters, with a vertical seismic resolution of ~ 20 meters.

73
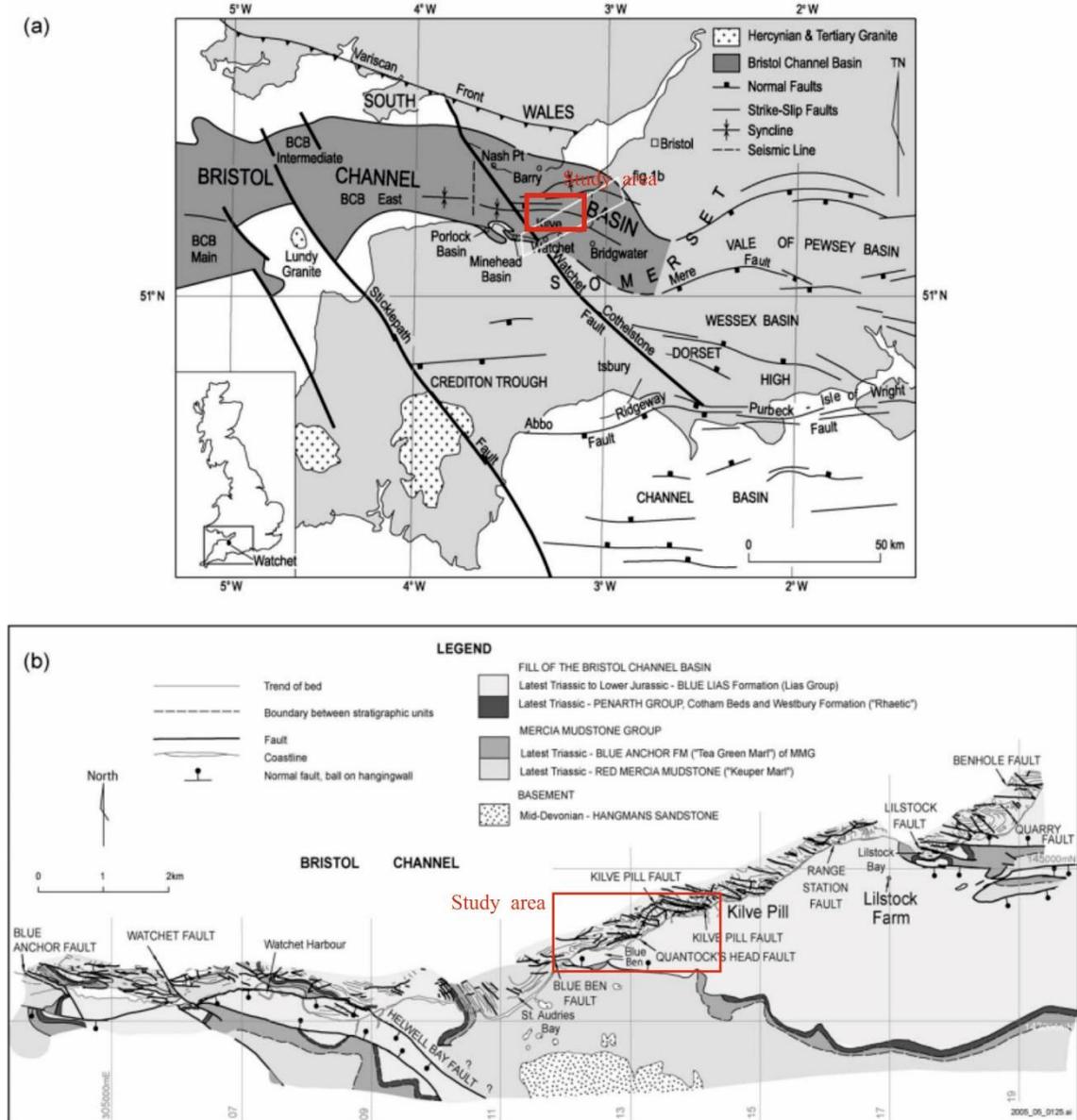
Fig. 2-3 Location of the area in the Somerset Coast (Kilve Beach) which sub-seismic faults were

measured for this thesis. Figure from R.A. Glen et al. (2005).

Fig. 2-4 Examples of sub-seismic faults in the Somerset coast (Kielve Beach).
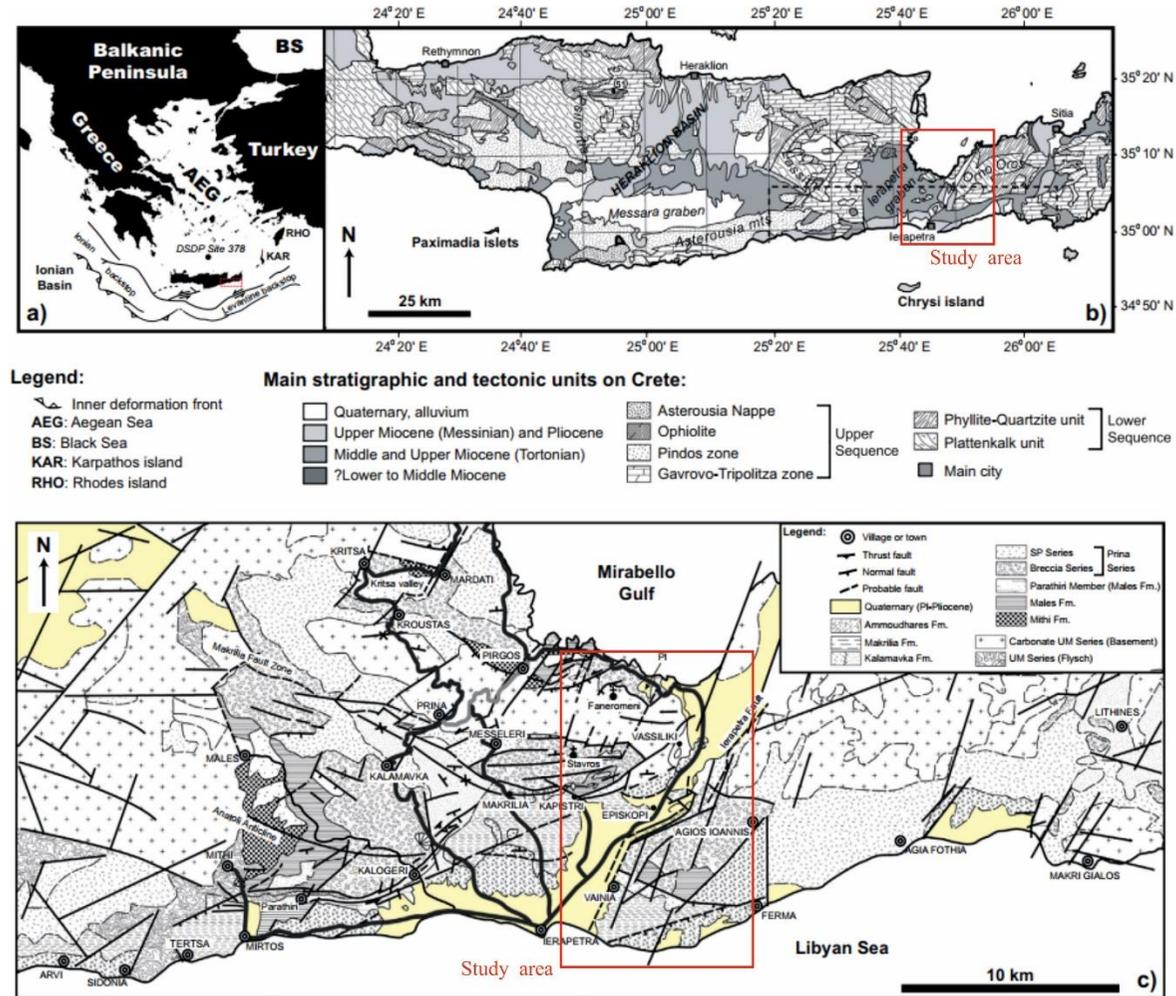
Fig. 2-5 Example of rift faults from the Ierapetra Fault Zone, SE Crete, as documented in this thesis. Modified from Alves et al. (2018).
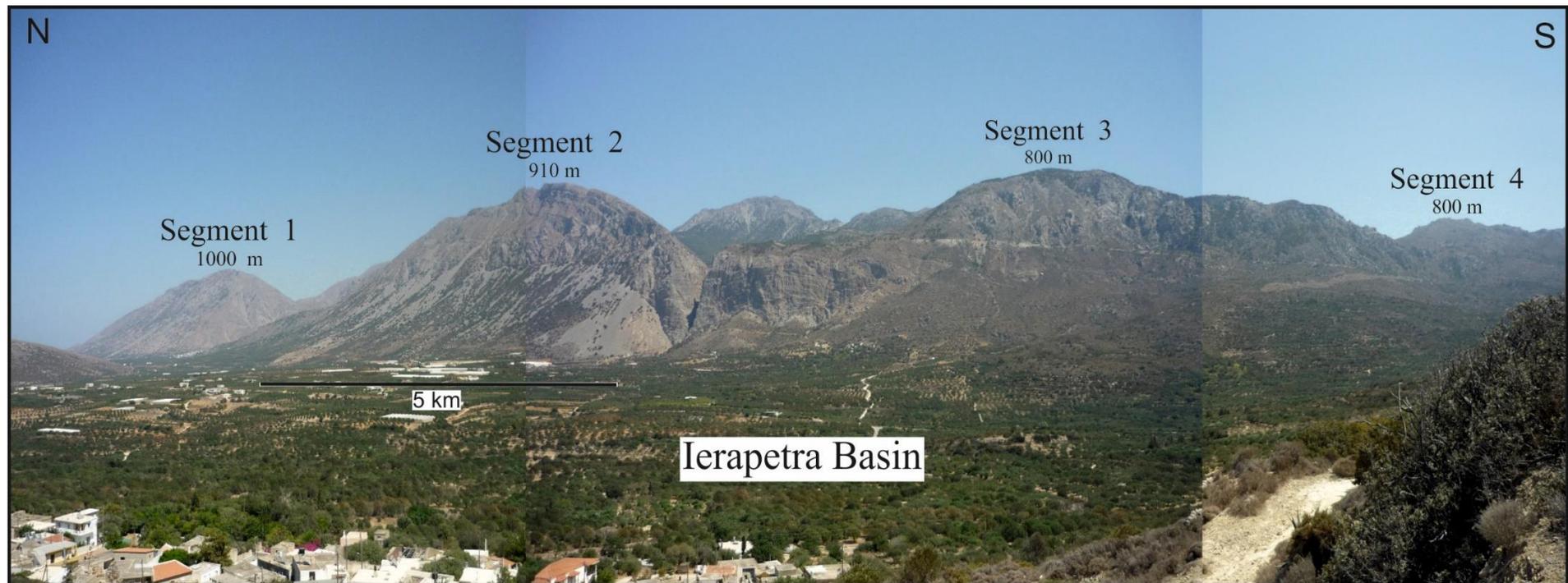
Fig. 2-6 Panoramic photo of rift faults used in the thesis from the Ierapetra Fault Zone, NE of Ierapetra, SE Crete. The fault comprises four distinct fault segments with elevations of 1000 m, 910 m, 800 m and 800 m respectively.

(13) sub-seismic faults with fault lengths ranging from 1.65 m to 7.55 m and maximum throw values ranging from 3 cm to 29 cm from Somerset, Bristol Channel (Figs. 2-3 and 2-4). Rift faults from the Ierapetra Fault Zone, SE Crete, were also analysed. They show lengths of 7.1-19.5 km and maximum throw values ranging from 0.27 km to 1.05 km (Figs. 2-5 and 2-6).

2.2.1 Seismic data in Chapter 4

The study area in Chapter 4 is located on a prominent NW-SE trending salt ridge with a width of 4 km and a length over 30 km (Fig. 2-7). This salt ridge separates two NE–trending salt-withdrawal basins (Fig. 2-7). Analysed faults cover an area of ~ 8 km^2 of the seismic volume.

2.2.2 Seismic data in Chapter 5

The study area in Chapter 5 covers an area of ~ 24 km^2 from the Northwest part of the seismic volume (Fig. 2-7). Three distinct underlying salt diapirs were identified in this region.

2.2.3 Data used in Chapter 6

The seismic-scale faults interpreted in Chapter 6 cover a large portion of the interpreted seismic volume, imaging crestal faults, radial faults, low-angle normal faults and faults within the limits of seismic resolution (Fig. 2-7). Faults from Somerset and Crete are used in this chapter to extend the analysis to the sub-seismic and rift scales (Figs. 2-3 to 2-6).

2.2.4 Seismic data used in Chapter 7

The seismic sections used in Chapter 7 cover a wide area of the 3D seismic volume used in this thesis (Fig. 2-7). See for Chapter 6 for details.
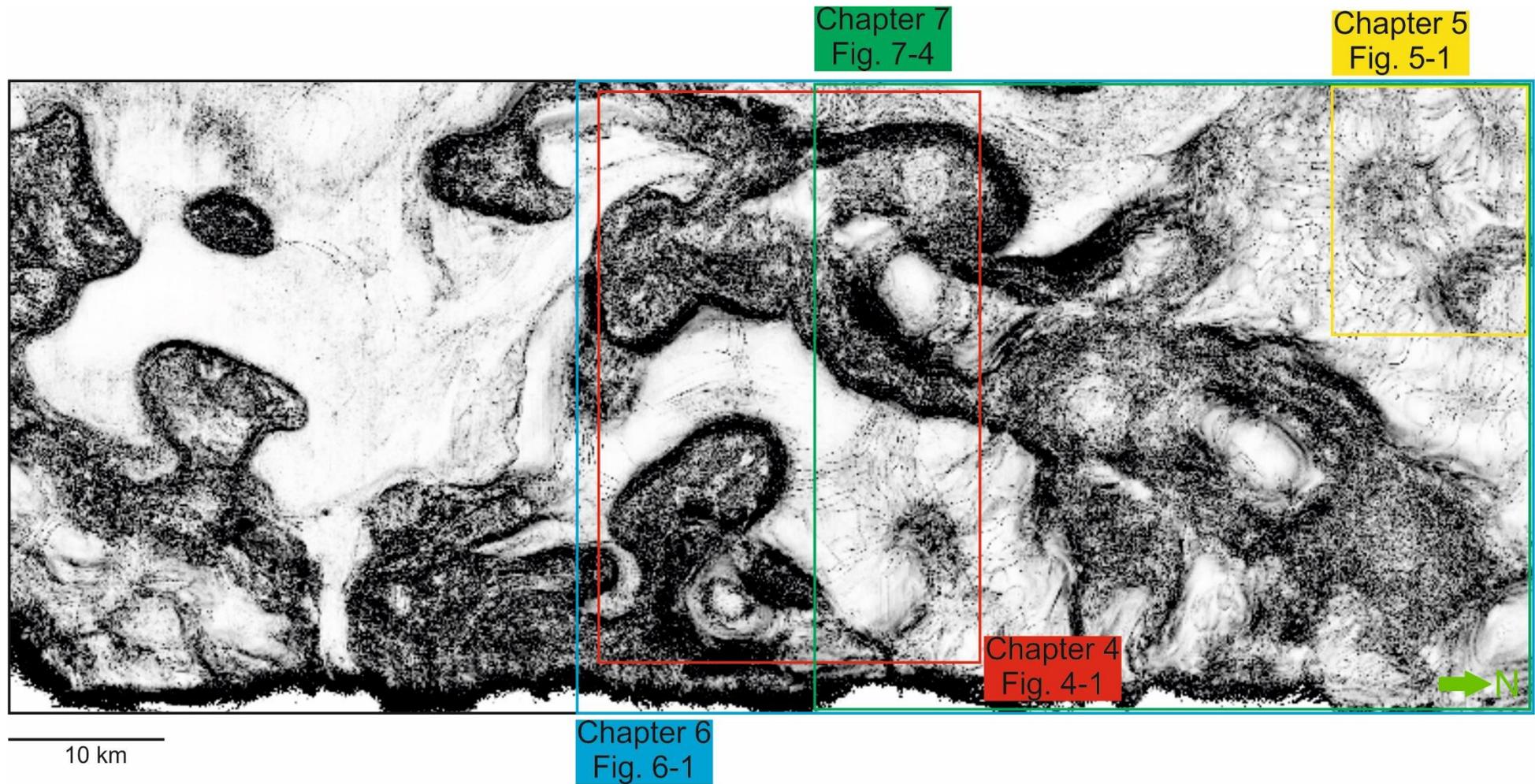
Fig. 2-7 Variance map shows the specific study areas mentioned in the Chapters relating to the Espírito Santo Basin. See Fig. 2-1 for the location of the map.

2.3 Seismic data interpretation

Seismic interpretation was undertaken in Schlumberger's Petrel®. Horizon and faults interpretation were undertaken manually with rigorous quality control. Volume attributes were produced to constrain the interpretations in this thesis, and to reveal the geometries of key geological features (e.g., variance attribute in Figure 2-7).

2.3.1   Structural interpretation

Seismic reflections on a seismic section are a result of impedance contrasts between two interfaces (Brown, 2011). An increase in acoustic impedance, which is calculated as:

$$Imp = V * \rho$$

Equation 2-1

will result in acoustic peaks on seismic sections, represented as red reflections in the seismic sections shown in this thesis (Fig. 2-2). The sea floor, for example, is revealed as a strong and continuous seismic reflection (Fig. 2-2).

The relative ages of interpreted seismic horizons were based on the published literature (Fiduk et al., 2004; Alves and Cartwright, 2009b, Baudon and Cartwright, 2008c, Chang et al., 1992b). Interpretation of seismic horizons was undertaken on Petrel® using a very closely constrained seeded 3D auto-tracking tool, in which reflections with similar total energy, phase and amplitude are picked automatically. When finding major interruptions on seismic reflector continuity such as major faults, channel thalwegs, erosional unconformities, diapirs, etc., the 3D auto-tracking usually stops. Apart from geologically significant interruptions, parameters constraining the 3D auto-tracking tool such as seed confidence and tracing angles also have a paramount influence on auto-tracking efficiency. When tracing a weak and discontinuous horizon, manual tracking was necessary to obtain an accurate horizon for interpretation.

Fault interpretation tools on Petrel® were used to interpret faults. Reflection disruption and offset are the most apparent characters used to identify faults on seismic data. As the major questions addressed in this thesis, crestal fault geometry, crestal fault growth histories and scale variations during fault analyses, are closely related to fault geometry and fault plane roughness, faults were interpreted under maximum horizontal seismic resolution, 12.5 m, every inline/crossline.

2.3.2   Seismic attributes

Seismic attribute maps were used to reveal key geological features. Key seismic attributes on seismic data derive from three key properties of seismic waves; amplitude, phase and frequency.

Amplitude reflects the maximum magnitude of a wavelet and can be either positive or negative. However, this attribute is variable due to depth (and acquisition) changes in acoustic impedance, which are also directly related to the density and velocity of a sediment layer (Equation 2-1). Velocity and density are sensible to properties such as lithology changes, porosity, and fluid content within the investigated media (Brown, 2011). Root-mean-square (RMS) amplitude represents the average squared amplitude of seismic wavelets within a defined seismic interval (Brown, 2011). RMS amplitude is first used to aid the interpretation of salt structures, faults, and mass-transport deposits. Later in this thesis, RMS amplitude is used to identify amplitude anomalies within salt structures which are, in most cases, closely associated with clastic sediment and fluid rich strata (see Chapters 5 and 7).

Apart from the amplitude attributes mentioned above, discontinuity attributes such as seismic coherence (variance) have been widely used to visualise major faults discernible from seismic profiles alone (Di and Gao, 2014). Dip magnitude or dip azimuth of a surface can also help the identification of key structural features (Bahorich and Farmer, 1995). Curvature is useful to the identification of subtle faults, or small faults beyond seismic resolution (Roberts, 2001). Coherence is calculated by comparing the similarity between adjacent waveforms in a volume of continuity (normal reflections), converting it into a volume of discontinuity. The time-sliced volumes generated in this work were used to reveal geological discontinuities in map sections, such as faults or

stratigraphic discontinuities, and are often free of interpretation bias (Brown et al., 2004). Coherence volumes are particularly used to assess the internal architecture of stratigraphic features identified on seismic data.

Curvature is a second-derivative based attribute useful to delineate faults and predict fracture orientation and distribution (Roberts, 2001). Gaussian curvature is defined as the product of the minimum and maximum curvatures. Dip curvature is the curvature extracted along the dip direction, whereas strike curvature is extracted along strike, perpendicularly to the dip direction. Strike curvature and dip component curvature are highly correlated with the presence of open fractures affecting different lithologies (Roberts, 2001).

Coherence (variance) is an attribute calculated through the application of filters controlling the continuity of the data set, comprising a mathematical conversion of a seismic-amplitude volume into a discontinuity volume. This attribute is used to highlight amplitude discontinuities, such as faults, fractures and salt structures (Brown, 2011). Coherence can also be used to identify major depositional features such as channels and carbonate reefs (Schlumberger, 2014).

The attributes mentioned above can be produced for an entire seismic volume before the interpretation of horizons and faults, helping seismic interpreters. All these attributes can also be produced based on a pre-determined structural interpretation, generating surface attributes. Surface attributes are produced for specific seismic horizons or fault surfaces to better understand key geological aspects. However, compared to volume attributes, the accuracy of surface attributes is strongly influenced by the interpreter's skills and structural knowledge.

Isochron maps are produced in this thesis (Chapter 5) to provide information on the thickness of sedimentary units, and their significance in terms of the regional and local tectonic settings.

2.4 Structural analysis

Throw measurements along fault strike and throw measurements with depth are key techniques in fault analyses throughout this thesis. Expansion index, maximum throw

depth locations for distinct fault families, and stress analyses are also completed to address key research questions.

2.4.1 Throw analyses

Displacement data is widely used to address the mechanisms of fault initiation and fault growth histories (Baudon and Cartwright, 2008; Cartwright and Mansfield, 1998; Cartwright et al., 2008). Displacement plots along the strike of a fault are particularly useful to identify the exact locations where maximum displacement occurs, any linkage zones, and the geometry of fault segments (Ze and Alves, 2016). The relationship between fault throw values and depth is an efficient tool to identify fault reactivation and vertical growth histories (Baudon and Cartwright, 2008).

2.4.1.1 Throw measurements on seismic data

Throw and heaves comprise the vertical and horizontal components of fault displacement (Fig. 2-8). For faults that are planar in a vertical direction, throw data is often considered as approaching true fault displacement. However, for low-angle and listric faults, heave often dominates fault displacement at increasing depths (Fig. 2-8). Throw measurements on seismic data were performed in distinct ways. With faults striking in N-S or E-W directions, throw data were measured every inline/crossline (12.5 m) at the maximum horizontal resolution (trace spacing) of the seismic data. Composite lines were used to undertake throw measurements for faults that striking away from E-W or N-S directions. Faults analysed in the study are not highly listric and rotated faults that, using throw as proximal for displacement is considered appropriate in the study.

When producing throw-distance (T-D) plots, throw measurements along key stratigraphic horizons were used in this thesis, with these horizons often comprising unconformities and marking important phase(s) of fault reactivation (Baudon and Cartwright, 2008; Ze and Alves, 2016). Throw-depth plots are produced at the location of maximum displacement (D_{max}) of a fault segment. For faults that comprise only one
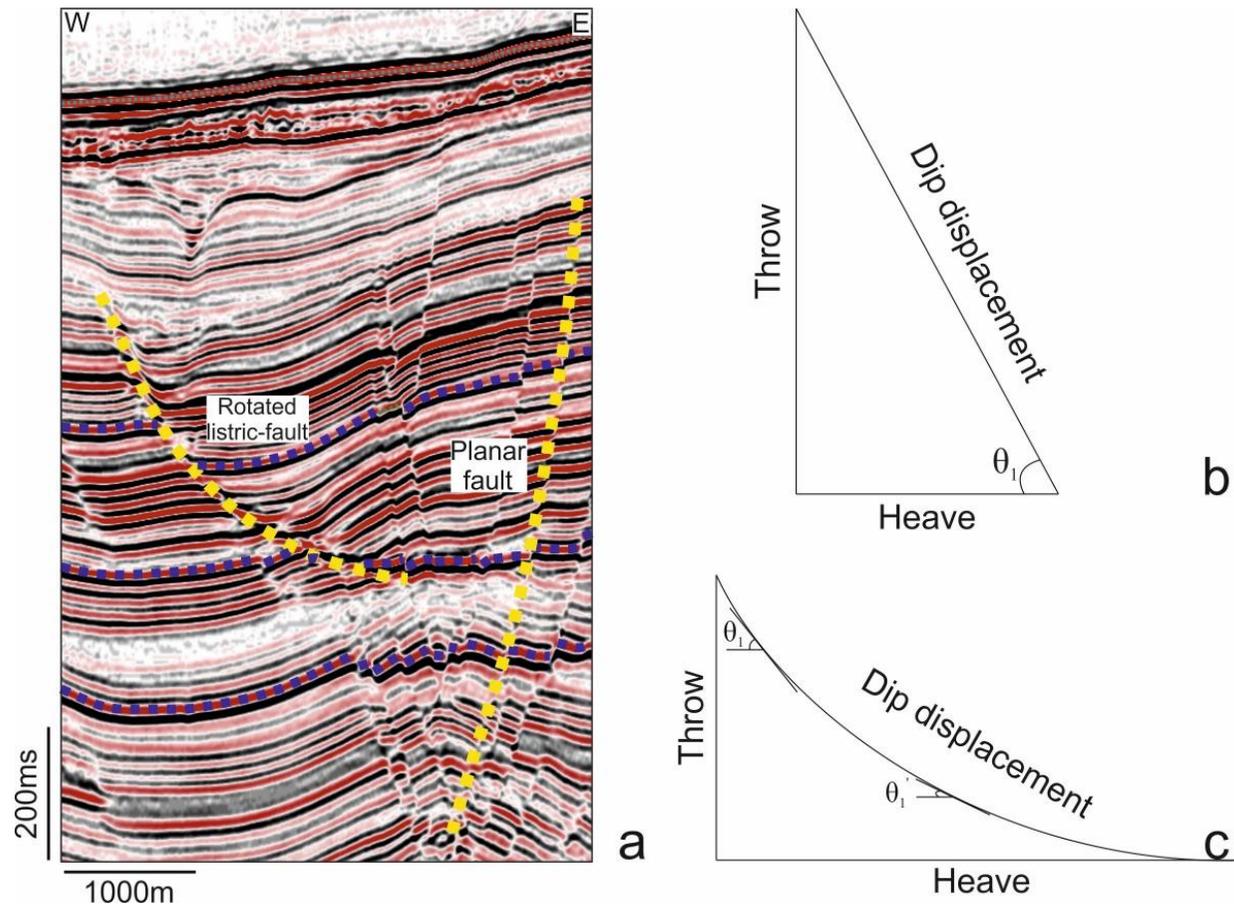
Fig. 2-8 Seismic sections illustrating the two components of throw and heave used to undertake displacement analyses in this thesis. a) Seismic section showing rotated listric and planar faults. b) For faults that are planar in a vertical direction, throw data is often used as a representative for fault displacement. c) For rotated listric faults, heave is often predominant and increases with increasing depth.

84

fault segment, a single T-Z profile for each one of the faults was produced, while for faults that are formed by segment linkage, a number of T-Z profiles were produced according to the segments identified for each of the fault segments identified.

2.4.1.2 Throw measurements from field examples

Throw measurements for faults in the field depend highly on their surface exposure. Faults from Somerset, Bristol Channel, are exposed at the surface with small offsets (Fig. 2-4). Throw values were in this thesis represented with the hanging-wall and footwall exposed on the two sides of the fault trace.

Throw values can be closely influenced by erosion, which can impact both hanging-wall and footwall areas. However, considering that no significant lithology variations are observed from the field examples in Somerset, and the throw values of these faults are of centimetre scales, it is considered that throw values are accurate and fullfil the purposes of this study.

Throw measurements for rift faults, specifically used in Chapter 6, were gathered from 1:50,000 maps from the Hellenic Mapping and Cadastral Organization, on which the geometry of the faults is clear when combined with panoramic photos (Fig. 2-6). The horizons used to produce throw-distance plots for these faults are two Holocene horizons (Fig. 2-9).

2.4.2   Maximum throw nucleation vs. depths

The analysis of maximum throw nucleation vs. depth is an efficient way to identify the depth in which faults first nucleated (Alves, 2012). However, this method is used under the assumption that space is available for faults to propagate both upwards and downwards, and loses its practical meaning when faults sole onto a detachment surface, the case of most of the faults analysed. To avoid such a caveat, this technique was used in faults not rooted in a detachment surface (Chapter 4).
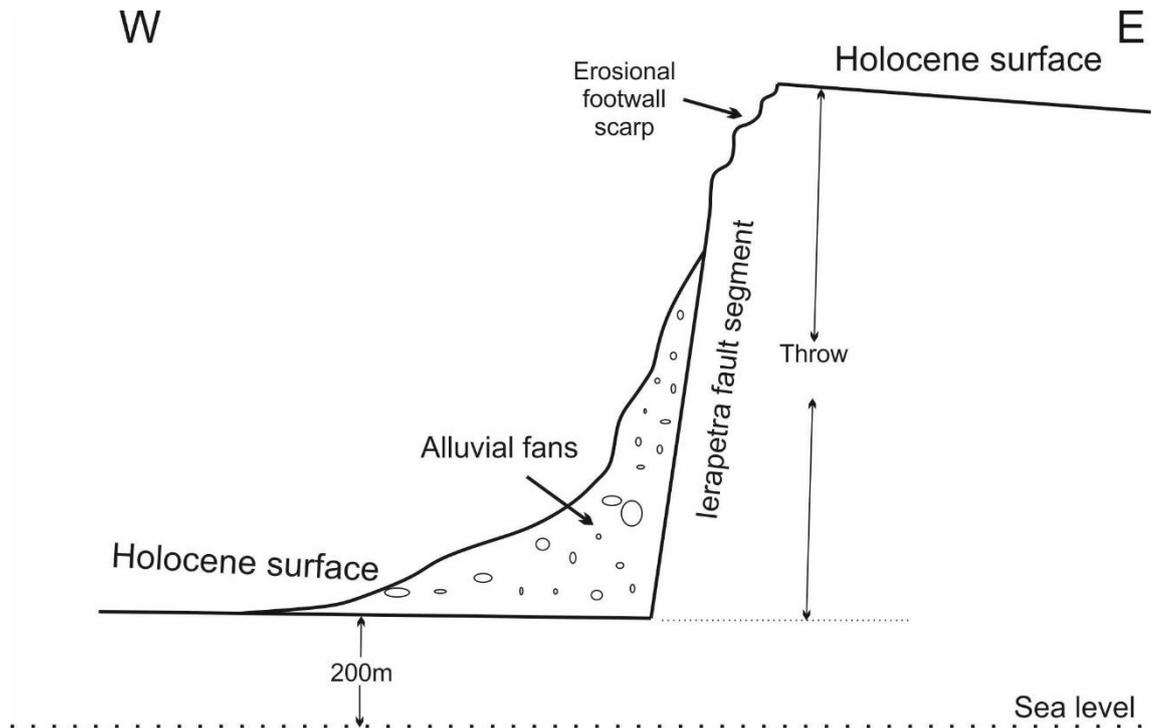
Fig. 2-9 Measurement of throw for the Ierapetra Fault followed two Holocene surfaces. Fault scarp of the foot wall is partially eroded, and bottom of the fault surface and the hanging wall is covered by alluvial deposits.

2.4.3   Expansion index (EI)

Expansion index (EI), the ratio between the thickness of hanging-wall and footwall strata (Lewis et al., 2013; Mansfield and Cartwright, 1996), is used to identify periods of significant fault growth. When EI > 1, representing hanging-wall thickening, active fault growth is interpreted (Omosanya et al., 2015). In this thesis, Expansion indexes are used to mark the relative timing of fault growth episodes in selected border faults (Chapter 4).

2.4.4   Stress analysis

On the basis of rigorous fault interpretation, which reaches the maximum horizontal resolution of the seismic data, stress inversions were undertaken using 3D Move®, following the inversion method of McFarland et al. (2012).

Stress analyses in this thesis produced coloured outputs such as slip tendency and leakage factors in a 3D view, both useful to identify faults that are likely to slip/reactivate or are prone to leak (Fig. 1-22). Regional stress data from the World Stress Map (Heidback et al., 2008) was used to constrain the inversion process. However, as the data available are distant from the study area and interpreted faults are locally influenced by halokinesis, the fault stress analyses only use the azimuths and magnitudes of the principal palaeostress tensors derived from fault inversions.

To understand scale variance during fault analysis (Chapter 6), fluid pressure is manually set in the modelling template; otherwise, hydrostatic fluid pressure is applied (Chapter 5).

2.5 Methods utilised in Chapter 6

Chapter 6 introduces for the first time two scale-independent parameters, the Sampling Interval/Fault length Ratio (δ) and Module Error (ε_i) to assess the accuracy of T-D plots produced using different sampling intervals. Figure 2-9 illustrates the

parameters and formulas proposed in this thesis for the first time. Fault length is represented by the parameter n in Figure 2-9. A T-D plot sampled at intervals similar to data resolution is represented in Figure 2-9a. The area bounded by the T-D plot and the horizontal axis is divided into n blocks (n is a positive integer) whose areas are represented by the parameter A_m (1≤m≤n, m is an integer). A T-D plot with a coarser sampling space of i (1<i<n, i is an integer) is reproduced in Figure 2-9b. The area bounded by this T-D plot and the horizontal axis is again divided into n blocks, and represented as $A_m^{'}$ (Fig. 2-10b). The difference in area between blocks measured using distinct sampling intervals is represented by the gradient ΔA_m (Fig. 2-10c), which is calculated as $\Delta A_m = |A_m - A_m^{'}|$. Hence, the Module Error (ε_i) represents the difference in area between a T-D plot compiled using sampling intervals that reach maximum data resolution, and a T-D plot sampled at i times the data resolution (Fig. 2-10c). In these conditions, the Module Error (ε_i) is calculated as:

$$\varepsilon_i = \frac{\sum_1^n \left| A_m - A_m^{'} \right|}{\sum_1^n A_m}$$

Equation 2-2

Equation 2-2 represents the relative error ε_i of a sampled entity or value. The module $\Delta A_m = |A_m - A_m^{'}|$ represents the absolute error of a measured entity, or value. In such an equation, the Sampling Interval/Fault length ratio δ is calculated as:

$$\delta = i/n$$

Equation 2-3

The analysis in this thesis presumes that T-D plots based on information acquired every 12.5 m for faults on seismic data, every 5 cm for sub-seismic faults and every 50 m for rift faults follow the most accurate sampling interval to identify fault geometry and segmentation. These sampling spaces are represented by the integer 1 in Figure 2-9. T-D

88

plots obtained following sampling intervals of 37.5 m, 62.5 m, 125 m, and 250 m for faults on seismic data, every 15 cm, 25 cm, 50 cm and 100 cm for sub-seismic faults, and every 0.1 km, 0.5 km, 1 km, 1.25 km and 2.5 km for rift faults, were produced in this work to calculate the Sampling Interval/Fault Length Ratio (δ) and the Module Error (εi) for further analysis (Fig. 2-10).
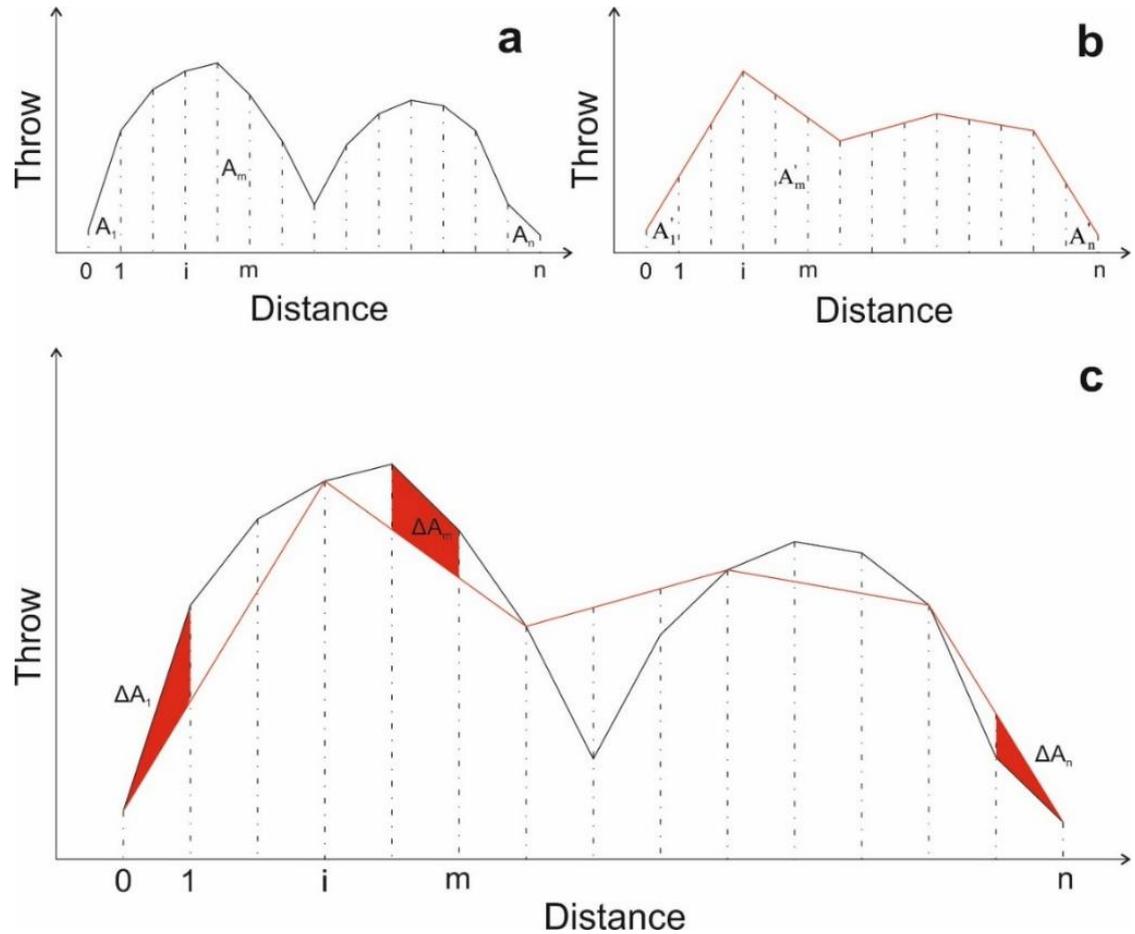
Fig. 2-10 Schematic map illustrates the parameters used in Equation 1. Fault length is represented with n. a) T-D plot with sampling intervals reaching data resolution, which is represented with 1. The area bounded by the T-D plot and horizontal axis is divided into n (n is a positive integer) blocks, represented with A_m ($1 \leq m \leq n$, m is an integer). 2) T-D plot with a sampling interval of i ($1 < i < n$, i is an integer) times data resolution. The area bounded by the T-D plot and horizontal axis is divided into n blocks, represented with A_m'. c) The area difference between every block with different sampling intervals is represented by ΔA_n which is calculated as $\Delta A_m = |A_m - A_m'|$. Module error ($\varepsilon_i$), which represents the area difference between T-D plot with a sampling interval reaching data resolution and i times the data resolution, is calculated as $\varepsilon_i = \frac{\sum_1^n |A_m - A_m'|}{\sum_1^n A_m}$. The Sampling interval/Fault length ratio δ is calculated as δ = i/n.

Chapter 3

Geological background

3.1 Introduction

The main study area with seismic data is located in the Espírito Santo Basin, offshore SE Brazil (Fig. 2-1). The 3D seismic data were used in the main result chapters (Chapters 4-6) (Fig. 2-7). The aims of this chapter are to first review the geological background of the Espírito Santo basin, SE Brazil, further narrowed to the specific study area, introducing at the same time the main stratigraphy frameworks for each of the main chapters (Figs 3-4 and 3-5). Chapter 6 uses field data collected in Somerset (Kilve Beach) and SE Crete.

3.2 Geological setting of the Espírito Santo Basin

3.2.1   Location of the Espírito Santo Basin

The Espírito Santo Basin is located in SE Brazil's continental margin. To the north, the basin is bounded by the Abrolhos Bank and to the south lays the Campos Basin (Fig. 2-1). The whole basin stretches from onshore to the deep sea, covering 200,000 km^2 of which 107,000 is offshore (Gamboa et al., 2010). Together with the Santos Basin and Campos Basin, the Espírito Santo Basin comprises one of the most prolific hydrocarbon-bearing basins in South Atlantic (Bruhn et al., 2003; Cobbold et al., 2001; Guardado et al., 2000; Milani et al., 2003).

3.2.2   Tectono-stratigraphic evolution of the Espírito Santo Basin

Sedimentary basins along South Atlantic margins formed after the break of supercontinent Gondwana (Chang et al., 1992). The breakup of the Brazilian and African continents occurred from south to north (Chang et al., 1992) (Fig. 3-1). The Espírito Santo Basin was first formed in the Late Jurassic/Early Cretaceous (Mohriak et al., 2008).

The evolution of the basin can be divided into pre-rift craton, intra-continental rift, transitional and passive continental margin phases. According to Chang et al. (1988), strata deposited along the Brazilian passive continental margin can be divided into five megasequences: i) continental syn-rift; ii) transitional evaporites; iii) shallow marine carbonate platform; iv) open marine transgressive and v) open marine regressive.

The basement of the Espírito Santo Basin is part of the São Francisco Craton, a terrain composed of migmatites, granulites and granitoids (França et al., 2007). The early post-rift sediment of the Espírito Santo Basin is dominated by a large quantity of evaporites in late Aptian (Demercian et al., 1993; Mohriak et al., 2008; Ojeda, 1982). As the basin kept deepening (Demercian et al., 1993), later propagation of marine clastic and volcaniclastic sediments onto the continental slope triggered halokinesis. Halokinesis in the Espírito Santo Basin peaked during the Late Cenozoic and is still occurring at present based on the complex sea floor morphology observed on 3D seismic data (Fiduk et al., 2004). Thin-skinned gravitational gliding of Aptian evaporites (Demercian et al., 1993; Fiduk et al., 2004) is recognised as the main trigger of salt tectonics and salt diapirism (Demercian et al., 1993; Vendeville and Jackson, 1992a, Vendeville and Jackson, 1992b). Salt deformation mechanisms in the basin also include differential loading by overburden sediments (Omosanya and Alves, 2013).

Due to the eastward tilting and continuous subsidence (Bruhn and Walker, 1997), three domains are observed offshore Espírito Santo (Gamboa et al., 2010; Mohriak et al., 2012; Rouby et al., 2003; Vendeville, 2005): proximal extensional, transitional domain and distal compressional (Fig. 3-2). Main structures in the extensional domain include salt rollers, salt walls along conjugate normal faults, turtle anticlines and rafts (Mohriak et al., 2008), the transitional domain is dominated by salt diapirs and the compressional domain is characterised by allochthonous salt (Demercian et al., 1993; Davison, 2007). The study area, located in ultra-deep waters (Gamboa et al., 2010), is marked by the presence of giant salt walls and salt diapirs (Omosanya and Alves, 2014), within the sub-mini-basins, numerous mass-transport deposits (Gamboa et al., 2010; Omosanya and Alves, 2013) and submarine channels playing a key role in the development of fault systems (Omosanya and Alves, 2014). Distinct authors proposed a fault growth history in Espírito Santo comprising: a) early halokinesis triggering extensional faults on top of rising salt anticlines, b) later mass-wasting and submarine channels stopping fault growth,
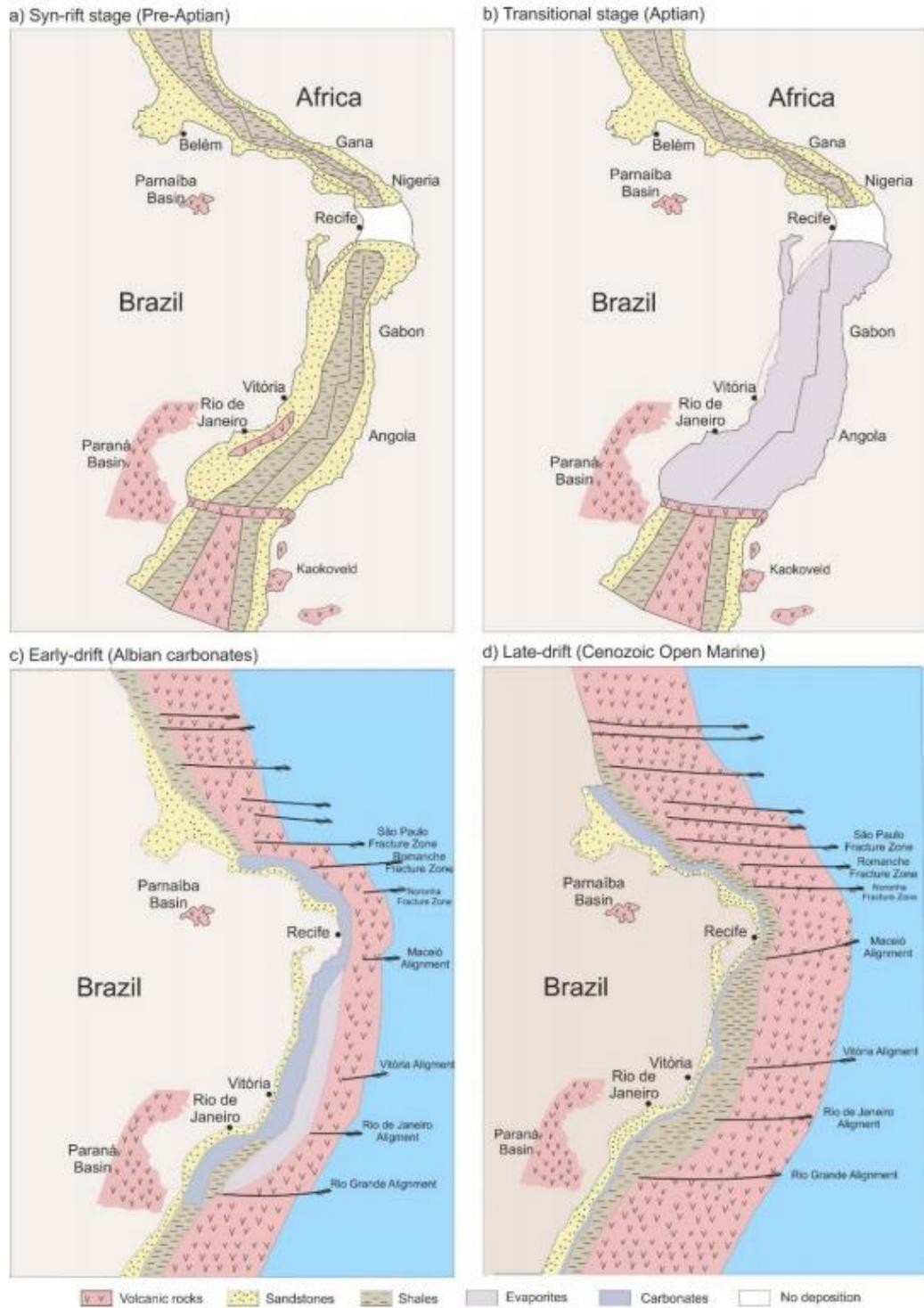
Fig. 3-1 Schematic diagram showing the major tectonic stages of the Brazilian margin. The location of the Espírito Santo Basin (ESB) is highlighted by the red box. a) Syn-rift phase dominated by continental environments. b) Transitional phase characterised by the deposition of evaporites. c) Early drift phase, documenting the formation of shallow-marine carbonate platforms. d) Late drift phase characterised by open marine sedimentation. Modified from Ojeda (1982).
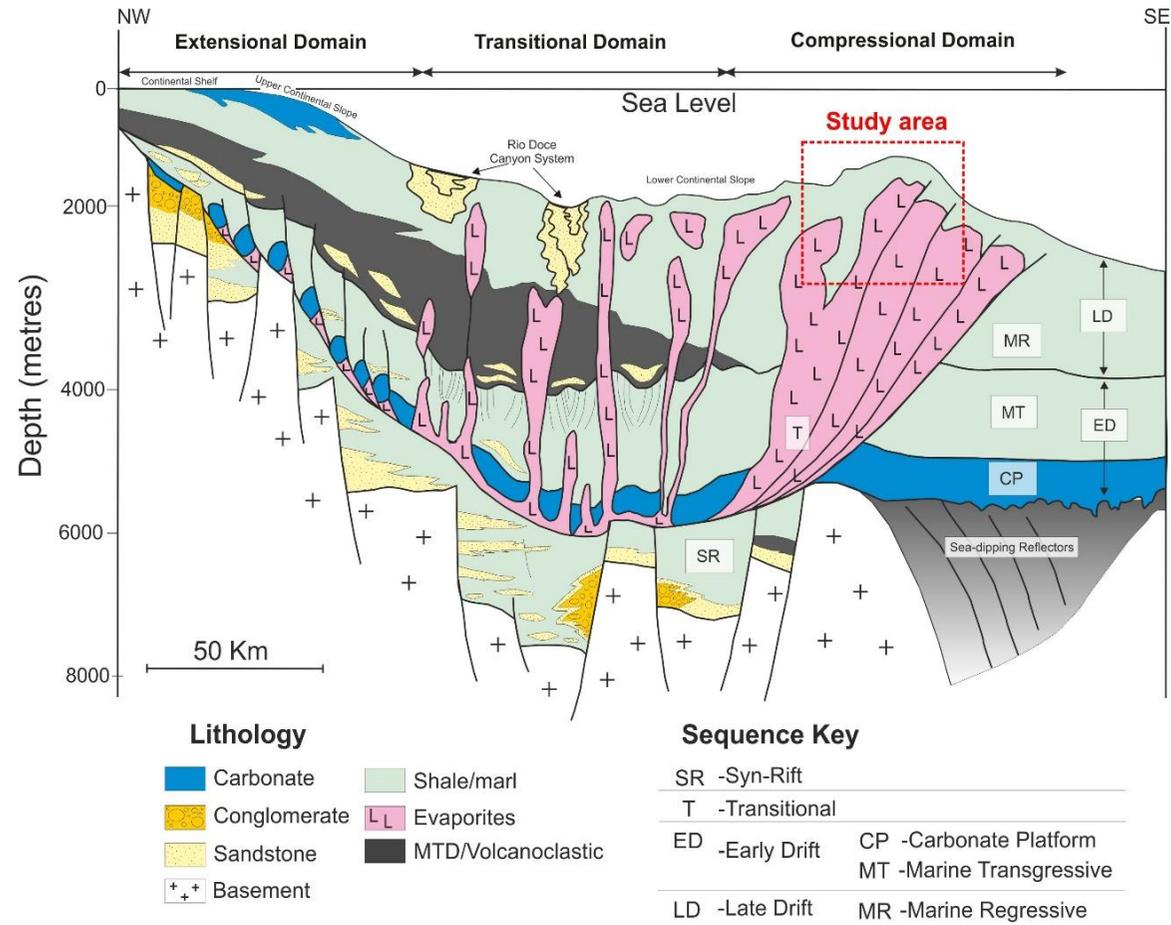
Fig. 3-2 Simplified regional cross-section of the Espírito Santo Basin revealing major depositional sequences. The relative location of the study area is indicated by the red box. Figure modified from Fiduk et al. (2004) and Gamboa et al. (2010).

eroding their upper tips (Omosanya and Alves, 2014), c) later reactivation of the faults due to continuous movement of salt diapirs (Alves and Cartwright, 2009b, Alves, 2012; Baudon and Cartwright, 2008c). The main erosional episode of these faults is estimated to be Eocene–Oligocene (Alves and Cartwright, 2009). Two main erosional episodes are recognised in interpreted seismic volume, revealing that fault growth history is more complex than that in Alves and Cartwright (2009).

3.2.3 Petroleum systems in the Espírito Santo Basin

Petroleum exploration in the Espírito Santo Basin was initiated in 1960s with onshore exploration contributing to bulk of hydrocarbon production at that time (Vieira et al., 2007). With new findings in the adjacent Santos and Campos Basins, offshore exploration started in 1974 in the Espírito Santo Basin, moving into deep-water areas in the last two decades. In the Espírito Santo Basin, current offshore exploration is focused on pre-salt plays charged from Upper Neocomian Shale, with thick Aptian salt acting as a regional seal.

3.2.3.1 Source rocks

The main source rocks in the Espírito Santo Basin comprise Cenomanian/Turonian deep-marine shales in the Urucutuca Formation, shallow to deep marine marls in the Albian Regência Formation (Post–rift I), fluvio-marine shales in the Aptian Mariricu Formation/Mucuri Member (Transitional), and lacustrine shales in the Barremian/Aptian Cricaré Formation/Sernambi member (Syn-rift) (Mello and Maxwell, 1990) (Fig. 3-3). Fine-grained lacustrine sediments consist of fine sand, silts and dark shales deposited in syn-rift depocentres (Ojeda 1982; Chang et al., 1992; Fiduk et al., 2004). The extreme anoxic conditions in syn-rift depocentres allowed for the accumulation of abundant organic matter in extensive shale units (Mello et al., 1994; Mohriak 2004).
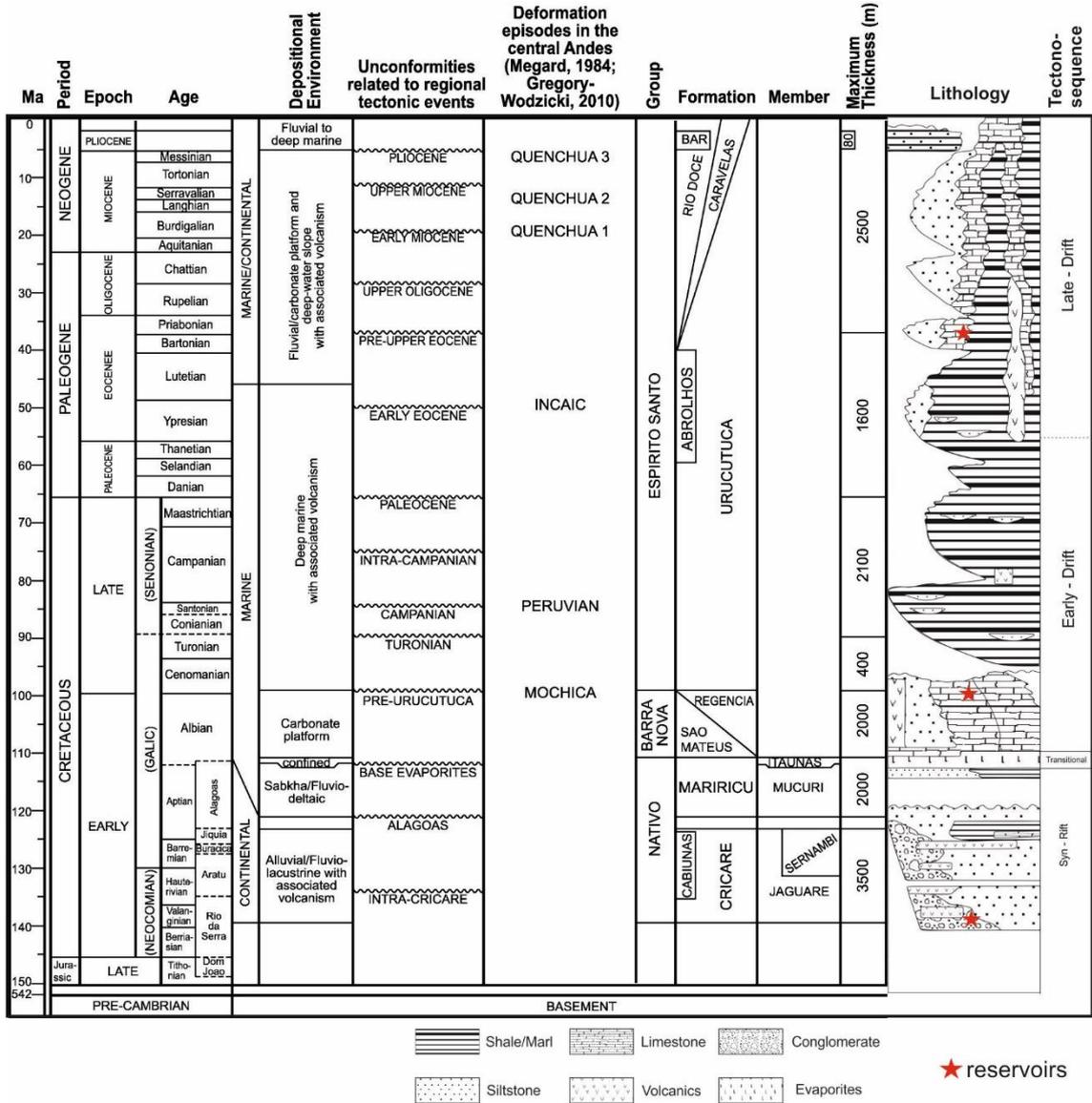
Fig. 3-3 Stratigraphic information from the Espírito Santo Basin, including stratigraphic unconformities pointing to regional tectonic episodes (França et al., 2007).

3.2.3.2 Reservoir rocks

Reservoir rocks in the basin comprise turbidites in the Urucutuca Formation. Hydrocarbons are associated with Upper Cretaceous and Tertiary turbiditic sandstones of the Fazenda Cedro palaeocanyon (Fig. 3-3). Reservoir rocks located north of the Espírito Santo Basin comprise sandstones of the São Mateus platform. Potential oil-bearing sediments also include Cretaceous continental deposits accumulated in rift valleys, and transitional shallow-marine strata stratigraphically trapped below the Aptian evaporites (Fig. 3-3). The main reservoir units in the Espírito Santo Basin can be grouped as Cretaceous/Palaeogene (turbidites in the Urucutuca Formation), Albian (Regência Formation), Aptian (Mariricu Formation/Mucurí Member) and Valanginian/Barremian (Cricaré Formation/Jaguaré member).

3.2.3.3 Traps in the Espírito Santo Basin

Trapping mechanisms in the Espírito Santo Basin include pre-salt horsts and grabens, and traps related to rollovers generated on the flank of salt diapirs. Palaeogeomorphic traps are commonly associated with the erosion of drift phase sediments by submarine channels and canyons. These kinds of traps are common in drift-stage carbonate platforms. Other types of traps include stratigraphic pinch-outs and complex traps created by allochthonous salt structures such as canopies and tongues. Cretaceous shales of the Urucutuca Formation are the major sealing units for post-salt strata. Other seals include Albian calcilutites and marls of the Regência Formation, and evaporites and shales of the Itaúnas and Mucurí Members, respectively (Fig. 3-3).

3.3 Seismic stratigraphy in the study area

Significant halokinesis makes it hard to make precise seismic stratigraphic correlations between each of the study areas in SE Brazil (Fig. 2-7). The following section will introduce the seismic stratigraphy of each of the result chapters separately.

3.3.1   Seismic stratigraphy of Chapter 4

Strata in the study area can be divided into four seismic-stratigraphic units, which are bounded by seven horizons (H1 to H7), with H1 representing salt surface and H7 representing the sea floor (Fig. 3-4). Additionally, four seismic horizons (H2-1 to H2-4) are interpreted between Horizon H2 and H3 to constrain the Expansion Index of faults (Fig. 3-4b). In order to constrain the age of strata on the crest of salt ridges, seismic-stratigraphic interpretations were extended to adjacent salt-withdrawal basins (Fig. 3-4a).

3.3.1.1 Unit 1 (Early Eocene?)

Unit 1 is bounded by H2 at its top and is characterised by strong to moderate amplitude internal reflections, which are chaotic at places (Fig. 3-4b). The bottom of Unit 1 is seldom identified in adjacent salt-withdrawal basins. Its top (H2) coincides with a regional unconformity of Mid-Eocene age (Fiduk et al., 2004; Gamboa and Alves, 2015). This thin unit deposited on top of the salt diapir (< 250 ms TWT) comprises remnants of Lower Eocene strata, hinting at continuous salt growth since the Late Cretaceous. In the adjacent salt-withdrawal basins, Unit 1 shows developed synclinal faults related to a syncline fold *sensu* Alves (2012) (Fig. 3-4b).

3.3.1.2 Unit 2 (Middle Eocene - Oligocene)

Unit 2 is bounded at its base by a mid-Eocene unconformity (H2) and at its top by Horizon H3 (Fig. 3-4). Strata within this unit show sub-parallel, high-amplitude internal reflections with good lateral continuity (Fig. 3-4). High-amplitude reflections in this unit are generated by volcaniclastic material sourced from the Abrolhos Bank from the Middle Eocene to the Oligocene (Fiduk et al., 2004; Gamboa et al., 2010a). Mass-transport deposits (MTDs) showing chaotic internal reflections are common on the flanks of the interpreted salt ridge (Fig. 3-4). Unit 2 is faulted on the crest of the salt ridge (Fig. 3-4) and thins sharply towards the east on top of this same salt ridge (Fig. 3-4).
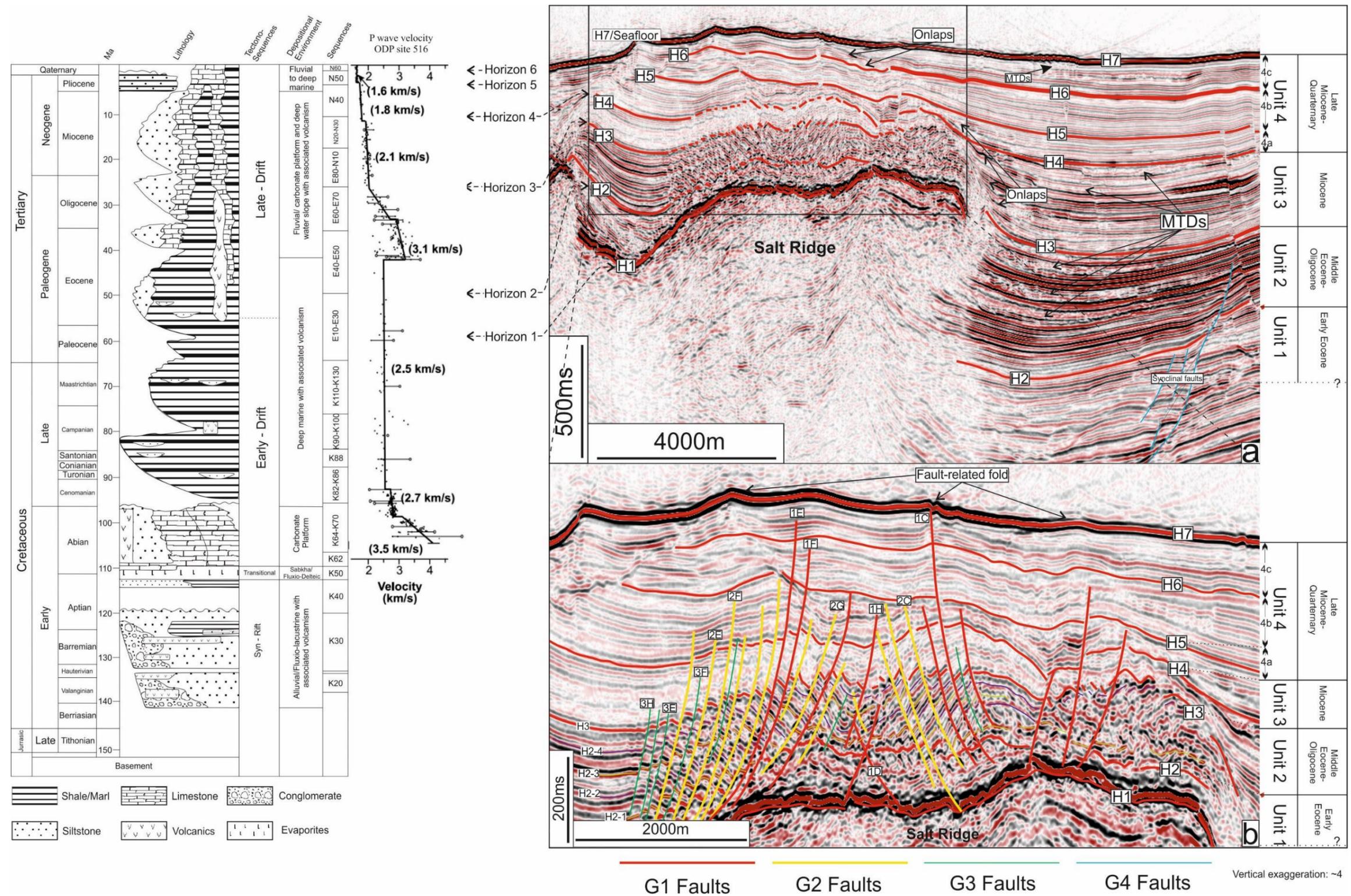
Fig. 3-4 a) Main stratigraphic units interpreted on the crest of the interpreted salt ridge. Seven horizons are interpreted, with H1 representing the top surface of a salt diapir and H7 representing the sea floor. b) Zoomed seismic section of the studied fault system. Correlations of the seismic stratigraphy are based on published literatures (Franca et al., 2007; Baudon and Cartwright, 2008c; Fiduk et al., 2004; Gamboa and Alves, 2015; Qin and Alves, 2016).

3.3.1.3 Unit 3 (Miocene)

Unit 3 is bounded by a moderate-amplitude continuous reflector on its top (Horizon H4, Fig. 3-4). Internal reflections vary in character on the salt ridge when compared to the adjacent salt-withdrawal basins (Fig. 3-4). It is characterised by transparent to low-amplitude internal reflections over the salt ridge, but shows strong reflections in the salt-withdrawal basin. Strata in these confining basins onlap the salt ridge (Fig. 3-4). The contrast in thickness between the crest of the salt ridge and equivalent strata in the salt-withdrawal basins reflects an important episode of salt growth during the Middle-Late Miocene, after which halokinesis weakened in the study area (Fiduk et al., 2004). As shown in Figure 5a, in the salt-withdrawal basin strata above H2 are thicker, with c. 1400 ms (TWT) in salt-withdrawal basins and c. 700 ms (TWT) on the crest of salt diapir. The contrast in thickness between the two areas is partly due to collapse and erosion on top of the salt ridge, resulting in the deposition of MTDs in salt-withdrawal basins and the generation of an erosional surface (Horizon 5) on top of the salt diapir (Fig. 3-4).

3.3.1.4 Unit 4 (Late Miocene - Quaternary)

Unit 4 shows internal reflections of moderate amplitude and is divided into three sub-units (Fig. 3-4). The lower sub-unit 4a is bounded at its base by Horizon H4, and at its top by H5 (Fig. 3-4). A large number of crestal faults terminate at H5 (Fig. 3-4). The middle sub-unit 4b is bounded on its top by an onlapping surface (Horizon H6; Fig. 3-4). Very few faults developed inside sub-unit 4b, but fault-related folding of the modern sea floor is observed (Fig. 5b). The uppermost sub-unit 4c extends to the sea floor (Horizon 7). Few faults propagate to the sea floor in sub-unit 4c (Figs. 3-4).

3.3.2   Seismic stratigraphy of Chapter 5

Strata can be divided into three seismic-stratigraphic units, which are bounded by six horizons (H1 to H6). Horizon H1 represents the top of the Aptian salt, whereas H6

represents the sea floor (Fig. 3-5). Seismic-stratigraphic interpretations were extended to the adjacent salt-withdrawal basin in order to constrain the age of the strata deposited on the crest of the interpreted salt ridge (Fig. 3-5).

3.3.2.1 Unit 1 (Upper Cretaceous to Paleocene)

Unit 1 is bounded at its top by Horizon H3, a high-amplitude and continuous seismic reflection tied to a regional Eocene unconformity (Baudon and Cartwright, 2008c, Fiduk et al., 2004; Gamboa and Alves, 2015). The thickness of this unit varies greatly from 750 to 1600 ms twt, with a value of 750 ms on top of the salt overhangs, and a maximum of 1600 ms within salt-withdrawal basins. Unit 1 mainly comprises prograding sandstones and shales, which are prevalent along the SE Brazilian margins (França et al., 2007).

The studied crestal faults offset a major regional unconformity (H3) (Fig. 3-5). The bottom of Unit 1 is characterised by a positive, high-amplitude reflection that coincides with the top of Aptian salt (Fig. 3-5). Internal reflections in Unit 1 are characterised by sub-parallel, continuous weak to strong reflectors (Fig. 3-5).

3.3.2.2 Unit 2 (Eocene – Oligocene)

Unit 2 is bounded at its base by Horizon H3, and at its top by Horizon H4, an early Miocene unconformity (França et al., 2007) (Fig. 3-5). The thickness of this horizon varies from 150 ms to 225 ms twt, and is markedly smaller above salt diapirs and overhangs. Strata in Unit 2 are of moderate to high amplitude, reflecting the presence of volcaniclastic sediment sourced from the Abrolhos Bank to the north (Fiduk et al., 2004). Regionally, Unit 2 comprises recurrent mass-transport deposits (MTDs) that are intercalated with coarse-grained turbidites and hemipelagites (Gamboa and Alves, 2015; Ze and Alves, 2016) (Fig. 3-5).
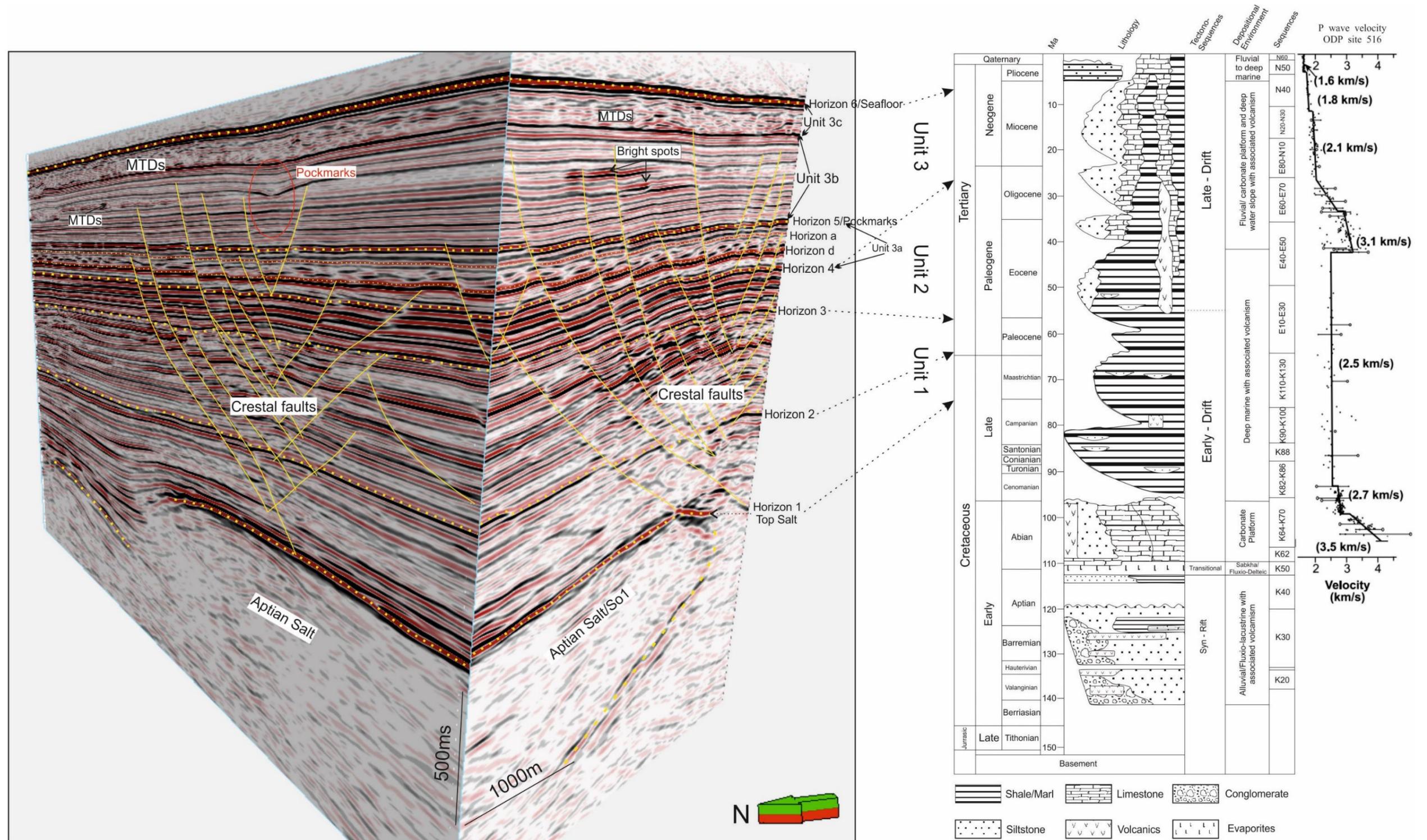
Fig. 3-5 Seismic-stratigraphic units in the study area. Ten horizons are interpreted, with Horizon 1 representing the top surface of the salt diapir and Horizon 6 representing the sea floor. Horizon 3 represents a regional Eocene unconformity and the onset of volcaniclastic deposition in the study area. Horizons a and d are the top and bottom horizon of the tier-bound interval with domino faults (Franca et al., 2007; Baudon and Cartwright, 2008c; Fiduk et al., 2004; Gamboa and Alves, 2015; Qin and Alves, 2016).

3.3.2.3 Unit 3 (Late Oligocene – Miocene)

Unit 3 shows sub-parallel, low- to moderate-amplitude internal reflections (Fig. 3-5). The base of Unit 3 is inferred to be Late Oligocene in age (Gamboa and Alves, 2015; França et al., 2007). Its top coincides with the sea floor (Fig. 3-5). Unit 3 is subdivided into three sub-units, and comprises a total thickness of 475-700 ms twt. The lowermost sub-unit 3a is bounded at its base by Horizon H4, and at its top by Horizon H5 (Fig. 3-5). Unit 3a comprises a thin densely faulted interval and shows low-amplitude internal reflections (Fig. 3-5). The thickness of this layer is ~ 190 ms twt, and denotes little variations. The top surface of subunit 3a comprises a field of pockmarks directly above a faulted interval (Fig. 3-5). Subunit 3b comprises transparent to moderate-amplitude, continuous reflections, MTDs, pockmarks and localised high-amplitude strata (Fig. 3-5). The uppermost subunit 3c comprises broad MTDs, characterised by chaotic internal reflections and by the presence of deformed blocks in their interior (Gamboa et al., 2010a, Alves, 2015) (Fig. 3-5).

3.4 Somerset

The Somerset coast is located on the southern margin of the Bristol Channel Basin, which is a Mesozoic basin between Wales and Somerset (Fig. 2-3). Seismic data reveal that the Bristol Channel Basin comprises a Mesozoic half-graben with a normal faulted basement developed over a reactivated Variscan thrust (Brooks et. al, 1988).

Deformation in the study area (Fig. 2-3) can be divided into five stages: 1) N-S extension associated normal faulting and folding during Mesozoic development of the Bristol Channel Basin; 2) reactivation of some of the normal faults formed during stage 1; 3) reverse-reactivation of Mesozoic and older structures in association with Alpine Orogenic phases south (Underhill and Patterson, 1998); 4) reverse-reactivation of normal faults cut by conjugate strike-slip faults (Dart et al., 1995); 5) jointing post-dating the Alpine-related fault reactivation (Rawnsley et al., 1998).

The Bristol Channel Basin is asymmetrical (Fig. 2-3). The southern margin, where the analysed faults located in the thesis (Fig. 2-4), is strongly deformed in to folds cut by

mainly east–west and WNW-trending faults, which also extend offshore (R.A. Glen et al., 2005). The Bristol Channel Basin comprise Permian to Oligocene strata, and Triassic–Early Jurassic sedimentary rocks outcrop on the southern margin (Fig. 2-4) (R.A. Glen et al., 2005). Along the southern margin, Triassic evaporites and mudstones represent initial rift subsidence, which is part of the Triassic Mercia Mudstone Group (Fig. 2-4), followed by deposition of lower Jurassic limestones in open shallow marine conditions. Strata along the southern margin are largely marly or muddy; and the limestone has strong influences on the spacing of small fractures, the tightness of folds, and intensity of fracturing (R.A. Glen et al., 2005).

The most significant structural feature in the southern margin of the Bristol Channel Basin is a central horst occupied by the Mercia Mudstone Group and separated from younger rocks by outwardly dipping faults (Fig. 2-3). According to R.A. Glen et al., (2005), six different types of fault structures are summarized as: 1) structures formed by north–south extension, which comprise planar normal faults; 2) structures formed by north–south contraction mainly including reverse reactivated planar normal faults; 3) structures formed by east–west contraction; 4) cross faults of north to north-northwest-trending set and northeast-trending set. Faults analysed in the thesis are from the Liassic limestones and shales (Peacock et, al. 2017).

3.5 Crete

The Ierapetra Basin is located between the Ierapetra and Mirabellou districts of the Prefecture of Lasithi, SE Crete (Fortuin, 1977) (Fig. 2-5). The Ierapetra normal fault is the biggest tectonic element of SE Crete with a length of more than 25 km inland, one of the most characteristic active faults of Crete (Fig. 2-5). This fault has a NNE–SSW direction and a dip to the NW, having played a crucial role in the evolution of the area (Gaki-Papanastassiou et. al, 2009). Due to its activity, thick sediments cover its hanging-wall, while immediate footwalls are barren of marine sediment feeling adjacent basins (Fig. 2-6). The Ierapetra normal fault consists of different segments with a step-like arrangement, each one having its own characteristics (Gaki-Papanastassiou et. al, 2009)

(Fig. 2-6). The fault plane is very steep and its lower part is covered by scree and talus cones (Fig. 2-6).

Tectonic units on Crete include an autochthonous basement, a system of nappes thrusted over the basement, and sediments of Neogene and Quaternary age (Gaki-Papanastassiou et. al, 2009). The latest Neogene and Plio-Pleistocene sediments comprise terrestrial, fluvial, brackish and marine phases. The lithology is composed mainly of marls, conglomerates, and marly limestones. Quaternary sediments lie over all the older formations and are composed of terrestrial, marine–brackish deposits, sands, pebbles, boulders and clays, loose or slightly consolidated (Papanikolaou, 1986).

Extension in the Aegean area is generally north–south, however in the southern part the present tectonics is dominated by east–west extension (Gaki-Papanastassiou et. al, 2009). The existing north–south normal faults in the area reflect this tectonic regime, such as the studied Ierapetra fault in the study area (Figs. 2-5 and 2-6). The active normal faults often have a north–south direction and are marked by sharp scarps that offset gullies on calcareous slopes or present traces of recent reactivation (Fig. 2-6). In more detail, the largest part of the area studied is covered by a thick sequence of Neogene marine sediments and the Pleistocene deposits have a great extent. In this part of Crete post orogenic sedimentation started with the deposition of Middle Miocene terrigenous clastics followed by Upper Miocene fluvial, lacustrine and open marine sediments, such is the case in the Ierapetra Basin, where thick alluvial deposits covered the hanging wall of the Ierapetra Fault (Fig. 2-6). The Ierapetra basin is aligned at an N20 direction, perpendicular to the main direction of the Alpine basement structures. Quaternary deposits are discernible in the marine terraces and the coastal sediments traced mainly along the southern coastal zone and in the alluvial deposits, screes and talus cones, developed along the whole length of the Ierapetra normal fault (Fig. 2-6). This fault has a NNE–SSW direction and a dip to the NW and has divided the graben having played a crucial role in the evolution of the area. Due to its activity, sediments of significant thickness cover the hanging wall, while in the footwall they are less developed and narrow (Fig. 2-6).

Chapter 4

The role of gravitational collapse in controlling the evolution of crestal fault systems (Espírito Santo Basin, SE Brazil)

Abstract

A high-quality 3D seismic volume from offshore Espírito Santo Basin (SE Brazil) is used to assess the importance of gravitational collapse in the formation of crestal faults above salt structures. A crestal fault system is imaged in great detail using seismic attributes such as curvature and variance, which are later complemented by statistical analyses of throw vs. distance (T-D) and throw vs. depth (T-Z). In the study area, crestal faults comprise closely spaced arrays and are bounded by large listric faults, herein called 'border faults'. Two episodes of growth were identified in two opposite-dipping fault families separated by a transverse accommodation zone. Statistical analyses for eighty-four (84) faults show that fault spacing is < 250 m, with border faults revealing the larger throw values. Fault throw varies between 8 ms and 90 ms for crestal faults, and 60-90 ms for border faults. Fault length varies between ~410 m and 1750 m, with border faults ranging from 1250 m to 1750 m. Data in this chapter shows that border faults accommodated most of the strain associated with salt growth and collapse. The fault growth history of crestal faults favours an 'isolated fault propagation model' with fault segment linkage being associated with the lateral propagation of discrete fault segments. Importantly, two episodes of fault growth are synchronous with two phases of seafloor erosion, rendering local unconformities as competent markers of fault reactivation at a local scale. This study has key implications to the understanding of fault growth histories as a means to assess drilling risk and oil and gas migration on continental margins with important salt tectonics. In fact, it demonstrates that: 1) a certain degree of spatial organisation occurs in crestal fault systems; 2) transverse accommodation zones can form regions in which fault propagation is enhanced, and where the regional dips of faults change in 4D.

4.1 Introduction

Crestal faults comprise a group of faults that root into the crest of salt diapirs (Jenyon, 1988; Randles et al., 2012). Despite their occurrence in multiple salt-rich basins, few studies have focused on the kinematic and dynamic evolution of crestal faults, in part because very few outcrops in the world expose these faults in their full length. Partial exposure of salt diapirs' flanks is only recorded in the Paradox Basin, Utah (Furuya et al., 2007), Colorado (Gutiérrez, 2004), La Popa Basin in Mexico (Rowan et al., 2003) and the Dead Sea basin (Alsop et al., 2015). These outcrops essentially reveal the main boundary faults of crestal fault systems, and erosion often obliterates fault families that were formed over growing salt structures. In parallel, diffraction and loss of signal around salt diapirs make most crestal faults hard to image on seismic data. With deeper burial depths, vertical and horizontal seismic resolutions can also be significantly reduced (Davison et al., 2000b).

Important new findings have occurred in the last few decades in terms of evaluating fault growth history through seismic, outcrop, numerical and analogue modelling data (Cartwright et al., 2000; Cartwright et al., 1995; Cowie and Scholz, 1992c, Morley, 2007; Jackson and Larsen, 2009; Cartwright, 2011; McLeod et al., 2000; Alves, 2012; Clausen et al., 2014; Jackson and Rotevatn, 2013b, Garcia et al., 2012; Bose and Mitra, 2010; Childs et al., 2009; Yin and Groshong, 2007). The early fault growth model of Barnett et al. (1987) was initially proposed to represent isolated normal faults propagating in a radial direction, and records no migration of maximum displacement points. Recent work focused on documenting changes in the dimensions and absolute fault displacements to build more reliable fault-propagation models (Mansfield and Cartwright, 2001; Walsh et al., 2002a). It is now widely recognised that mature faults are a result of fault-segment linkage associated with propagation in both the vertical and horizontal directions (Lohr et al., 2008; Cowie et al., 2000; Cartwright et al., 1995; Stewart et al., 1997). Following the latter concepts, Jackson and Rotevatn (2013b) summarised two mechanisms of normal fault propagation in 'isolated' fault and 'coherent' fault models. The isolated fault model is supported by many researchers, but recent work stresses that the coherent fault model is the dominant fault growth process in many an extensional setting (Giba et al., 2012; Walsh et al., 2002b, Walsh et al., 2003; Morley, 1999). In the 'coherent' model faults first

propagate laterally to reach a length close to their maximum, recording cumulative displacement in a second throw-dominated stage. Nevertheless, as argued by Lohr et al. (2008), most faults grow by the coalescence of several smaller faults, whereas tip propagation is of relatively minor importance. Acknowledging this latter process of fault growth Cartwright et al. (2000), McLeod et al. (2000) and Sibson (1985) argued that the geometry of large faults is essentially controlled by several small existing fault segments, rather than by a large fault created at quasi-instantaneous geological scales. Against this backdrop, the propagation history of crestal fault families is still poorly understood.

An important concept in this work is that of *border faults*. The concept was first introduced for rift basins forming prominent fault escarpments on their shoulders (Crossley and Crow, 1980), often with large displacement and length (Ebinger et al., 1987), and accommodating most strain and stress. Boundary faults on salt structures are also a type of border fault following these criteria (Randles, 2014). This chapter follows the concept that faults with the largest displacement and throw values within a crestal fault family comprise border faults.

Accommodation (or transfer) zones are also important structures revealed in this study. Previous studies on accommodation zones have largely focused on rift basins in the scale of 10s and 100s of kilometres (Coffield, 1987, Morley et al., 1990, Smith et al., 2001). However, accommodation zones can occur at different scales (Fossen and Rotevatn, 2016, Liu et al., 2015, Schlische and Withjack, 2009) and in different regimes and settings, such as in areas of significant salt tectonics (Randles et al., 2012). This chapter follows the definition of Faulds and Varga (1998), who considered accommodation zones as structures that accommodate strain and stress between overlapping normal faults systems, or families. In the published literature, accommodation zones generated during the propagation of normal faults have an important control on the sub-surface distribution of hydrocarbons by: a) influencing the deposition of reservoir and source rocks, b) facilitating or restricting fluid migration, and c) forming structural traps (Langhi and Borel, 2008, Morley et al., 1990).

Crestal faults are important structures as they deform strata on the crests of growing salt diapirs, forming natural traps where fluids can accumulate (Rowan et al., 1999; Baars and Stevenson, 1982). Fault systems developed on the crest of salt structures can also generate surface topography, leading to significant erosion on the sea floor. In fact, the

movement of crestal faults is an important trigger of submarine landslides and submarine channel erosion on continental slopes (Gee and Gawthorpe, 2006). Crestal faults are also important elements of structural traps associated with salt diapirs, either enhancing reservoir porosity or, instead, acting as conduits for sub-surface fluid (Gay et al., 2007; Cartwright et al., 2007). An important feature of crestal faults is their ability to grow (and reactivate) during successive episodes of crestal collapse (Walsh et al., 2002a). Thus, systematic studies of crestal faults have practical implications in assessing geohazards (Lisle and Srivastava, 2004), fault seal capability (Holdsworth et al., 1997), and CO2 sequestration in regions recording important salt tectonics (Jung et al., 2014; Van der Veer, 2013).

The study area in this chapter, in ultra-deep areas of the Espírito Santo Basin, SE Brazil (Fig. 4-1), reveals the development of large salt walls and diapirs (Gamboa et al., 2010a) (Fig. 4-1). Here, the continental slope is deformed by growing NW- and NE-trending salt structures (Fig. 4-1), and local processes such as slope instability and submarine channel incision are associated with the development of near-seafloor fault systems (Omosanya and Alves, 2014; Gamboa et al., 2010a). Previous work showed that halokinesis is capable of triggering extensional faults on top of rising salt anticlines, with subsequent mass-transport deposits (MTDs) and submarine channels marking the last stages of fault growth over active salt structures (Alves, 2012; Alves and Cartwright, 2009a, Baudon and Cartwright, 2008c). A multi-stage evolution is therefore expected, in the study area, for crestal faults generated above active salt structures (Baudon and Cartwright, 2008c).

This chapter presents new data on fault families developed over the crest of a main salt ridge in SE Brazil (Fig. 4-1b). The studied fault system is located above a prominent N-striking salt ridge with a developed depression above (Figs. 4-1 and 4-2). The bottom of the salt ridge is not observed in the studied seismic volume (Fig. 4-3). However, halokinesis is revealed by the presence of an active salt intrusion that noticeably deformed the sea floor (Fig. 4-3). Significantly, an accommodation zone kinematically and dynamically linked with the interpreted crestal fault families is documented for the first time on a developed salt structure. Opposite-dipping fault families, and the associated accommodation zone are analysed using a high-resolution 3D seismic volume with a vertical resolution approaching 8-10 m near the sea floor (Fig. 4-4).
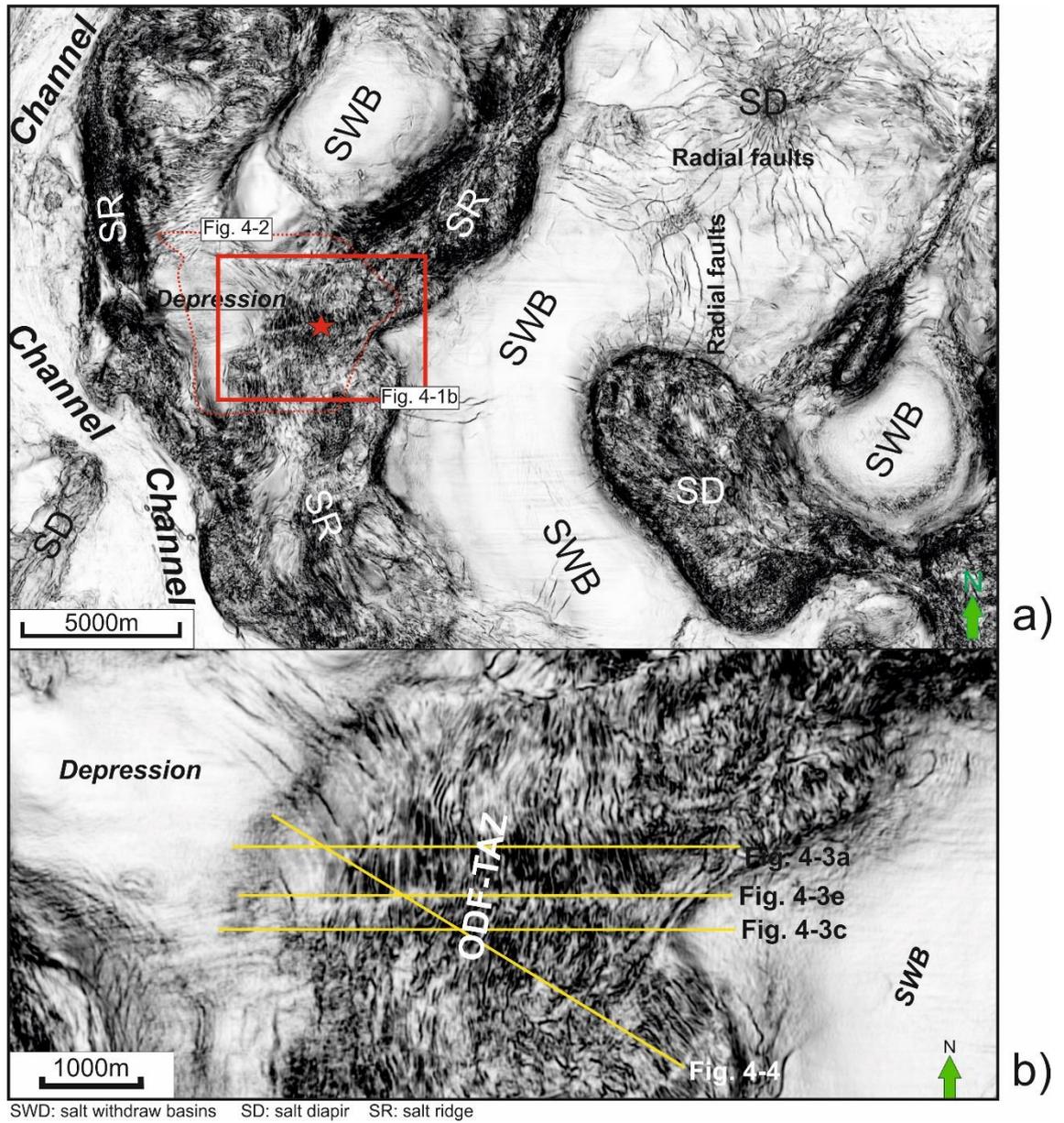
Fig. 4-1 Variance map (Z=3140 ms two-way time, or TWT) of the study area. The red box indicates the location of the studied crestal fault system. b) Enlarged variance map of the studied fault system.
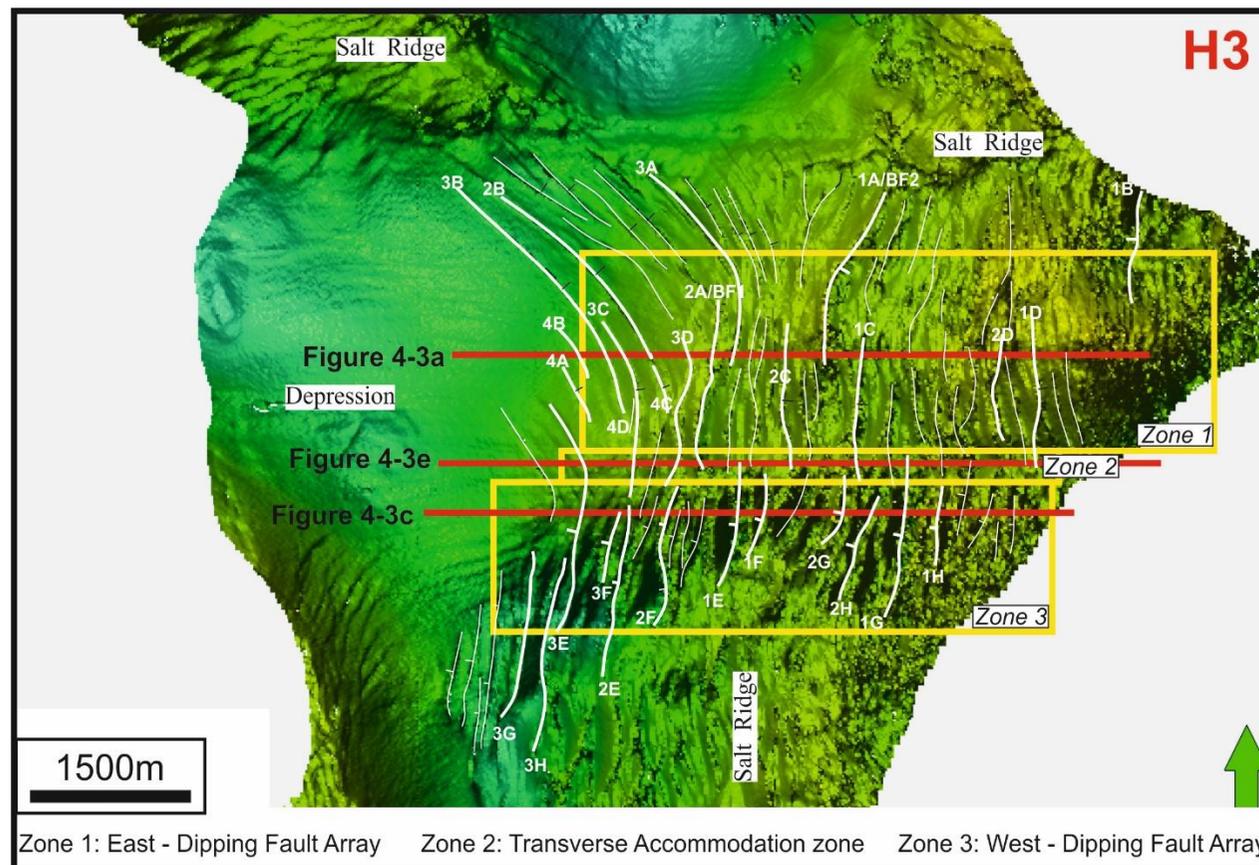
Fig. 4-2 TWT structural map depicting the geometry of Opposite-Dipping Fault arrays (ODF; Zone 1 and Zone 3) and the Transverse Accommodation Zone in Zone 2 (TAZ). The area highlighted in the yellow box highlights the location of the studied ODF-TAZ system. The interpreted horizon is H3 (see also Fig. 4-3 and 4-4), the numbered faults were subsequently analysed (see Figs. 4-7 to 4-10). The interpreted area of horizon H3 is shown in Figure 4-1a.

112
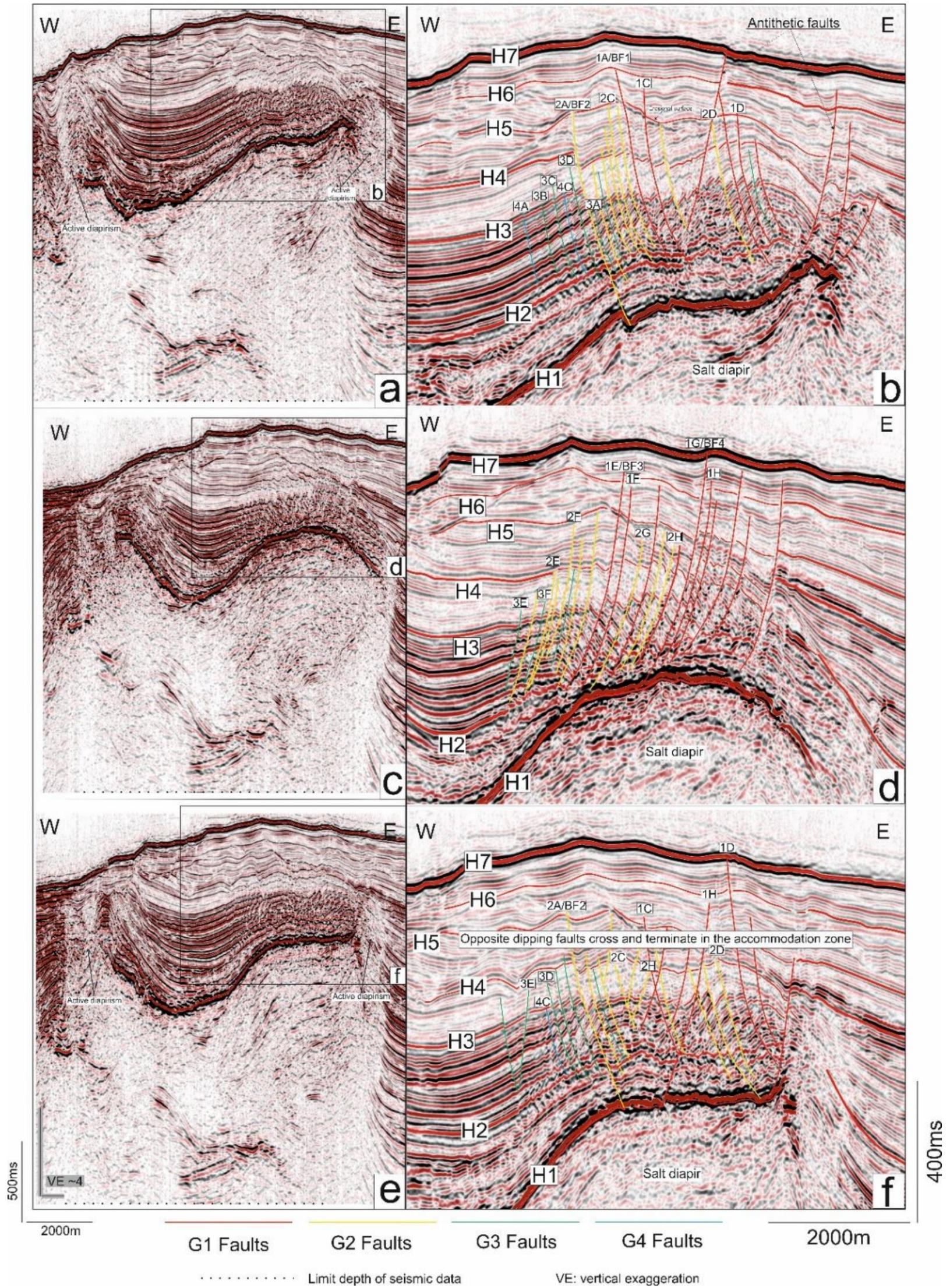
Fig.4-3 Uninterpreted seismic sections and enlarged interpreted sections for Zones 1-3. a-b) Seismic sections of an E-dipping fault array with a few antithetic faults forming graben-like structures (Zone 1). c-d) Seismic sections of a W-dipping fault array dipping uniformly to the west (Zone 3). e-f) Seismic sections across the transverse accommodation zone in which the two opposite dipping fault arrays interact (Zone 2). Locations of the seismic sections are shown in Figures 4-1b and 4-2. The different colours represent the four groups of faults considered in this study. Faults subsequently analysed are also labelled.

In summary, this study aims at:

a) Documenting the geometry of fault families developed above a well-imaged salt ridge in SE Brazil;

b) Analysing the growth and reactivation histories of crestal fault families and the role of border faults exerting on the fault system, extrapolating the results to salt structures on other continental margins;

c) Examining the style(s) of propagation of crestal fault families, and their relationship with stratigraphic unconformities developed above the interpreted faults.

4.2 Fault geometry

4.2.1   Fault geometry and density

The crestal fault families interpreted in this study can be subdivided into four groups according to the relative depth in which their upper tips terminate (Figs. 4-2, 4-3 and 4-4). Group 1 contains faults that breach Horizon H5, a main erosional surface developed over the investigated salt ridge (Fig. 4-3a). Few Group 1 faults reaching the sea floor (Figs. 4-3 and 4-4) indicate active salt diapirism (Fiduk et al., 2004). Group 2 faults comprise faults that breach H4 but terminate beneath H5, with Horizon H4 comprising a major truncation surface at the bottom of Unit 3 (Figs. 4-3 and 4-4). Group 3 faults comprise structures that breach the top of Unit 1 (Horizon H3) and terminate within Unit 2 (Figs. 4-3 and 4-4). Group 4 faults are confined to Unit 2 (Figs. 4-3a and 4-4).

Groups 1 and 2 share approximately the same number of faults (30 and 29 faults, respectively). Group 1 comprises the faults with the largest displacement in the study area (Figs. 4-4). Group 4 faults are rare, with only a few being imaged within a central depression developed on the crest of the salt ridge (Fig. 4-4). These latter faults show the smallest length and displacement values (Figs. 4-2 and 4-3). All in all, the four groups of

114
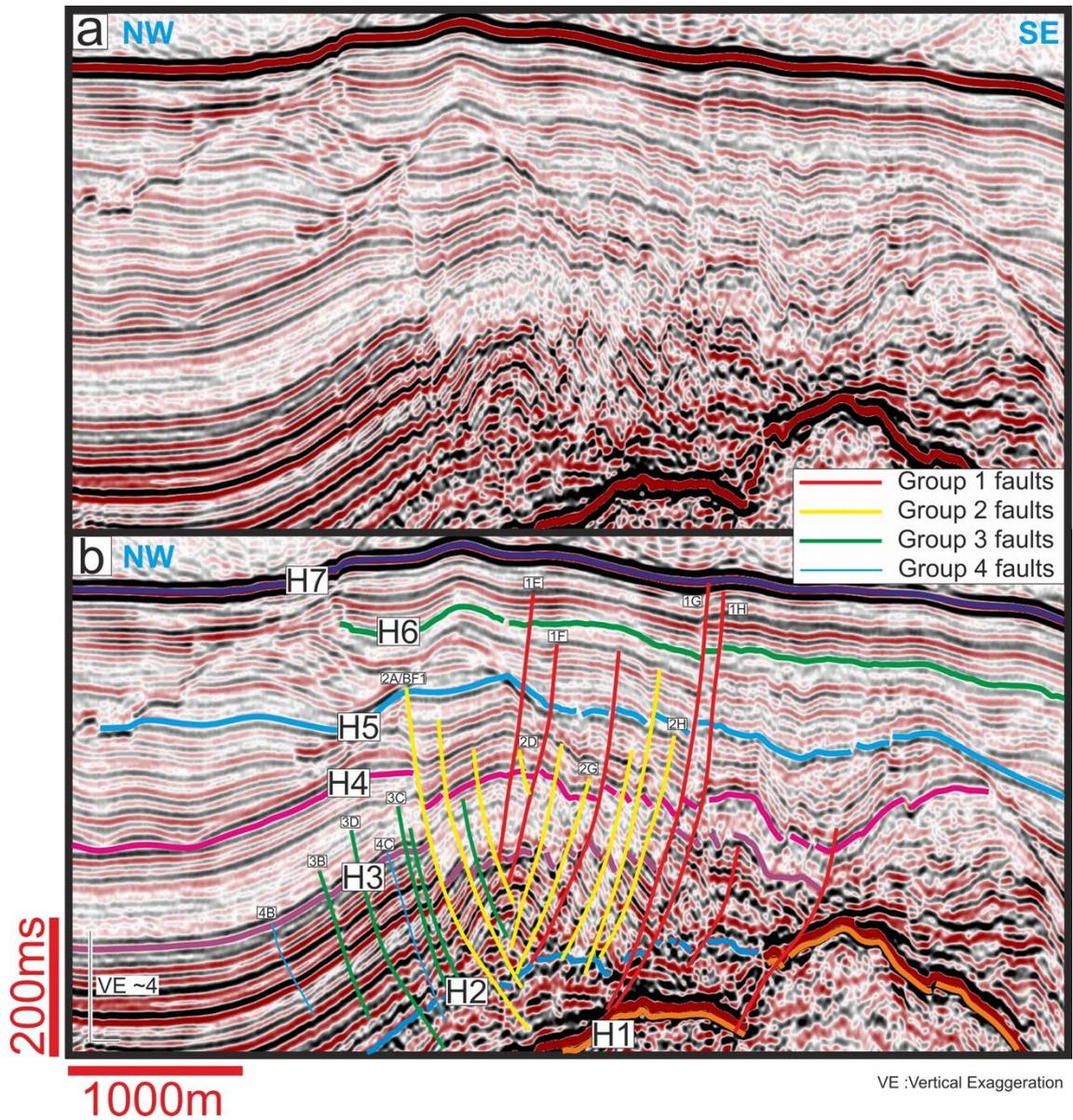
Fig. 4-4 Seismic sections illustrating the four groups of faults (Groups 1 to 4) interpreted on the crest of the salt ridge. a) Uninterpreted seismic section, shown in Figure 4-1b. b) Interpreted seismic section. Faults offset H5 and some propagate towards the sea floor. Group 2 is bounded by H5 and offsets H4 – the top surface of Unit 2. Group 3 faults are only observed in Unit 2. Group 4 faults are also limited to Unit 2.

faults form two distinct fault families towards the northern (Zone 1) and southern (Zone 3) halves of the interpreted salt ridge (Figs. 4-2 and 4-3).

Fault 1A and 2A in Zone 1 have large length and the largest maximum throw values. Based on the criterion that faults with the largest displacement and length accommodate the bulk of strain and stress, faults 1A and 2A are interpreted to form border faults in Zone 1. Following the same criteria, faults 1E and 1G are considered to form border faults in Zone 3 (see details of maximum throw of these faults in section 6).

Faults in Zone 1 dips to the east, with a few antithetic faults occurring at the edge of the salt ridge and forming graben-like structures (Fig. 4-3a). The average strike of faults dipping to the east in Zone 1 is 5º NNE and its average dip angle approaches 35º (Fig. 4-5a). Border fault 1 (BF1) strikes N-S close to Zone 2, but gradually changes its strike to NNE into Zone 1 (Fig. 4-2). Border Fault 2 changes its strike from NNW to NNE in a south to north direction (Fig. 4-2). Both border faults are listric, dipping to the east (Fig. 4-3a). Antithetic faults in Zone 1 show an average strike of 20º NNE and dip angle of 36º (Fig. 4-5b). In contrast to the northern part of the salt ridge, faults in Zone 3 dip uniformly to the west. Their average strike direction is 5° NNE and the average dip angle is 35° (Fig. 4-5c). Border faults 1E and 1G strike also NNE (Fig. 4-2). Most of the faults in Zone 3 are listric and slightly curved in map view (Figs. 4-2 and 4-3b).

Figure 4-6 presents density of resolvable faults in the study area. Figure 4-6a separately shows fault density on the concave side and convex side of BF1 from south to north (Figs. 4-2 and 4-3a). This data plot indicates that fault density in the hanging-wall block is larger than in the footwall (Fig. 4-6a). To the south, closer to Zone 2 (Fig. 4-2), fault density is similar on both blocks, with fault density approaching a number of 12 faults/km (Fig. 4-6a). On the footwall block of BF1 fault density decreases to the north, revealing a denser fault distribution closer to Zone 2. Figure 4-6b shows fault density in Zones 1 and 3; the data showing that fault density in Zone 1 (8–12 faults/km) is larger than fault density in Zone 3 (6–8 faults/km).
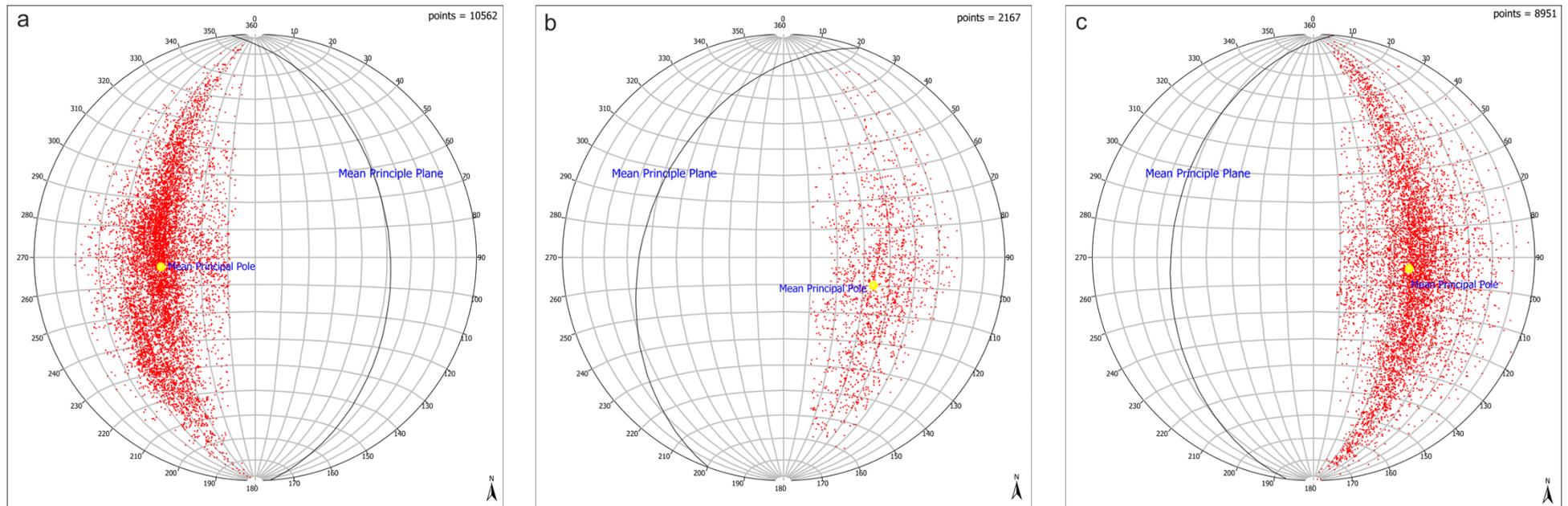
Fig. 4-5 Lower-hemisphere and equal-area projections of poles to fault planes showing the strike directions and dip angles of the crestal fault system. a) Average strike direction (354^0 NNW) and dip angle (35^0) of faults dipping to the east in Zone 1. b) Average strike direction (20^0 NNE) and dip angle (36^0) of faults dipping to the west in Zone 1. c) Average strike direction (5^0 NNE) and dip angle (35^0) of faults in Zone 3. Faults are divided into fault meshes according to fault interpretations in Petrel, and each of the fault meshes indicates a point on the Stereoplots.
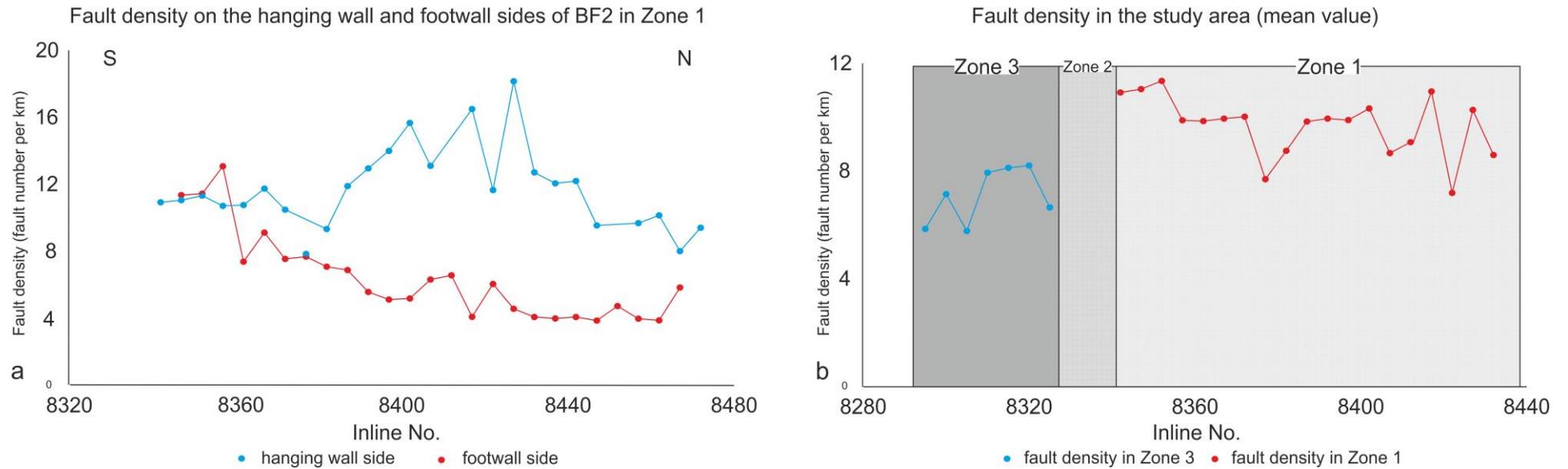
Fig. 4-6 a) Statistical data for fault density on both the hanging-wall and footwall blocks of border fault 1 (Zone 1) as compiled from specific seismic sections in a south to north orientation. b) Fault density acquired on selected seismic sections in both Zones 1 and 3.

4.2.2   Geometry of the accommodation zone

The accommodation zone separating faults in Zones 1 and 3 is described following the definition in Faulds and Varga (1998). To these authors, accommodation zones comprise belts of overlapping fault terminations that separate either systems of uniformly dipping normal faults or adjacent domains of opposite-dipping normal faults. In the study area, the strike direction of an interpreted accommodation zone is near-perpendicular to the overall strike direction of the normal faults that terminate into it (Fig. 4-2).

The strike direction of this transverse accommodation zone (TAZ) is E-W. The TAZ is approximately 4500 m-long and 200 m-wide, with numerous opposite-dipping faults terminating or propagating into it (Figs. 4-2 and 4-3c). The TAZ was formed in association with the growth of two opposite-dipping fault families in Zones 1 and 3. With continuing lateral fault propagation in both Zone 1 and Zone 3, the transverse accommodation zone becomes narrower.

4.3 Evidence for fault growth, reactivation and segment linkage

Throw vs. depth plots and throw vs. distance plots are used in this section to analyse the growth history of the faults (Baudon and Cartwright, 2008c, Baudon and Cartwright, 2008b, Durogbitan, 2016a). Non-reactivated faults are generally characterised by M-type or C-type throw-depth profiles, with throws tipping out towards the lower tip without a clear detachment (Baudon and Cartwright, 2008b). Reactivated faults exhibit stepped throw-depth profiles (double-C throw profile with one episode of reactivation) and their lower parts show a similar throw profile to non-reactivated faults. Fault reactivation modes are divided into upward reactivation and dip-linkage reactivation (Baudon and Cartwright, 2008b). However, crestal faults usually show small throw values (Morley, 2007), making it difficult to differentiate between these two modes. In this chapter, reactivation is referred both to upward and dip-linkage reactivation. Fault segmentation is analysed with throw-distance profiles. Faults that show only one fault segment often present a maximum throw value at their centre, diminishing towards both tips (Lohr et al., 2008, Mansfield and Cartwright, 2001). Faults that are formed by lateral linkage of different segments often present several peak values in throw, with lower throw values in the linkage area (Walsh et al., 2003).

4.3.1   Group 1 faults

Group 1 comprises a set of faults with the largest displacements on the salt ridge (Fig. 4-3). A few of Group 1 faults are still active and propagate onto the sea floor (Figs. 4-3 and 4-4). Faults 1A to 1D in Zone 1, and 1E to 1H in Zone 3, were analysed in terms of their growth history (Fig. 4-7, see Figs. 4-2 and 4-3 for their locations), with fault 1A comprising border fault 1 (BF1) in Zone 1 and faults 1E (BF3) and 1G (BF4) comprising border faults in Zone 3.

Faults 1A and 1B in Zone 1 are interpreted to form two hard-linked fault segments, whereas both fault 1C and 1D only comprise one fault segment (Fig. 4-7). The reactivation history of faults in Zone 1 is constrained by Horizon H3 and H5, which are two main erosional surfaces identified on top of the salt diapir (Fig. 4-3). Profiles 1B-e show typical examples of fault reactivation bounded by horizons H3 and H5 (Fig. 4-7). Note that profiles 1B-e, 1B-f, 1C-h, 1C-i and 1D-j clearly show a first episode of fault reactivation in Zone 1, which is marked by Horizon H3, with only one exception in 1B-d where fault reactivation happened earlier. The second episode of reactivation in Group 1 faults (Zone 1) is marked by Horizon H5, as shown in profiles 1A-b, 1A-c and 1B-e. The T-Z plots for 1B-d and 1D-k indicate that this second episode fault reactivation occurred slightly earlier than H5, whereas 1B-g and 1D-j show that fault reactivation happened after H5 (Fig. 4-7).

Faults 1E and 1H in Zone 3 are interpreted to comprise a single fault segment, with fault 1F and 1G comprising two fault segments (Fig. 4-7). Similar to Zone 1, fault reactivation of Group 1 faults in Zone 3 also shows two distinct episodes marked by H3 and H5 (Fig. 4-7). The first episode of fault reactivation in Zone 3 is revealed by the T-Z plots of 1E-b, 1G-j, 1G-k and 1H-l to 1H-n (Fig. 4-7). The second episode of fault reactivation, marked by horizon H5, affected the T-Z profiles in 1E-b, 1E-c, 1F-d, 1F-e, 1G-1 to 1G-i, 1H-m and 1H-n.

Even though two episodes of fault reactivation are identified in both Zone 1 and 3, not all faults record two episodes of fault reactivation. Exceptions are fault 1C in Zone 1 and faults 1F and 1G in Zone 3, which reveal one single episode of fault reactivation.
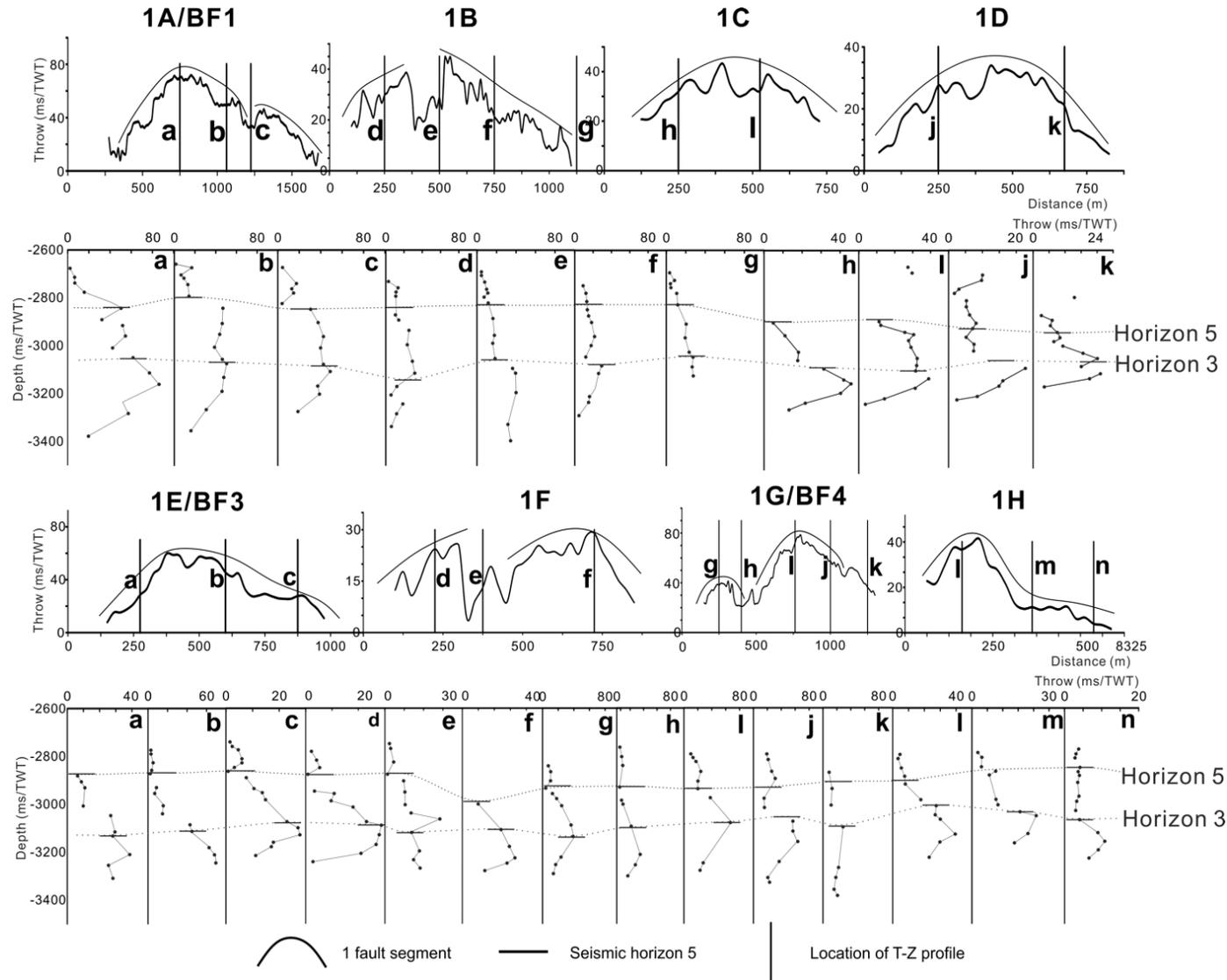
Fig. 4-7 T-D and T-Z plots for Group 1 faults. The locations of Faults 1A to 1H are labelled in Figure 4-2. The vertical lines a-k in the T-D plots indicate the location of the T-Z plots shown. Two episodes of fault reactivation are identified across horizons H3 and H5.

121

Maximum throw values of Group 1 faults vary from 30 to 80 ms TWT, with border faults 1A, 1E and 1G reaching a maximum of 80 ms TWT. Away from the border faults, maximum throw value can reach a maximum of 40 ms TWT in other Group 1 faults (Fig. 4-7).

4.3.2   Group 2 faults

Faults interpreted as part of Group 2 are named 2A to 2D in Zone 1, and 2E to 2H in Zone 3 (Fig. 4-8, see Figs. 4-2 for their location).

Fault 2A, also referred as Border Fault 2, has a maximum throw value of ~60 ms TWT (Fig. 4-8). Except for this latter, faults in Zone 1 comprise two fault segments, with fault 1A showing one single fault segment. Fault reactivation of Group 2 faults occurs around Horizon H3 (Fig. 4-8). However, this group of faults shows a complicated reactivation history. Profiles 2B-e to 2B-g and fault 2C-j reveal two episodes of fault reactivation (Fig. 4-8). Profiles 2B-d, 2C-h and 2D-k are 'C' type faults on T-Z data, a character indicating the absence of reactivation. An important aspect is that faults 2C and 2D comprise two fault segments of distinct length (Fig. 4-8), with the shorter fault segment showing a non-reactivated T-Z profile (profile 2C-h of fault 2C and profile 2D-k of fault 2D). Conversely, the longer fault segment reveals fault reactivation. Fault 2B, which comprises two comparable fault segments, also shows a non-reactivated fault segment (profile 2B-d) and a reactivated one (2B-e to 2B-g) (Fig. 4-2).

Group 2 faults in Zone 3 comprise two fault segments except for fault 2H, which is interpreted to form one single segment (Fig. 4-8). Fault reactivation history in Zone 3 also occurred around Horizon H3. The corresponding T-Z plots generally indicate one episode of fault reactivation, with exceptions in profiles 2E-a, 2G-h and 2G-i (non-reactivated) and profile 2E-j with two episodes of fault reactivation. Similar to faults 2B to 2D in Zone 1, fault 2E and fault 2G also indicate that one fault segment is reactivated while the other is not (Fig.4-8).
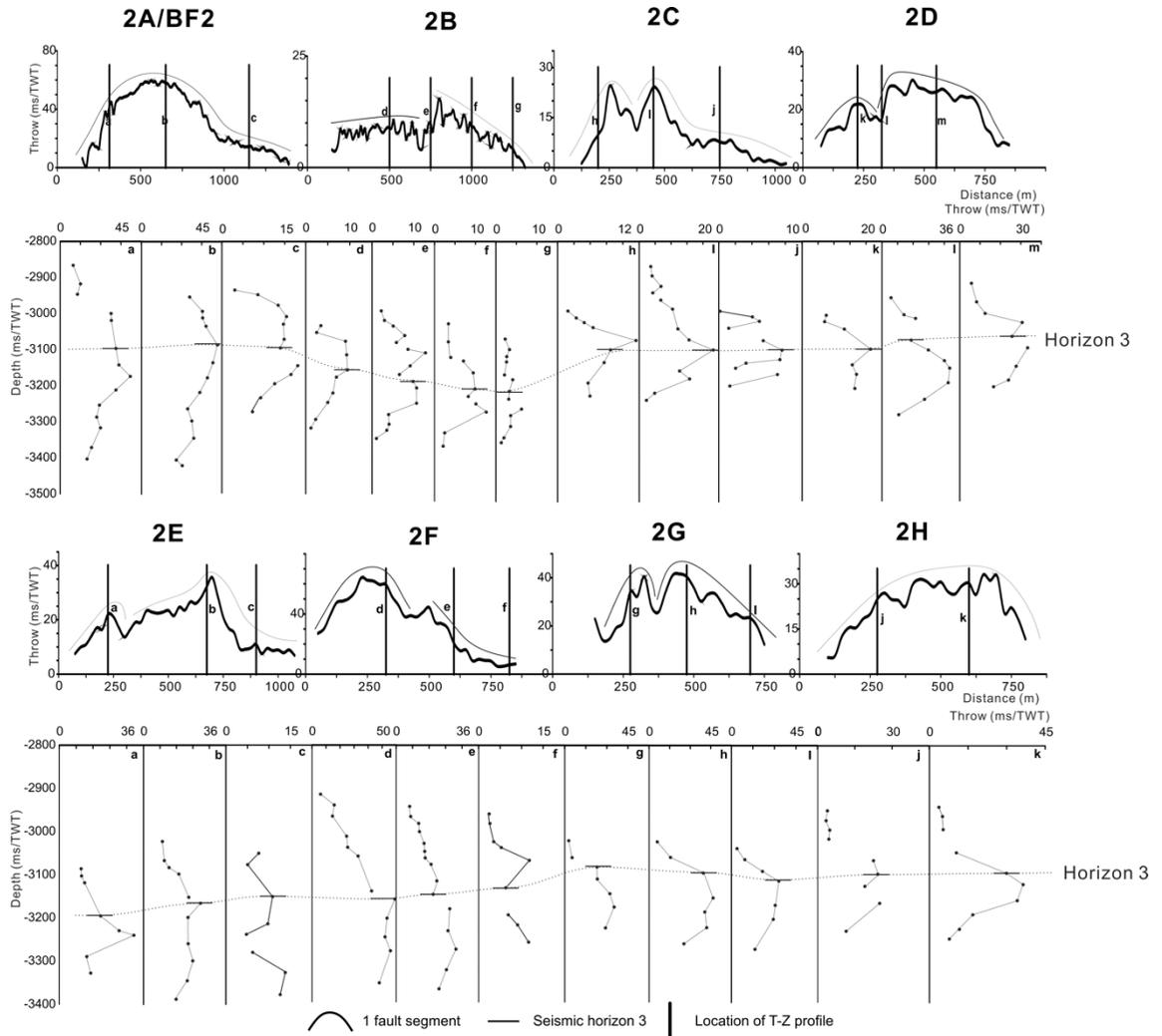
Fig. 4-8 T-D and T-Z plots for Group 2 faults. Locations of Faults 2A to 2H are labelled in Figure 4-2. The vertical lines a-m in the T-D plots indicate the locations of the T-Z plots. One episode of fault reactivation, marked by horizon H3, is recognised.

Except for fault 2A, maximum throw values for Group 2 faults vary from 30 to 40 ms TWT, values that are far greater than the maximum throw of faults in Groups 3 (12–15 ms TWT) and 4 (4–8 ms TWT).

4.3.3   Group 3 faults

Faults named 3A to 3D (Zone 1) and 3E to 3H (Zone 3) comprise Group 3 faults (Fig. 4-9). In Zone 1, faults 3A, 3C and 3D are formed by two hard-linked fault segments and fault 3B comprises three fault segments (Fig. 4-9). In Zone 3, faults 3F and 3H are interpreted to be single fault segment, fault 3E has two hard-linked fault segments, and fault 3G comprises four linked fault segments (Fig. 4-9).

One single episode of fault reactivation is recognised in Group 3. In Zone 1, fault reactivation is recorded at Horizon 3 (Profiles 3A-a, 3D-h and 3D-i). However, fault profiles 3A-b 3B-d and 3C-f indicate an earlier episode of fault reactivation. In Zone 3, the reactivation happened earlier than Horizon H3 (profiles 3E-a, 3F-c, 3H-g and 3H-h).

Similar to faults 2B to 2E, and fault 2G in Group 2, faults 3B, 3C, 3E, 3F and fault 3G in Group 3 comprise at least two fault segments with distinct reactivation histories (Fig. 4-9). Some of these segments show no reactivation. Maximum throw values for Group 3 vary from 12 ms to 15 ms TWT, a value larger than the maximum throw of Group 4 faults (Fig. 4-9).

4.3.4   Group 4 (non-reactivated) faults

Group 4 faults are restricted to Zone 1 (Fig. 4-3a). Four distinct faults named 4A to 4D were analysed through the compilation of T-Z plots (Fig. 4-10a-h) and by measuring absolute throw values along horizon H3 (Fig. 4-10). This group of faults were not reactivated, with maximum throws showing relatively small values between 4 ms and 8 ms TWT (Fig. 4-10). These values are within the resolution limits of seismic data, which was processed with sampling rate of 2 ms. Throw-depth (T-Z) plots for this group of faults show a typical 'C' shape profile (Baudon and Cartwright, 2008b). The upper tips
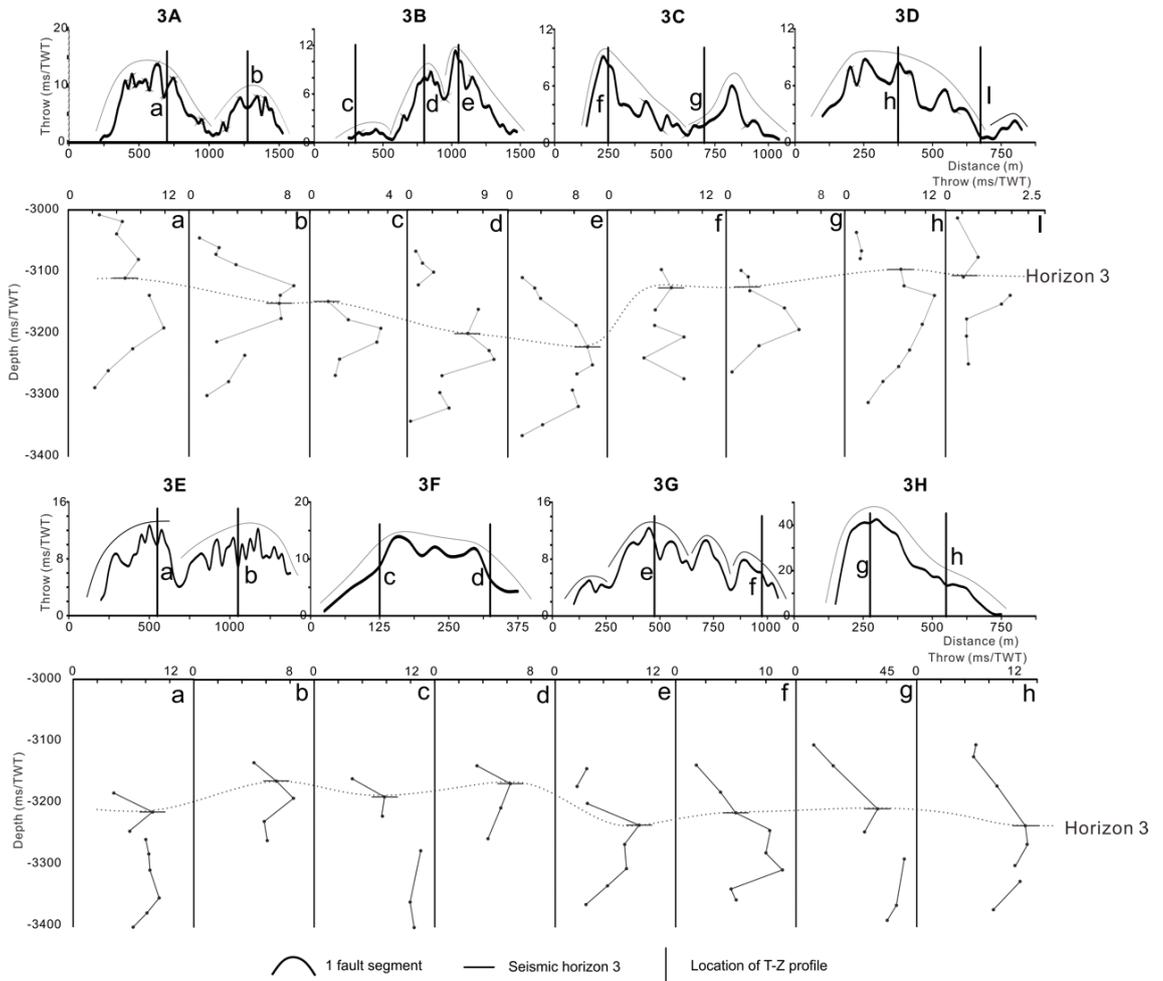
Fig. 4-9 T-D and T-Z plots for Group 3 faults. Locations of Faults 3A to 3H are labelled in Figure 4-2. The vertical lines a-l in the T-D plots indicate the location of the T-Z plots. Reactivation is recorded at horizon H3 in Zone 1. Fault reactivation in Zone 3 occurs earlier than H3.
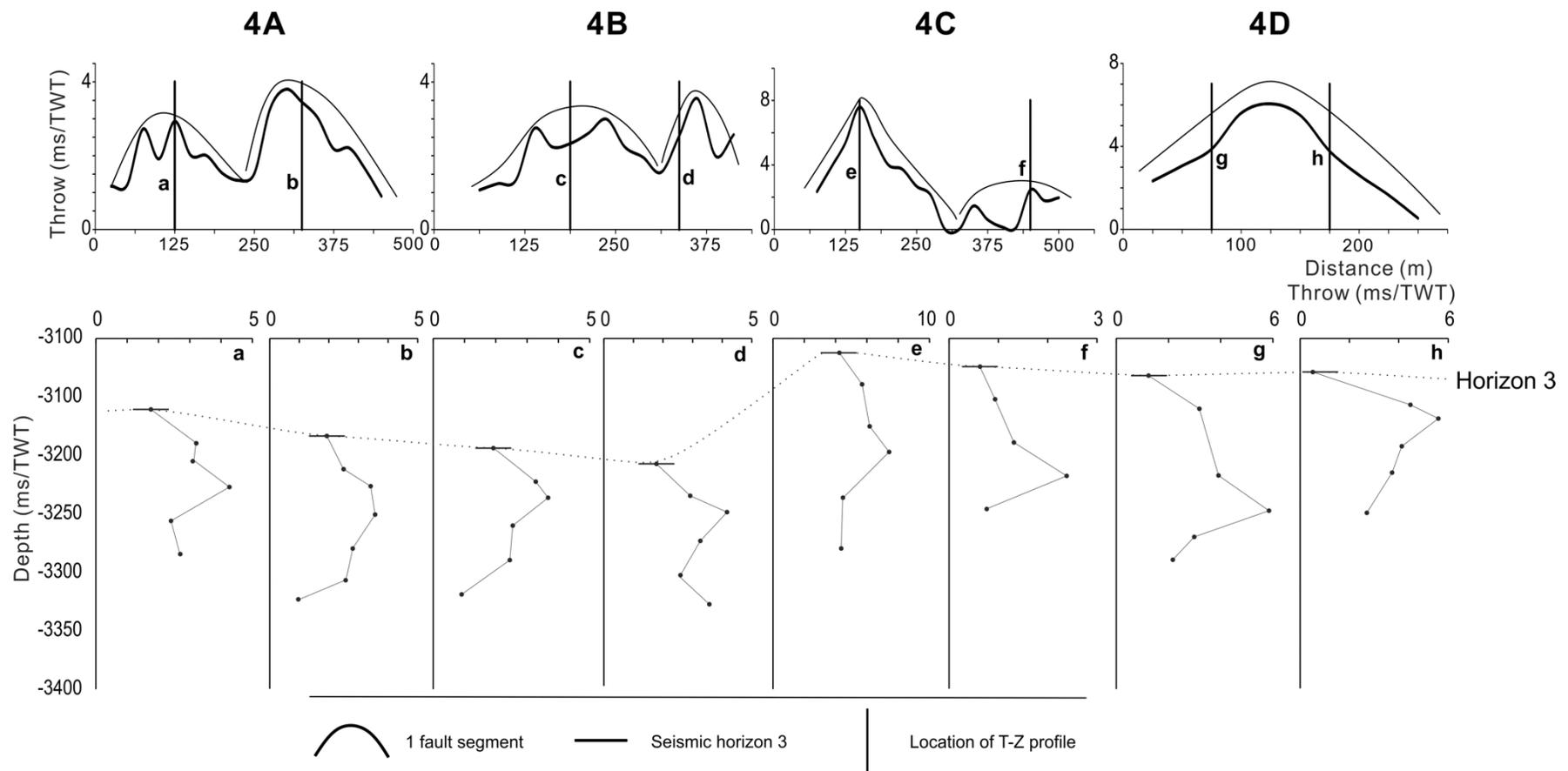
Fig. 4-10 T-D and T-Z plots of faults in Group 4. Locations of Faults 4A to 4D are labelled in Figure 4-2. The vertical lines a-h in the T-D plots indicate the location of the T-Z plots.

All the T-Z plots show a typical 'C' shape, a character indicating that faults were not reactivated.

of these faults are eroded away at Horizon H3 (Fig. 4-10). Throw-Distance profiles for fault 4D show a single throw peak, suggesting the development of a single fault segment. Throw-length profiles for faults 4A, 4B and 4C show asymmetrical "M" shapes, which reflect the linkage of two distinct fault segments.

4.4 Geometry of crestal faults in time and space

Crestal fault families are often hard to document on seismic data or at outcrop (Randles et al., 2012). Nevertheless, Alves (2012) proposed that gravitational gliding contributes to the formation and evolution of crestal fault families. In addition, Yin and Groshong (2007) recognised that the evolution history of crestal fault families is controlled by master fault(s), referred to as border fault(s) in this work. According to the latter authors, master faults are initiated during the early stages of faulting and are capable of developing a more complicated fault pattern. Some other common characteristics of crestal faults include: a) their relatively small length, which normally does not exceed 2.3 km (Alves, 2012), and b) their relatively small throws, often below 50 ms TWT (Morley, 2007).

A second key characteristic, implying that fault throw is below 50 ms TWT, is not followed by the border faults in this study (see Randles et al., 2012). Four border faults are identified in the study area; faults 1A and 2A in Zone 1, and faults 1E and 1G in Zone 3 (Fig. 4-2). Without exception, all border faults show an average throw of ∼70 ms TWT for a maximum of 90 ms TWT (Figs. 4-7 and 4-8). This distinct throw distribution confirms that most of the stress and strain on the crest of the interpreted salt ridge has been accommodated by border faults. Fault density of the crestal fault system in the Espírito Santo Basin varies from 4 to 8 per km on the footwall of the border faults, to 10–18 per km on their hanging-wall block (Fig. 4-6a), which implies that border faults might have hindered fault growth farther from the salt edge (Fig. 4-2). Comparing fault density in Zones 1 and 3, Zone 3 has a higher fault density than that in Zone 1 (Fig. 4-6b), which might reflect distinct fault-initiation processes.

The analysis of maximum throw vs. depth is an efficient way to identify the depth faults first nucleated (Alves, 2012). However, this method is used on the basis that space

is available for faults to propagate both upwards and downwards, and this method loses its practical meaning when faults sole into a detachment surface. In this case, faults are most likely to propagate upwards, with maximum throw developing only in an upward direction. To avoid this caveat, Group 3 and Group 4 faults were selected to compile maximum throw vs. depth plots as these two groups of faults are not detached on the salt ridge (Fig. 4-3). The Expansion Index (EI), which is the ratio between the thickness of hanging-wall and footwall strata (Lewis et al., 2013; Mansfield and Cartwright, 1996), was used to identify periods of significant fault growth. When EI > 1, representing hanging-wall thickening, active fault growth occurs (Omosanya et al., 2015). In this chapter, selected border faults (faults 1A and 2A in Zone 1, faults 1E and 1G in Zone 3) that are still tectonically active, were selected to calculate their expansion index and to estimate relative timing of fault growth episodes.

The maximum throw vs. depth plot in Figure 4-11 shows that faults in both Zone 1 and Zone 3 are nucleated within Unit 1 to Unit 3, with maximum throw located within Unit 2. The nucleation of faults reveals that faults in both Zone 1 and Zone 3 were formed during the middle-late Eocene, when the Abrolhos Bank was being formed and volcaniclastic sediment was transported into the Espírito Santo Basin, inducing local halokinesis (Fiduk et al., 2004). Comparing the relative depth of maximum fault throws in Zones 1 and 3, it becomes obvious that faults in Zone 3 (Fig. 4-2) were formed before faults in Zone 1, and present relatively deeper maximum throw locations (Fig. 4-11).

Expansion indexes of border faults in Zone 1 and Zone 3 (Fig. 4-12) also indicate that faults in Zone 3 formed earlier than faults in Zone 1. The first growth episode in Zone 1 occurred between H2-1 and H2-2, with expansion indexes above 1.0. In Zone 3, the first episode of fault growth occurred between H2 and H2-1 i.e., earlier than the first episode of fault growth in Zone 1. Combining maximum throw values vs. depth and expansion index data for border faults in Zones 1 and 3, this chapter concludes that faults in Zone 3 formed earlier than their counterparts in Zone 1.

4.5 Discussion

4.5.1   Controlling factors on fault reactivation offshore Espírito Santo

The growth of faults is often controlled by reactivated basement structures (Pinheiro and Holdsworth, 1997). Bellahsen and Daniel (2005) later suggested that the relationship between the orientation of existing faults and the orientation of stresses to be key parameters leading to fault growth and reactivation. If the strike direction of existing faults and the orientations of principle stresses are favourable, faults are easier to grow and reactivate (Baudon and Cartwright, 2008b). In the study area, the main strike direction of faults varies from NW to NE (Fig. 4-2). Except from faults 3B, 2B, 3A, 4B, 3C, 4C, which show a concentric pattern (Fig. 4-2), crestal faults strike N-S to NNE in the study area, a direction matching positively with the overall direction of extension for the South Atlantic margin (Chang et al., 1992; Petri, 1987), and with the regional stresses recorded on the margin at present (Heidbach et al., 2008). However, extension alone cannot justify the recorded variations in the strike of the interpreted crestal faults as local stresses on the flanks of salt structures change sharply in space and time, influencing fault growth (Hubbert and Rubey, 1959; Jain et al., 2013; Wiprut and Zoback, 2000). In addition, known factors influencing fault growth and reactivation around salt structures include salt dissolution (Randles et al., 2012) and multi-phase salt growth, both potentially associated with fault reactivation in the study area. Faults that show a concentric pattern (faults 3B, 2B, 3A, 4B, 3C, 4C; see Fig. 4-2 for location) reflect salt withdrawal beneath the central depression generated on the salt ridge (Ge and Jackson, 1998; Ward et al., 2016).

This chapter proposes that border faults accommodated regional E-W extensional stresses recorded offshore Espírito Santo (Chang et al., 1992; Jacques, 2003). The growth of faults in the study area follows two distinct stages. Stage 1 records the growth of border faults, followed later by collapse of the salt ridge in distinct styles. In such a setting, crestal faults closer to border faults were harder to initiate and grow than those further away (Fig. 4-13). Border fault 1 was reactivated during a second episode of fault reactivation, which is marked by horizon H5 (Fig. 4-7). Throw-depth (T-Z) data for BF1
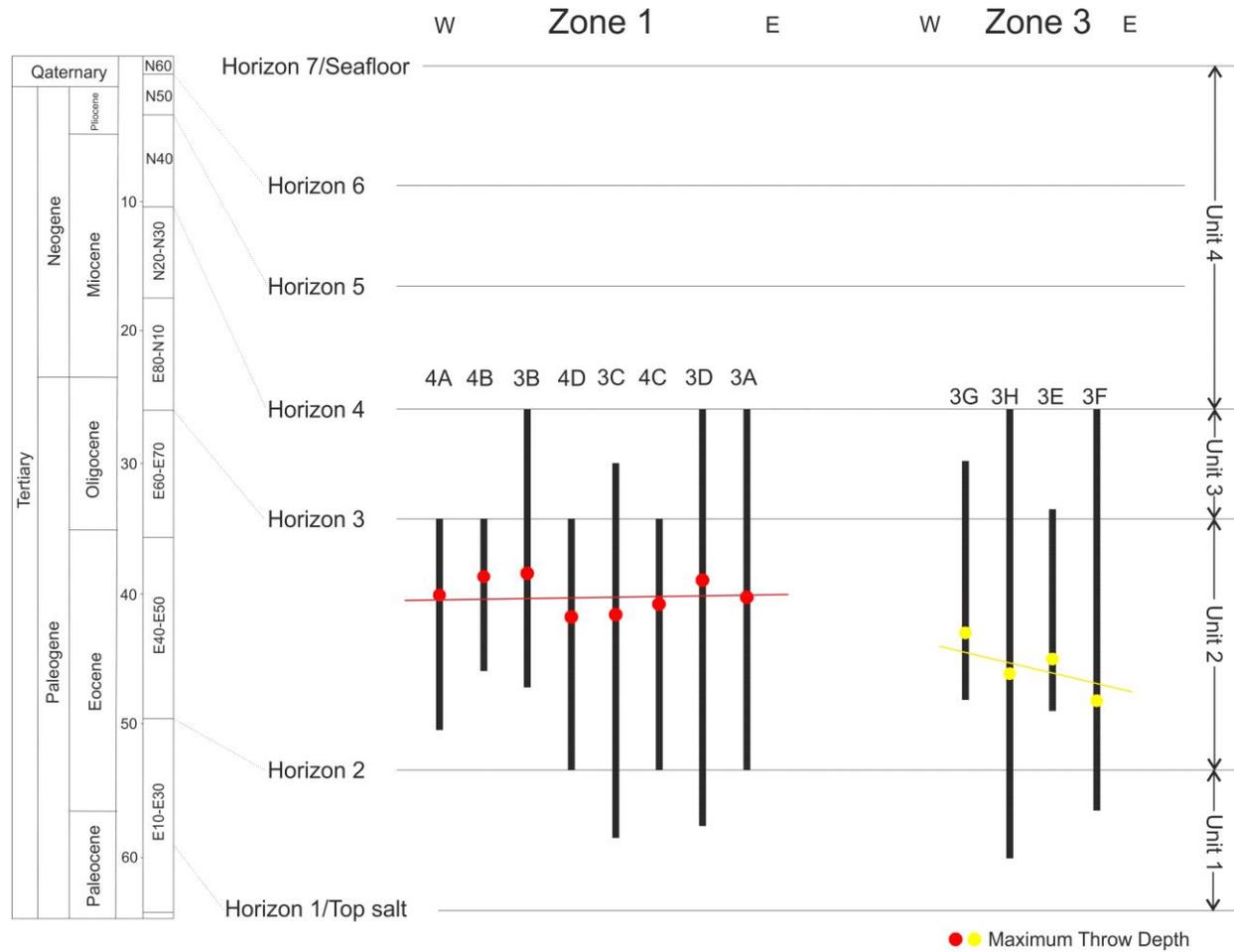
Fig. 4-11 Maximum throw locations for Group 3 and 4 faults in Zone 1 and Group 3 faults in Zone 3. The analysed faults are tied to seismic stratigraphy units. The figure indicates that the formation of faults in Zone 3 is earlier than that of Zone 1.
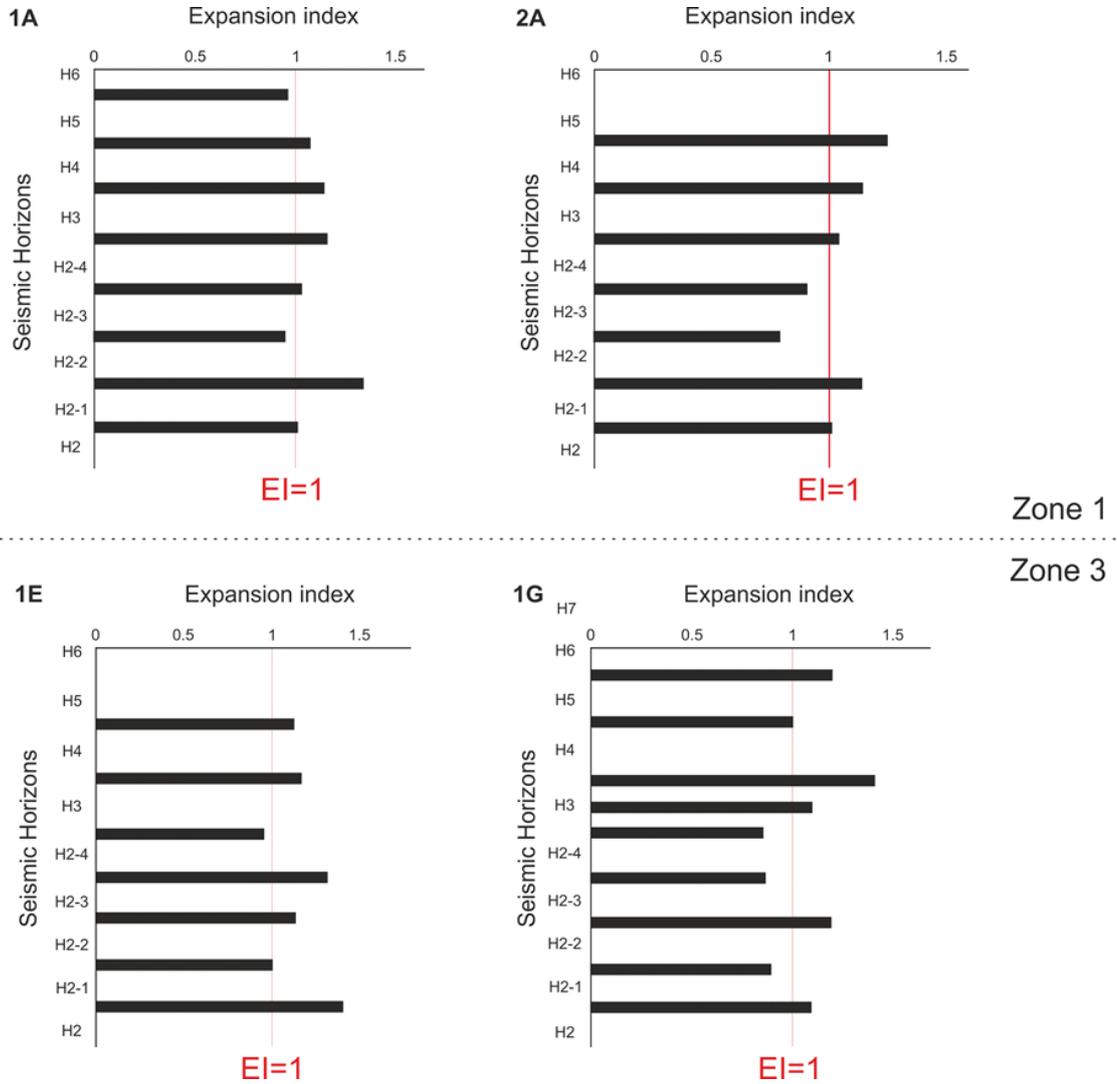
Fig. 4-12 Expansion Indexes (EI) for major faults showing variation in strata thickness across their hanging-wall and footwall blocks. An EI of >1 implies thickening of strata in the hanging-wall section, whereas EI < 1 means thinning of hanging-wall strata relative to the footwall block. Maximum throw locations of Group 3 and 4 faults in Zone 1 and Group 3 faults in Zone 3 as tied to seismic stratigraphy units. The figure indicates that the formation of faults in Zone 3 is earlier than that of Zone 1.

(Fig. 4-7) indicates that fault throw reaches a minimum value around H3, with a second peak in throw recorded after the second erosion phase is identified on the crest of the salt ridge (H5 in Figures 4-3a and 4-4). This suggests that border faults kept accommodating strain and stress on the crest of the salt ridge - once crestal faults were far enough from border faults, they tended to grow and reactivate (Fig. 4-13). In Zone 1, faults surrounding BF1 and BF2 chiefly comprise faults in Groups 2 and 3 (Fig. 4-2) which have far smaller displacement and length and a simpler reactivation history than the border faults (Figs. 4-7 to 4-10). Noting that faults closer to BF2 belong to Group 3 (Fig. 4-2), farther to the east Group 2 faults were firstly dominant before the generation of BF1. In Zone 3, in both sides of fault 1E, maximum fault throws tend to decrease ($T_{max2F} > T_{max2E} > T_{max3F}$ to the west and $T_{max1F} > T_{max2G} > T_{max2H}$ to the east) (Figs. 4-7 to 4-10).

The propagation history of the interpreted fault families does not agree with the 'coherent model' of Jackson and Rotevatn (2013), as faults commonly comprise two or more linked segments (Giba et al., 2012; Morley, 1999; Walsh et al., 2002; Walsh et al., 2003) (Figs. 4-7 to 4-10). In the 'coherent model' of Jackson and Rotevatn (2013), faults have similar length and throw profiles and are linked early in their development to form large segments. This work proposes that larger fault segments in the study area propagated and were reactivated to link with smaller fault segments, and then evolved together as a set of related structures (Fig. 4-14). The larger, mature faults result from the linkage of several fault segments, and this mode is here identified as the predominant mode of lateral fault propagation in the study area (Figs. 4-7 to 4-10). The generation of larger faults is thus interpreted to have been controlled by several small existing fault segments, rather than by a large fault generated at the start of fault propagation.

Throw-depth (T-Z) plots have been assessed for their accuracy as a method to identify fault growth and reactivation. In particular Lohr et al. (2008) pointed out that in listric faults, especially those in areas of important salt tectonics, throw values can approach zero and their practical meaning is quantitatively lost. However, in most published cases, throw is a reliable proxy for fault development and reactivation episodes. Even though the T-Z plots in time domain compiled in this study show well-expressed fault reactivation histories (Figs. 4-7 to 4-9), difficulties still exist when interpreting these T-Z plots. In the study area, throw values for crestal faults are often less than 80 ms TWT (generally <50 ms TWT), causing some difficulties in interpreting fault reactivation with
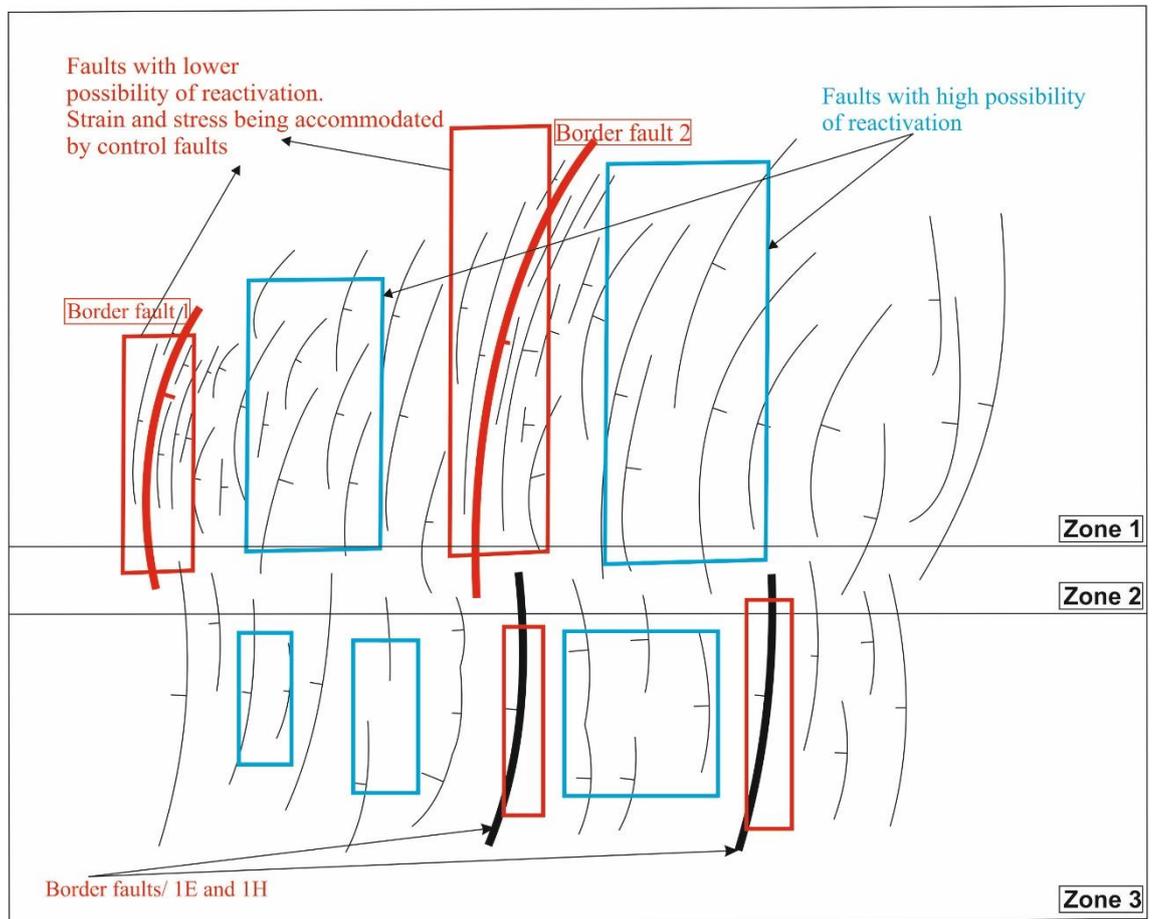
Fig. 4-13 Schematic illustration of the reactivation history of crestal faults in this study. Red boxes highlight zones of low fault reactivation close to the border faults. Blue boxes indicate zones of important reactivation away from the border faults.
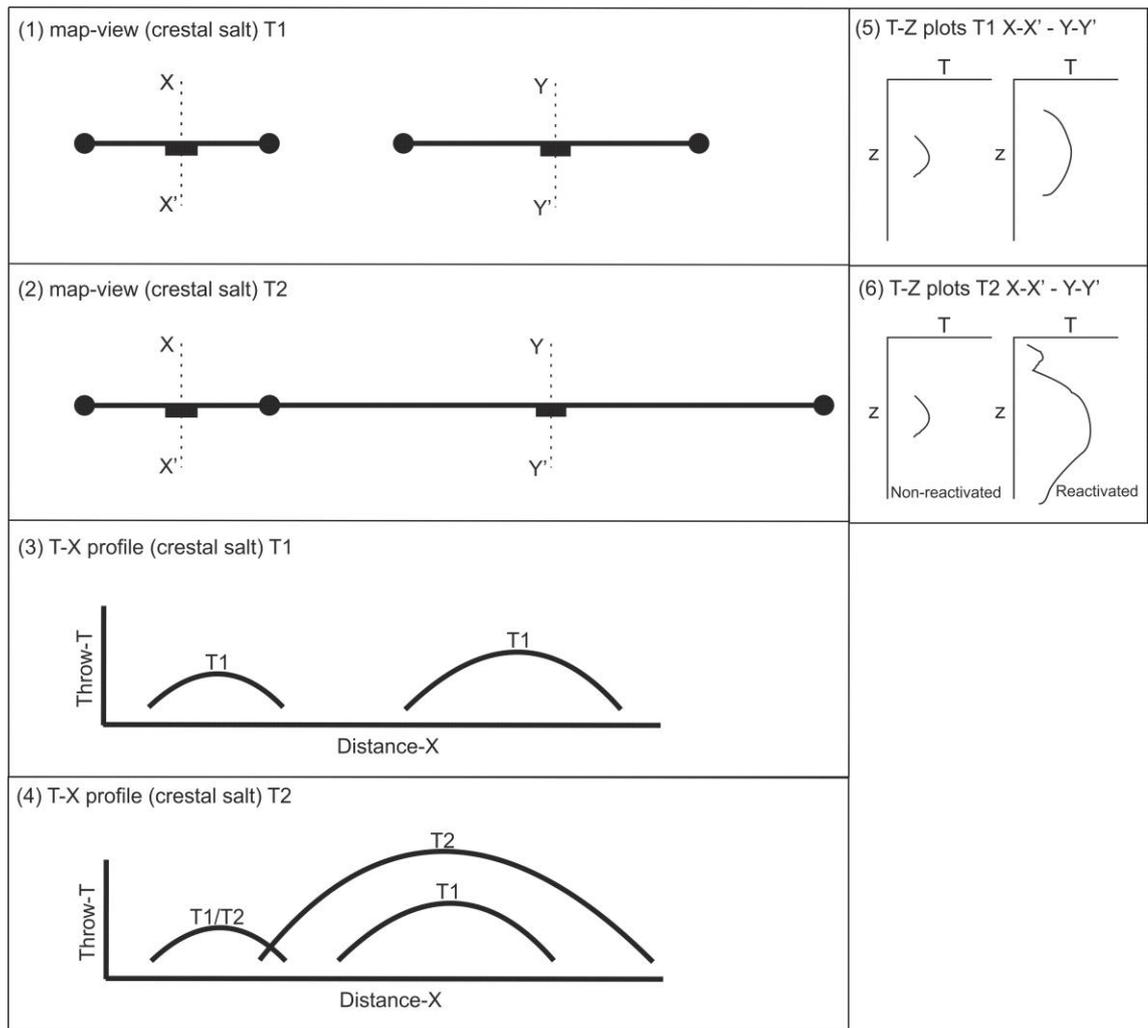
Fig. 4-14 Alternative "isolated model" of fault propagation. Larger faults propagated and reactivated while small fault segments remain undisturbed until two fault segments are linked together. (1-2) map view; (3-4) T-D profile; (5-6) T-Z profile. The larger fault segments can be either reactivated or non-reactivated.
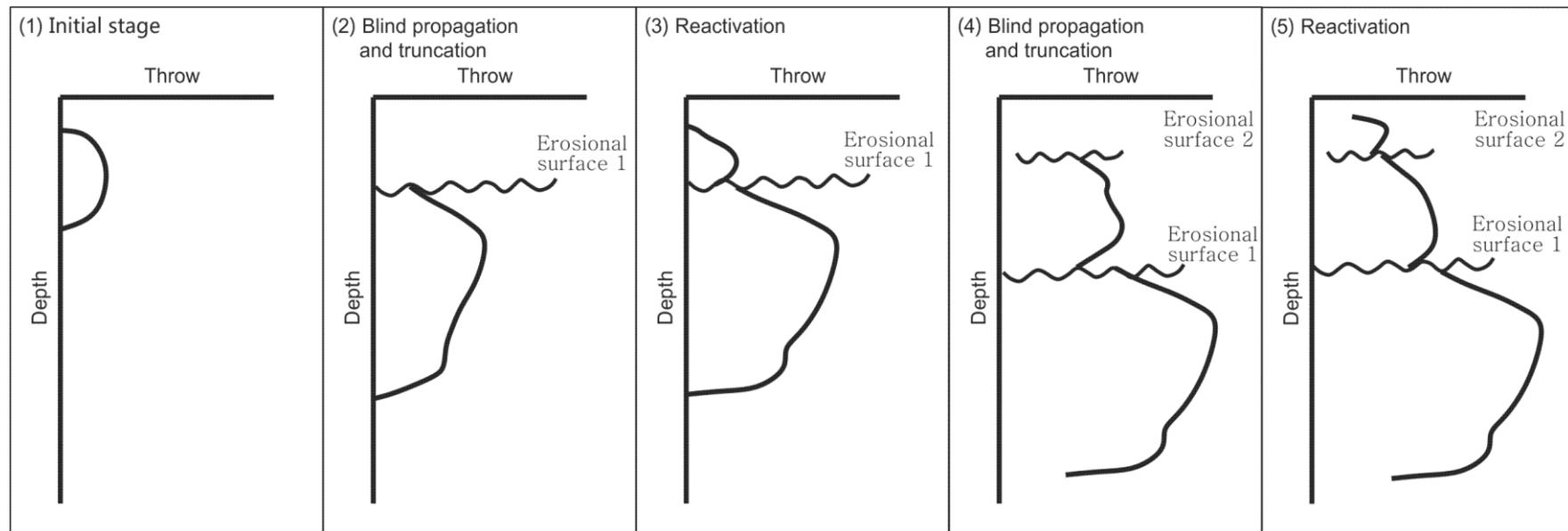
Fig. 4-15 Schematic graph showing throw-depth plots vs. recurring fault reactivation on the crest of salt ridges. Each reactivation episode is associated with an erosional surface in the study area of SE Brazil.

accuracy. However, fault reactivation episodes are better constrained when using two erosional surfaces as temporal markers, H3 and H5. Thus, it is suggested that erosional surfaces comprise markers for identifying fault reactivation on the crest of salt structures. In combination with T-Z plots, interpreters can have a better evaluation of fault reactivation history by using key stratigraphic markers. In the studied crestal fault system, H3 and H5 are recognised as key markers to assess fault reactivation (Figs. 4-7 to 4-10). These two erosional surfaces also mark the boundaries above which faults were not reactivated; for instance, not all faults offset H3 or H5 (Fig. 4-3). Fault 2A (Fig. 4-8) is a good example, as this fault offsets H3 and stops at H5, with no further evidence of reactivation above this latter stratigraphic marker. As a corollary of this chapter, fault propagation above the interpreted salt ridge is more complex than documented by Baudon and Cartwright (2008b) on other salt structures of the Espírito Santo Basin. The three-stage model of fault growth proposed by these latter authors is thus expanded in this work into a five-stage model (Fig. 4-15). The T-Z profiles of faults 1A (a), 1B (d and e), 1D (j and k), 1E (b) and 1H (m and n) (Fig. 4-9) exemplify this five-stage fault growth model. See T-Z profile j of fault 1D for instance; fault throw shows a first peak around 3100 ms TWT, while the second growth phase is indicated with a small peak at H5. A third growth episode is marked with increasing throw close to the sea floor (Fig. 4-7).

4.5.2   Importance of accommodation zones on the crest of salt structures

Numerous studies have been carried out to understand the formation of accommodation zones (Bosworth, 1985; Colletta et al., 1988; Langhi and Borel, 2008; Tesfaye et al., 2008). Fault systems that form accommodation zones in rifts are genetically related faults formed at approximately the same time (Coffield, 1987; Ebinger, 1989; Farhoud, 2009; Faulds et al., 1990; Kong et al., 2005). In the study area, the northern fault system (Zone 1) created multiple E-dipping faults that dip in an opposite direction to faults in Zone 3, with an E-trending accommodation zone separating these two zones (Fig. 4-2). Faults in Zones 1 and 3 are formed due to gravitational processes, however, with distinct faulting intensity, gravitational collapse and gravitational gliding can predominant over another. Gravitational collapse often reveals significant offset on crest of salt structures, and crest of salt structures mainly play as a detachment surface for

the development of crestal fault system. In our study area, the northern fault system (Zone 1) showing geometries of collapse structures, that crestal faults offset the top of salt diapirs (Fig. 4-2), whereas the southern fault system (Zone 3) resembles faults formed by gravitational gliding (Fig. 4-3b) during salt withdrawal of the depression developed on top of the salt diapir (Fig. 4-2). The interpreted top salt does not match with these mechanisms as this salt diapir is growing at present (Fig. 4-3). The different mechanisms for the two opposite-dipping fault families hint at distinct timings for the formation of opposite dipping fault systems. The depth in which maximum throw is observed indicates that fault nucleation in Zone 3 happened earlier than in Zone 1 (Fig. 4-11). The expansion indexes of border faults in Zone 1 and Zone 3 also indicate that the southern gravitational fault array formed slightly earlier than the northern collapsed fault array (Fig. 4-12). In Zone 1, concentric faults are likely associated with the dissolution (and quick) collapse of salt underneath the post-salt overburden, which shows significant throw values for BF1 on top of the salt surface (Fig. 4-3a). Zone 3, in contrast, shows the predominance of gravitational gliding over the interpreted fault ridge. For instance, in Figure 4-3b, the uniformly west-dipping fault array shows a continuous and smooth salt surface and some of the faults detach on the top of the salt; no significant faults intersect the top of the salt package (Fig. 4-3b). Furthermore, fault density in Zone 1 is higher, which indicates a relative predisposition for fault initiation in Zone 1. Despite these distinct mechanisms, faults in Zones 1 and 3 are kinematically linked and resulted in the generation of the TAZ in Zone 2. The distinct mechanisms observed (gliding vs. dissolution) resulted in locally focused, changing styles of crestal faulting.

Figure 4-16 illustrates the formation of the TAZ. Few faults formed by gravitational gliding in Zone 3 in a first stage due to gradual salt withdrawal and generation of the depression on top of the salt ridge (Fig. 4-2). The sudden collapse of the ridge crest resulted in the formation of two opposite-dipping fault families in Stage 2. Further propagation of the faults in Zones 1 and 3 resulted in the formation of the TAZ, and faults stopped propagating horizontally across the accommodation zone (Figs. 4-16 and 4-17). However, this did not hinder later stages of vertical propagation in the interpreted faults, with structures oriented favourably for reactivation revealing blind vertical propagation towards the surface. This characteristic is again shown in Figure 4-3, in which most of the faults are still active and propagate to the present sea floor.
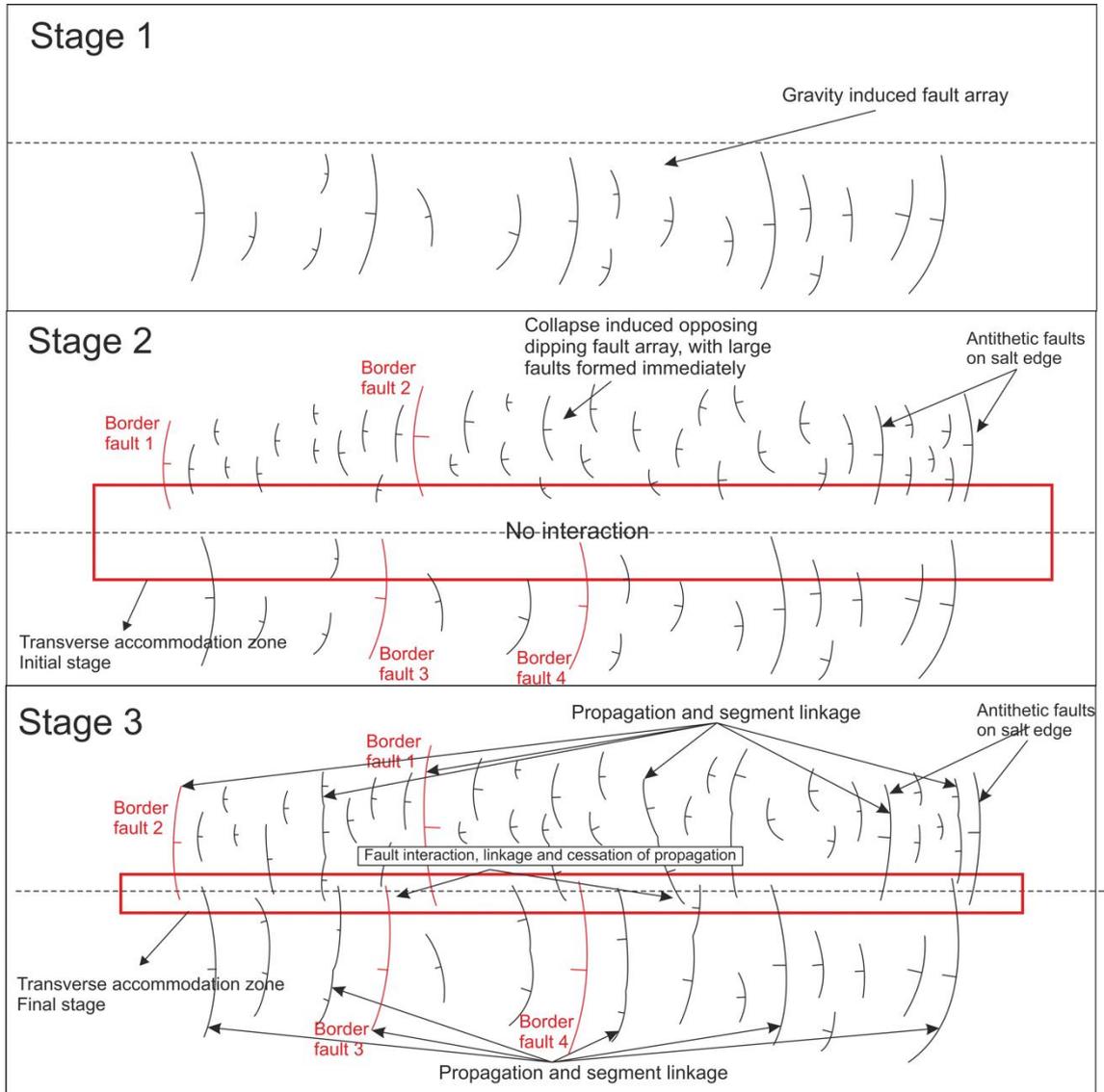
Fig. 4-16 Schematic map illustrating the formation of a transverse accommodation zone. Stage 1 - Formation of a W-dipping fault array. Stage 2 - Crestal collapse, which was controlled by crestal faults generating multiple small-scale faults dipping to the east. West-dipping fault arrays kept propagating at this stage. Stage 3 - Late evolution stage of faults, with both fault systems intersecting each other to form an accommodation zone.

.
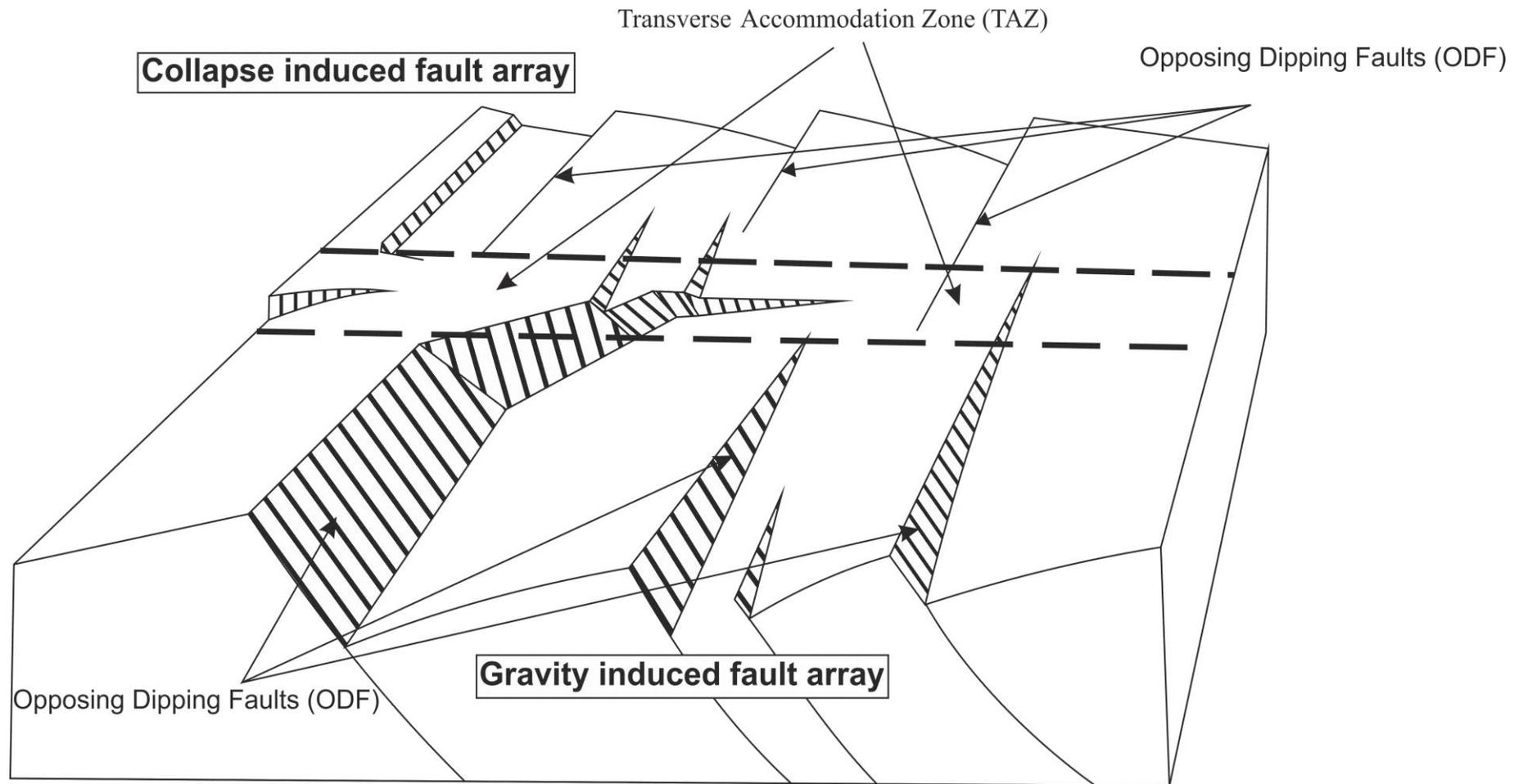
Fig. 4-17 Schematic 3D panel highlighting the relationship between the transverse accommodation zone (TAZ) and crestal faults in the study area. The strike directions of the accommodation zone and faults are nearly perpendicular.

Chapter 5

Localised strata-bound domino faulting offshore Espírito Santo (SE Brazil): The case for sudden release of fluid in salt-withdrawal basins

Abstract

Hydraulic-driven faults and fractures comprise important subsurface fluid flow pathways, yet their seismic expressions are still poorly documented. This chapter uses high quality 3D seismic data to investigate curved, strata-bound domino style faults above which a pockmark field is observed and interpreted as being associated with their formation. The faulted layer covers an area of 24 km^2, for a thickness of ~ 100 m. Faults show a concentric pattern with an average fault spacing of 120 m, while fault throws are ~ 10 ms TWT. Apart from the strata-bound domino faults, and associated pockmarks field, random pockmarks in the study area indicate episodic fluid flow. In contrast to vertically stacked pockmarks, random pockmarks are interpreted to have formed in association to rapid burial of continental slope strata, resulting in the elevation of fluid pressure in underlying soft sediment. Strata-bound domino faults were formed due to overpressure build-up and release in a mud-dominated sequence, with their geometry responding to the local dip of the salt-withdrawal basin in which they occur. Further overpressure build-up resulted primarily from fluid migration through underlying crestal faults, and secondarily through capillary permeability within permeable strata. This chapter concludes that strata-bound domino faults are a typical feature of fluid flow on salt-rich continental margins. During their formation, strata-bound domino faults form significant conduits for migrating fluid into soft, porous strata, away from regional and local structural traps.

5.1 Introduction

The recognition of sub-surface fluid flow features is key to a complete understanding of the hydrocarbon potential of sedimentary basins (Sun et al., 2012a, Hunt, 1990). The seismic expression of fluid flow commonly includes amplitude anomalies (bright spots), dim spots, flat spots, phase reversals, reduced or increased seismic reflection continuity, and Bottom Stimulation Reflectors (BSRs) (Cartwright, 2007; Løseth et al., 2009). Other features of interest include pockmarks, mud volcanoes, sand injections, gas hydrates, gas chimneys, pipes, sediment injections, carbonate mounds, polygonal faults, seeps and related diagenetic phenomena (Andresen, 2012). Fluid flow in sedimentary basins is often associated with excess pore pressure (Osborne and Swarbrick, 1997; Mourgues and Cobbold, 2003; Flemings, 1998; Dugan and Flemings, 2000; Crutchley et al., 2013; Guo et al., 2016). In addition, disequilibrium compaction, tectonic compression, aquathermal pressuring, dehydration reactions, hydrocarbon generation, hydrocarbon migration, and thermal cracking of oil to gas, are common processes generating excess pore pressure in sedimentary basins (Guo et al., 2016; Tingay et al., 2009; Guo et al., 2011; Guo et al., 2010; Tingay et al., 2007). Combinations of these mechanisms are often revealed in the form of overpressured compartments in subsurface strata.

An interesting and vital question, when investigating fluid flow in sedimentary basins, is whether excess pore pressure within a specific compartment is a function of *in-situ* or external fluid sources. Overpressure typically builds-up close to where fluid is generated (Swarbrick and Osborne, 1998; Bowker, 2007). However, overpressure in sedimentary basins is often transferred between pressure compartments by means of active faulting or fracturing (Grauls and Baleix, 1994), giving rise to 'vertically transferred' overpressure (Tingay et al., 2007).

The present study focuses on a highly faulted area located on top of a main salt diapir in SE Brazil (Fig. 5-1), where crestal faults formed with small lengths and throw values (Morley, 2007; Alves, 2012). The growth history of crestal faults is known to be closely associated with salt growth and withdrawal and, consequently, they present more complex propagation and reactivation patterns than other types of faults (Ze and Alves, 2016). The uniqueness of crestal faults, which are often formed by segment linkage and

are partly reactivated, make their evaluation as local sealing structures as essential to hydrocarbon exploration and production. Other important structures in this chapter are the so-called domino or domino-style faults. The concept of 'domino faults' was first introduced by (Mandl, 1987), who described their formation as similar to a series of books (or domino pieces) toppling over a shelf. Domino fault systems comprise a series of sub-parallel faults that rotate during extension (Buchanan and McClay, 1992). Prior to the definition of the term 'domino faults', this phenomenon had been recognised over a century (Axen, 1988).

Both physical models and outcrop analogues have been previously used to explain the evolution of domino fault systems (Nur et al., 1986; Axen, 1986; Stewart and Argent, 2000a, Maloney et al., 2012), but previous studies are often based on the analysis of faults of large scales, with fault displacements of several kilometres and fault lengths of hundreds of kilometres (Maloney et al., 2012). Physical experimental models indicate that formation of domino faults results from both bed and fault rotation (Axen, 1986), a geometry often requiring a certain amount of local extension above a basal detachment (Nur et al., 1986; Axen, 1988; Buchanan and McClay, 1992; Mandl, 1987; McClay, 1990a, Maloney et al., 2012). In this chapter, the term 'domino faults' defines strata-bound sets of faults that are evenly spaced and dipping in the same direction. The mechanisms forming these strata-bound domino faults will be carefully examined.

This study shows an example, on high-quality 3D seismic data, of strata-bound domino faults that are distinct from those in Cartwright and Dewurst (1998). The high resolution of the interpreted seismic data permitted a detailed characterisation of this style of faults, including how they relate to other elements such as crestal faults, fluid flow features and local slope instability. As shallow fluid flow and leakage through faults is a prevalent phenomenon in many a salt-rich basin (Andresen et al., 2011; Andresen and Huuse, 2011; Vadakkepuliyambatta et al., 2013), this study will further examine the importance of strata-bound domino faults to fluid flow and overpressure build-up in a selected area of SE Brazil. Particularly, this chapter aims at:

a) Documenting a set of domino faults that is strata-bound and associated with fluid flow features;

b) Examining the character and mechanisms of formation of the investigated domino faults;

c) Assessing how the strata-bound domino faults can provide insights into fluid flow evolution of the Espírito Santo Basin and regions with similar halokinetic structures;

d) Understanding the role of crestal faults in the migration of fluid towards the surface, and towards the strata-bound domino faults investigated here.

This study is not only an important case-study for other strata-bound domino faults on continental margins, but also contributes to understanding how fluid flow evolves in salt-rich sedimentary basins.

5.2 Fault distribution and displacement analyses

Crestal faults in the study area are subdivided into four (4) zones based on their relative locations, heights, geometries and orientations (Ze and Alves, 2016; 2017) (Fig. 5-2). Faults in zone 1 are located within the area of the strata-bound domino faults (Fig. 5-2), showing a strike direction of E-W. All faults in Zone 1 dip to the North (Fig. 5-2). Faults in Zone 2 are located in the western part of the study area (Fig. 5-2). This group of faults is NE-striking, dipping to the SSE - near opposite trends to faults in Zone 1 (Fig. 5-2). Faults in Zone 3 are located between Zone 1 and 2, and are oriented NW-SE to NE-SW. Faults in Zone 3 are the so-called transfer faults that accommodate the stress rotation between faults in Zone 1 and Zone 3 (Schlische and Withjack, 2009). Faults in Zone 4 are located on the southern edge of the area with domino faults (Fig. 5-2). Faults in Zone 4 are parallel or near perpendicular to the edge of the area with domino faults (Fig. 5-2).

Thirty-four (34) faults in Zones 1 to 4 were selected in the study area for displacement analyses; faults 1A-1G, 2A-2I, 3A-3H, and 4A-4I in Zone 1 to Zone 4 respectively (Fig. 5-2).

Legends: So - Salt overhang   Sd - Salt diapir   PM - Pockmark   Rfs - Radial faults   Pfs - Polygonal faults   Cfs - Concentric faults

Fig. 5-1 Variance maps of the study area show the structural configurations of salt diapirs, crestal faults and layer-bound domino faults in this study.
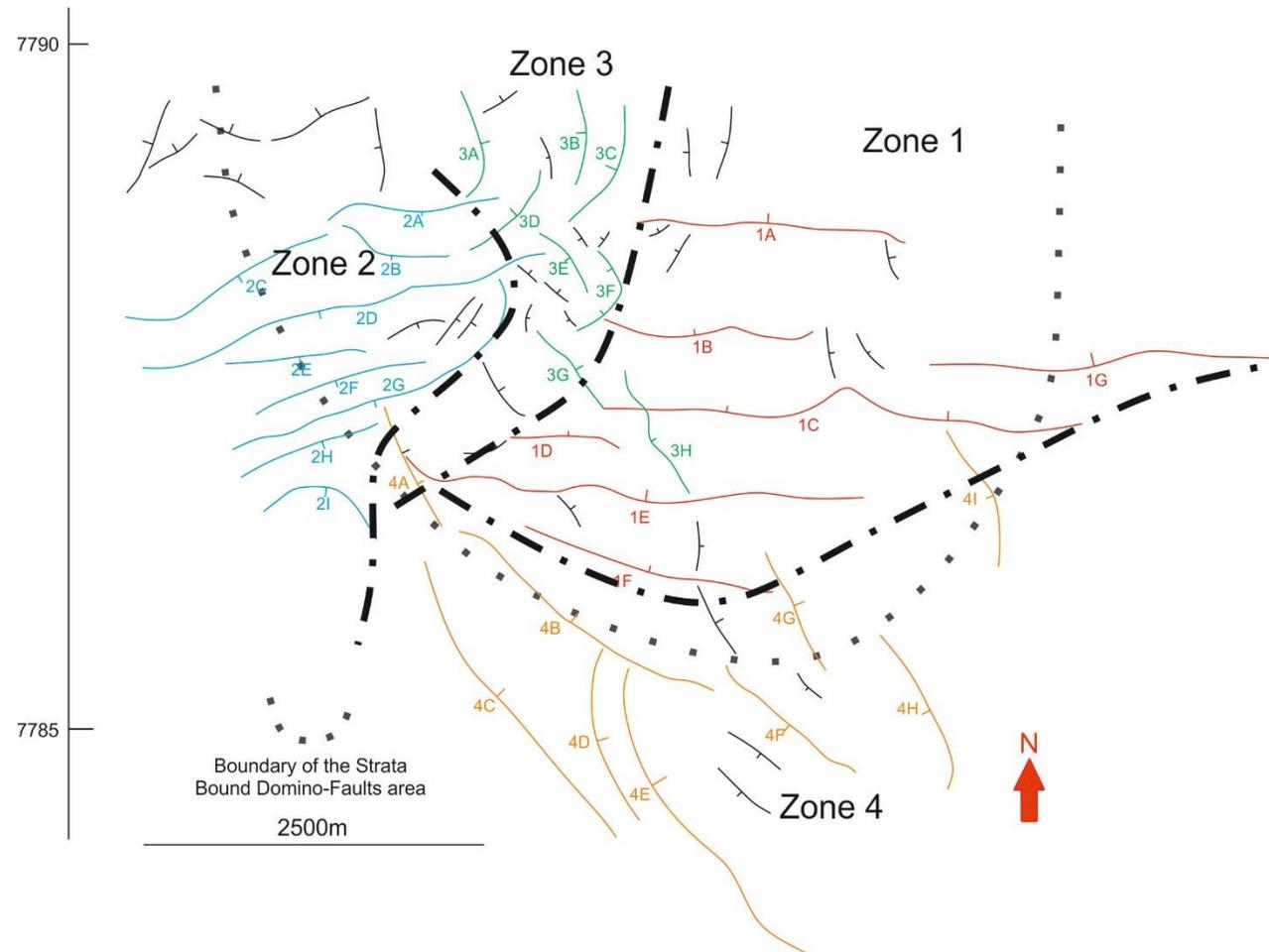
Fig. 5-2 Subdivision of faults into four zones (see Fig. 3-5 for horizon 4). Faults in Zones 1 and 2 dip mainly to the north and SSE, respectively. Faults in Zone 3 are near-perpendicular to faults in Zones 1 and 2, and faults of Zone 4 dip both to NE and SW.

146

5.2.1   Throw-distance (T-D) data

Throw-Distance profiles (Fig. 5-3) are used to identify fault segmentation (Baudon and Cartwright, 2008c), with multiple peaks being interpreted to have formed by the linkage of individual segments, either following the 'Isolated fault model' of Walsh et al. (2002) in which distinct fault segments propagate laterally and link up, or the model proposed by Ze and Alves (2016) in which one fault segment propagates to merge with other isolated segments in the same fault domain. Throw-distance (T-D) profiles showing broad top shapes with maximum throw values that diminish towards both tips (Lohr et al., 2008; Mansfield and Cartwright, 2001), indicate faults comprising only one fault segment. Faults in Zone 1 show maximum throw values ranging from 15 ms (TWT) to 40 ms (TWT). In terms of fault length, values vary from 750 m to 3750 m (Fig. 5-3). Faults 1A, 1D, 1F and 1G are interpreted as comprising only one fault segment (Fig. 5-3). Fault 1C, however, shows a peak throw value but is interpreted to have formed through the linkage of two separate fault segments as the maximum throw value is a peak point rather than a broad top (Fig. 5-3). The strike of faults 1B and 1C in Figure 5-2 clearly presents the linkage point of two fault segments as a sharp turn in strike direction. Faults 1B and 1E are interpreted to derive from the linkage of two separate fault segments (Fig. 5-3).

Maximum fault throw values in Zones 2, 3 and 4 vary from 20 ms to 70 ms, 10 ms to 20 ms and 10 ms to 35 ms, respectively (Fig. 5-3). Fault lengths vary from 750 m to 2000 m in Zone 2, 400 m to 1000 m in Zone 3, and 600 m to 2500 m in Zone 4 (Fig. 5-3). Faults 2C and 2D show the largest throw values in this area (Fig. 5-3). Faults in Zone 3 are also called transfer faults, which are located within the transfer zone formed by the two opposite dipping Zones (Zone 1 and 2) (Fig. 5-2). Faults developed in Zone 3 have smaller lengths and maximum throw values than other groups (Fig. 5-3).

5.2.2   Throw-depth (T-Z) data

Throw-depth (T-Z) plots for thirty-four (34) faults are used to characterise the reactivation histories of distinct fault groups. Non-reactivated faults commonly show C-

type or M-type throw-depth profiles, with faults tipping out in both up-tip and down-tip directions (Baudon and Cartwright, 2008c, Durogbitan, 2016b). Reactivated faults often present vertically stepped throw-depth profiles, and typical double-C throw-depth profiles (Baudon and Cartwright, 2008c). Profiles of the analysed 34 faults include C-, M-, skewed M-types (Fig. 5-4).

The throw-depth plots indicate two episodes of fault reactivation. The first episode occurred around the level of Horizon 3, a regional Eocene unconformity (Figs. 3-5 and 5-4) (Baudon and Cartwright, 2008c, Ze and Alves, 2016). The second episode occurred in association with Horizon a (Figs. 3-5 and 5-4). Throw-depth profiles for 1B-b and 1G-j suggest that these two faults were reactivated in the first episode. Throw-depth profiles for 1C-e, 1E-h, and 1F-i indicate that fault 1C (east segment), 1E and 1F were reactivated during the second episode (Fig. 5-4). Similarly, faults 2B (c), 2F (h and i) and 2H (m) in Group 2, 3D (d), 3H (h) in Group 3, 4D (e) and 4G (i) in Group 4 were only reactivated during the first episode (Fig. 5-4). Faults 3C (c) and 3F (f) of Group 3 and faults 4F (g) were reactivated during the second episode (Fig. 5-4). The only exception is fault 3G (g), which was reactivated twice (Fig. 5-4).

The depth in which the maximum throw depth of faults occurs can reflect the point of nucleation of faults (Barnett et al., 1987; Walsh and Watterson, 1987). From the analysed faults, maximum throws are located either around Horizon H3 or immediately below (Fig. 5-4). The only exceptions are faults 1A, 2G and 3E. Most of the faults were generated before the deposition of volcaniclastic strata in Unit 2 (Horizon 3 marks the boundary between units 2 and 3), leading one to consider that most of the faults were formed from Late Cretaceous to Paleocene. For reactivated faults, secondary maxima in throw are located above Horizon a, indicating that a significant number of faults were generated (and reactivated) during the Miocene (see for examples T-Z plots for faults 1C (e), 1E (h), 3C (c), 3F (f) and 3G (g)) (Fig. 5-4).
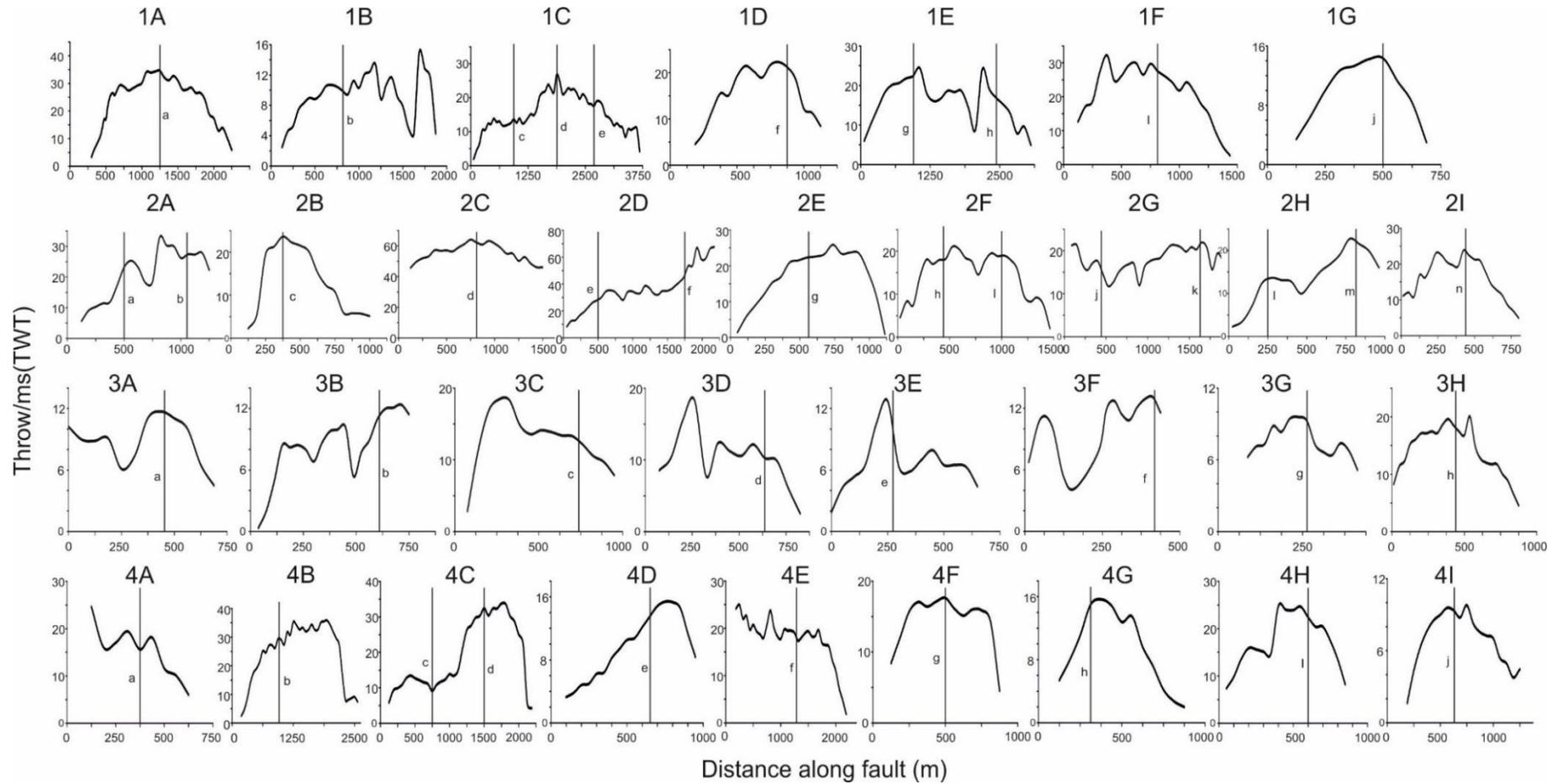
Fig. 5-3 Throw-distance (T-D) plots of the four groups of faults developed in the study area. Vertical lines on each T-D plot indicate the locations of the T-Z plots in Figure 5-4. Faults analysed in each zone indicate complex fault geometries and fault linkage patterns (Ze and Alves, 2016)
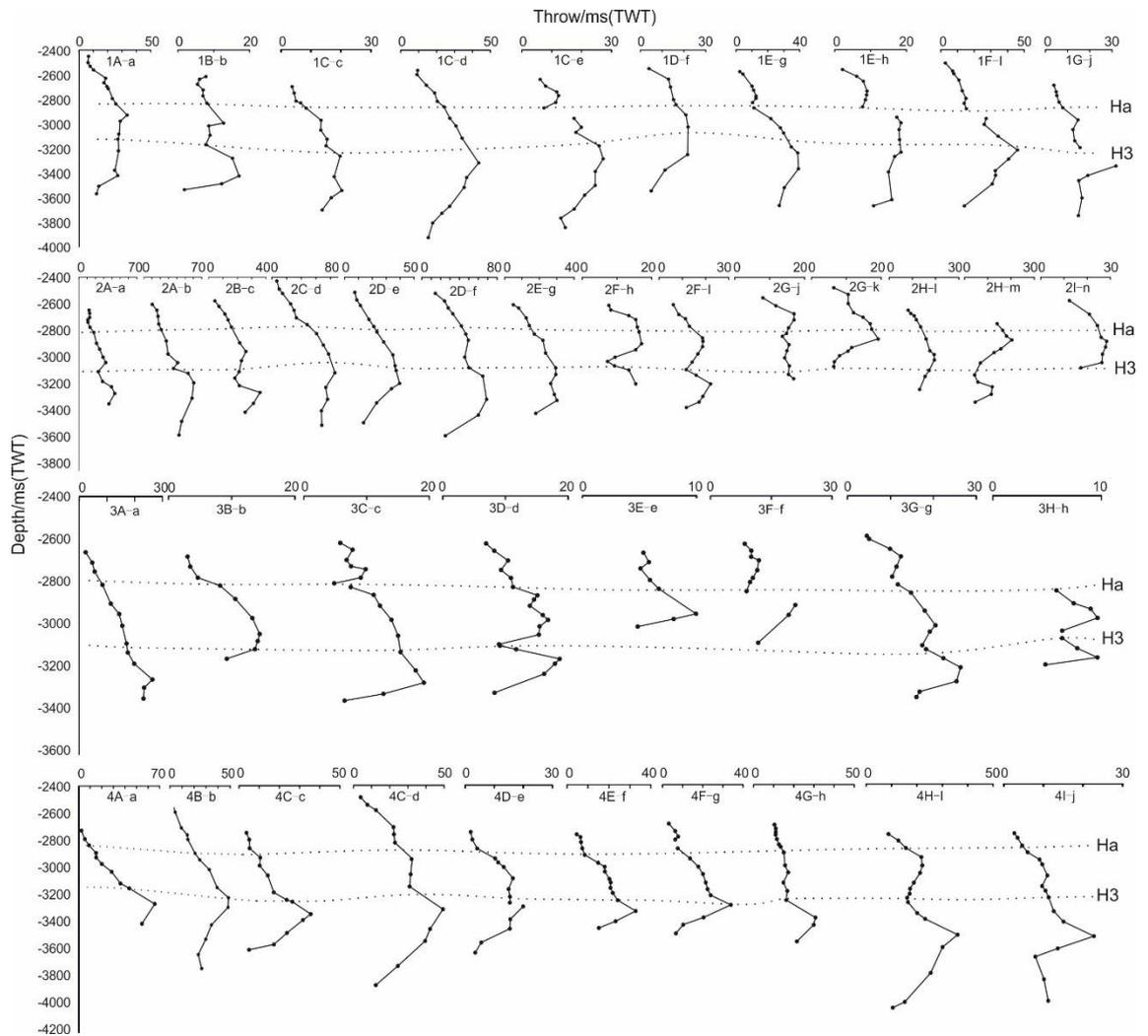
Fig. 5-4 Throw-depth (T-Z) plots for selected faults in the study area. Two episodes of fault reactivation are identified and marked by Horizons 3 and a. Horizon 3 represents an Eocene unconformity of regional significance across the SE Brazilian margin.

5.3 Slip tendency and leakage factors

To determine a regional stress tensor is impossible in the study area due to the fact that: 1) only one recorded earthquake focal mechanism exists in the Espírito Santo Basin, which is close to the Victoria-Trindade High (Heidbach, 2016); 2) limited seismological coverage in the study area, and 3) low number of stress measurements for SE Brazil's offshore basins (Lima et al., 1997). Furthermore, post-salt deformation is considered to be gravitationally driven, and independent of any basement tectonics (Demercian et al., 1993). The faulting styles in the study area all point towards an extensional regime on crest of the salt structures. Stress inversions for a set of faults in the study area confirm the interpretation of Chang et al. (1992) and is in consistence with the inversion result by Mattos et al., (2018) by computing a sub-vertical σ1 plunging -69.7° along an N115.9° azimuth (Table 5-1). A sub-horizontal σ3 plunging 18.7° along an N92.2° azimuth was also estimated. Considering that halokinesis resulted in the development of faults with different preferential strike directions, results from each of the zones are computed with stress inversion to perform slip tendency and leakage factor analysis (Figs. 5-5 and 5-6). Stress inversions in zone 1 indicate a sub-vertical σ1 plunging -58° along an N102.3° azimuth and a sub-horizontal σ3 plunging 30.8° along an N84.6° azimuth (Table 5-1).

Normalised slip tendency for all the faults varies from 0.0 to 0.67 (Fig. 5-5). Faults in Zone 3 and Zone 4 indicate larger slip tendency values than faults in Zone 1 and Zone 2, with strata-bound domino-faults showing the minimum values (Fig. 5-5). Despite the observation that faults in Zone 4 show larger values, the results clearly show that the upper parts of faults in Zone 4 have higher slip tendency than the lower parts (Fig. 5-5). In Zone 2, specific parts of faults show larger slip tendency values than others (Fig. 5-5).

In terms of the leakage factor, which is a parameter indicating fluid transmissivity of faults (Morris et al., 1996), the inversion indicates that with an assumption of hydrostatic pore pressure, the values vary from 0.0 to 0.7, with most of the values are between 0.0 to 0.4 (Fig. 5-6). In Zone 1, parts of the faults indicate far higher leakage factors than others (Fig. 5-6). Fault 1C, which is segment linked by two fault segments, shows larger leakage factor at the point of segment linkage (Fig. 5-6). Faults in Zone 2 all indicate smaller leakage varying between 0.0 and 0.4. Faults in Zone 3, to the north,

shows small values, however, faults 3G and 3H show greater values (Fig. 5-6). Faults in Zone 4, similar to faults in Zone 1, show smaller leakage factors (Fig. 5-6).

Through slip tendency and leakage factor analyses, it is suggested in this thesis that faults in Zones 3 and 4 accommodate most of the strain and stress in the study area. However, Faults in Zone 1 and Zone 3 are the structures most prone for fluid to leak (Figs. 5-5 and 5-6).

Area	$\sigma 1$		$\sigma 2$		$\sigma 3$	
	Plunge	Azimuth	Plunge	Azimuth	Plunge	Azimuth
Total area	-69.7°	N115.9°	-7.6°	N4.7°	18.7°	N92.2°
Zone 1	-58°	N102.3°	8°	N7.5°	30.8°	N84.6°
zone 2	-69.7°	N115.9°	-7.6°	N4.7°	18.7°	N92.2°
zone 3	-73.5°	N222.7°	-2.9°	N122.8°	16.2°	N211.9°
zone 4	-73.1°	N147°	0.6°	N59.1°	16.9°	N149.3°

Table 5-1 Stress inversion values obtained considering the total number of faults and each fault family. Results from paleostress inversions indicate that a sub-vertical $\sigma 1$ and sub-horizontal $\sigma 3$ predominate in the study area.

5.4 Evidence for fluid flow on seismic data

Buried pockmarks comprise the most significant fluid flow features, which are further divided into two categories as randomly distributed pockmarks (RPs) and non-random pockmarks (NRPs) (Riboulot et al., 2013; Pilcher and Argent, 2007). Non- random pockmarks comprise a field of pockmarks at the level of Horizon H5 (Fig. 5-7a). The field show pockmarks with diameters that do not exceed 100 m. Randomly distributed pockmarks include vertically stacked pockmarks and single isolated pockmarks (Figs. 5-8 to 5-11).
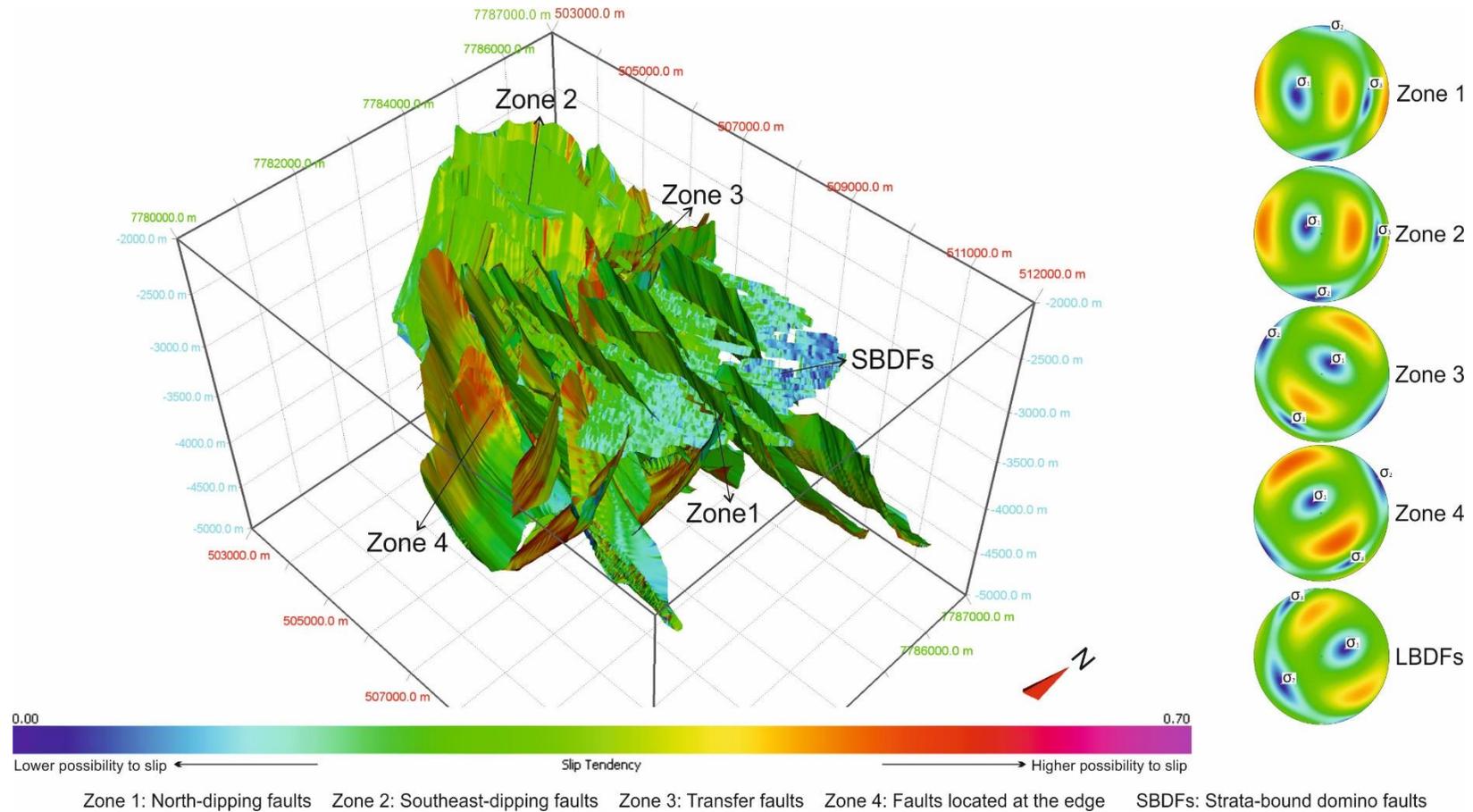
Fig. 5-5 Slip tendency data for the faults in the study area. Faults in Zones 3 and 4 show larger slip tendencies than faults in Zones 1 and 2, with strata-bound domino faults revealing the smaller values of slip tendency. In Zone 2, specific parts of faults show larger slip tendency than others. The upper parts of faults in Zone 4 have higher slip tendency than their lower parts.

153
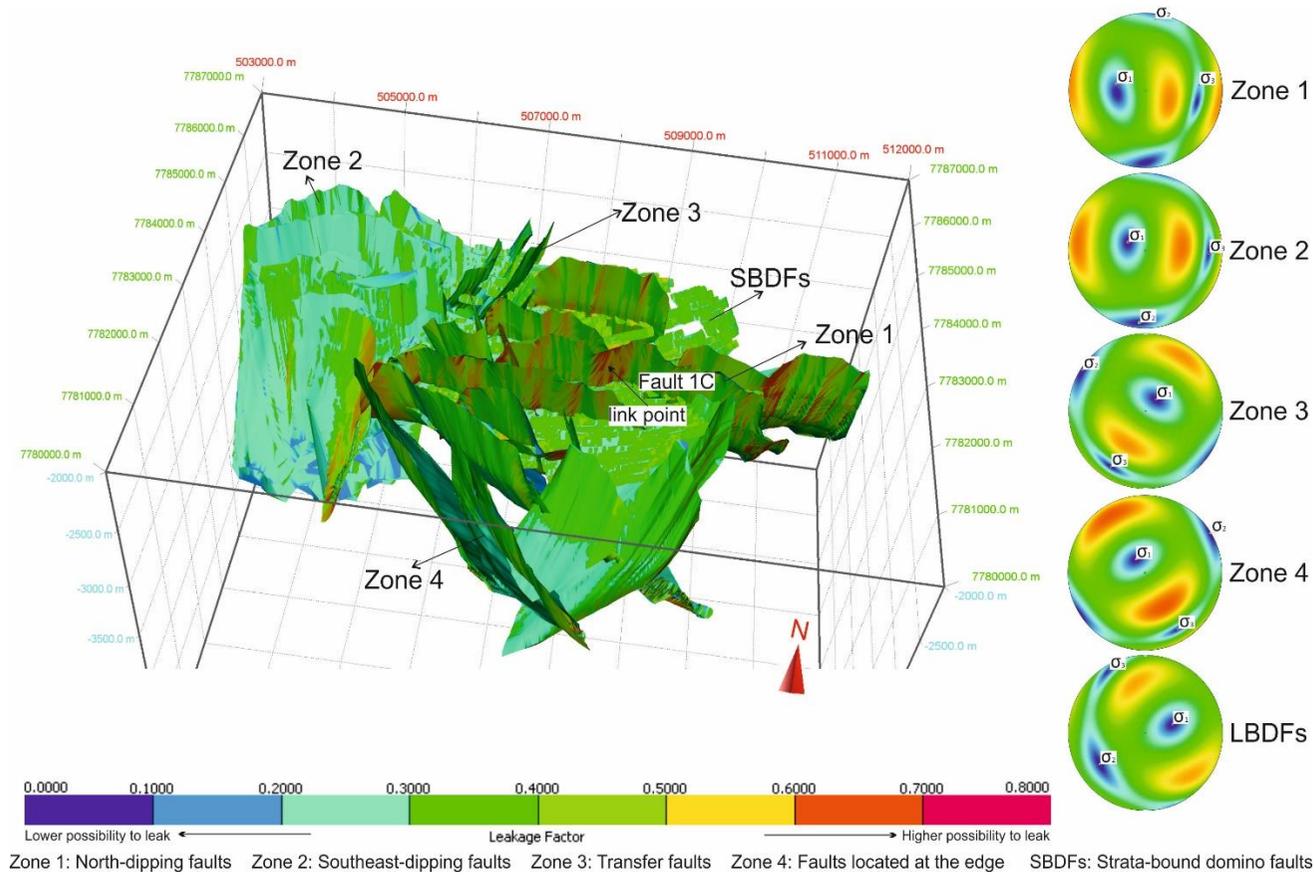
Fig. 5-6 Leakage factor analysis for the faults developed in the study area. Leakage factors of faults in Zones 2 have small values when compared to faults in Zones 1 and 4. In Zone 1, parts of the faults indicate relatively higher leakage factors, especially at the linkage point with fault 1C. In Zone 3, Leakage factors of faults to the south have higher values when compared to the faults visible to the north

154

5.4.1 Pockmark field (non-random pockmarks)

The roots of the pockmarks cannot be clearly defined on the seismic data, but a significant number is rooted in the fractured layer (Horizon 5 in Figure 5-8). In this latter case, the source of fluids forming these pockmarks also coincides with this densely fractured layer (Hovland and Judd, 1988; Pilcher and Argent, 2007; Judd and Hovland, 2007). The diameters of these concentrated (i.e. non-random) pockmarks range from a few 10s meters to a maximum of 100 m, showing circular to sub-circular shapes (Fig. 5-7b).

The observation that the pockmarks are rooted in the strata-bound domino faults indicates the source of the fluids forming these pockmarks is the same (Riboulot et al., 2013). In addition, the pockmarks are markedly buried at the same level at Horizon 5 (Figs. 5-8 and 5-9).

5.4.2 Randomly distributed pockmarks (RPs)

Randomly distributed pockmarks occur in the northern part of the study area (Figs. 5-8 to 5-11). Single isolated mega-pockmarks (Fig. 5-8, 5-10 and 5-11) and vertically stacked pockmarks are observed in this region (Figs. 5-8 and 5-9).

The single pockmark shown in Figure 5-8 is ~ 500 m in diameter, making it a mega-pockmark (Pilcher and Argent, 2007). The root of the pockmark is located between adjacent faults (Fig. 5-8). The top of the pockmark has a gentle expression on the modern sea floor (Fig. 5-8), which leads us to infer that the pockmark is still active at present, with fluid being released on the sea floor. Pockmarks 1 and 2 root into a transparent layer, which played an important role as a fluid-bearing interval at this stage (Fig. 5-8). Pockmarks 2 and 3 are separated by a high-amplitude, positive seismic reflection (Fig. 5-8). Pockmark 3 migrated back towards salt diapir 1 (Fig. 5-8). The top of pockmark 3 is filled by MTDs (Fig. 5-8). Pockmark 4 is located below the MTDs in sub-unit 3a (Fig. 5-8).
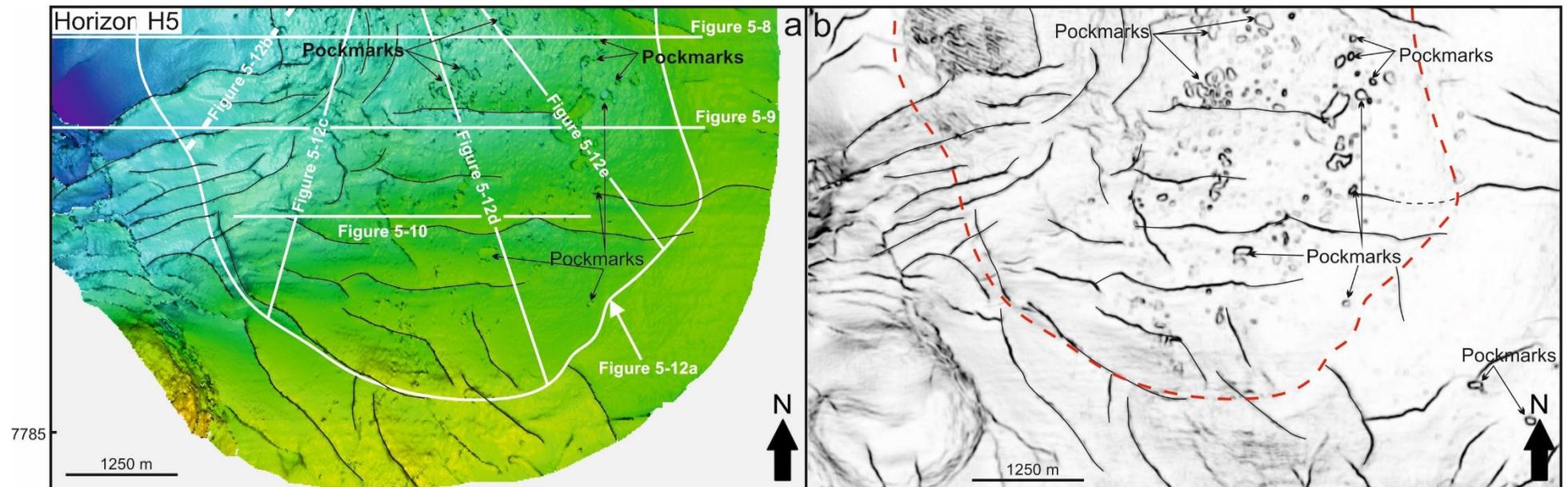
Fig. 5-7 a) Surface map of seismic horizon 5 showing a pockmark field. b) Variance maps reveal this same pockmark field. Pockmarks show circular to sub-circular shapes with diameters ranging from 30 ft (~ 10 m) to 330 ft (100 m). The area of the pockmark field is limited within the red dotted line (mainly coinciding with Zone 1), which also represents the area of the TBFs.

156
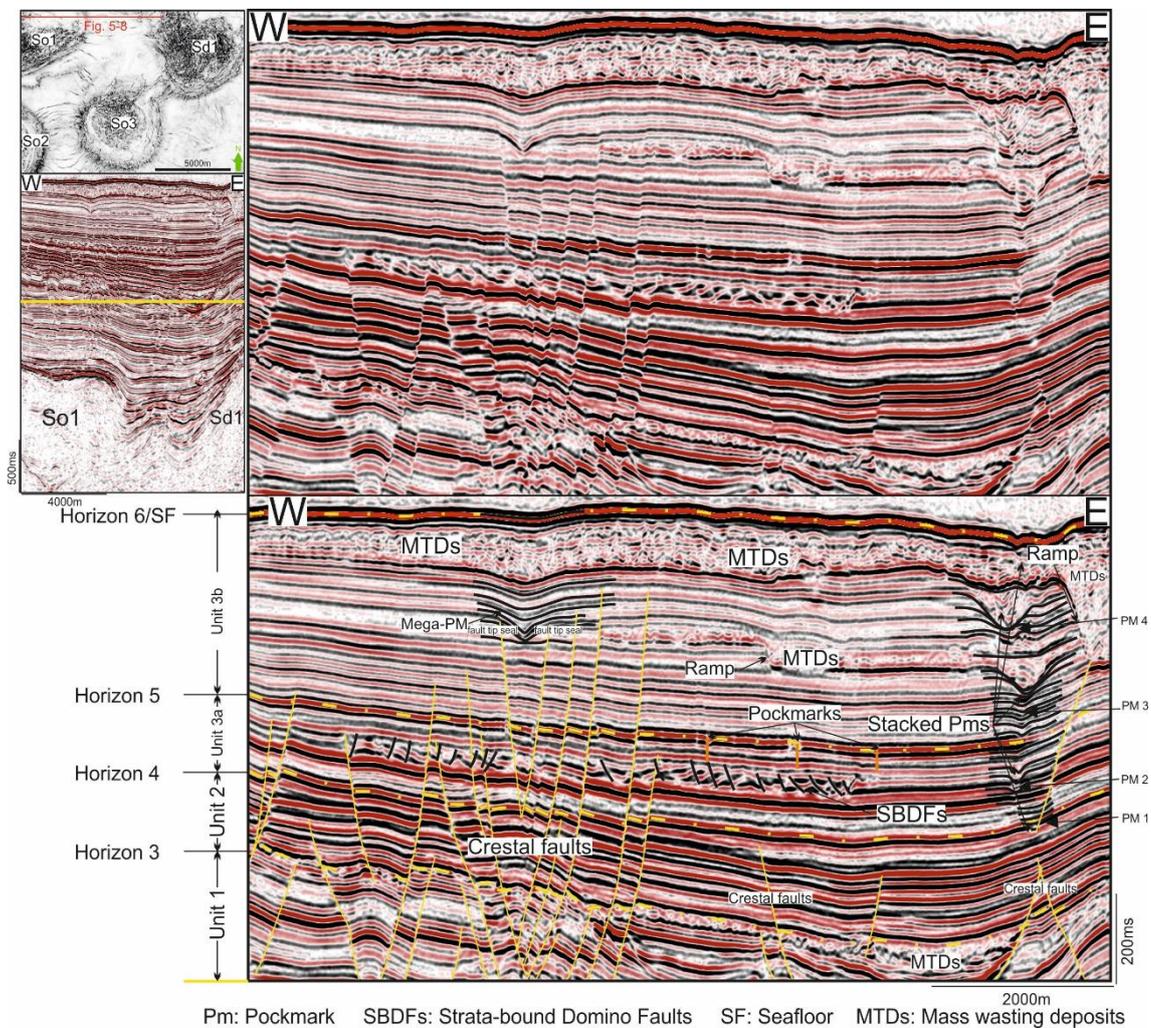
Fig. 5-8 Random pockmarks observed in the study area. Uninterpreted (above) and interpreted (below) seismic sections. Vertically stacked pockmarks are located at the edge of Sd1. Each of the vertically stacked pockmarks is rooted into a transparent interval. The mega-pockmark identified in the figure is located in the central of the crestal fault system, with its root located within two crestal faults.
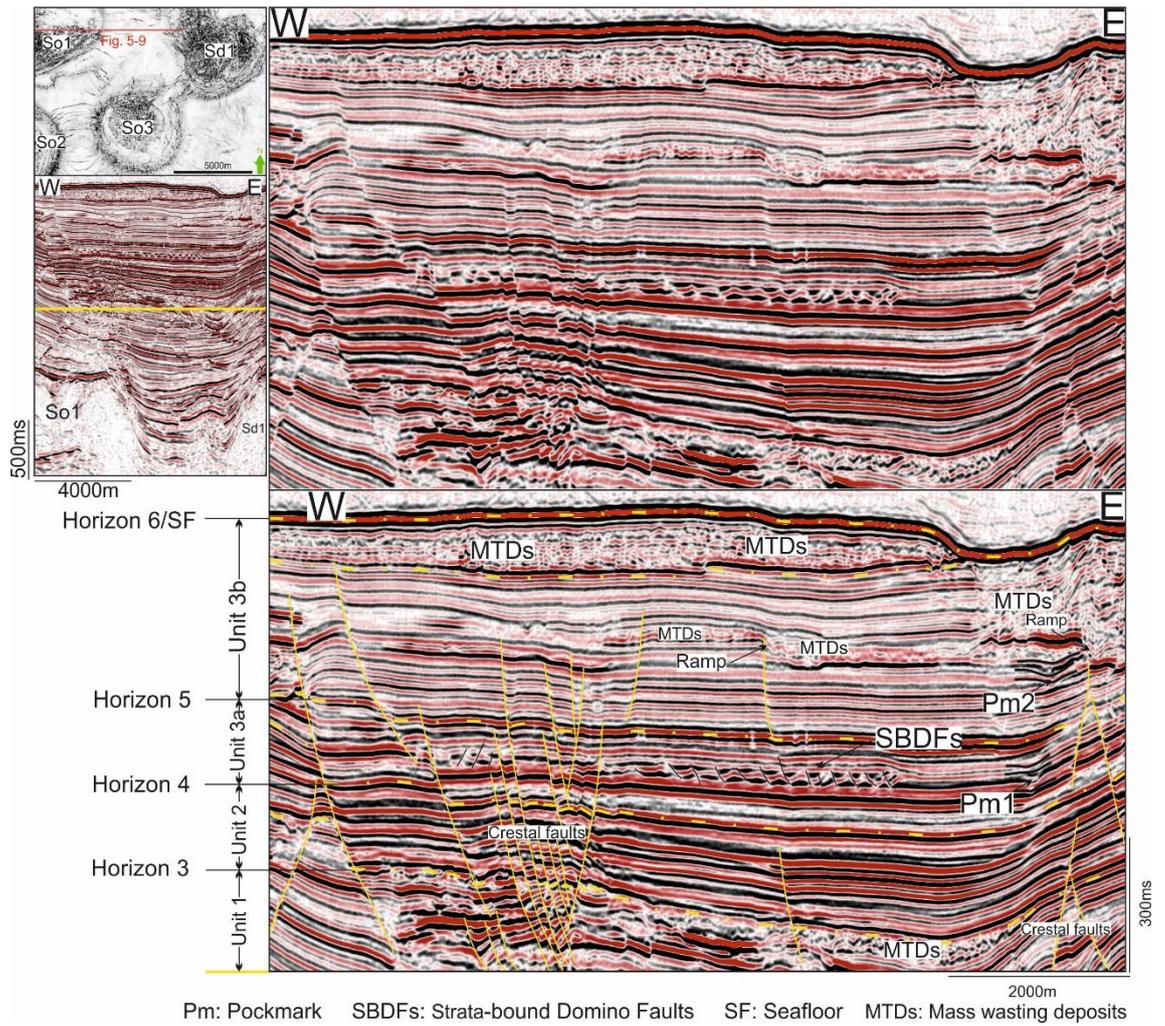
Fig. 5-9 Random pockmarks observed in the study area. Uninterpreted (above) and interpreted (below) seismic sections. The pockmarks identified are located at the edge of Sd1, which are rooted in a transparent layer in the study area.

Pockmark 1 in Figure 5-9 is rooted into a transparent layer (Fig. 5-9), suggested here as comprising the source layer for fluid escaping through the pockmark. The top of pockmark 2 (Fig. 5-9) is buried by the MTD that is interpreted to be the same as the one that buried pockmark 3 in Figure 5-8. Mega-pockmarks identified in Figures 5-9 and 5-11 have similar diameters of ~ 300 m (984 ft). Mega-pockmark 1 in Figure 5-10 and mega-pockmark in Figure 5-11 show high-amplitude reflections, which are identified as bright spots, an indicator of migrating fluid at present (Figs. 5-10 and 5-11). Mega-pockmarks 2 and 3 in Figure 5-10 show chaotic internal reflections, which are filled with MTDs (Fig. 5-10). Similar to the mega-pockmark interpreted in Figure 5-8, the roots of mega-pockmark 1 in Figure 5-10 and pockmark in Figure 5-11 are also located between adjacent faults, with faults acting as seals for fluid flow (Fig. 5-10).

Observed on seismic sections, the thickness of the fractured layer is thicker than the adjacent sediments, which indicates under-compaction of the domino-fault layer (Figs. 5-12c and 5-12d). The domino faults are slightly curved in map view (Fig. 5-12). Not all the faults are apparently listric as they have small throws and displacements. However, the fault blocks are highly rotated on all seismic sections (Figs. 5-12a and 5-12d). The internal character of this densely fractured layer shows a strong and continuous seismic reflection, interpreted to be horizon c (Fig. 5-12)

5.5 Fault growth and reactivation histories

Faults interpreted in this chapter are typically crestal faults with small lengths (< 2500 m) and throw values (< 50 ms TWT) (Figs. 5-3 and 5-4) (Alves, 2012; Morley, 2007). Two episodes of fault reactivation are identified in the study area, in agreement with a previous study by Ze and Alves (2016). The first episode of fault reactivation is identified around H3, which is a main regional unconformity in the study area (França et al., 2007) (Fig. 5-4). This episode of fault reactivation, however, is postulated to be closely associated with local halokinesis likely induced by enhanced overburden loading by Unit 2 (Fig. 3-5). The second episode of fault reactivation is identified by Horizon a (Fig. 5-4). This episode of fault reactivation suggests a close relationship with the formation of the strata-bound TBFS, which was putatively formed by reactivation (uplift)
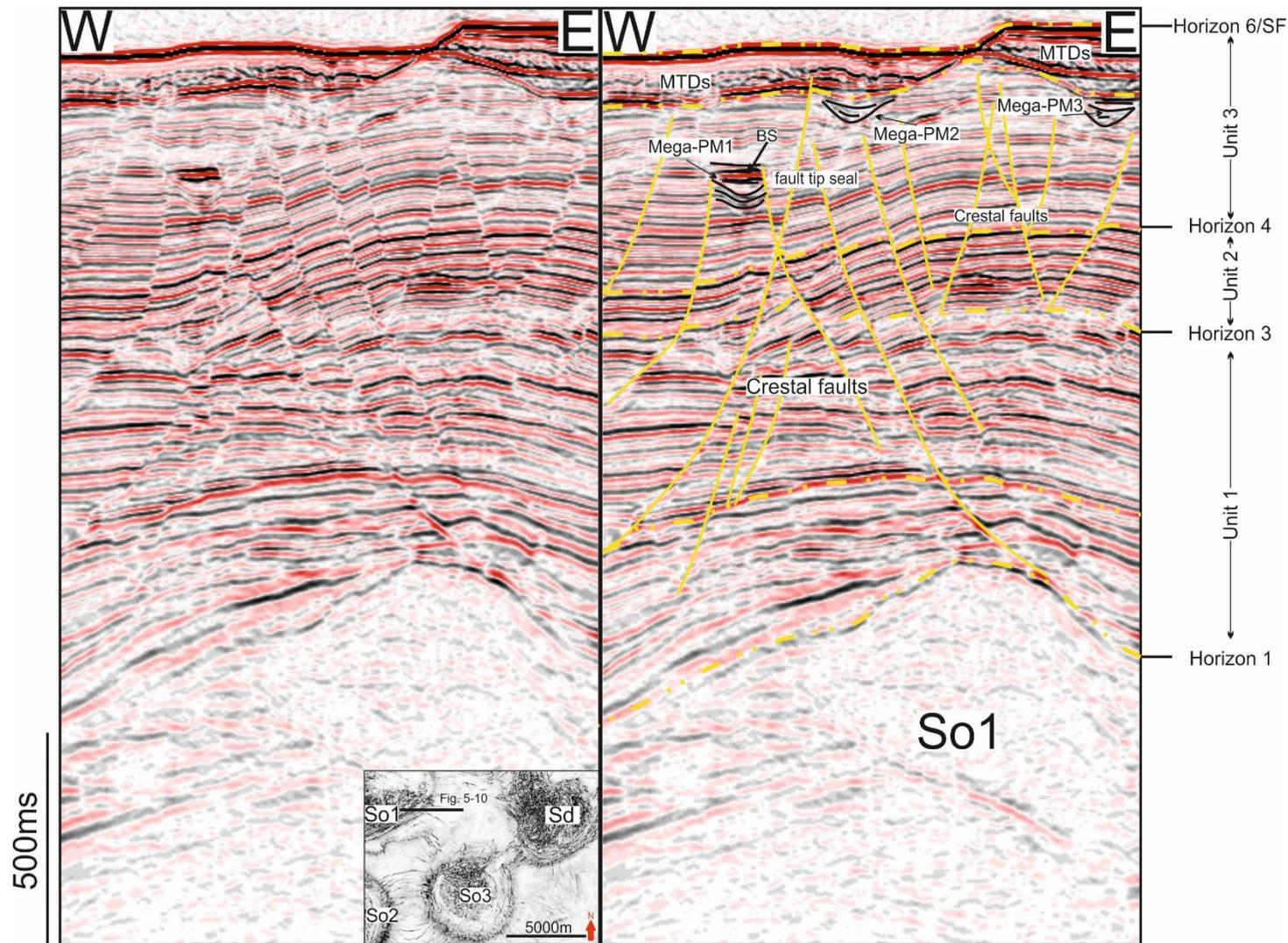
Fig. 5-10 Random pockmarks observed in the study area. Uninterpreted (left) and interpreted (right) seismic sections. Pockmarks are defined as mega-pockmarks with diameters of ~ 300 m. Mega-pockmark 1 shows high-amplitude reflectors, which is defined as bright spot, indicating the existence of fluid. The root of mega-PM1 is located between adjacent crestal faults, which also act as seals for fluid flow. Mega-PM2 and mega-PM3 are filled with MTDs showing chaotic internal reflections.

Pm: Pockmark   SF: Seafloor   BS: Bright spot   MTDs: Mass wasting deposits
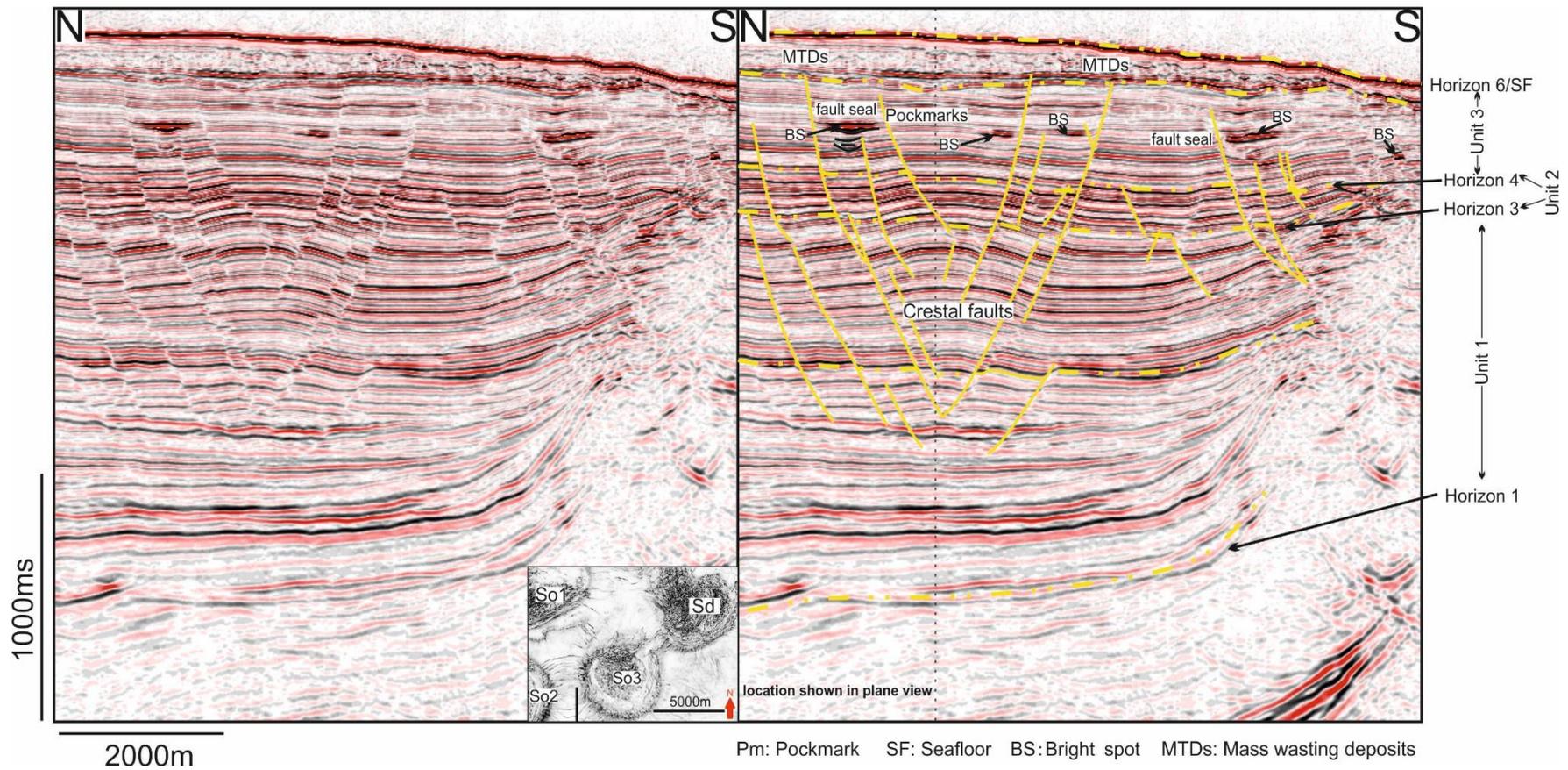
Fig. 5-11 Random pockmarks observed in the study area. Uninterpreted (left) and interpreted (right) seismic sections. The pockmark is defined as a mega-pockmark with a diameter of ~ 300 m. The pockmark is filled with fluid-saturated strata, which show high-amplitude reflections, or bright spots. Bright spots are observed in this area, with faults forming local seals, i.e. fault-related structural traps for fluid.
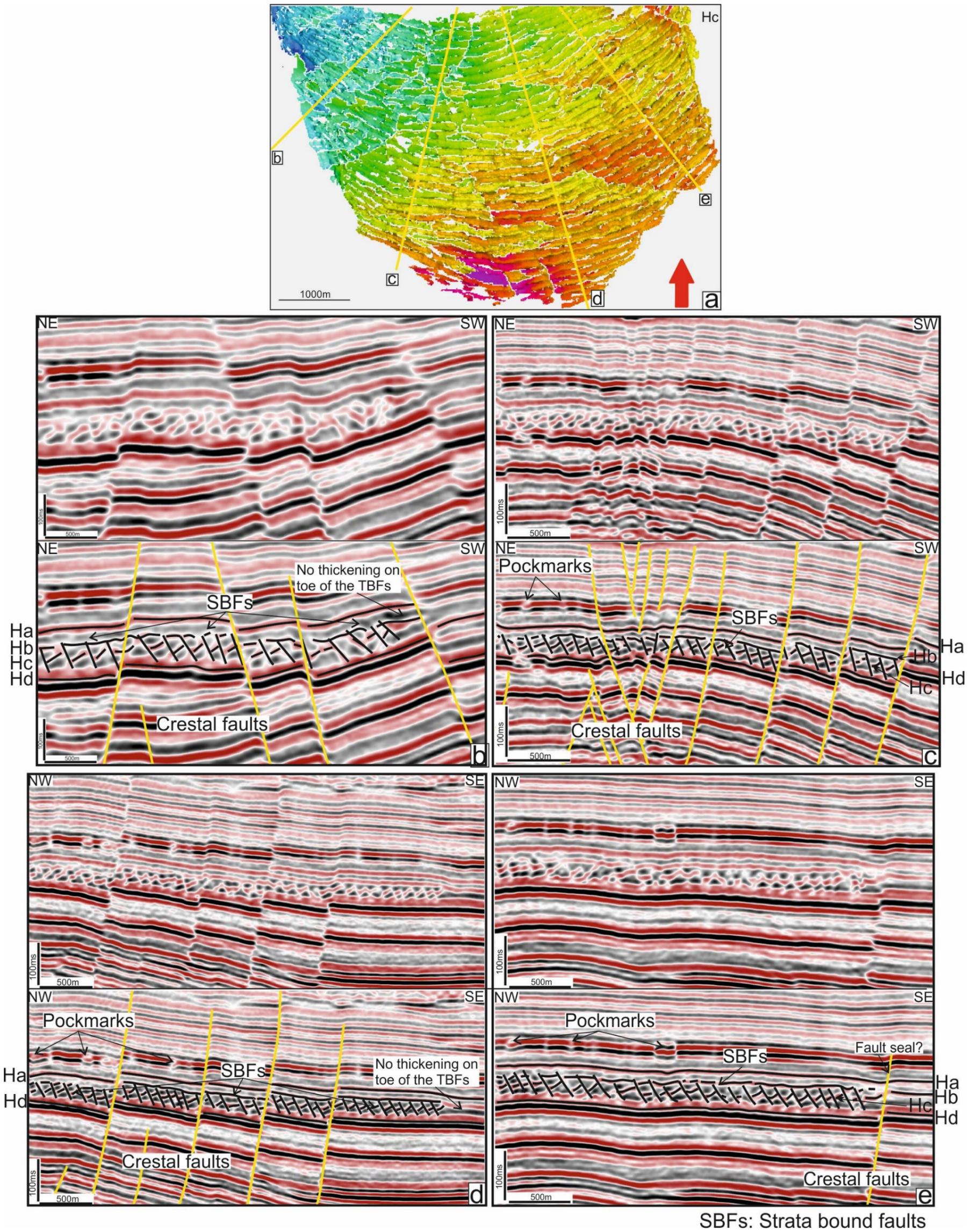
Fig. 5-12 Map view and seismic sections perpendicular to the strike directions of the strata-bound domino faults. a) Seismic horizon c. b-e) Seismic sections perpendicular to the strike directions of the strata-bound domino faults.

of strata flanking an adjacent salt diapir (Fig. 5-1). With the second episode of fault reactivation, some of the crestal faults were reactivated and propagated through the TBFS (Fig. 5-8).

Fault slip tendency and leakage factor values indicate that faults in Zone 3, identified as transfer faults, are prone to slip (Fig. 5-5). These faults are modelled reaching at the limit of horizontal data resolution (12.5 m). A fault plane can be rough, and the range of fault damage zone also has paramount influence in modelling fault sealing behaviours. Nevertheless, the results in this chapter indicate that faults that are developed within complex stress orientations often act as fluid leaking structures. Moreover, wherever isolated faults propagated and linked they become prone to develop a more complex damage zone, thus favouring fluid flow through these same regions (link point for fault 1C, for example) (Fig. 5-6).

5.6 Discussion

5.6.1   Triggering mechanism of strata-bound domino faults

Previous studies on extensional domino-style faults focused on either tectonic scales (Maloney et al., 2012; Gillard et al., 2016) or analogue models (McClay, 1990b, Axen, 1988; Buchanan and McClay, 1992; Mandl, 1987; Stewart and Argent, 2000b). The most prevalent of strata-bounded (tiered) extensional faults is expressed either as polygonal faults, or as the proximal areas of MTDs (Lonergan et al., 1998; Andresen, 2012; Gamboa and Alves, 2016).

In plan view, the faulting pattern in the ESB is similar to MTDs in which an extensional domino fault array can be observed in their proximal extensional domains (Gamboa and Alves, 2016). This observation supports the idea that the TBFS is associated with local slumping. However, comparing the internal seismic character of this system (Figs. 5-12b-e) to a typical MTD (Gamboa et al., 2010a, Omosanya and Alves, 2014; Gamboa and Alves, 2016) (see also MTDs interpreted in Figures 5-8 to 5-11), the TBFS shows continuous internal reflections with high- to moderate amplitudes (Hc in Figure 5-12). In addition, the thickness map of this same faulted interval (Fig. 5-13d) indicates no

major thickness variations (Fig. 5-12). If the studied TBFS were an MTD, chaotic internal reflections (Omosanya and Alves, 2013a), thickness variations (Gamboa et al., 2010a) and/or convergence zones at the toe of the strata-bound domino faults would be observed.

A second possible mechanism is buckling of strata-bound, brittle sediment during diapir growth, resulting in the generation of two sets of conjugate domino fault sets. Often, the dip and strike directions of faults generated by this mechanism follow a defined pattern that is associated with the shape of adjacent salt structures (Alves, 2012). Often, the salt structure is located at the centre of opposite-dipping fault arrays. When observing the studied domino fault system, no conjugate fault set can be observed both on planar view and on seismic sections (Figs. 5-1 and 5-12).

This chapter proposes that the likely triggering mechanism forming the strata-bound domino faults is local overpressure resulting from fluid flow and growth of salt overhang 1 (So1; Fig. 5-1). The first evidence that this fractured layer comprised an important pressure compartment is provided by the pockmarks field that lies above the faults, which is rooted into this same faulted interval (Figs. 5-8 and 5-9). The formation of the pockmarks field was due to disequilibrium compaction in this area with fast sedimentation resulting in excess pore water being kept in this layer. After the initial focusing of fluid flow through the pockmarks, they were buried also as a consequence of local subsidence due to the release of pressure within the undercompacted layer (Figs. 5-8 and 5-9). In a second stage, this interval was charged with fluid migrating through the underlying crestal faults. The crestal faults had not breached the layer by the time the domino faults were formed, as no hanging wall thickening is observed in this interval (Fig. 5-13b-d). Thus, after continuous fluid charging into this under-compacted interval, a second episode of excess pore pressure was generated. With the presumed growth of the adjacent salt diapir 1, crestal faults were reactivated (Fig. 5-4) and triggered a release of the excess pore pressure - resulting in the formation of the domino fault set. As the growth of the salt diapir tilted the sediments above, imposing a localised change in dip and steepened slope gradient in adjacent strata, the domino faults dips uniformly with the dip direction of the salt withdrawal basin surrounding diapir 1 (McClay, 1990b, Axen, 1988) (Figs. 5-12c and 5-12d).

Isochron maps of key seismic stratigraphic units
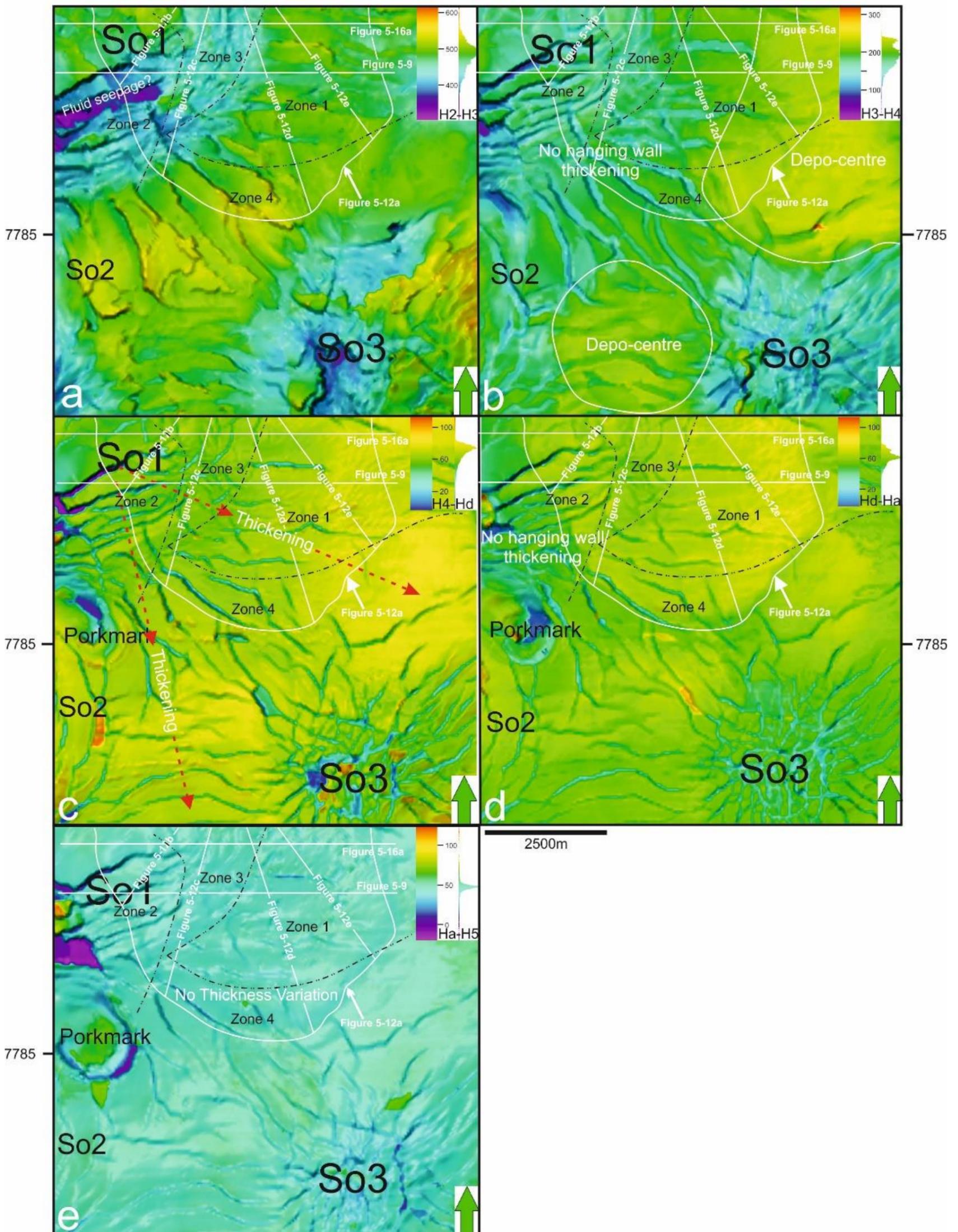
Fig. 5-13 Isochron maps of key seismic stratigraphy units. a) H2 to H3. Strata thickness in Zones 2 and 3 is smaller than in Zones 1 and 4. b) H3-H4. Strata thickness is the same in the four zones except for the eastern part in Zone 1, which is part of a depocentre, indicating a quiescent episode of salt overhang 1. c) H4 to Ha. Strata thickness increases slightly from Zone 2 to Zone 1, with the depocentre indicated in Figure 5-13b showing the largest thickness. d) Hd to Ha. Strata thickness inside the area with strata-bound domino faults shows little variation, but is larger than in adjacent areas. These thickness differences are interpreted to have formed by disequilibrium compaction between the faulted succession and adjacent (undeformed) strata. e) Ha to H5. No thickness variations in the study area, suggesting quiescent halokinesis.

A key question in this work is why all the faults are extensional and how the extension within this domino fault set was accommodated. Possible mechanisms of extension within a restricted sediment layer included dewatering process and block rotations (Cartwright, 1994; Axen, 1988; McClay, 1990b). Considering that the burial process might be of a minor importance to explain the local extensional features observed, except for excess pore pressure release, dewatering process is of minor importance (McClay, 1990b), which is also proved with obvious block rotations observed on the seismic sections (Figs. 5-12b-e). Three key elements in forming a strata-bound domino fault system. Three key elements are: 1) a basal detachment, which in this study is Horizon d (Fig. 5-14), and below which a transparent unit indicates 'soft' strata, 2) an increased slope gradient, which in this case is caused by the slight inflation of salt overhang 1 (Fig. 5-1), and 3) excess pore pressure within the faulted layer in the studied case (Fig. 5-14).

5.6.2   Episodic fluid flow through supra-salt sediment

A minimum of three distinct episodes of fluid flow (Fig. 5-14) are identified in the study area. The first episode is marked by a field of pockmarks (Horizon 5, Figs. 5-7 to 5-9). High sedimentation rates and lithology variations are here considered as the reasons for local disequilibrium compaction during this first episode, contributing to the formation of overpressure within specific compartments (Sun et al., 2012b, Swarbrick and Osborne, 1998; Trincardi et al., 2004).

The second episode of fluid release is identified with the formation of the strata-bound domino faults (Figs. 5-8, 5-9 and 5-12). As discussed in the previous section, elevated pore pressure was key in the formation of strata-bound domino faults. As indicated by Luo (2015), repeated overpressure build-up and release is possible if the source of overpressure is maintained. After the release of excessed pore pressure within the under-compacted layer, pore pressure dropped back to hydrostatic level. Further pore pressure build-up is due to continuous fluid charging into this layer through the underlying crestal faults. During the charging process, crestal faults did not breach Unit 2, as proven by the absence of hanging wall thickness variations between Horizons H4 -

Hd and Hd - Ha (Fig. 5-13c and 5-13d). With continuous fluid charging into the interval of domino faulting, excess pore pressure was built in a second stage. With further salt growth, crestal faults were reactivated (Fig. 5-4), and formed conduits for fluid migration and overpressure build up.

Slip tendency for selected faults indicates that transfer and edge faults are most likely to slip and reactivate at a shallower burial depth (Fig. 5-5). Leakage factors indicate that faults in Zone 1, intersecting the overpressured interval, were responsible for the release of excess fluid pressures (Fig. 5-6).

The third episode of fluid flow in the study area is marked by a single giant pockmark (Fig. 5-8). The root of the pockmark is located within unit 3b, suggesting that the fluid forming this pockmark was sourced from the imaged crestal faults (Fig. 5-8).

Apart from the three main episodes of fluid flow, localised vertically stacked pockmarks in Figure 5-8 suggest episodic fluid flow within the salt-withdrawal basin. The vertically stacked pockmarks 1 to 4 in Figure 5-8 can be seen as four phases of localised fluid flow (Fig. 5-8). Phase 1 pockmark (PM1) root into a transparent layer, which played an important role as a fluid-bearing interval at this stage (Fig.5-8). Phase 2 pockmark (PM2) migrated away from salt diapir 1 (Fig. 5-8), with their root located in a transparent layer (Fig. 5-8). Phase 2 (PM2) and 3 (PM3) pockmarks are separated by a strong, positive seismic reflection (Fig. 5-8). Phase 3 (PM3) pockmarks migrated back towards salt diapir 1 (Fig. 5-8). The top of Phase 3 pockmark (PM3) is filled by MTDs (Fig. 5-8). The strong reflector separating PM 2 and 3, the MTD filled PM 3, the tilting pockmark flanks and the horizontal migrating pockmarks all indicate salt growth (or withdrawal) of salt overhang 1 (Figs. 5-1 and 5-8).

5.6.3   Fluid flow and their relationship with the TBFS and crestal faults

Faults act as both conduits and seals for fluids in sedimentary basins (Wiprut and Zoback, 2000; Berndt et al., 2003; Berndt and Gay, 2007; Gay et al., 2007; Seebeck et al., Davison, 1995; Manzocchi et al., 2010; Sirat et al., 2014). In parallel, the propagation of crestal faults suggests that crestal faults are often formed by the linkage of distinct fault
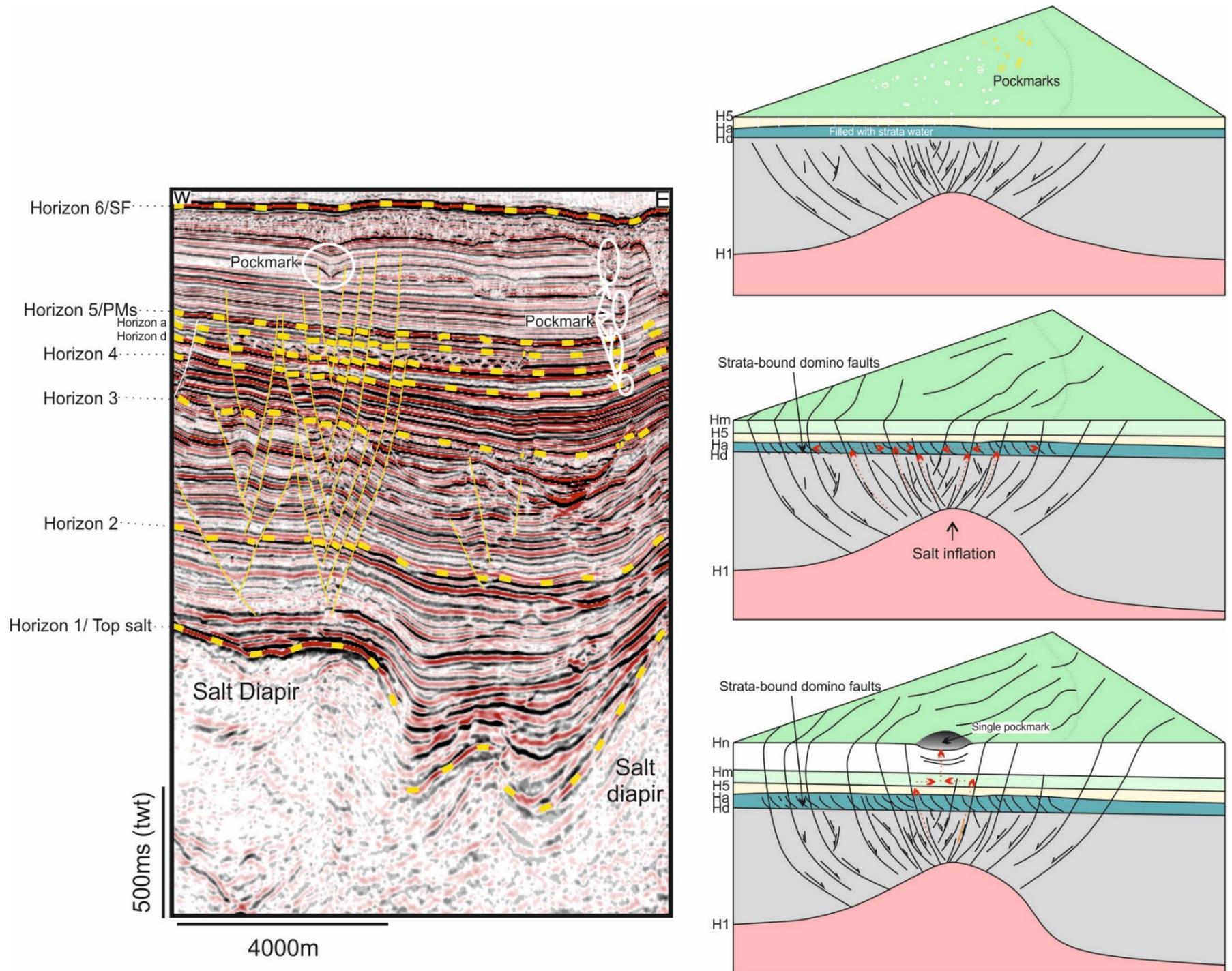
Fig. 5-14 Schematic model of episodic fluid flow for the study area. Phase 1) fast sedimentation within a restricted area caused disequilibrium compaction trapping in-situ fluid. With increasing pore pressure, fluid was released to form the pockmark field observed in seismic horizon 5 (Fig. 5-7); Phase 2) fluid charges into the previous overpressured layer, forming the second episode of excess pore pressure in this same layer. With subsequent salt growth, which triggered fault reactivation, fluid is released through the crestal faults. During this phase of fluid flow, the layer-bound domino faults were formed within the overpressured layer; Phase 3) after the second episode of fluid release, fluid continued to migrate upwards through the crestal fault system into overlying sediment. However, the tip of the crestal faults formed a local seal to upward-moving fluid flow, and fluid consequently accumulated in hanging-wall strata. The mega-pockmark formed at the centre indicates this process.

segments (Ze and Alves, 2016), especially in border faults within a crestal fault system (Ze and Alves, 2016; Randles, 2014; Mattos et al., 2016a). The analysis of fluid flow features indicates that a single crestal fault can either play as a seal or conduit. Continuous charging of fluids into the under-compacted layer, resulting in the second episode of fluid flow, stresses the fact that crestal faults form important conduits for deeper fluids migrating into shallower strata. In terms of fault seal, fluid-saturated infillings of mega-pockmark 1 in Figure 5-10 and bright spots interpreted in Figure 5-11 indicate that faults are significant seals to form structural traps in salt tectonics (Figs. 5-10 and 5-11). Slip tendency and leakage factor analyses demonstrate that faults in Zone 3 and 4 are most likely to reactivate, accommodating most the strain and stress in the study area (Figs. 5-5 and 5-6). In terms of leakage factor, the model shows that faults in Zone 1 are competent fluid pathways (Fig. 5-6).

The crestal faults in this study area were, therefore, both seals and conduits for fluid flow, depending on their geometry and the local stress conditions they were subjected to. However, if considering a crestal fault system as a whole, seal capability is a big question. The complexity of crestal fault growth (Ze and Alves, 2016) and episodic fluid migration indicate that crestal fault system is a negative seal system. Considering that not all crestal faults propagated vertically to reach the sea floor, detailed analysis of faults within a crestal fault system can offer possible insights into locating supra-salt reservoirs.

The triggering of crestal fault reactivation can be varied and include discrete phases of diapir growth, halokinesis and gravitational movements in salt (Omosanya and Alves, 2014; Alves, 2012). The analysis of the observed crestal fault system indicates that the reactivation of crestal faults can play as an important marker of fluid flow in salt tectonics and a possible marker for locating possible supra-salt reservoirs. In the studied case, the observed strata-bound fault is formed through pore pressure elevation within a supra-salt compartmentalization. The top tips of the crestal faults are located below Horizon 3 before the domino fault set formed. With the formation of the domino style fault set, excess fluid requires pathways to release that the crestal faults are reactivated, which offer the conduit which is essential to the formation of the domino fault set.

Chapter 6

Data sampling and its effects on the interpretation of normal faults' propagation and linkage

Chapter 6 is under review in Tectonophysics as Ze, T., and T. M. Alves. Data sampling and its effects on the interpretation of normal faults' propagation and linkage.

Abstract

Throw-distance (T-D) and throw-depth (T-Z) data are widely used to address the propagation histories of normal faults. This study uses high-quality three-dimensional (3D) seismic and outcrop data to review the effect of data sampling on the interpretation of normal faults' propagation and linkage. Results show that the accuracy of T-D and T-Z data, and of resulting fault slip tendency and leakage factor analyses, are strongly dependent on the sampling strategy followed by interpreters and field geologists, i.e. on a *Sampling Interval/Fault Length Ratio* (δ) for discrete faults. In particular, this work demonstrates that significant errors in T-D plots occur when a *Module Error Margin* (ε_i) for the ratio δ is larger than 6%-9% for faults of all scales and growth histories. With no prior knowledge on fault segmentation, a δ value of 0.05 should be applied when interpreting faults to fulfill the pre-requisite of a $\varepsilon_i < 6$-9 %, i.e. a minimum number of measurements should be gathered on discrete faults to produce T-D and T-Z plots, depending on fault length. The analysis shows that maximum δ value of 0.05 (throw acquired at regular distances that are < 5% of the fault length) should be applied to faults that are composed of distinct segments, whereas a maximum δ value of 0.1 (throw measured at a spacing < 10% of the fault length) can be applied to faults that comprise only one fault segment. With relatively low T-D ratios, smaller δ should be considered when sampling throw along faults via T-Z plots. In all faults analysed, slip tendency and leakage factors were systematically misrepresented with increasing δ values. A new tool for interpreters and structural geologists is presented here so as to understand the resolution limits beyond which they should interpret throw and displacement data. It is suggested that the interpretation of fault systems, either isolated or segmented, should work close to the δ and ε_i limits proposed in this work. Disregarding these limits will result in: 1) systematic disregard for the isolated fault growth model, 2) systematic misrepresentation of correct fault geometries and related damage zones, 2) the collation of unreliable fault scaling relationships, and 3) ultimately, in unreliable interpretations of fault sealing properties.

6.1 Introduction

Two end-member models explaining the growth of normal faults are the 'isolated fault model' (Childs et al., 1995; Walsh et al., 2002a, Walsh et al., 2003), and the 'constant length' fault model (Cowie and Scholz, 1992c, Cartwright et al., 1995; Morley et al., 1990; Jackson and Rotevatn, 2013b). In the isolated fault model, faults at distinct scales of observation are initially formed by discrete, isolated segments that propagate to link-up laterally with time (Walsh et al., 2003; Ze and Alves, 2016; Ze and Alves, 2017). In 'constant length' growth models, faults establish their near-final length at an early stage of their evolution, a phenomenon that is followed by fault propagation in a vertical direction, e.g. dip-linkage reactivation (Cartwright et al., 1995). The published literature argues that faults formed under the same geological conditions follow either of the two-end member fault growth models. However, as indicated by Fossen and Rotevatn (2016), the two end-member fault growth models might equally occur in the same region. Competing with these two fault growth models are faults with relatively large throw-length relationships, i.e. the increasing d_{max}/L ratio of Kim and Sanderson (2005). Constant d_{max}/L ratios can also be recorded by specific faults. Geometrical and kinematic coherence can be achieved for distinct fault segments through a combination of growth histories and geometries for distinct fault segments (Walsh et al., 2003; Mason et al., 2006). This means, in practice, that coherent faults can comprise segments that grow, at smaller scales, through any of the four growth models presented by Kim and Sanderson (2005).

A key step in the recognition of 'isolated' vs. 'constant length' end-member models is the identification of fault segmentation (and throw distributions) in 3D via the compilation of systematic T-D and T-Z data along the length of resolvable faults (Childs et al., 2005; Baudon and Cartwright, 2008a). The detailed identification of fault segmentation and reactivation has important implications for: 1) the correct understanding of fault propagation histories so to postulate proper fault growth models (Jackson and Rotevatn, 2013b, Baudon and Cartwright, 2008a, Giba et al., 2012), 2) the critical assessment of faults' sealing properties (Pei et al., 2015; Seebeck et al., 2014; Worum et al., 2004; Lohr et al., 2008), 3) the quantification of fault damage zones (Pei et al., 2015; Choi et al., 2015), 4) the assessment of seismic hazards (Zhang et al., 1991;

Pizzi and Galadini, 2009; Turko and Knuepfer, 1991), 5) locating ideal CO_2 storage sites (Jung et al., 2014), and 6) the study of sedimentation processes, drainage-systems' evolution and local palaeotopography (Booth-Rea et al., 2004; Hemelsdaël and Ford, 2016; Athmer and Luthi, 2011; Schlische and Withjack, 2009). Incorrect sampling strategies can also lead to gaps in information when analyzing scale relationships for faults of different scales, as shown by Kim and Sanderson (2001) and Torabi et al. (2004).

Key methods to identify fault segmentation and reactivation includes but not limited to: 1) the use of structural maps and seismic attributes of key intervals, e.g. RMS amplitude, seismic variance and coherence so that faults resolved in map view are analysed independently (Ze and Alves, 2016; Alves, 2012; Mattos et al., 2016b, Ward et al., 2016b, Bahorich and Farmer, 1995); 2) displacement analyses including Throw-Distance (T-D) and Throw-Depth (T-Z) plots (Mattos et al., 2016, Jackson et al., 2017; Wilson et al., 2013; Jackson and Rotevatn, 2013b, Baudon and Cartwright, 2008c, Baudon and Cartwright, 2008a, Baudon and Cartwright, 2008b); 3) the use of Expansion indexes (EI) (Mohammedyasin et al., 2016; Ze and Alves, 2016); 4) isochron analyses. Geomorphological analyses of knickpoints in rivers developed in active rift basins can also provide constraints on the growth and linkage of fault systems (Whittaker and Walker, 2015). Among these techniques, T-D and T-Z plots are widely used in the identification of fault segmentation and reactivation on seismic data, showing minimal effects of phenomena such as compaction, variable sedimentation rates between hanging-wall and footwall strata (Imber et al., 2002), and fault scarp erosion (van Gent et al., 2010), caveats that often affect EI and isochron data. It is also important to stress that allostratigraphic, rather than chronostratigraphic boundaries, are widely used in the petroleum industry, and that T-D and T-Z plots can compensate for this fact when acquired systematically at successive horizons, and at high sampling intervals (e.g. Alves, 2012).

Despite the general acknowledgment of the latter interpretation caveats, sampling strategies in published T-D and T-Z still vary significantly (e.g. Ze and Alves, 2016; Tvedt et al., 2016; Baudon and Cartwright, 2008c, Ryan et al., 2017). In particular, quantitative methods are still lacking in the literature to critically assess the accuracy of T-D plots and ancillary T-Z data when interpreting data at different scales. In addition, seismic quality has also an important control on how accurate fault geometries are

resolved on seismic data (Manzocchi et al., 2010). This chapter focus on how important is the sampling interval of fault throw (or displacement) data to the accuracy of T-D data and subsequent fault analyses. Data used in this chapter covers a wide range of faults ranging from sub-seismic scales to rift scales (Figs. 6-1 to 6-3). This chapter aims at:

1) Critically assessing how distinct sampling strategies to acquire throw (T-Z) data can influence the accuracy of T-D plots in the three dimensions;

2) Understanding the possible consequences of unreliable T-D plots;

3) Understanding the influence of data sampling intervals on the analysis of fault sealing properties;

4) Suggesting a new quantitative method that interpreters and structural geologists can use to avoid the collection of incomplete T-D data.

Two new parameters are introduced to address these key research questions, the *Sampling Interval/Fault length Ratio* (δ) and *Module Error* (ε_i) of faults to quantify and assess how reliable are T-D plots, and associated T-Z data, at different scales of observation. To better understand the methods proposed in this work, relevant terminologies are introduced as follows:

T-D plots: Throw-Distance (or D_{max}/L) plots comprise systematic measurements of throw along the full length of resolved faults on structural maps, seismic data, or outcrops; the 'trace length in map view' as defined by Kim and Sanderson (2005). Maximum throw is measured along normal faults or, preferably, interpreters should collect throw/depth (T-Z) data along the fully resolved length of faults to then collate T-D plots (Ze and Alves, 2016).

Fault length: For faults that are displayed on seismic data, fault length refers to the longest horizontal or sub-horizontal dimension along a fault plane (Kim and Sanderson, 2005). For faults that are measured in the field, fault length refers to the longest trace of a fault that is exposed on the surface.

Fault segment: an individual fault or other type of fracture plane that is part of a set of sub-parallel faults or other types of fractures that together form a fault zone or fracture zone (e.g., Segall and Pollard, 1980). Fault segmentation in the thesis is identified combining variance maps, field observations that are independent from throw-distance maps.

Throw: the throw of faults as observed on seismic data is the vertical component of fault displacement between hanging-wall and footwall reflections, which is in milliseconds as the seismic data available is in time domain. Throw values for faults that are measured in the field, fault length refers to the longest trace of a fault that is exposed on the surface.

Sampling interval: Mathematically, the sampling interval in T-D and T-Z plots is the distance, time or depth, between two distinct throw measurements are acquired and recorded. These measurements are obtained along the 'trace length' of a fault and may record strong aliasing due to seismic-data horizontal resolution, data decimation (shot-point spacing), or poor imaging. The sampling interval can also be an important source of inaccuracy in field data if fault throws are sampled at too coarse an interval.

Sampling point: Comprises the exact point, along the 'trace length' of faults, in which the throw values are measured; either at its maximum value, or its relative value across a fault surface (i.e. relative to depth along a fault surface).

Accurate/reliable throw-distance profiles: Throw-distance (T-D) profiles that are produced reaching data resolution are defined as accurate T-D plots, i.e. T-D plots produced with a sampling interval of 12.5 m for fault that are interpreted on seismic data are defined as accurate T-D plots. If T-D plots produced with an increasing sampling interval have minimum effect on the identification of fault segmentation compared to T-D plots that are produced reaching data resolution, these T-D plots are also identified as accurate T-D plots.

Accuracy: For a given sampling interval, the produce T-D profiles for a group of faults are compared to the accurate T-D profiles, numbers of faults that are with accurate T-D profiles divide total number of faults id defined as accuracy in the thesis.
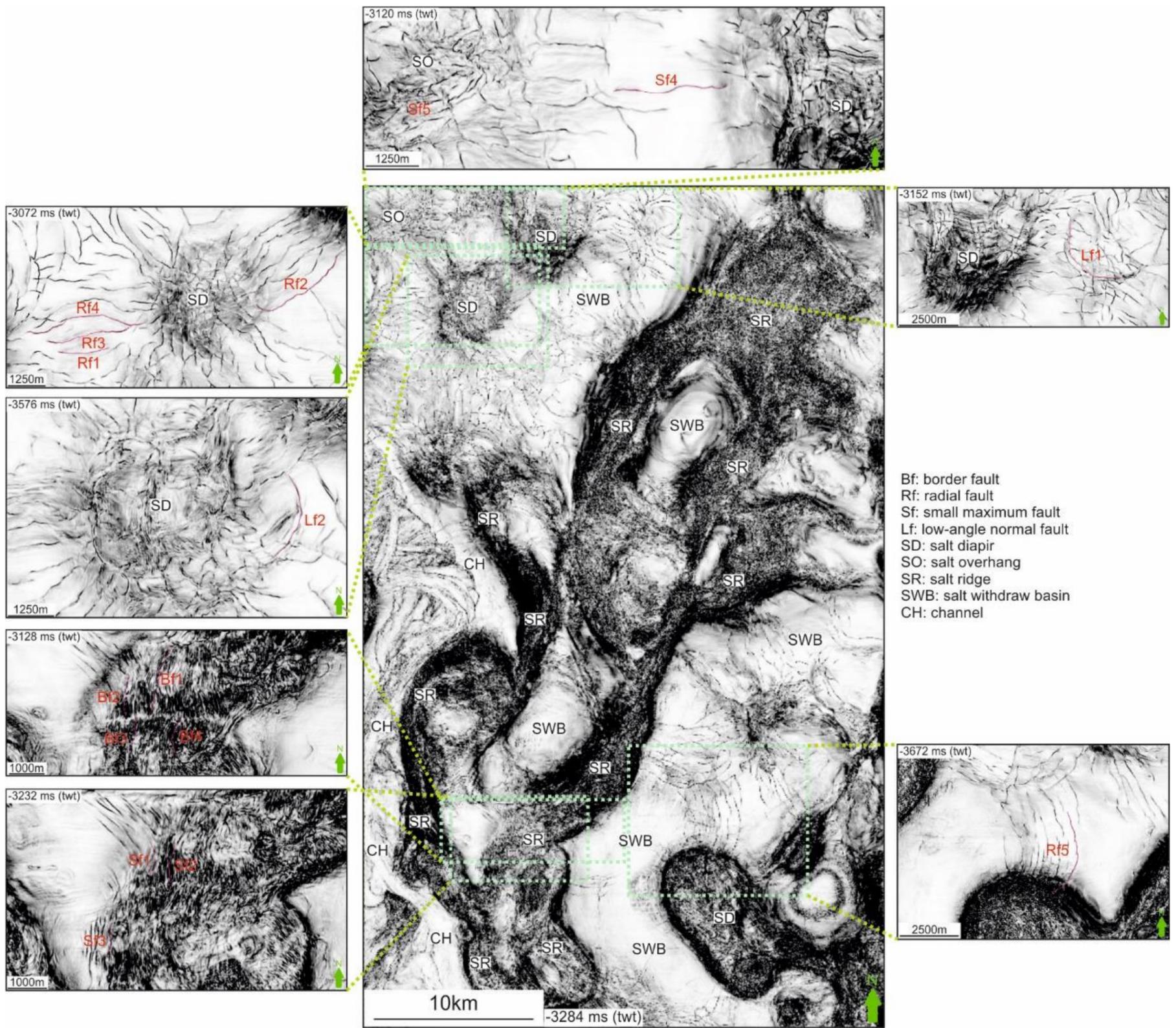
Fig. 6-1 Variance map depicting the faults analysed in this chapter.

Bf: border fault   Rf: radial fault   Sf: small maximum fault   Lf: low-angle normal fault
Vertical exaggeration: 4
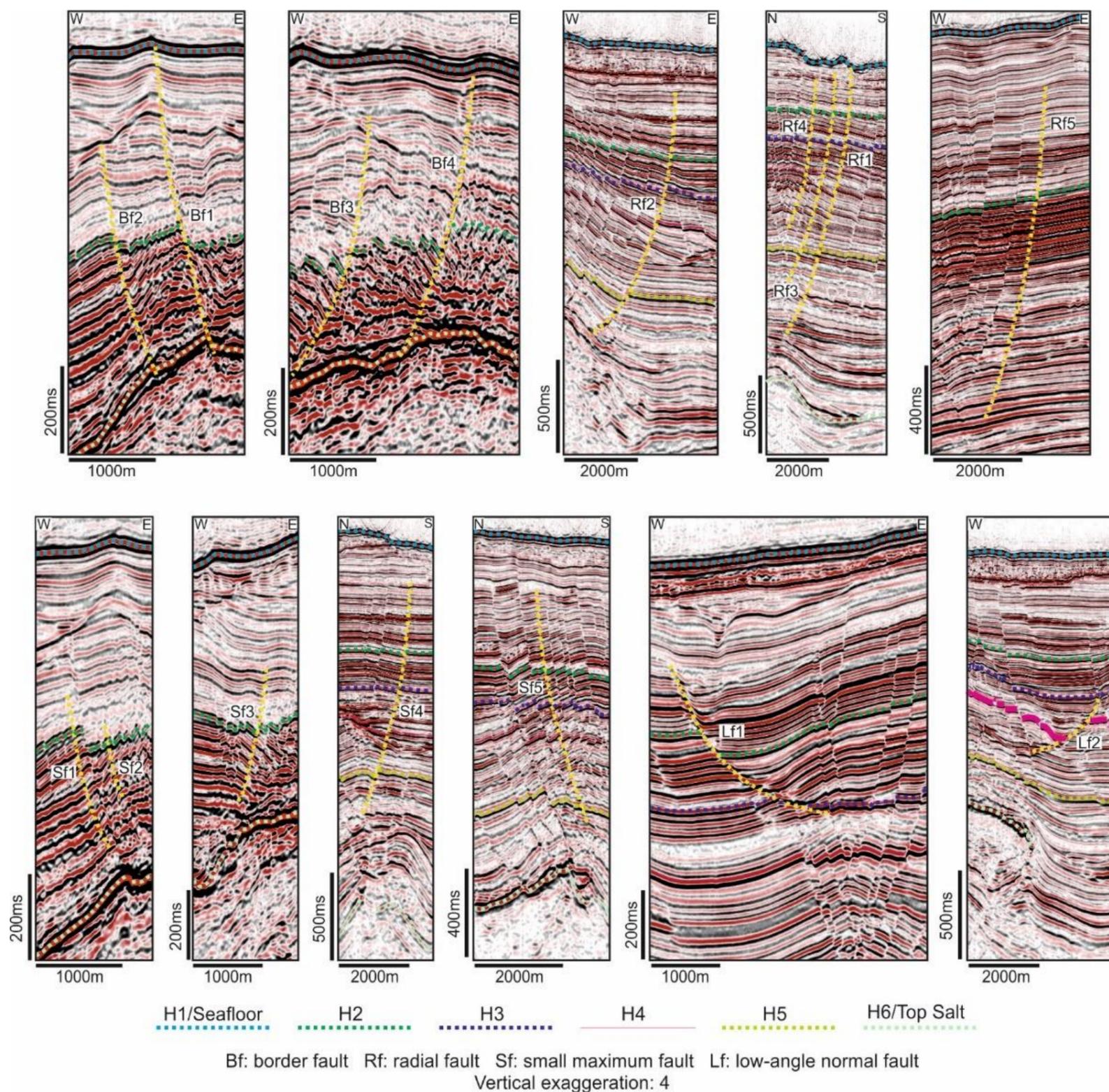
Fig. 6-2 Seismic sections showing some of the faults subsequently analysed in this chapter.
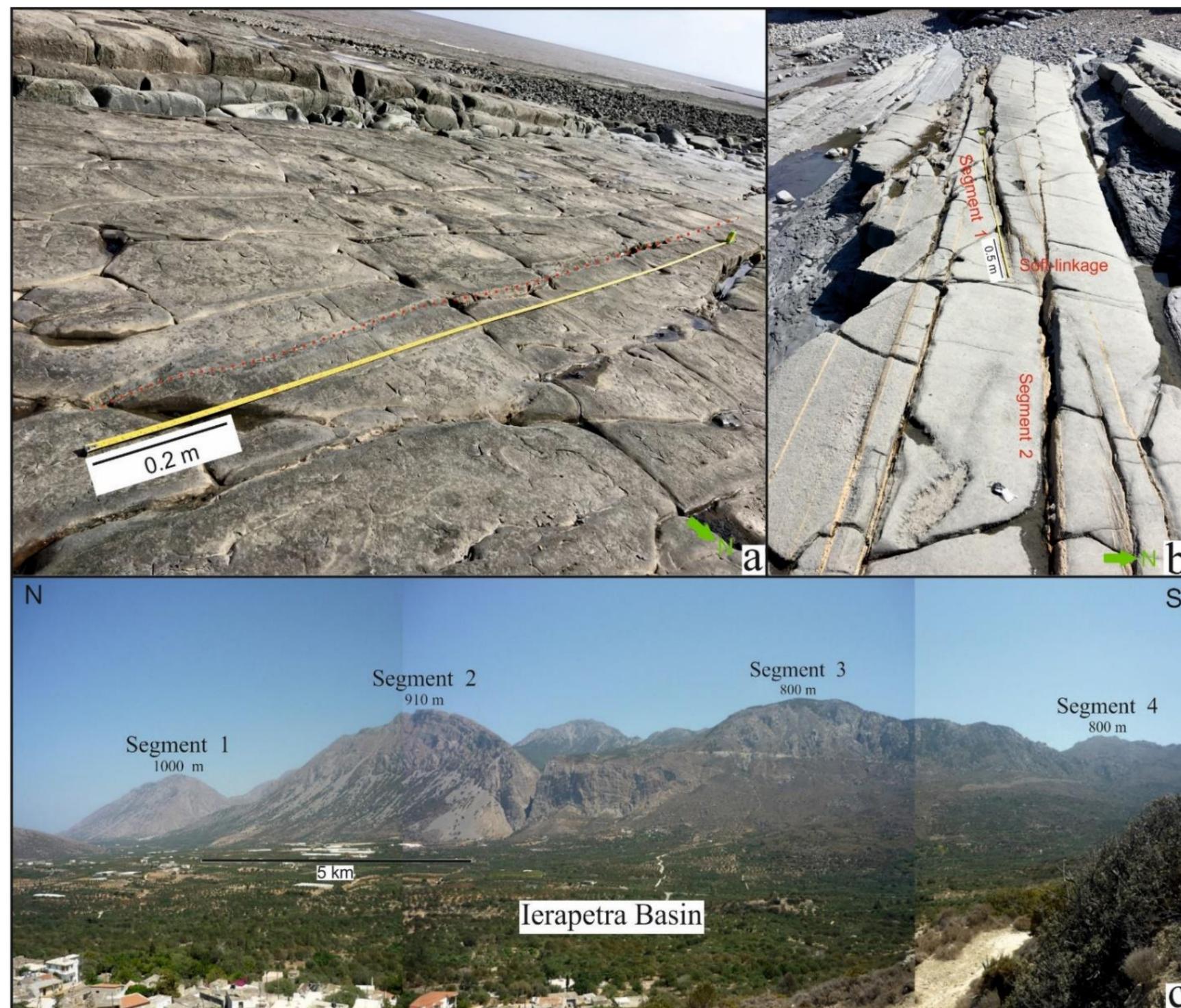
Fig. 6-3 a) Sub-seismic fault segment (Kilve Beach, Somerset). b) Sub-seismic fault comprising two soft-linked fault segments (Kilve Basin, Somerset). c) Ierapetra Fault Zone, NE of Ierapetra, SE Crete. The fault zone comprises distinct rift-related fault segments with distinct histories.

6.2 Results

6.2.1   T-D plots produced at different sampling intervals for rift-related faults in SE Crete

This section shows examples of T-D plots produced at different sampling intervals for one discrete fault (Fault A in Figure 6-4) and for a fault zone (Ierapetra Fault Zone) composed of five (5) linked (rift) fault segments (Fault B in Figure 6-4).

For the discrete, isolated Fault A one fault segment can always be identified for all sampling intervals adopted in Figure 6-4. However, the geometry of Fault A changes significantly when sampling interval increases to 125 m, (Fig. 6-4-a4). The maximum throw curve (T) shows an arching top with a measuring space of 12.5 m (Fig. 6-4-a1). However, details of the maximum throw area in Figures 6-4-a4 and a5 are quantitatively lost when sampling intervals are significantly larger. The apex of the fault (maximum throw point) is also changed (Fig. 6-4-a4). For Fault A, a maximum measuring space of 62.5 m is regarded as necessary to obtain accurate T-D plots (Fig. 6-4-a3), i.e. reflecting accurate fault geometries without losing significant detail.

For Fault B, T-D data gathered at sampling intervals of 50 m indicates the fault zone as comprising five (5) distinct segments with a maximum throw of 1000 m (Fig. 6-4-b1). When the sampling interval increases to 500 m details of fault segment 1 are lost, in effect masking a significant area where fault interaction occurs (Fig. 6-4-b3). When the sampling interval increases to 1000 m, linkage zones between segments 1 and 2, and segments 2 and 3, are represented by only one minimum throw point whose width and geometry are significantly changed (Fig. 6-4-b4).

With a sampling interval over 1000 m, maximum throw values are significantly underestimated and fault segment 5 becomes unrecognizable (Fig. 6-4-b4). When measuring space increases to 1250 m, confusion arises between segments 2 and 3, with their linkage zone being represented with one minimum throw in the wrong location D (Fig. 6-4-b5). When sampling interval increases to 2500 m, only two fault segments can be identified and the maximum throw value Fault B is underestimated (Fig. 6-4-b6). A sampling interval of 100 m is suggested as the minimum value to resolve distinct segments in Fault B (Fig. 6-4-b2).

179

Fault A

a1 — Max. T = 41 ms, SI = 12.5 m

a2 — Max. T = 41 ms, SI = 37.5 m, ε_i = 0.019, δ = 0.056

a3 — Max. T = 41 ms, SI = 62.5 m, ε_i = 0.032, δ = 0.093

a4 — Flattened top; Changed geometry; Max. T = 40 ms, SI = 125 m, ε_i = 0.06, δ = 0.185

a5 — Underestimated Max. Throw; Dramatically changed geometry; Max. T = 37 ms, MS = 250 m, ε_i = 0.273, δ = 0.37

Fault B

b1 — Max. T = 1000 m, SI = 50 m; Segment 1, Segment 2, Segment 3, Segment 4, Segment 5

b2 — Max. T = 1000 m, SI = 100 m, ε_i = 0.004, δ = 0.005

b3 — Lost details of fault interactions; Max. T = 1000 m, SI = 500 m, ε_i = 0.03, δ = 0.026

b4 — Lost details of fault interactions; Changed geometry of fault linkage zones; Underestimated Max. Throw; Lost fault segment; Max. T = 950 m, SI = 1000 m, ε_i = 0.071, δ = 0.05

b5 — Lost details of fault interactions; Changed geometry of fault linkage zones; Underestimated Max. Throw; Max. T = 950 m, SI = 1250 m, ε_i = 0.073, δ = 0.065

b6 — Dramatically changed geometry; Underestimated Max. Throw; Max. T = 950 m, SI = 2500 m, ε_i = 0.178, δ = 0.128

Max. T: Maximum throw value   SI: Sampling interval ε_I : Module Error δ: Sampling interval/Fault length ratio

180

Fig. 6-4 T-D plots for faults comprising one fault segment (Fault A) and five fault segments (Fault B). Fault A has a fault length of 675 m, with a maximum throw value of 41 ms (twt). a1) T-D plot with data acquired every 12.5 m, i.e. the trace spacing of the seismic volume used in this study, reveals the most accurate information for Fault A. a2) T-D plot for Fault A with a sampling interval of 37.5 m, ε_i=0.019, δ=0.056. a3) T-D plot for Fault A with a sampling interval of 62.5 m, ε_i =0.032, δ=0.093. a4) T-D plot for Fault A with a sampling interval of 125 m, ε_i =0.06, δ=0.185. a5) T-D plot for Fault A with a sampling interval of 250 m, ε_i =0.273, δ=0.37. b1) T-D plot of every 50 m for Fault B, which reveals the most accurate information. b2) T-D plot for Fault B with a sampling interval of 100 m, ε_i =0.004, δ=0.005. b3) T-D plot for Fault B with a sampling interval of 500 m, ε_i =0.03, δ=0.026. b4) T-D plot for Fault B with a sampling interval of 1000 m, ε_i =0.071, δ=0.05. b5) T-D plot for Fault B with a sampling interval of 1250 m, ε_i =0.073, δ=0.065. b6) T-D plot for Fault B with a sampling interval of 2500 m, ε_i =0.178, (δ=0.128. Noting that, with a sampling interval of 125 m for Fault A (a4), maximum throw value is underestimated and geometry of fault maximum throw area and right side of Fault A is significant changed. With a sampling interval of 250 m, produced T-D plot has completely lost its practical meaning. For Fault B, when measuring space is 500 m, details of fault segment 1 is lost (red circle in b3), which might be a significant zone of fault interaction. With a sampling interval of 1000 m (b4), maximum throw value is significantly underestimated, fault segment 5 is unable to identify. With a sampling interval over 1250 m (b5 and b6), maximum throw values, fault geometry and fault segmentation have lost their real meaning.

6.2.2   Relationship between data sampling and accuracy

Due to caveats resulting from increasing spacing intervals applied to T/D plots: 1) fault geometry is significantly changed (Figs. 6-4-a4, a5, b4, b5 and b6), 2) maximum throws are underestimated (Figs. 6-4-a5, b4, b5 and b6), 3) fault segmentation is lost on close analysis (Figs. 6-4-b4, b5 and b6), 4) the geometry of fault linkage points is changed (Figs. 6-4-b4, b5 and b6), 5) the width(s) of fault linkage zones is underestimated (Figs. 6-4-b4, b5 and b6), 6) fault interaction zone (relay ramps, step-overs, hard-linkage points) are lost (Fig. 6-4-b3).

The accuracy of T-D plots was calculated for 58 faults interpreted on seismic data, and 13 sub-seismic faults measured in the field (Supplementary data). For the analysed seismic faults (58), accuracies are 90% (52), 46% (27), 10% (6) and 0% (0) respectively for sampling intervals of 37.5 m, 62.5m, 125m and 250 m. For sub-seismic faults, an accuracy of 100% (13), 38% (5), 7.7% (1), and 0% (0) are calculated for sampling intervals of 15 cm, 25 cm, 50 cm and 100 cm respectively (Fig. 6-5).

An important result is that the accuracy of T/D plots for seismic faults sampled at intervals of 37.5 m (i.e. every 3 shot points) on seismic data is not 100% (Fig. 6-5), which means that 10% (6) of the faults should be measured at sampling intervals of 12.5 m to be correctly resolved, a value approaching the horizontal seismic resolution of the interpreted seismic data (12.5 m).
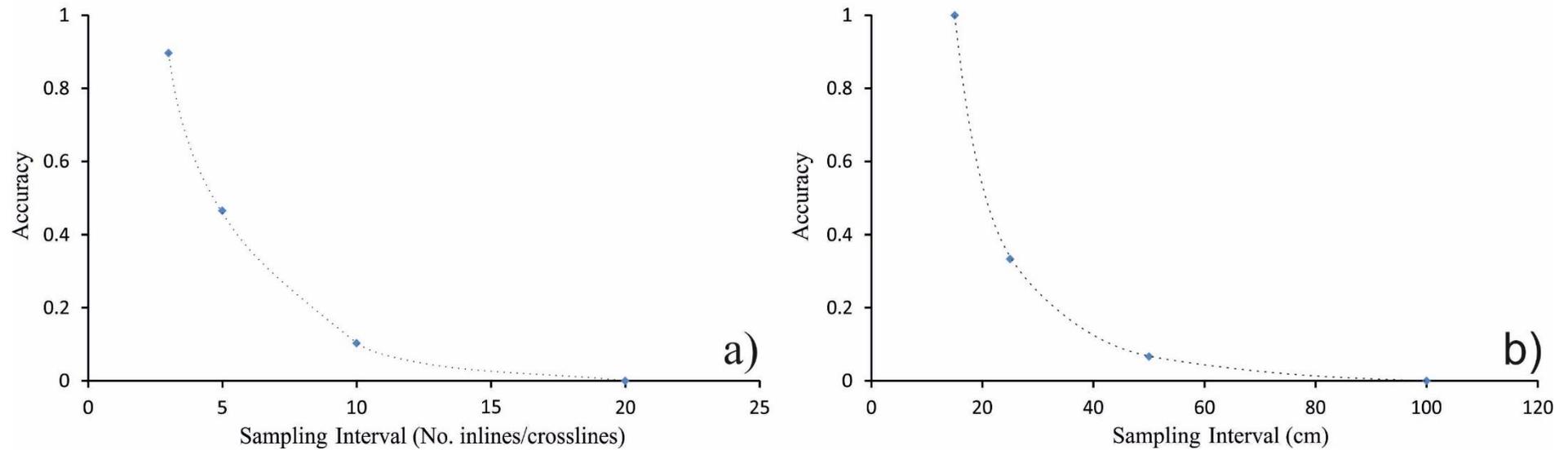
Fig. 6-5 Relationship between T-D plots accuracy and sampling interval. For the faults interpreted on a seismic volume with a bin spacing of 12.5 m, T-D plots accuracy decreases dramatically with increasing sampling interval, showing accuracies of 90%, 46%, 10% and 0%, respectively, for sampling intervals of 37.5 m, 62.5m, 125m and 250 m. For sub-seismic faults, accuracies are 100%, 38%, 7.7%, and 0% with sampling intervals of 15, 25, 50 and 100 cm respectively. Noting that 10% of the T-D plots for faults interpreted on seismic data are inaccurate with a sampling interval of 37.5 m, which indicates that some of the faults have to be measured every 12.5 m, which is the trace spacing, in order to obtain reliable T-D plots.

6.3 Relationships between parameters δ, ε_i and fault geometries

6.3.1 Relationship between Sampling Interval/Fault Length (δ) and Module Error (ε_i)

All caveats leading to unreliable T-D plots result in significant changes in fault geometry, i.e., the area delimited by the T-D plots and horizontal axis (Fig. 2-10). In order to quantify to what extent the change of fault geometry will lead to the compilation of inaccurate T-D plots and, consequently, erroneous fault growth analyses, module errors were calculated for all the 73 faults used in this chapter using different sampling intervals (supplementary data). Due to the fact that fault length varies from 1.65 m to 19.5 km for the 73 interpreted faults, using sampling interval alone loses its practical meaning when addressing T/D plot accuracy at distinct scales.

The results show that the *Module Error* ε_i increases to the ratio δ (Fig. 6-6). Hence, to obtain reliable T-D data from normal faults, ε_i should be less than 0.09 (Fig. 6-6a). Values that are above a ε_i of 0.09 will return inaccurate T-D (Fig. 6-4). The primary value of ε_i for accurate T-D plots varies slightly between seismically resolved faults and faults analysed at the outcrop in SE Crete, showing ε_i values of 0.09 and 0.08 respectively (Fig. 6-6b and 6-6c). Even though a ε_i value of 0.09 can be indicated as a threshold figure beyond which T-D plots become inaccurate, 92% of the plotted T-D data still have ε_i values below 0.06 (Fig. 6-6).

In terms of the *Sampling Interval/Fault Length Ratio* δ, the results show that a threshold value of 0.1 is valid for faults of all scales, i.e. sampling should occur at a spacing of < 10% the fault length in order to get fairly accurate T-D data (Figs. 6-6). Yet again, 74% of the analysed faults show δ values that are less than 0.06, i.e. sampling should be undertaken at < 6% the fault length (Fig. 6-6a), with a percentage of 71% for seismic faults with δ < 0.07 and 83% for field faults with δ < 0.06 respectively (Figs. 6-6b and 6-6c).

Fault segmentation has a significant effect on ε_i, most of the module errors are derived from the areas where fault segments are linked (Fig. 6-4). In order to understand and postulate a valid threshold δ value for faults that are isolated or composed of linked segments, all reliable T-D measurements were selected and differentiated in Figure 6-7
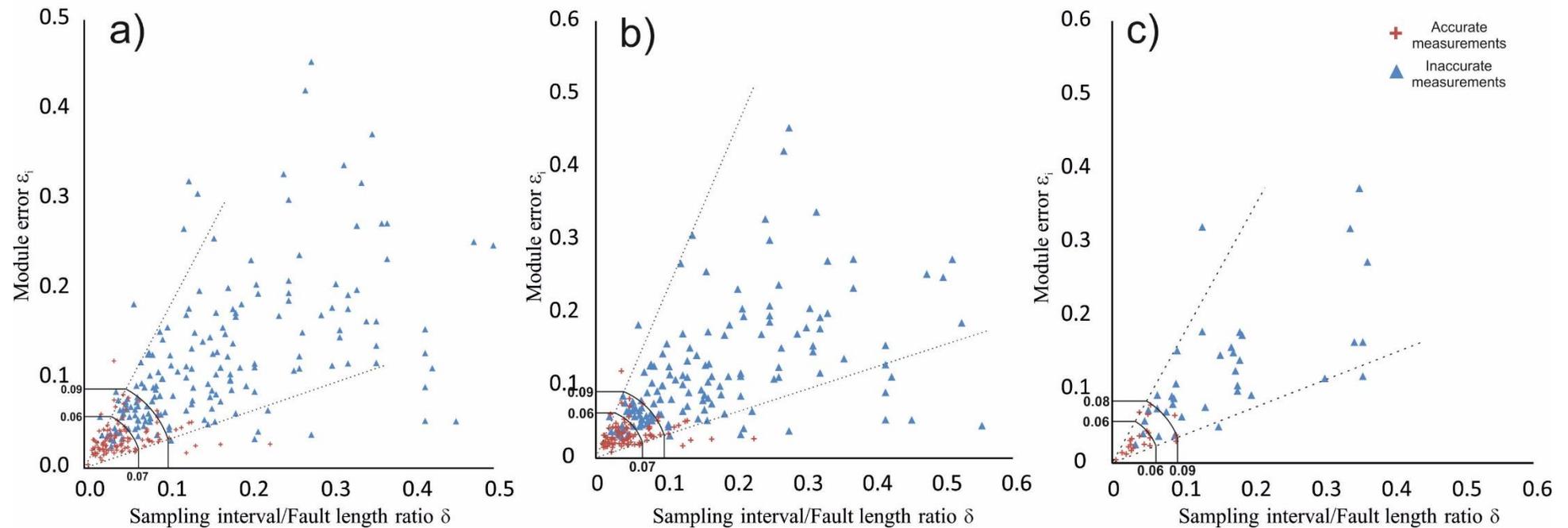
Fig. 6-6 Relationship between sampling interval/length ratio (δ) and module error (ε_i). Module error increase rapidly with increasing sampling interval/length ratio. a) To have accurate T-D plots for faults of all scales, the ε_i value should be less than 0.09, with a δ value of 0.1. Note that 92% of all accurate measurements are located within a threshold of $\varepsilon_i <$ 0.06, δ < 0.07. b) Relationship between δ and ε_i for seismic faults. For accurate T-D plots, $\varepsilon_i < 0.06$ and δ < 0.07 should be applied. c) Relationship between δ and ε_i for sub-seismic faults. For accurate T-D plots, $\varepsilon_i < 0.06$ and δ < 0.06 should be applied.

Relationship between faults comprising one fault segment and those composed of multiple linked segments
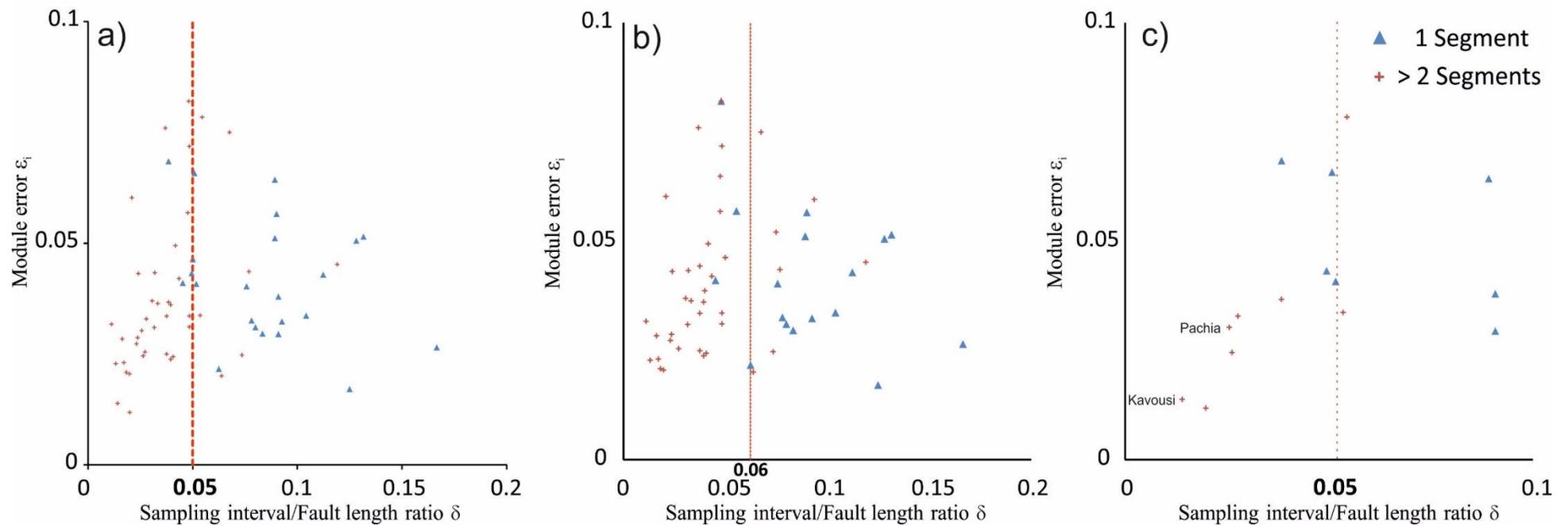
Fig. 6-7 Accurate sampling interval/length ratio (δ) for faults comprising one fault segment and ≥ 2 fault segments. a) A boundary of $\delta = 0.05$ is shown for faults of all scales. b) A boundary of $\delta = 0.06$ is shown for seismic faults. c) A boundary of $\delta = 0.05$ is shown for faults analysed in the field.

according to segments each fault comprises. The results show a clear boundary between isolated and segmented faults when considering the δ values needed to obtain accurate T-D data (Fig. 6-7a). A threshold value of δ=0.05 is shown in Figure 6-7 for faults of all scales. This value correlates with threshold values of δ=0.06, and δ=0.05 for seismically resolved, and faults in the field, respectively (Figs. 6-7b and 6-7c). The δ=0.05 threshold value suggests that, for faults of any scale, sampling should be undertaken at intervals that are < 5% of the fault length if they are segmented faults, whereas for faults comprising only one fault segment, a spacing of < 10% of the total fault length is necessary (Fig. 6-7). However, without previous knowledge of fault segmentation, a δ value of 0.05 is strongly suggested as a minimum threshold for interpreters and structural geologists (Fig. 6-7c).

6.3.2   Relationship between fault length and the δ ratio

The relationship between fault length and the δ ratio shows a robust power-law relationship; with increasing fault lengths, the threshold value of δ necessary to produce reliable T-D plots decreases significantly (Fig. 6-8). For faults interpreted on seismic data showing a length varying from 275 m to 5000 m, the threshold δ value becomes constant when fault length exceeds 3500 m, and a value of $\delta \sim 0.02$ is indicated in Figure 6-8a.With longer faults, such as the rift faults in SE Crete, threshold δ values to obtain reliable T-D data are 0.025 and 0.018 respectively. This proves that, for faults that are longer than 3500 m, a threshold δ value of 0.02 provides reliable T-D data (Fig. 6-8a).

6.3.3   Relationship between average fault-segment length and module error (ε_i)

As indicated in the previous section, in order to obtain reliable T-D plots for rift faults (which have larger fault lengths and larger average fault-segment lengths), a smaller δ value should be considered. This result indicates that fault length and average fault segment length have an influence on the final δ value needed to produce reliable T-D plots. The relationship between ε_i and average fault segment length shows that, for the interpreted faults on seismic data, the ε_i values decrease with longer average fault segment
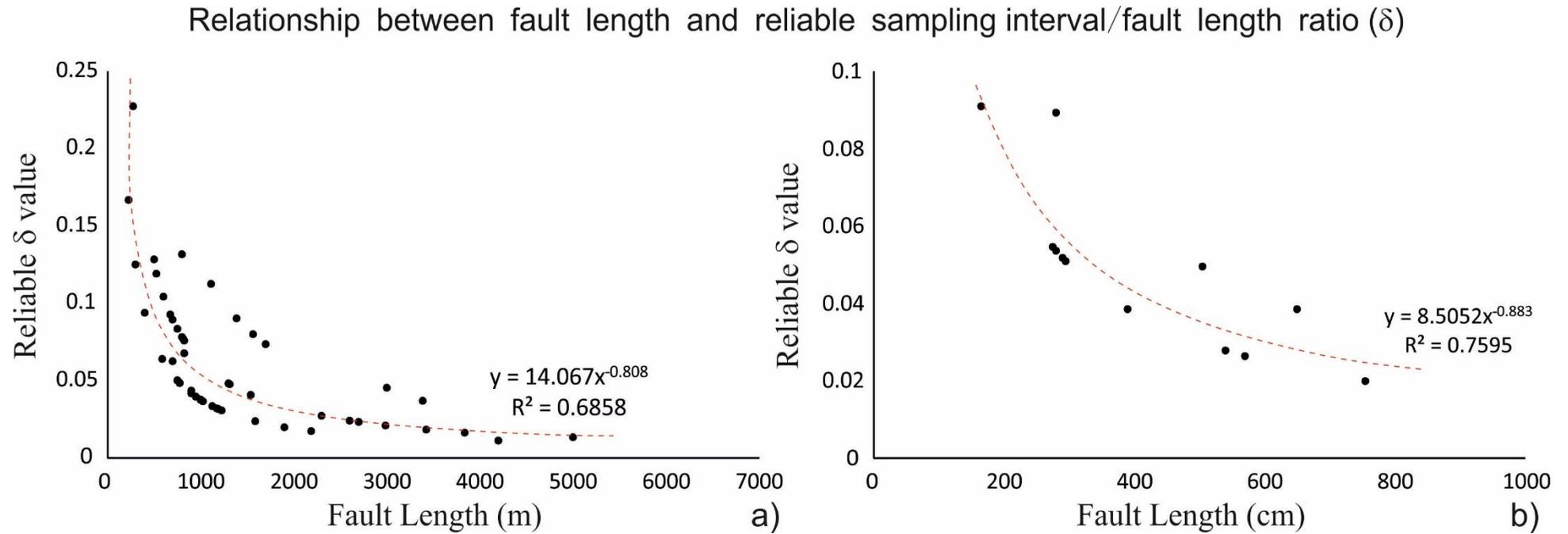
Fig. 6-8 Relationship between fault length and reliable sampling interval/length ratio (δ). The results indicate a power-law relationship between L and δ, in which δ reliability decreases with longer fault lengths. a) For seismic faults, reliable δ values (δ=0.03) become constant with fault lengths $\geq$ 3500 m. b) For sub-seismic faults, reliable values of δ also decrease rapidly with increasing fault lengths.

187

Relationship between average fault segment length and Module Error (εi)
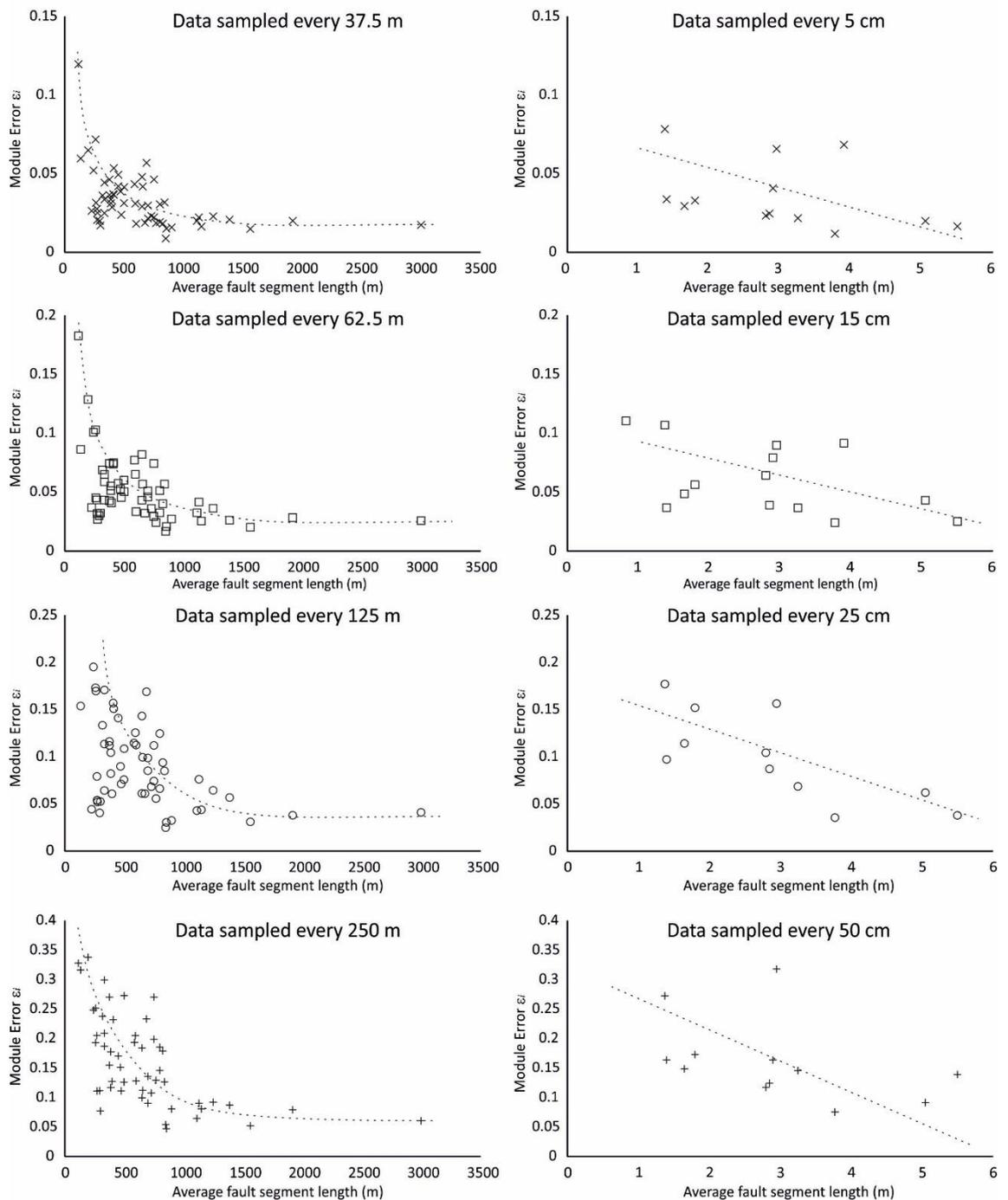
Fig. 6-9 Relationship between average fault segment length and module error with given sampling intervals. All results show that module error decreases rapidly with longer average fault segment lengths, a character indicating that for smaller fault segment require smaller sampling intervals in order to produce reliable T-D plots.

lengths (Fig. 6-9). The *Module Error* ε_i regresses to a stable value of 1.7%, 2.6%, 4% and 6% respectively for T-D data that measured every 37.5 m, 62.5 m, 125 m and 250 m (Fig. 6-9). The *Module Error* (ε_i) for faults below seismic scales also shows a negative relationship with average fault segment lengths (Fig. 6-9), i.e., module error decreases with increasing average fault segment lengths.

6.3.4   Relationship between T-D ratios and δ

In this work, faults composed of discrete fault segments show double or even three times the length of isolated faults. However, maximum throw values are almost the same, resulting in a smaller T-D ratio. In constant-length growth models, faults have increasing T-D ratios and fault length reaches its final value very early, increasing fault displacement in a vertical direction with time. The relationship between the T-D ratio and δ shows that, with a smaller T-D ratio, the values of δ are smaller (Fig. 6-10), i.e. more measurements should be undertaken for faults that are composed, at any time in their evolution, of distinct segments, a result consistent with the data in Section 6.3.1 (Fig. 6-7).

6.4 Effect of data sampling on fault slip tendency and leakage factor analyses

Estimated values of slip tendency and leakage factor under pre-established stress values of are dependent on the roughness, geometry and orientation of fault planes relative to acting stresses (Lohr et al., 2008). In order to understand the effect of δ on slip tendency and leakage factor analysis, a modeled fault from the SE Brazil seismic volume was exported from Petrel® with sampling intervals of 12.5 m, 37.5 m, 62.5 m and 125 m, so to produce a fault model (Fig. 6-11). The exported fault surfaces were modeled for slip tendency and leakage factor using 3D Move® and assuming pore pressures of 0 MPa, 5 MPa and 10 MPa (Fig. 6-11). The analysis assumes that fault surfaces interpreted every 12.5 m, which is the horizontal seismic resolution of the SE Brazil 3D seismic volume, reveal the most accurate slip tendency and leakage factor. The fault analysed comprises two fault segments (Fig. 6-11). The two fault segments have similar maximum throw values and lengths (Fig. 6-11).
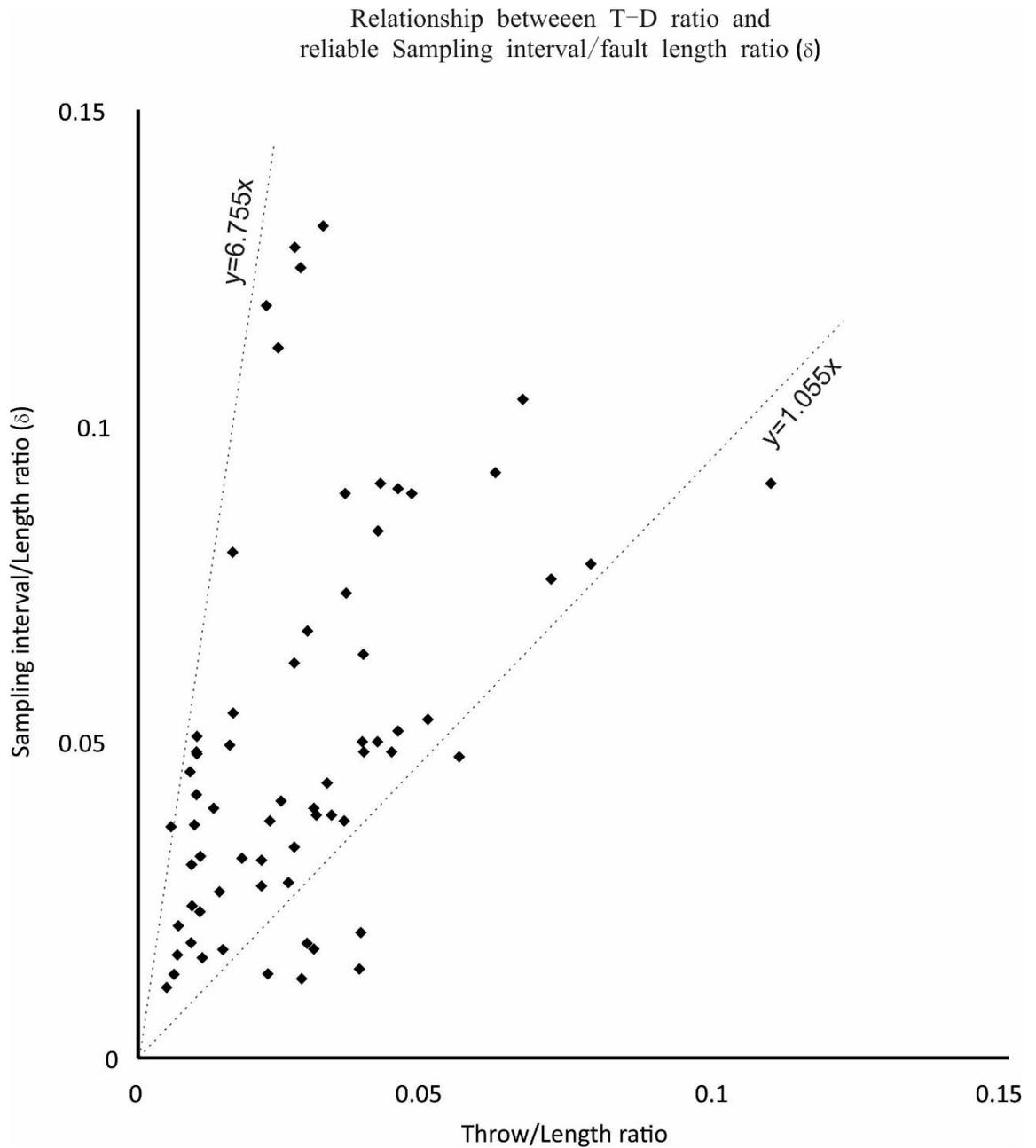
Fig. 6-10 Relationship between maximum throw/length ratio and sampling interval/length ratio (δ). The results roughly suggest a positive relationship insofar as, with a smaller maximum throw/length ratio, a smaller sampling interval/length ratio (δ) should be applied. For a constant fault growth model, maximum throw/length ratio increases. Conversely, for an isolated fault, maximum throw/length ratio decreases or stays constant with subsequent stages of fault growth. Thus, the sampling interval/length ratio (δ) used to produce T-D plots will have significant influence on the subsequent interpretation of fault growth histories.

6.4.1   Slip tendency variations for distinct sampling intervals

For a pore pressure value of zero (0) MPa, the areas with high slip tendency remain similar on the fault surface interpreted every 37.5 m, compared to the fault surface interpreted every 12.5 m (Figs. 6-11-a1 and 6-11-a2). However, the magnitude of slip tendency decreases with larger sampling intervals, i.e. with a coarser interpretation (Fig. 6-11-a2). When the fault was interpreted every 62.5 m, slip tendency in its lower part changed significantly (Fig. 6-11-a3). When picking faults every 125 m, the fault surface becomes so smooth that slip tendency is underestimated (Fig. 6-11-a4).

For pore pressure values of 5 MPa and 10 MPa, the results of modeling slip tendency are similar to that of pore pressures reaching zero (0) MPa. With larger sampling intervals: 1) slip tendency is underestimated, and where high slip tendency occurs the values are dispersed (Fig. 6-11-b2 and c2), 2) areas of high slip tendency are lost (Fig. 6-11-b3 and c3), and 3) slip tendency is systematically underestimated (Fig. 6-11-b4 and c4).

6.4.2   Leakage factor variations for distinct sampling intervals

For a pore pressure value of zero (0) MPa, and when interpreting the fault surface every 12.5 m, leakage factor in its upper part is 0.3-0.4 (Fig. 6-11-d1). However, this value is reduced to 0.2-0.3 with larger sampling intervals (Fig. 6-11-d2 and d3). In addition, zones of higher leakage factors are narrowed (Fig. 6-11-d2 and d3) and lost (Fig. 6-11-d4).

For a pore pressure value of 5 MPa, sampling intervals of 62.5 m and 125 m for the fault surface result in a systematical underestimation of leakage factors (Fig. 6-11-e3 and e4). With a sampling space of 37.5 m, zones of high leakage factor remain similar, but the magnitude of the calculated leakage factor decreases (Fig. 6-11-e2).

For a pore pressure value of 10 MPa, zones with high leakage factor are the same as with sampling intervals of 12.5 m and 37.5 m. However, leakage factors are relatively lower with a sampling space of 37.5 m (Fig. 6-11-f1 and f2). When the sampling space increases to 62.5 m, there is systematically overestimation of leakage factors in the lower
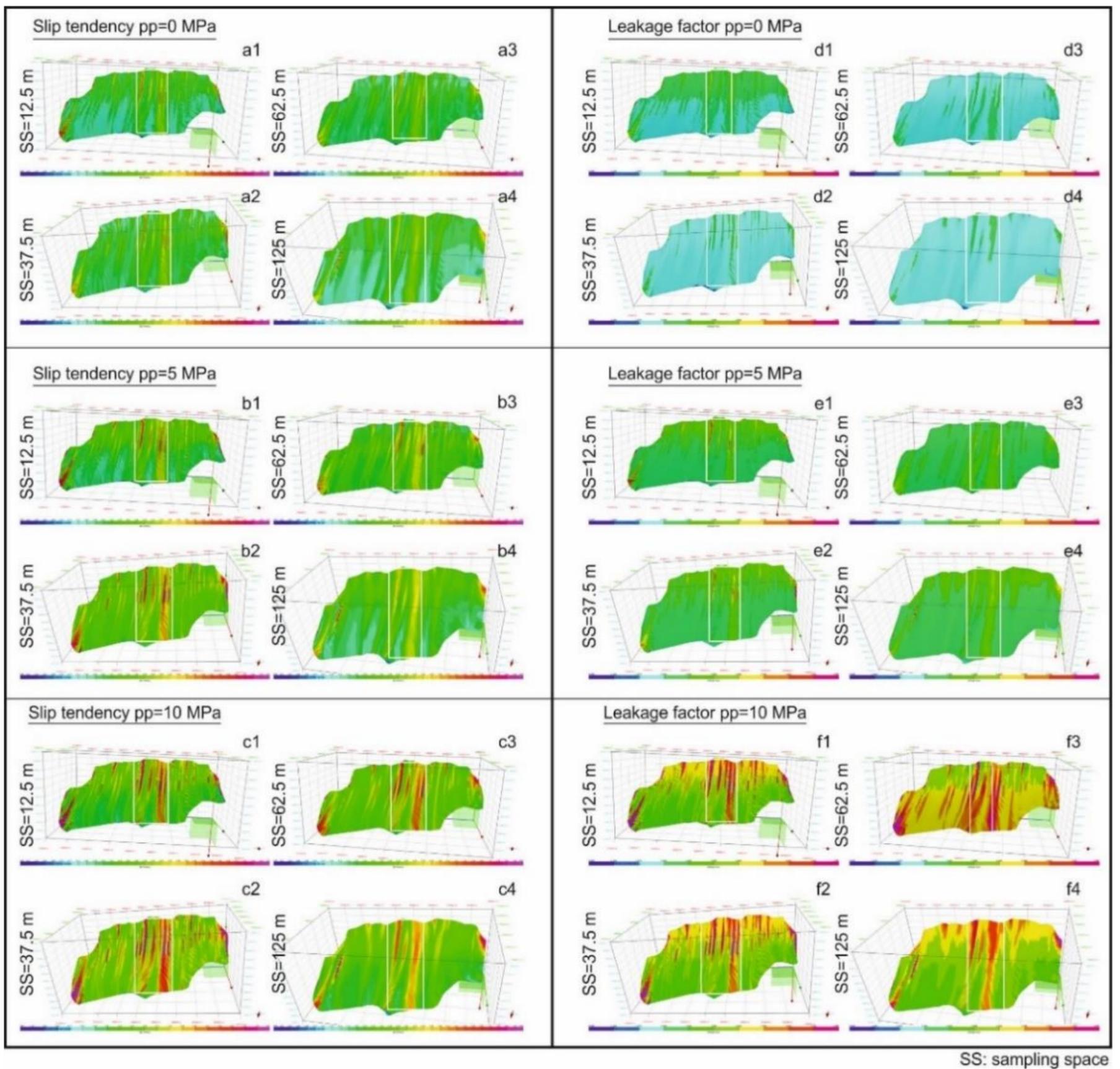
Fig. 6-11 Influence of sampling interval on fault slip tendency and leakage factor analyses. Left) Slip tendency analysis under pore-pressures of 0 MPa, 5 MPa and 10 MPa with different sampling intervals. Right) Leakage factor analysis under pore pressures of 0 MPa, 5 MPa and 10 MPa with different sampling intervals. White boxes in the figures refer to the segment linkage zone, where higher slip tendency and leakage factors occur. a1-a4) Slip tendency under pore-pressure of 0 MPa. With increasing sampling intervals, the magnitude of slip tendency decreases (a2-a4). In Figures 6-11-a2 and a3, slip tendency at the lower part of the fault is overestimated. In Figure 6-11-a4, fault surface becomes smooth with a sampling interval of 125 m, that areas of higher slip tendency is blurred. b1-b4, c1-c4) results of slip tendency under pore-pressure of 5 MPa are similar to that of hydrostatic pore-pressure that both magnitude and areas of higher slip tendency are significantly changed with an increasing sampling interval. d1-d4) Leakage factor analysis under hydrostatic condition, that leakage factor at the upper area of the fault is systematically underestimated and areas with higher leakage factor values are also underestimated. e1-e4) Leakage factor under a pore-pressure of 5 MPa shows similar results to that under a hydrostatic condition. f1-f4) With a pore pressure of 10 MPa, a sampling interval of 37.5 m (f2) show similar results with a sampling interval of 12.5 m (f1), except that the magnitude of leakage factor is slight smaller. When the sampling interval increases to 62.5 m, the lower part of the fault shows abnormally high values (f3). At the same time, areas with high leakage factors are blurred and markedly different from that with a sampling interval of 12.5 m (f1). When sampling interval increases to 125 m, leakage value and areas of higher leakage factors are systematically underestimated (f4).

part of the fault, while the high leakage factor zones are enlarged (Fig. 6-11-f3). When the sampling space increases to every 125 m, a systematical underestimation of both the value and areas with high leakage factors are observed (Fig. 6-11-f4).

6.5 Discussion

Sampling intervals close to seismic data resolution result in the most accurate T-D plots, fault slip tendency and leakage factor analyses. However, the process of interpreting faults on seismic data, or acquiring closely-spaced measurements for outcropping faults, is time-consuming.

This chapter introduces two new parameters, the Sampling Interval/Fault Length Ratio (δ) and Module Error (εi), as quantitative guidelines for future fault analyses. Fulfilling the set values for these two parameters will avoid misinterpretations of fault growth histories. The parameter of Module Error (εi) reflects the effect of distinct sampling intervals on the accuracy of fault geometry measured through T-D plots. With Sampling Interval/Fault Length Ratio (δ) distinct from data resolution, εi decreases rapidly (Fig. 6-6). The latter parameter δ is suggested for faults of all scales based on the interpreted data sets.

6.5.1   Effects of data sampling on fault growth models

Theoretically, unless throw-distance (T-D) data are obtained with sampling intervals close to maximum data resolution, T-D plots can be significantly altered in terms of their geometry (thus reflecting increased ε_i values) in multiple ways (Fig. 6-12):

1)   Fault geometry is significantly changed,
2)   Maximum fault throw values are underestimated,
3)   Fault segments are overlooked,
4)   The geometry of fault linkage zone(s) is changed,
5)   The width of fault linkage zone is underestimated,

6) Fault interaction zones are lost (Fault B in Figure 6-4).

In order to constraint the changes that increasing sampling intervals have on fault geometry, the *Module Error* ε_i is proposed in this work. The analysis suggests that, when ε_i is over 0.09, the geometries of T-D plots are significantly altered, which means that fault analysis based on these same T-D plots loses its practical meaning. More specifically, ε_i should be well below 0.06, so that 92% of the analysed data are located within a threshold of 0.06 for distinct fault lengths (Fig. 6-6).

One of the key factors directly related to fault sealing properties is the roughness of fault planes (Lohr et al., 2008). When modeling slip tendency and leakage factor for faults interpreted on seismic data, details of fault planes rely on both the interpreters' accuracy and on fault-stick sampling intervals adopted (Fig. 6-11). With a larger sampling interval, which imposes artificial roughness on faults and especially for segmented faults, slip tendency and leakage factor analyses might be significantly changed (Fig. 6-11).

The results indicate that under defined pore-pressures, zones of high slip tendency are enlarged with larger sampling space. However, the values of maximum slip tendency are decreased (Fig. 6-11). In terms of leakage factors, the results indicate that with coarser sampling space, leakage factors are systematically underestimated, especially within areas where fault segments are linked, known to be potentially fluid pathways (Fig. 6-11).

Based on this analysis, it is strongly recommended the acquisition of fault data reaching maximum resolution when modeling fault slip tendency and leakage factors. Regardless the changes an increasing sampling space has on fault roughness and geometry (Yukutake et al., 2014), systematic misinterpretations of fault slip tendency and leakage factor will occur, hindering the complete understanding of fluid flow in sedimentary basins (Reis et al., 2013).

Module error (ε_i) increases significantly with increasing sampling intervals for T-D plots (Fig. 6-6). A new parameter δ is thus used to guide future measurements for T/D plots. In this analysis, the accuracy for the produced T/D plots was reduced to 46% with a data sampling space of 62.5 m (Fig. 6-5), i.e. every 5 inlines/crosslines. Hence, it is strongly recommended that data sampling every 37.5 m, i.e. every 3 inlines/crosslines
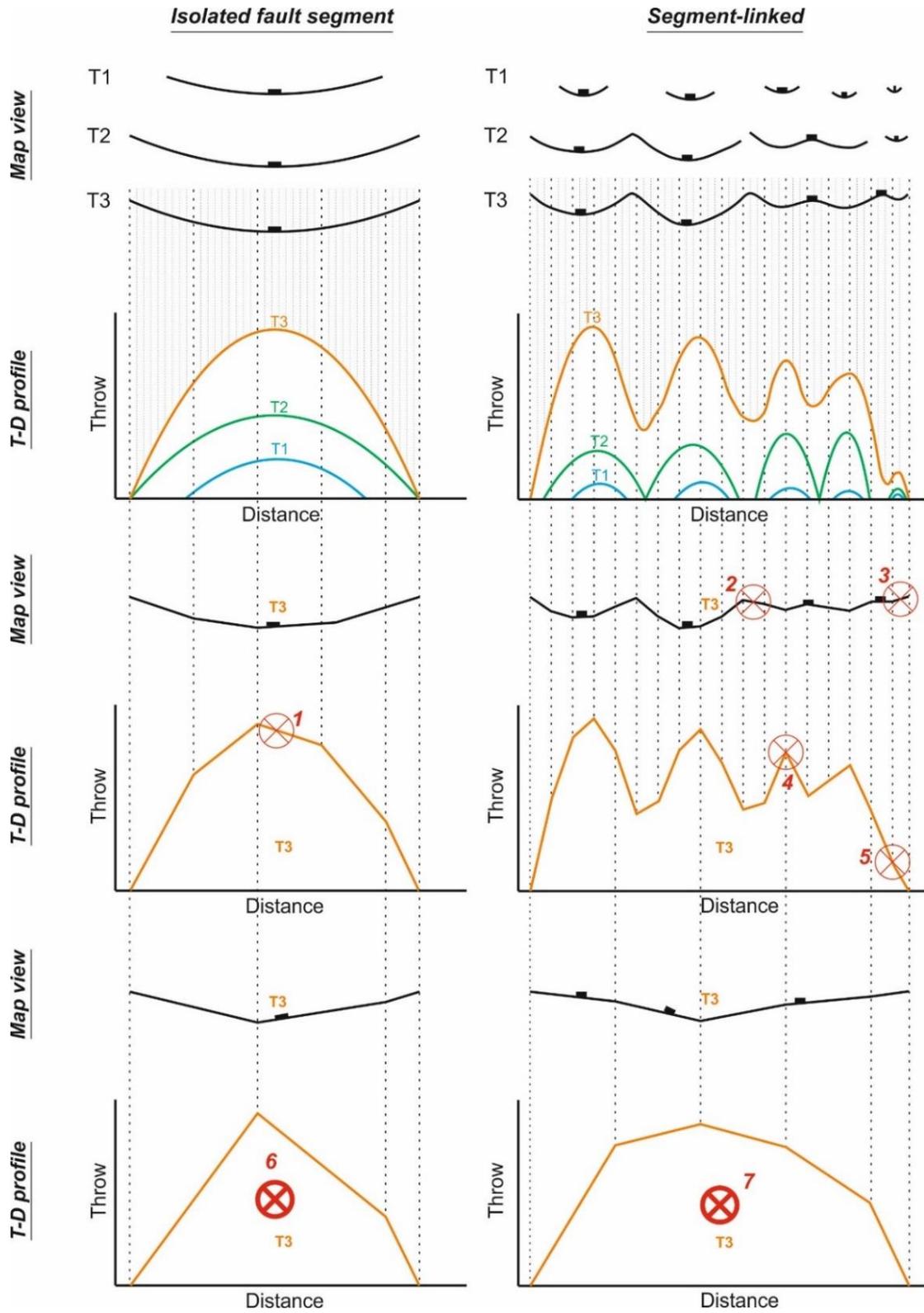
Fig. 6-12 Schematic sections showing the effects of sampling intervals on fault analyses. 1. Fault geometry is changed from symmetric to asymmetric. 2. The geometry of the fault linkage zone is significantly changed. 3. The geometry of an entire fault segment is changed. 4. Fault linkage zone geometry and width are significantly changed. 5. Fault segment is lost.

with an accuracy of 92% is used to collate T/D plots for faults that are interpreted on seismic data with a horizontal resolution of 12.5 m. For the sub-seismic faults, when the sampling interval increased to 25 cm, accuracy decreased to 37%, which means most of the T/D plots are unreliable, thus a maximum measuring spacing of 15 cm is suggested here (Fig. 6-5). For the rift-related faults in SE Crete, a maximum measuring space of 100 m is recommended.

6.5.2 Minimum values of δ necessary to constrain the two end-member fault propagation models

Even though the analysis in this chapter is capable of giving minimum sampling interval values to obtain reliable T/D plots for the seismic data from SE Brazil (acquired with a bin spacing of 12.5 m and a vertical data sampling rate of 2 ms twt), in academia and industry, seismic data reflect various horizontal resolutions, while measurements for sub-seismic faults are also scale-variant. Hence, a fixed sampling interval loses its practical meaning to guide producing T-D and T-Z plots for faults that are scale variant and resolution dependent. The ratio *Sampling Interval/Fault Length Ratio* δ eliminates the resolution and scale variance on fault analysis.

The results suggest that a maximum value δ=0.06 should be applied to faults of all scales to produce T/D plots for, i.e. measurements at < 6% of the fault length. More precisely, for faults interpreted with a sampling interval of 12.5 m on seismic data, a maximum value δ=0.07 is suggested. For outcropping faults in the Bristol Channel, a maximum δ value of 0.06 is indicated (Fig. 6-6c). For rift-related faults in SE Crete a maximum δ of 0.03 is recommended (Fig. 6-7c). Even though a threshold value for δ is suggested here as a basic principle, this work stresses that there is a clear difference in the minimum δ values for faults comprising only 1 fault segment and fault composed of distinct segments exists. This clearly shows that, without pre-existing knowledge on fault segmentation, a δ value of 0.05 should be used, i.e. throw should be sampled at intervals < 5% of the fault throw to produce reliable T-D plots (Fig. 6-7). This threshold δ value is valid for fault lengths ranging between 275 m and 3500 m (Fig. 6-8).

In Figure 6-6, a significant number of measurements are located within the threshold δ value set by this work. These measurements are regarded as inaccurate. The reason for this is that the required δ value necessary to produce reliable T-D plots decreases rapidly with increasing fault lengths (Fig. 6-8). A minimum δ of 0.03 for faults that are over 3.5 km is suggested during fault analyses as the required δ becomes relatively constant beyond these fault length values (Fig. 6-8). The δ required for the rift-related faults analysed (with fault lengths of 7.1 km and 19.5 km respectively) also examined that, for even longer faults, a smaller δ is essential, however, the value of δ is well around 0.03 (Fig. 6-7c). For smaller scales of analysis, faults in the Bristol Channel also shows a negative relationship with increasing fault length, i.e. smaller δ values should be applied when fault lengths increases (Fig. 6-8b).

This is the first work setting a standard value δ to produce reliable T-D plots at all scales. The results suggest that for different purpose(s), the required δ value(s) to produce accurate T-D plots also differs. However, if the research aim is to understand fault segmentation and linkage patterns, to analysis fault damage zones and to better postulate fault interactions, a minimum sampling interval of δ=0.05 should be adopted by interpreters and structural geologists. This means, in practice, the acquisition of throw (or displacement) data through T-D and T-Z plots at intervals reaching 5% of the total fault length. If this threshold δ value is not adopted, serious underestimations of fault segmentation, fault interaction, fault linkage zone width, and fault damage zones will necessarily occur.

Chapter 7

Discussion

7.1 Summary of main findings in the thesis

This section will briefly summarise the main findings in each of the main result chapters in this thesis. Chapter 4 presents novel results that focus on the evolution of a crestal fault system on a main salt ridge in the Espírito Santo Basin, SE Brazil (Fig. 7-1). The character and evolution of crestal fault families are presented in this chapter (Fig. 7-1). A transverse accommodation zone is recorded and documented for the first time on a developed salt structure, being kinematically and dynamically linked with the interpreted crestal fault system. The geometry of an 'opposite dipping fault arrays and a transverse accommodation zone' system was documented, indicating a potential weak zone on the crest of salt structures (Fig. 7-1). These findings have practical applications in the drilling safety assessments. Important findings include the scale of crestal faults, methods of identifying reactivation episodes over a developed salt diapir, propagation models of crestal fault families, evolution of a transverse accommodation zone, and weak zones on the crest of a salt diapir. With this novel result, it is suggested careful studies of crestal fault families before any drilling is decided over and around salt structures.

Chapter 5 presents focus on a system of faults comprising crestal faults, a strata-bound domino fault system and fluid flow features (Fig. 7-2). Key information on the evolution of strata-bound domino faults is presented in this chapter (Fig. 7-2). Specifically, mechanisms forming strata-bound domino faults are carefully examined. The results show that strata-bound domino faults comprises one of the most significant fluid flow features in sedimentary basins, which is closely associated with crestal faults reactivation and local slope instability. The results have practical applications in understanding fluid flow in salt-rich basins and promote the understanding of strata-bound domino faults formation. The research first examined the reactivation and propagation histories of crestal faults using throw vs. depth and throw vs. distance analysis for 34 crestal faults.

Slip tendency and leakage factors were subsequently computed for crestal and layer-bound domino faults. Following these statistical analyses, fluid flow features such as pockmarks were documented. This thesis suggests that strata-bound domino faults comprise one of the most significant fluid flow features in areas of important salt tectonics.
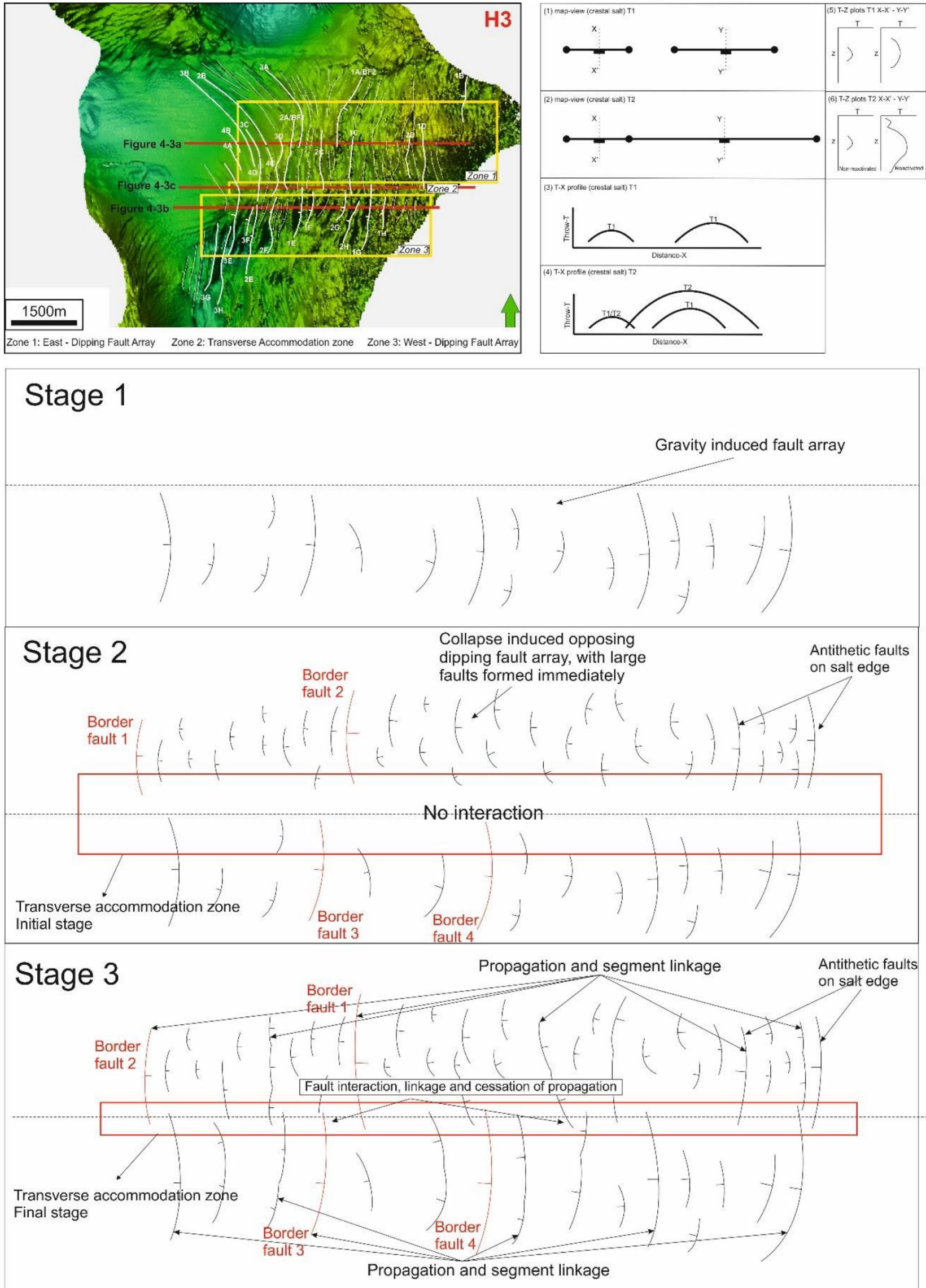
Fig. 7-1 Summary of the main findings and results from Chapter 4. Key findings include the recognition of the true geometry of crestal faults, a new method for identifying reactivation episodes on a developed salt diapir, the identification of varied propagation models for crestal fault families, the identification of a transverse accommodation zone and other weak zones on crest of a salt diapir.
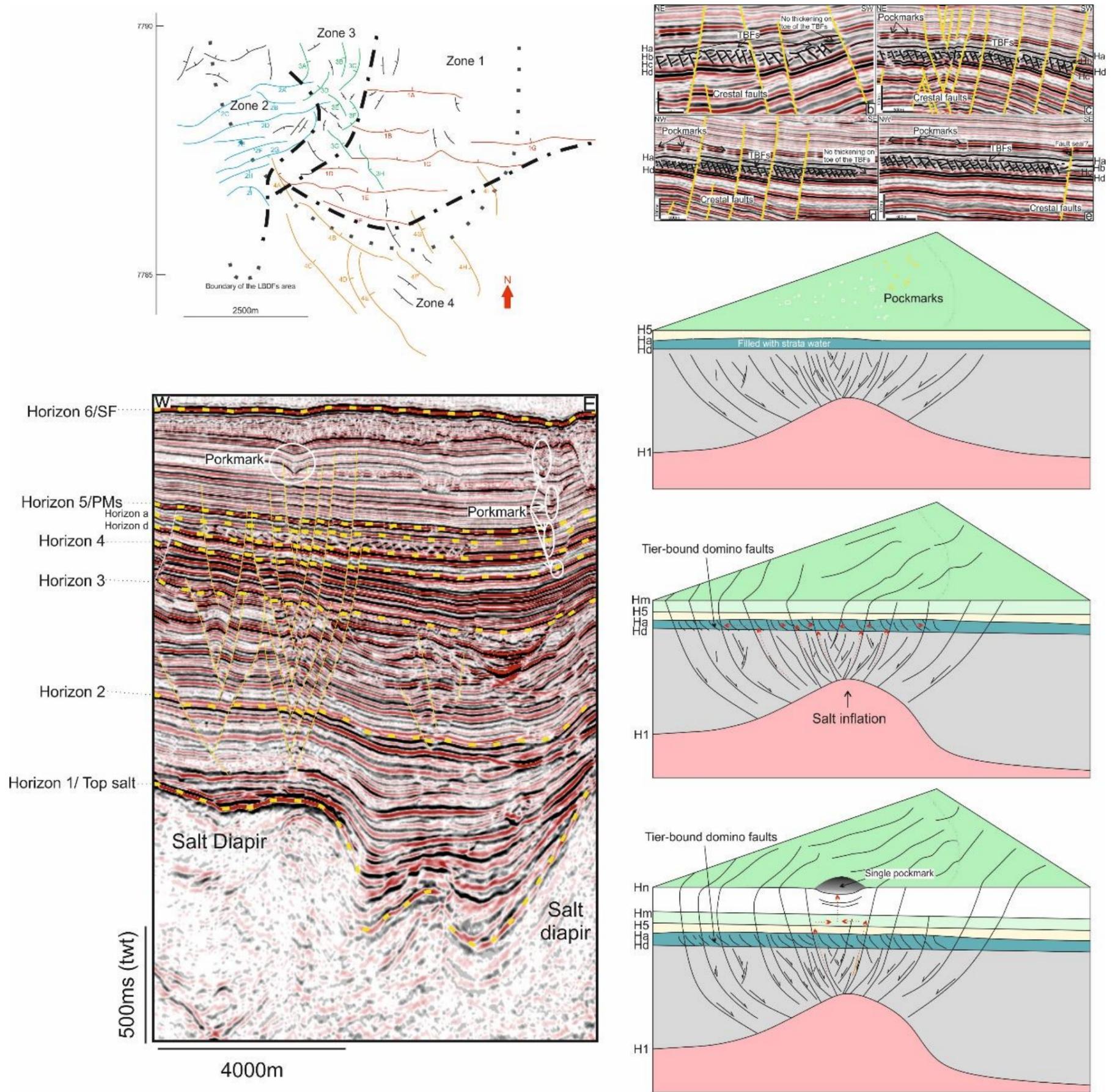
Fig. 7-2 Summary of the main findings and results from Chapter 5. Episodic fluid flow events are systematically documented in this Chapter. Importantly, a set of strata-bounded domino style faults (TBFs) is documented, and is subsequently analysed in terms of the mechanisms forming this fault family. The relationship between TBFs and crestal fault evolution is also addressed in Chapter 5. This chapter concludes that the formation of TBFs is associated with episodes of fluid release in regions dominated by salt tectonics.

Another important geological feature in this chapter is an oblique transfer zone with distinct geometry and evolution when compared to the transverse accommodation zone presented in Chapter 4 (Fig. 7-1). With the crestal fault system presented in Chapter 4 (Fig. 7-1), border faults are referred to as the main mechanism to accommodate the strain and stress. 'Border faults' in Chapter 5, however, plays only a secondary role in accommodate the strain and stress, that transfer faults in zone 3 are primary mechanisms for stress release within the study area.

Chapter 6 presents a new method to constrain the accuracy of fault interpretation (Fig. 7-3). Two parameters, *Sampling Interval/Fault Length* ratio (δ) and Module Error (ε_t) are proposed, with module error reflecting changes in fault geometry when coarser sampling intervals were adopted by interpreters (Fig. 7-3). The sampling intervals proposed in Chapter 6 offers guidance to structural geologists on how to obtain reliable data to interpret fault linkage models (Fig. 7-3). Chapter 6 is based on the limited understanding of crestal faults due to the fact that data resolution and limited (small) scale of crestal fault families makes them difficult to interpret. Thus, how data resolution and scale variance can really influence interpretation of fault growth histories are the focus of Chapter 6, which also directly relates its findings to the results in Chapters 4 and 5. Hence, main results in Chapter 6 include:

1. Sampling intervals have a significant influence on the analysis of fault growth histories in multiple ways: a) fault geometry is significantly changed; b) maximum fault throw values are underestimated; c) fault segments are unrepresented; 4) the geometry of fault linkage zones is changed; d) the width of fault linkage zone is underestimated; e) fault interaction zones are lost.

2. A sampling interval/fault length ratio of 0.05 is recommended for fault displacement analyses undertaken without prior knowledge of fault segmentation, and for fault lengths under 3500 m. The threshold of sampling interval/fault length ratio can be as high as 0.1 for faults that comprise only one fault segment. The threshold of sampling interval/fault length ratio of 0.03 is suggested for faults longer than 3500 m.
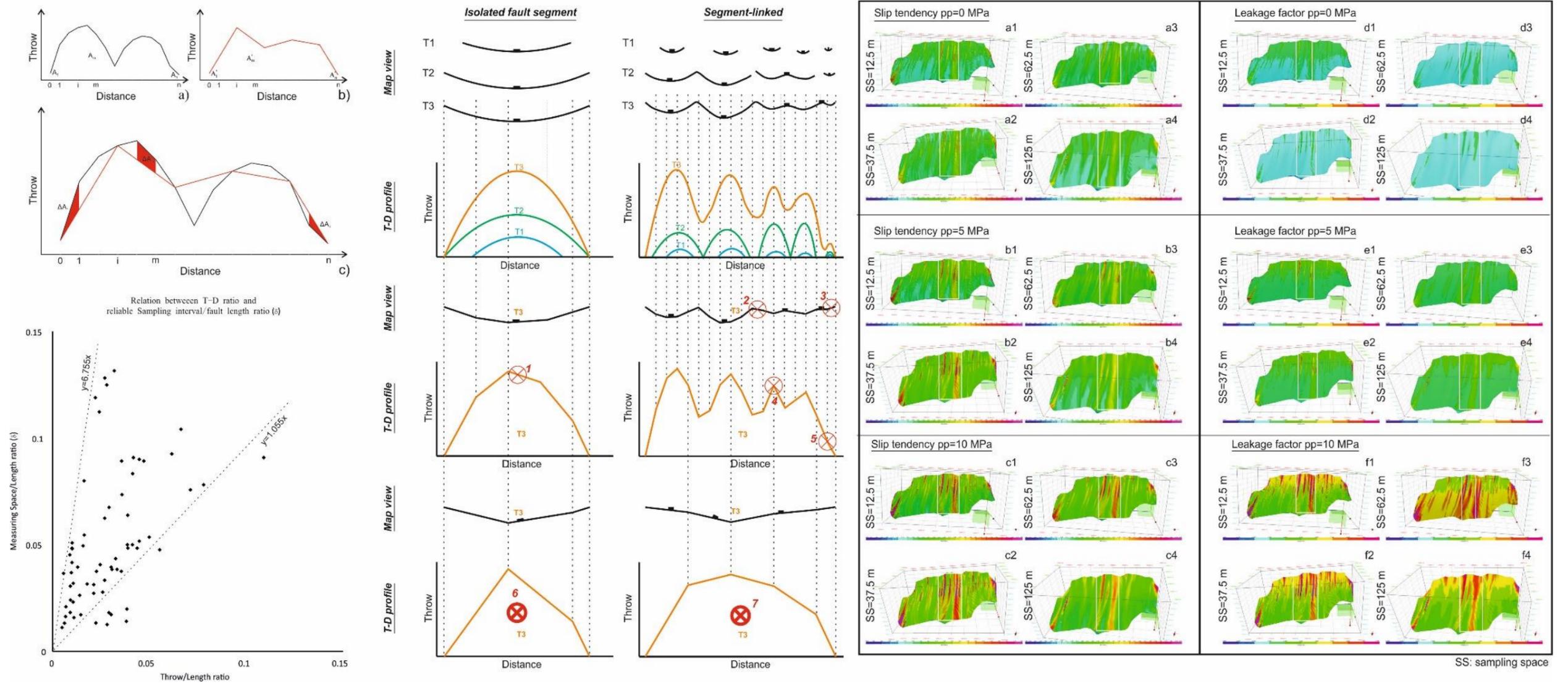
Fig. 7-3 Summary of the main findings and results from Chapter 6. A new method is proposed in this chapter to guide fault analyses using throw plots.

3. For detailed fault slip tendency and leakage factor analyses, a sampling interval/fault length ratio reaching maximum data resolution is strongly suggested to interpreters so to avoid systematic misinterpretations of fault sealing properties. This means T-Z picks at every single seismic reflection, fault sticks at every shot point and the use of Lidar data, or very small sampling distances in field-based analyses.

7.2 A discussion in the effect of scale variance on the interpretation of fault geometries, throw distributions and growth histories

Interpreted faults in this thesis for crestal faults are either associated with single, isolated, fault planes (e.g. Faults 1C, 1D, 2H in Figures 4-7 and 4-8) on time-structure maps or, instead, reflect segmented structures that experienced very moderate reactivation when compared to rift-related faults (e.g. Faults 2A/BF2 and 2C in Figure 4-8). They are all relatively young faults developing on top of an active salt ridge (Fig. 4-3). Analysis of faults in the thesis include seismic attributes such as curvature and variance, were later complemented by analyses of throw vs. distance (T-D) and throw vs. depth (T-Z). Faults analysed in Chapter 4 have fault lengths varying between ~410 m and 1750 m, with border faults ranging from 1250 m to 1750 m, i.e. values 2-3 times larger than the smaller segments highlighted on their T-D plots. When plotting T-D curves side-by-side, along the strike of successive faults, the observed data do not add up to a cumulative T-D distribution similar to Walsh et al. (2003) definition of a 'coherent' fault array. In addition, coherent T-D and T-Z distributions are not observed when comparing successive faults across the strike of the salt ridge. Instead, faults and fault segments identified on T-D plots (representing throw data collected along discrete faults at every single shot-point), and vertical seismic profiles, suggest an early stage of growth *sensu* the 'fault-linkage' (Kim and Sanderson, 2005) or 'isolated' growth models (Walsh et al., 2003) (Figs. 4-7 to 4-10).

7.2.1. Coherent and isolated fault models as complementary to the propagation history of faults

Based on Walsh and Watterson (1991), Walsh et al. (2003), Kim and Sanderson (2005) and Fossen and Rotevatn (2016), published definitions of 'isolated' vs. 'coherent' fault growth modes are based on geometrical and kinematic information so that one distinguishes faults formed under the two models on vertical seismic profiles, and not only through the compilation of isochron maps, via estimations of *Expansion Indexes* (EI), or using other techniques (see Alves, 2012). Geometric coherence, for instance, was defined by Walsh and Watterson (1991) as the existence of regular and systematic displacement patterns in a family of faults. Kinematic coherence reflects the existence of synchronous slip rates and slip distributions that are arranged such that *geometric coherence* is maintained (Peacock et al., 2000). In contrast to the latter concepts, T-Z data (and seismic profiles) for Group 1 to 4 faults in Chapter 4 show that they first nucleated in strata with multiple ages and thicknesses (Fig. 4-7 to 4-10). While including a significant number of structures propagating upwards from the 'top salt' horizon, the investigated salt ridge is dominated by faults that offset strata close to, or above horizons H2 and H3 showing, at places, thin growth intervals of distinct ages and geometries (Figs. 4-1 to 4-3). As Walsh et al. (2003) rightly stated (...) *failure to recognise that segments are components of a larger fault will inevitably lead to an over reliance of models on the growth of faults by linkage of isolated segments*. This important caveat leads to the classified (and identified) larger faults in separate groups (Groups 1 to 4, Fig. 4-4). This thesis suggests seismic and structural interpreters to follow a similar approach adopted in Chapter 4: to divide faults in distinct groups at the start of their analyses for the reason that their geometries, heights, T-Z and T-D patterns, are strikingly different (Figs. 4-13 to 4-17).

7.2.2. Scale variance in T-Z and T-D plots

It is essential to distinguish (and map) seismically resolvable faults from the moment one begins to analyse them. Faults analysed in Chapter 4, and their constituting

segments, show distinct orientations and curved geometries, characteristics that continue to the north and south of the study area around distinct salt structures (Figs. 4-1 and 4-2). The larger faults are seldom laterally linked and are cross-cut by a transverse accommodation zone (TAZ). The approach suggested in this thesis is: a) to distinguish and map the larger resolvable faults, and b) to understand their plan-view geometries using detailed structural maps, is important and precedes the recognition of fault segments using T-D plots. Fault segment recognition, however, is known to be scale-variant (Chapter 6), not depending on absolute throw (or displacement) values, but rather on the distinction of meaningful throw gradients representing segment linkages on T-D (or D_{max}/L) plots, accompanied by their analysis on vertical seismic profiles, time-structure maps, field structural maps, or at outcrop (Kim and Sanderson, 2005). It is also a known fact that distinct fault segments often present diverse T-D (or D_{max}/L) relationships due to multiple geological, and methodological, reasons when interpreting 3D seismic and outcrop data (Kim and Sanderson, 2005). Thus, one crucial question arising is that, at what scale(s) should one distinguish 'isolated' from other fault growth models (e.g. Fig. 7 in Kim and Sanderson, 2005). Based on the fault geometries observed in the study area, and on the size(s) of interpreted salt structures, this work considers that emphasis should be given to the 'isolated' faults in Groups 1 to 4, which clearly dissect the crest of multiple salt ridges and diapirs (Figs. 4-1 and 4-2), not only to their constituting segments.

To understand how scale variance can influence proper fault propagation models, analysis in Chapter 6 proposed the first quantitative methods on interpreters' selection of what the thesis defined as sampling intervals (Fig. 2-10). Findings in Chapter 6 suggests that ignoring effects of sampling interval for distinct fault families will lead to systematically misinterpretation of fault growth histories (Fig. 6-12).

7.2.3. Compilation of EI and isochron maps from synkinematic sequences

Fault analyses in Chapter 4 tested how could one ascertain the development of crestal faults above a salt ridge in SE Brazil when it is understood that crests of salt structures constitute broad areas of uplift, extensional collapse, fault reactivation and near-seafloor erosion without (or with truncated) synkinematic sequences. EI (*Expansion*

206

Index sensu Thorsen, 1963 in Groshong, 2006) data is often relevant to the analysis of large structures in rifts, or regional salt-detached extensional faults. However, the *larger* faults in the study area (namely Groups 1 in Figure 4-7) are still relatively small, curved and listric. The larger faults were also too often reactivated, and offset by opposite-dipping faults (*crossing conjugate faults* in Ferrill et al., 2000). The use of EIs in fault analyses is important but should be undertaken with great care. Sedimentation rates are hardly similar when comparing syn-tectonic growth strata in hanging-wall depocentres with correlative units on adjacent footwall blocks. Fault scarp erosion and enhanced deposition close to active structures, often via the accumulation of fan deltas, megabreccias and associated fault-degradation products, result in important caveats when estimating EIs for regional faults. The time-, climate- and lithology-dependent erosional processes that affect basin-bounding footwall scarps add further complexity to seismic and structural interpretations based solely on EIs.

7.2.4. Vertical resolution as a function of data sampling

Faults with offsets of 8 ms and less are clearly identified in the seismic data used in the thesis (Fig. 4-10). The value of 8-10 m suggested for *near seafloor strata* is, to all effects and purposes, a very conservative estimate used in virtually published works dealing with the interpretation of seismic data. It is based on the dominant frequency of the acquired seismic data and, specifically for the study area, was estimated taking into account the low frequency of seismic reflections observed in sediment drifts accumulated below the modern sea floor (e.g. Alves et al., 2012; Gamboa et al., 2015). Upon careful analysis, one can use the wiggle display on a seismic workstation to verify that trace (or wiggle) spacing, and the *de facto* vertical seismic resolution at the depth of the analysis, is at least 4 ms for the high-frequency strata below Horizon H5, in which the majority crestal faults are observed (Fig. 4-3). Fault offsets below 4 ms were often resolved in the interpreted seismic volume when approaching the faults' lateral tips, hence seismic vertical resolution is surely beyond 1/4 of the characteristic wavelength (i.e. still a higher resolution than 8-10 m), or dominant frequency. Seismic and structural interpretations to measure definite, unequivocal fault offsets are suggested. In the study area, only the four (4) faults in Group 4 present average offsets around 4-8 ms two-way time (Fig. 4-10).

The other 80 faults mapped show offsets of 20 ms or more, in average, reaching more than 80 ms over the crest. These are values 5 to 20 times larger than the sampling interval of the seismic volume, i.e. significant values when considering that this thesis images shallow structures (< 0.75 s two-way time below the sea floor).

7.2.5. Propagation styles of crestal faults

Comprehensive information on physical models and seismic-based studies of salt-related faults, from Letouzey et al. (1995), Schuster (1995), Ge et al. (1997), Ge and Jackson (1998) to Rowan et al. (1999), Cotton and Koyi (2000) and more recent work, have shown that areas of gravitational movement of overburden strata above evaporites, when developing in similar geological settings as the study area, will form discrete fault segments, often concave-shaped, that link together in later stages of crestal collapse (see also Vendeville, 1991; Childs et al., 1993; Vendeville et al., 1995; Vendeville, 2005; Morley, 2007; Clausen et al., 2014). Importantly, Fossen and Rotevatn (2016) consider these same geometries as occurring naturally in systems that comprise competent strata (sandstone, limestone, basalt layers) over a softer or viscous unit (shale or salt) or, instead, in clastic sediments sliding on a low-angle décollement of evaporites or overpressured shale on a passive margin. They lead to the development of 'isolated' faults. Based on the analysis of faults in this thesis, it is interpreted that the great majority of crestal faults in the study area as having been formed in association with recurrent episodes of salt growth, subsidence (crestal collapse) and associated crestal erosion, following an 'isolated' fault growth model (Fig. 4-15). The thesis also postulates that gravitational collapse is a significant process in the study area, and that border faults (and transverse accommodation zones) are key features controlling this same collapse, separating areas on a salt ridge with distinct fault geometries. The complex fault geometries observed in in Chapter 4 are essentially a result of the gravitational component (variable in space and time) that, ultimately, generated 'isolated' faults separated by a transverse accommodation zone (Figs. 4-14 to 4-16).

7.2.6. Summary

Misinterpretation of fault propagation histories result from an important, and often overlooked, paradigm concerning the use of T-D and T-Z plots in fault analyses: the scale(s) at which one collects and interprets fault throw (or displacement) data should be defined early in any structural analysis (Walsh and Watterson, 1991; Kim and Sanderson, 2005; Torabi and Berg, 2011). In the examples analysed in Chapter 4, the predominance of curved faults, curved fault segments, and throw minima between adjacent faults (and between fault segments), indicate lateral propagation of fault tips prior to segment linkage. This is particularly true when considering the structures interpreted as archetypal examples of crestal faults during their early growth stages (see Fossen and Rotevatn, 2016). Knowing that the interpretation of fault propagation styles using T-D and T-Z data is scale-variant (Chapter 6), and geometric coherence should occur at smaller scales of observation in even the most 'isolated' of faults (Walsh and Watterson, 1991), one is compelled to stress that interpretation errors are bound to occur if one systematically overlooks the effects of scale, and data sampling, on structural analyses. This caveat is most evident in an era of ever-so-quickly improvements in the quality and resolution of 3D seismic data, remote sensing imagery and outcrop-based studies. It is suggested that structural interpretations of high-quality seismic data should be based on the recognition of the 'trace length in map view' or 'the longest horizontal dimension' of distinct faults (Cartwright et al., 1995; Schultz and Fossen, 2002; Kim and Sanderson, 2005), with further detail being built upon the recognition of these primary structures.

7.3 Salt seal failure for fluid flow

Salt giants, which comprise vast thick and vast volumes of evaporites (Hübscher et al., 2007), commonly show acoustically transparent internal reflections on seismic data, and have been previously regarded as lithologically homogeneous (Schoenherr et al., 2007b). With improved seismic data acquisition and processing, the internal character of salt giants has been progressively revealed in detail. Recent studies indicate that salt rock is impure (Warren, 2016; Davison, 2009; Schoenherr et al., 2007b), and that hydrocarbon

residuals exist in fractures inside these 'impure' evaporite intervals (Schoenherr et al., 2007b). New seismic data have also revealed seismically resolved strata and internal deformation within salt giants (Alsop et al., 2015; Jackson et al., 2014). This clearer imaging of salt structures has challenged the intrinsic view that salt rock is a perfect seal, in contrast to results from laboratorial experiments. These latter experiments indicate that the permeability of salt rock is often nanodarcy or less (Popp et al., 2001; Schulze et al., 2001), but with increasing burial depths and elevated temperatures, intercrystalline or polyhedral permeability in rock salt can reach that of sandstones (Lewis and Holness, 1996). Furthermore, with increasing pore pressures, i.e. with a decreasing effective stress within rock salt, faulting or fracturing will occur within salt intervals (Davison, 2009).

Examples of the first time intra- and supra-salt fluid flow features in SE Brazil (Figs. 7-4 and 7-5) are presented in the following sections so to understand seal failure mechanisms in salt giants and how they are related to supra-salt fluid flow as revealed in Chapter 5. Robust evidence for fluid flow both within a salt giant and within its supra- salt sediments are presented. New models of fluid flow through salt intervals are suggested in this section, and shown to be potentially applicable to other regions in the world with important salt tectonics.

7.3.1   Fluid flow sourced from salt overhangs

Interpreted fluid flow features chiefly comprise gas chimneys (Figs. 7-5a to 7-5e), active salt intrusions, bright spots (some of which are interpreted to be free gas accumulations), dissolution pockmarks on top of salt structures, and polygonal faults (Fig. 7-5). A number of gas chimneys are located directly over various salt structures and provide direct evidence that fluids forming the gas chimneys are sourced from within these same salt structures (Fig. 7-5). The geometries associated with salt dissolution, mega-dissolution pockmark (with a diameter of ~ 1257 m, Fig. 7-5a), gas chimneys, polygonal faults and free gas accumulations indicate that a significant volume of fluid existed and flowed through salt structures (Fig. 7-5a). Pushed-down seismic reflections within salt structures, and giant dissolution pockmarks on the crests of these latter, agree with data from the Mediterranean Sea (Bertoni and Cartwright, 2015), and relate to
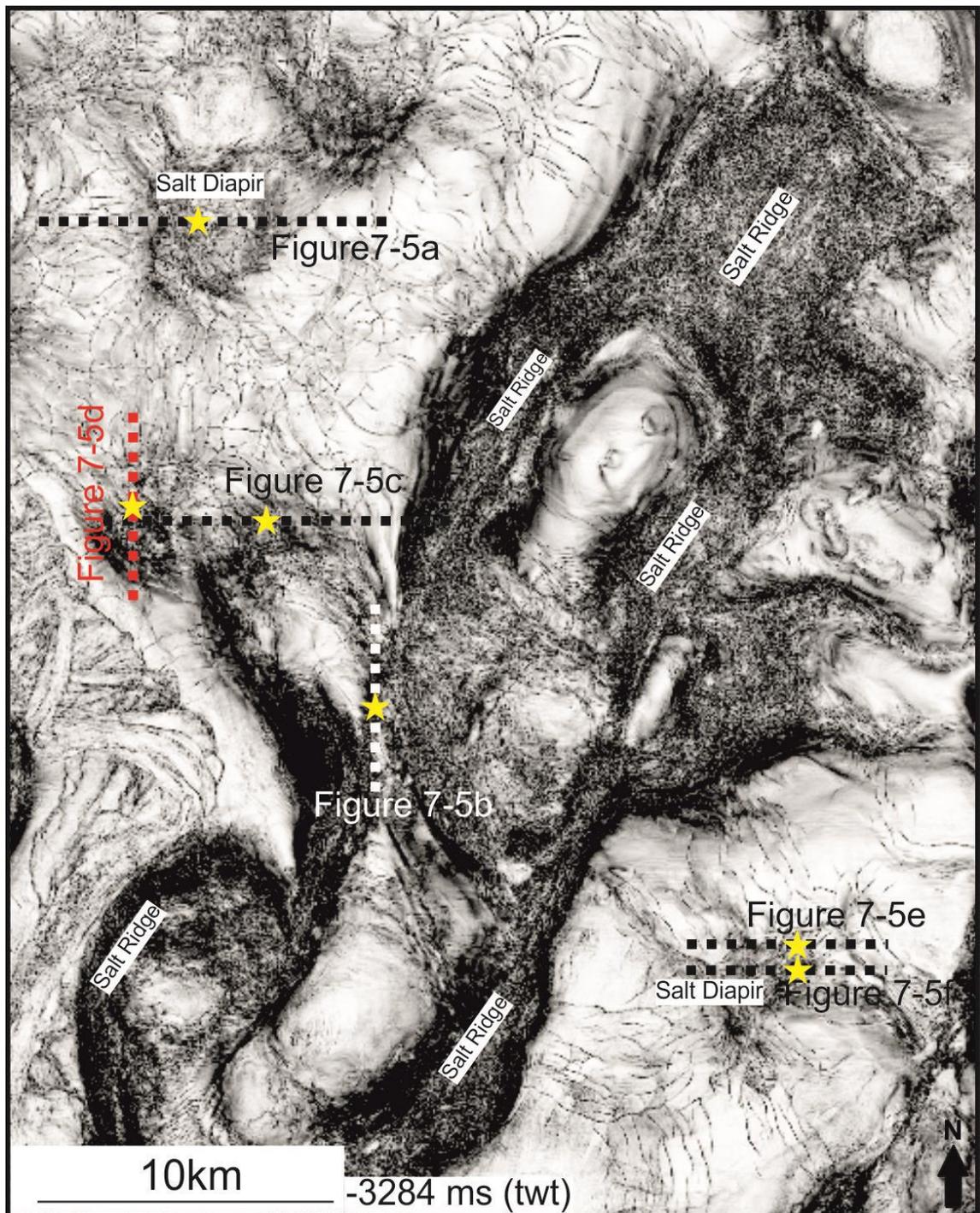
Fig. 7-4 Locations of the interpreted fluid flow features in Figure 7-5.
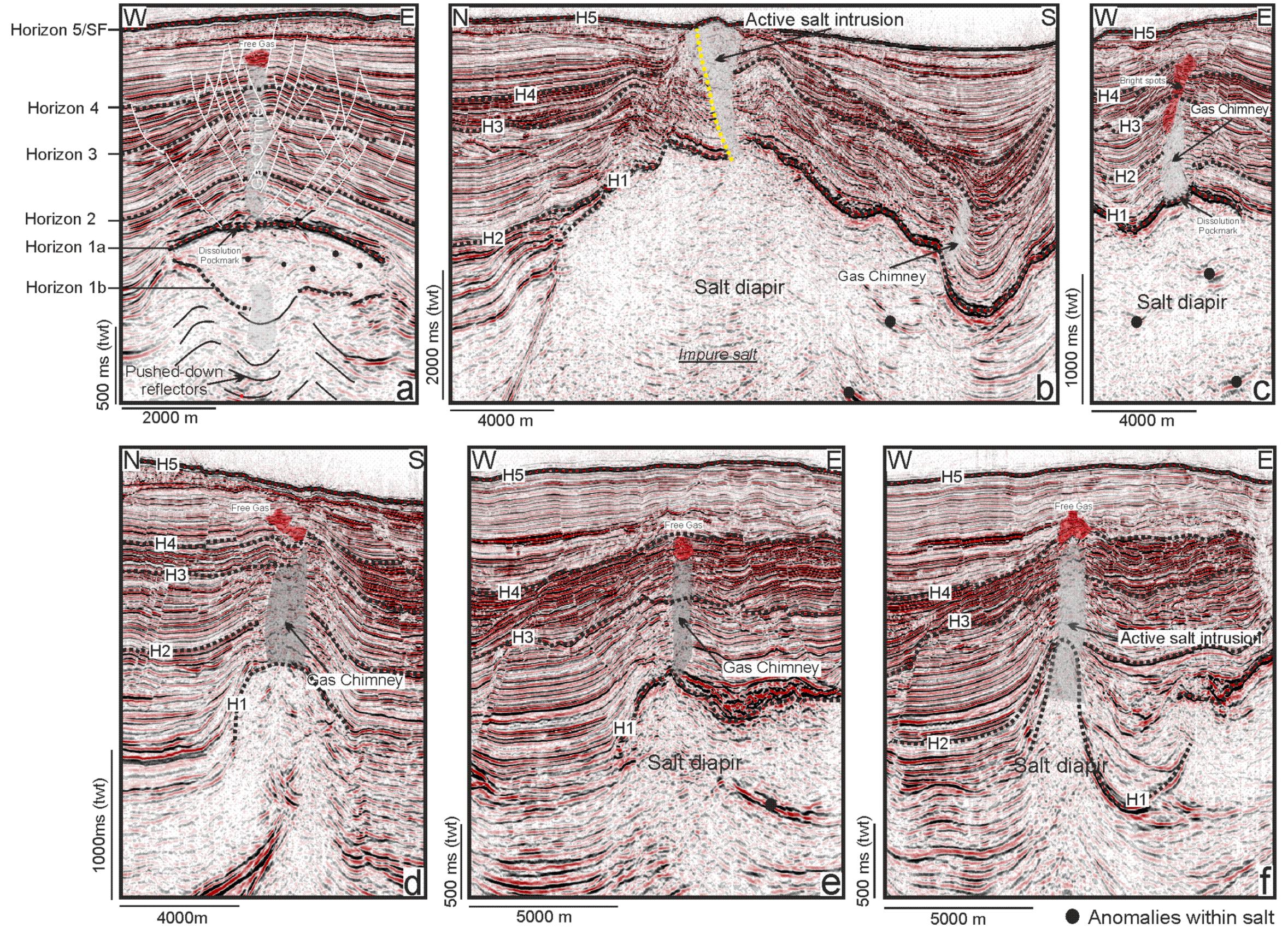
Fig. 7-5 Intra-salt anomalies comprise dissolution-related 'pushed-down' seismic reflections (a and c), continuous strata reflecting impure salt (b), and continuous intra-salt sediment packages with high amplitude (d and e). Post-salt fluid flow anomalies chiefly comprise gas chimneys (a, c, d and e), active salt intrusions (b and f), bright spots (some of which are interpreted as free gas accumulations) (a and c-f), dissolution pockmarks on top of salt structures (a and c), and polygonal faults (a). a) A system of 'pushed-down' reflections and high-amplitude reflections within the salt overhang, upright gas chimney, polygonal fault system and bright spots on top of this same gas chimney; b) high-amplitude anomalies within salt diapirs. Active salt intrusion along a large crestal fault (which is defined as a border fault by Ze and Alves, 2016), shaping the modern sea floor, and a tilted gas chimney. The dashed yellow line indicates the relative location of the border fault; c) upright gas chimney and bright spots, which are located on top and beside the gas chimney; d and e) upright gas chimney; f) active salt intrusion. The roots of the gas chimneys are located on the crest of the underlying salt structures, with burial depths of ~ 1500 m based on velocity data from Deep Sea Drilling Project (DSDP) Site 516 (Baker, 1983). The active intrusion in b) has a smaller overburden thickness than the gas chimneys in a, c, 3d and e.

localised (dissolution-related) upwards migration of fluids. As an example, Figure 3c presents a mega dissolution pockmark, with a diameter of ~ 1000 m, on the crest of a salt diapir. In addition, internal salt deformation in Figure 7-5c is associated with pushed-down seismic reflections that, similarly to Fig. 7-5a, suggest dissolution-related fluid flow through salt to be the main mechanism responsible for salt seal-failure in this case (Fig. 7-5c).

Apart from the examples of dissolution-related fluid flow from salt giants into supra-salt sediments, small-scale salt intrusions also indicate a close relationship with fluid flow (Hovland et al., 2006) (Figs. 7-5b, 7-5e and 7-5f). The active salt intrusion in Figure 7-5b shows strong and continuous internal reflections, demonstrating active fluid flow prior to salt intrusion or, instead, at the same time as the salt intrusion. Figure 7-2f shows an active salt intrusion with no apparent high-amplitude and continuous internal reflections. However, moving further north (Fig. 7-4), the active salt intrusion changes into a gas chimney (Fig. 7-5e). Evidence for bright spots on top of the active salt intrusion (Fig. 7-5f), and the concomitant presence of the same gas chimney to the north (Fig. 7-5e), prove that active salt intrusion was accompanied by significant sourcing of fluids from the salt diapir towards the sea floor.

7.3.2   Active salt intrusion associated with crestal faults

In the study area, crestal faults are well developed (Ze and Alves, 2016). This type of faults are active conduits for fluid flow. As indicated by Ze and Alves (2016), border faults show the largest throw values within a crestal fault system, and remain active during the propagation of crestal fault system. The active salt intrusion in Figure 7-5b presents one of the best published examples in which salt uses crestal faults on top of the salt to intrude younger strata (Fig. 7-5b). The yellow line in Figure 7-5b indicates the relative location of a main crestal fault with a throw value of over 100 ms twt. According to Alves et al. (2009) and Ze and Alves (2016), this particular crestal fault has an abnormally large throw, a character defining it as a border fault on the crest of the salt diapir. In this case, the active salt intrusion is likely to have used this crestal fault as a weak point for salt to intrude. However, as indicated in the previous section, the salt intrusion is also associated with important fluid flow.

7.3.3   Location of fluid flow features

The study area is located in the compressional zone of the Espírito Santo Basin (Ze and Alves, 2016), which is currently experiencing significant halokinesis. As a result, most of the post-salt strata above are highly faulted, with salt occurring close to the sea floor (Fig. 7-5b). The observed examples of focused fluid flow are chiefly located on top of large salt diapirs (Figs. 7-1 and 7-2). A marked phenomenon is that, where the gas chimneys occur, post-salt sediment thickness is relatively similar, approaching values of 1370 ms (Fig. 7-5a), 1590 ms (Fig. 7-5b), 1380 ms (Fig. 7-5c), 1310 ms (Fig. 7-5d) and 1435 ms (Fig. 7-5e), respectively. The root of the gas chimney in Figure 7-5b is deeper than the other salt structures due to continuous growth of the main salt body towards the sea floor. In parallel, the fact that the gas chimney in Figure 7-5b is tilting to the south, while other gas chimneys are clearly upright, also indicate the continuous uplift of salt diapir after the formation of this same chimney (Fig. 7-5b).

Bright spots and free gas interpreted in the study area are located directly above the gas chimneys in Figures 7-5a, 7-5c, 7-5d and 7-5e. Horizon 4 is interpreted to be Late

Oligocene in age, with the underlying continuous, high-amplitude strata representing volcaniclastic material deposited from the Eocene to Late Oligocene (Fiduk et al., 2004; Ze and Alves, 2016). Bright spots in Figures 7-5a, 7-5d and 7-5f are located within Unit 3, and the gas chimney pierced through the brittle volcaniclastic unit. In Figures 7-5c and 7-5e, bright spots are located within the volcaniclastic unit, a character indicating that the marine mud-rich succession deposited above worked as a regional seal interval.

7.3.4   Intra-salt anomalies

Intra-salt anomalies are summarised as dissolution-related push-downs (Figs. 7-5a and 7-5c), and relatively continuous high-amplitude reflections in intra-salt sediment packages (Figs. 7-5 to 7-8). These intra-salt sediment packages are postulated to be clastic deposits, or rafts. However, examples given by Jackson et al. (2015) also indicate that the same high-amplitude reflections are due to different salt compositions. The base of the salt structures cannot be revealed in the 3D seismic volume interpreted in this study, thus it is hard to tell the exact origin of these packages. Such intra-salt seismic features are, nevertheless, relevant in terms of its origin, composition and relationship with fluid generation and compartmentalisation within salt structures.

7.3.5   Summary

The study area records significant halokinesis and comprises pre-salt successions that form the reservoirs with the largest economic importance in SE Brazil (Fiduk et al., 2004). It is inferred that even though salt giants can comprise perfect seals for fluid flow, they can bear sufficient fluids and act as direct paths for fluid flow into shallower successions. As indicated by physical models (Dooley et al., 2015), outcrop data (Schléder et al., 2008) and seismic studies (Strozyk et al., 2012; Davison, 2009; Bertoni and Cartwright, 2015), if fluid pressure reaches a critical value or a percolation threshold
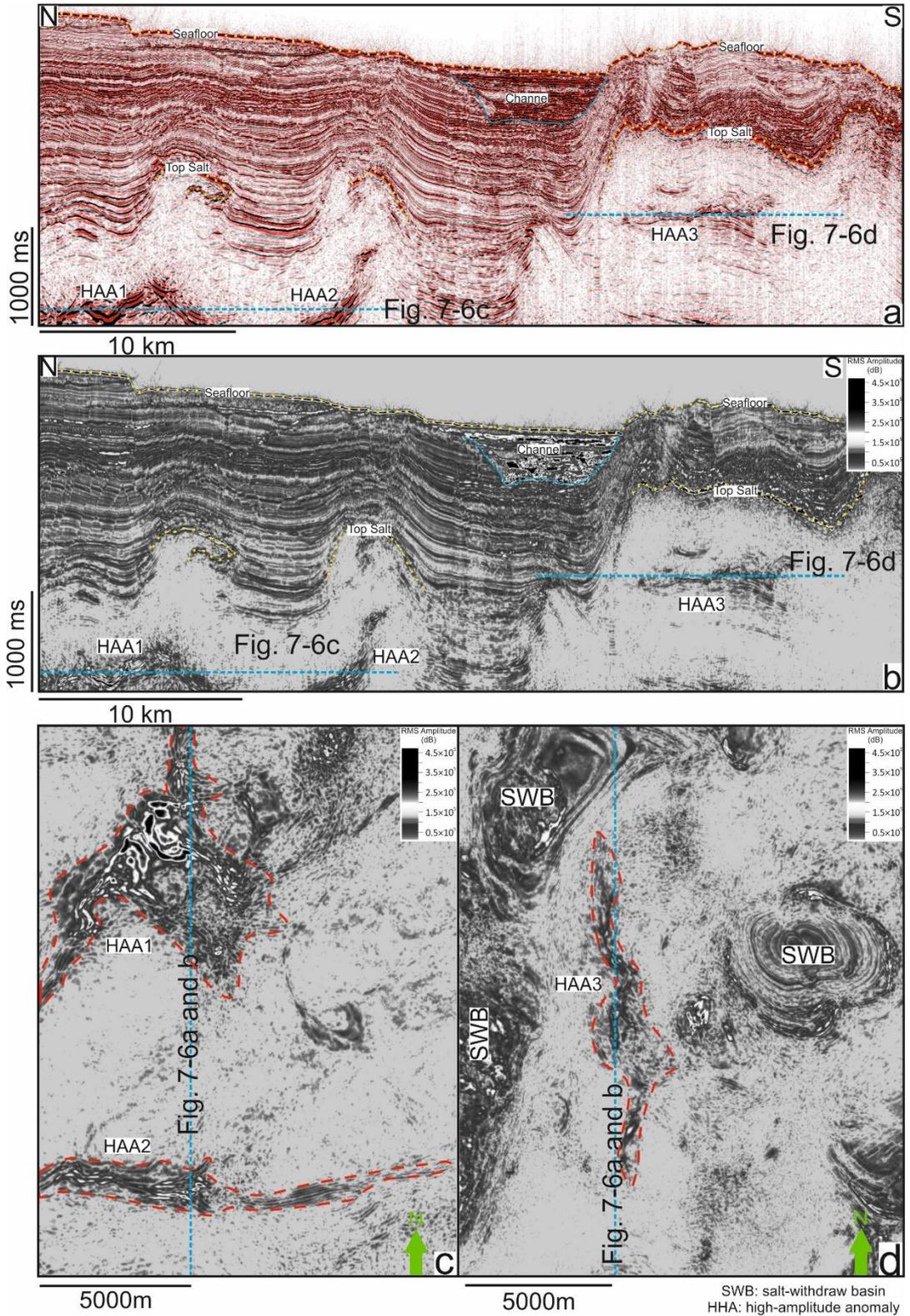
Fig. 7-6 Seismic section (a) and root-mean-square (RMS) amplitude maps (b-d) show intra-salt anomalies of relatively high amplitude. High-amplitude and continuous reflections within salt giants are clearly presented and interpreted by RMS amplitude maps, which reflect the presence of clastic sediments or anhydrite layers. Either of these lithologies can potentially generate large volumes of fluid, which will significantly change the physical properties of salt giants.

216
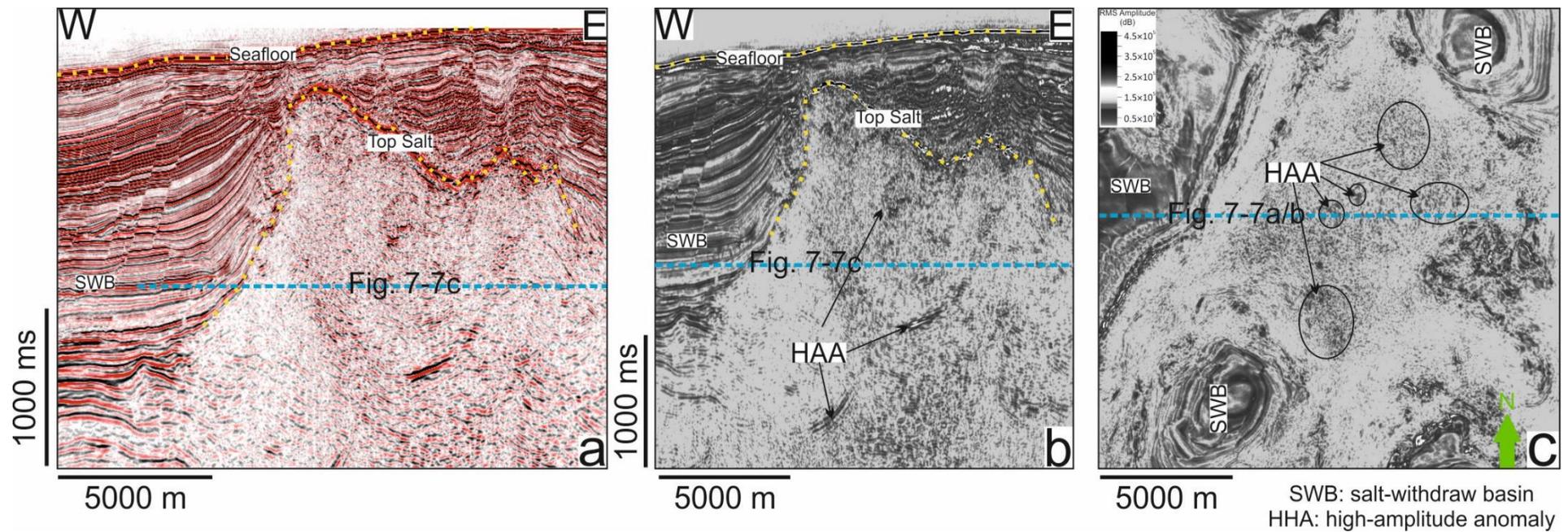
Fig. 7-7 a) Seismic section, b-c) root-mean-square (RMS) amplitude maps show intra-salt high-amplitude anomalies. Intra-salt sediment packages with high-amplitude continuous reflections are broadly documented in the study area (Fig. 7-6). Amplitude anomalies without continuous reflections are interpreted as impure rock salt.
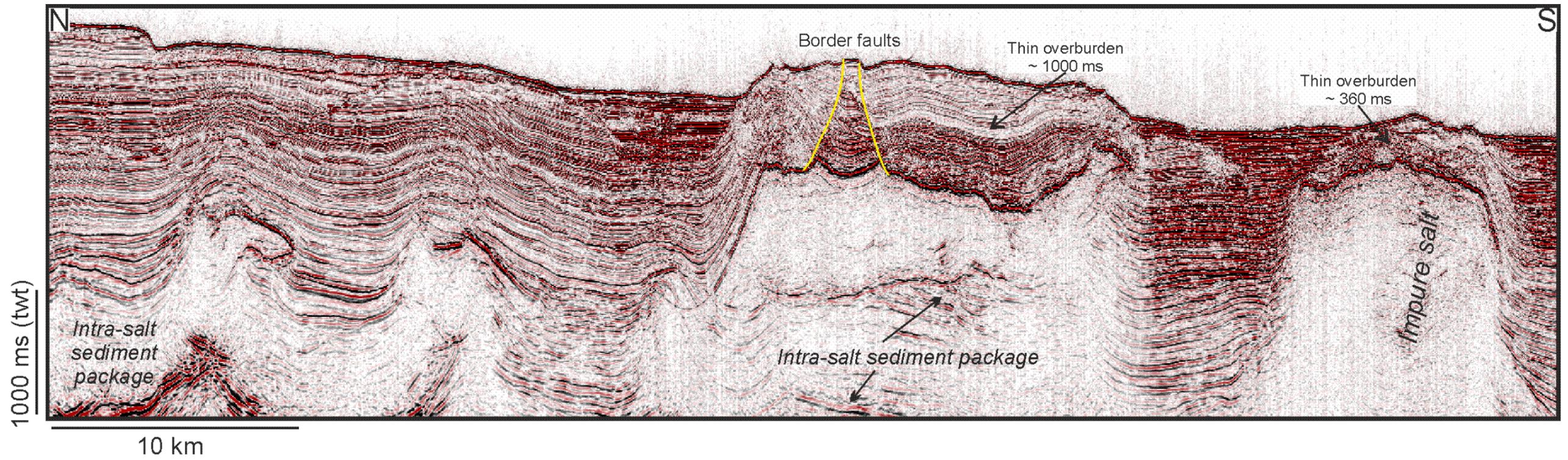
Fig. 7-8 Seismic section showing intra-salt high-amplitude anomalies and thickness of post-salt strata. With thinner post-salt sediment thickness, scarce examples of post-salt fluid flow features are observed.

218

is reached, pore networks within salt diapirs become connected, enhancing the permeability of salt structures and allowing fluid to be transferred within salt structures (Ghanbarzadeh et al., 2015; Popp et al., 2001). Residuals of bitumen have been widely documented within salt rock (Schoenherr et al., 2007a). Furthermore, internal deformation is prevalent and complex within salt structures (Jackson et al., 2014; Jackson et al., 2015; Alves et al., 2017), favouring fluid flow within salt giants.

The 3D configuration of the giant pockmarks, gas chimney, polygonal faults and free gas offshore Espírito Santo also agree with the inference that fluids forming focused fluid flow events in the study area originate from salt diapirs (Fig. 7-5a). Hence, this study proposes a conceptual model for fluid accumulation and flow through giant salts based on the interpreted data from SE Brazil (Fig. 7-9).

Pre-salt sediment bear large volumes of fluid in underlying structural traps in the ESB (Fiduk et al., 2004), a character generating excess pore pressure underneath salt diapirs. If the fluids comprise mainly water, dissolution-related fluid upwelling might pierce through the salt structure and form pockmarks both at the bottom and top of salt diapirs (Bertoni and Cartwright, 2015). However, pre-salt successions in the Espírito Santo Basin are known to bear large reserves of oil and gas. Thus, a second possible mechanism is through the maturation of organic matter in intra-salt sediment packages. Rock salt is thermally conductive (McBride et al., 1998), which indicates that even if organic matter in adjacent salt-withdrawal basins may have not reached maturation windows, organic matter within the intra-salt sediment packages may be mature and generating oil and gas (Fig. 7-9b). As the study area is located within the regional compression regime and allochthonous salt bodies such as salt canopies are common in the study area, the underlying pre-salt clastic sediments might play as a pathway for fluids from adjacent salt-withdrawal basins transferred into the salt body (Figs. 7-5 and 7-9c).

Dissolution in the upper part of the salt structures indicates the existence of water within them, a result of any of the mechanism illustrated above (Figs. 7-9a to 7-9c), or from hydrite dewatering processes generating layers of anhydrite within giant salt (Jackson et al., 2014). This study also shows strong and continuous reflection intervals within the salt giants (Figs. 7-5 to 7-8), hinting at the existence of anhydrite layers within the salt package or within intra-salt clastic sediment packages.
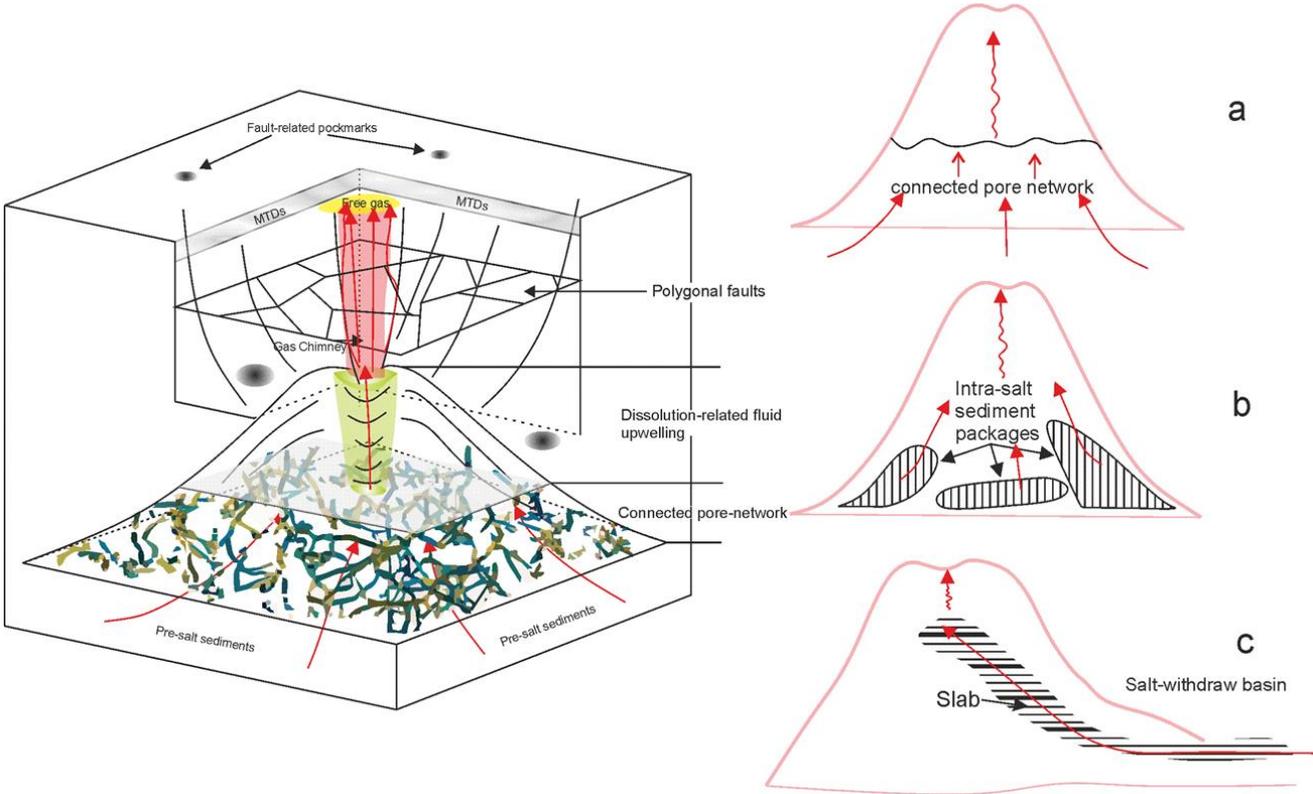
Fig. 7-9 Conceptual models for salt (seal) failure, based on the case studies in this thesis (SE Brazil). a) Active pre-salt fluid percolation into the salt structure through connected pore networks at the lower part of the salt structures comprise, in this case, the main mechanism for the accumulation of fluid within salt structures. b) Oil and gas generated from the maturation of organic matter within intra-salt sediment packages, and/or water generated from hydrite dewatering processes become the main mechanisms for fluid accumulation within salt structures. c) Fluid transferred into the salt structures through slabs that stretches into salt-withdrawal basins are, in this case, the main mechanisms for fluid accumulation within the salt structures. With a significant volume of fluid within salt structures, dissolution-related fluid flow into the supra-salt succession is the main mechanism for salt-seal failure.

220

Regardless of a thermogenic or diagenetic origin for fluid in the study area, the results suggest that focused fluid flow will form gas chimneys above salt giants when at least two critical conditions are observed: 1) a certain thickness of overburden strata on top of the salt structures, 2) the generation of highly developed large crestal fault systems. Even though the threshold overburden thickness in which fluid chimneys are observed off Espírito Santo reaches values around 1400 ms twt, or ~ 1500 m, this same values should vary elsewhere in SE Brazil depending on the effective pressure within the salt giant and the intrinsic composition of supra-salt sediments. It is therefore postulated that if overburden strata is thinner than a certain value, or pressure imposed by growing salt increases, active salt intrusion occurring together with fluid flow should replace focused fluid flow through salt giants.

7.4 Relating fluid flow features on seismic data with subsurface trap geometries (Espírito Santo Basin, SE Brazil)

7.4.1 Trap types in the Espírito Santo Basin

The correct identification of hydrocarbon traps comprise an important part of oil and gas exploration. A variety of trap types exist in all sedimentary basins. It is arguable whether the supra-salt succession in the study area of the Espírito Santo Basin has reached the 'cooking kitchen' to generate oil and/or gas, and whether the supra-salt successions have any economic reservoirs. However, seismic sections in Section 7.3 provide direct evidence that fluid sourced from pre-salt successions contributes to supra-salt fluid accumulations (Fig. 7-5). Traps in Figure 7-5 reveal a prevalent type of traps in salt tectonics, traps on top of diapiric salt structures, which are often sealed by shale/mud successions deposited at the stage of quiescent stages in salt tectonics (Figs. 7-5).

Three broad categories of traps are classified in the literature as: structural traps, stratigraphic traps, and combination traps, the latter of which exhibit both structural and stratigraphic elements. The following section relates fluid flow features (mostly seismic amplitude anomalies) in the Espírito Santo Basin to trap geometries. Six types of traps are classified within supra-salt successions of the study area (Fig. 7-10).

Type I and type II traps are fault traps acting as competence seals (Figs. 7-11 and 7-12). With type I traps, fluid migrated through faults and entered reservoirs located on both sides of the same fault (Fig. 7-11). Often, a succession with weak/transparent reflections, interpreted as a muddy unit, lies on top of the traps acting as top seals (Fig. 7-11). With type II traps, high-amplitude anomalies often lie between two faults, with both faults playing as seals for further fluid flow (Fig. 7-12). With the given examples, type I traps are more prevalent than type II traps in the study area, and are often have larger lateral extents (Figs. 7-11 and 7-12).

Type III, IV and V traps are defined as lithology traps, in which the top and lateral seals are controlled by lithology (Figs. 7-13 to 7-15).

Type III traps are often associated with U/V shaped depressions (Fig.7-13). The trap can be located at the bottom of the depression (Figs. 7-13c and 7-13e), within the depression (Fig. 7-13f), or on top of the underlying depression (Figs. 7-13a, b and d). A common characteristic of all these traps is that, above the traps, a soft succession shows weak and transparent reflections (Fig. 7-13).

Type IV traps are of smaller scales compared to type III traps (Fig. 7-14). This type of traps is readily identified by their relative locations on top of pockmarks (Fig. 7-14), indicating that fluid injected into these traps are sourced from deeper reservoirs through the pockmarks (Fig. 7-14). Top and side seals for this type of trap are again soft successions showing weak and transparent reflections (Fig. 7-14). Type V traps are typical lithology traps, and no apparent faults can be associated with the amplitude anomalies in Figure 7-15. Type V traps are often tilted, with soft sediments at the bottom and laterally, acting as seals (Fig. 7-15). Parts of type V traps is are within a succession with strong and continuous seismic reflections, likely porous but relatively fine-grained sediments (Fig. 7-15). Migration of fluid into this type of trap occurs by lateral migration through the porous and fine-grained material (Fig. 7-15). This type of trap reflects an important fluid migration mechanism in salt tectonics; migration along salt flanks.

When comparing the three types of lithology traps, type III shows the largest dimensions. Type IV traps are often very small in scale. Type V, however, are often the largest and thickest (Figs. 7-13 to 7-15).
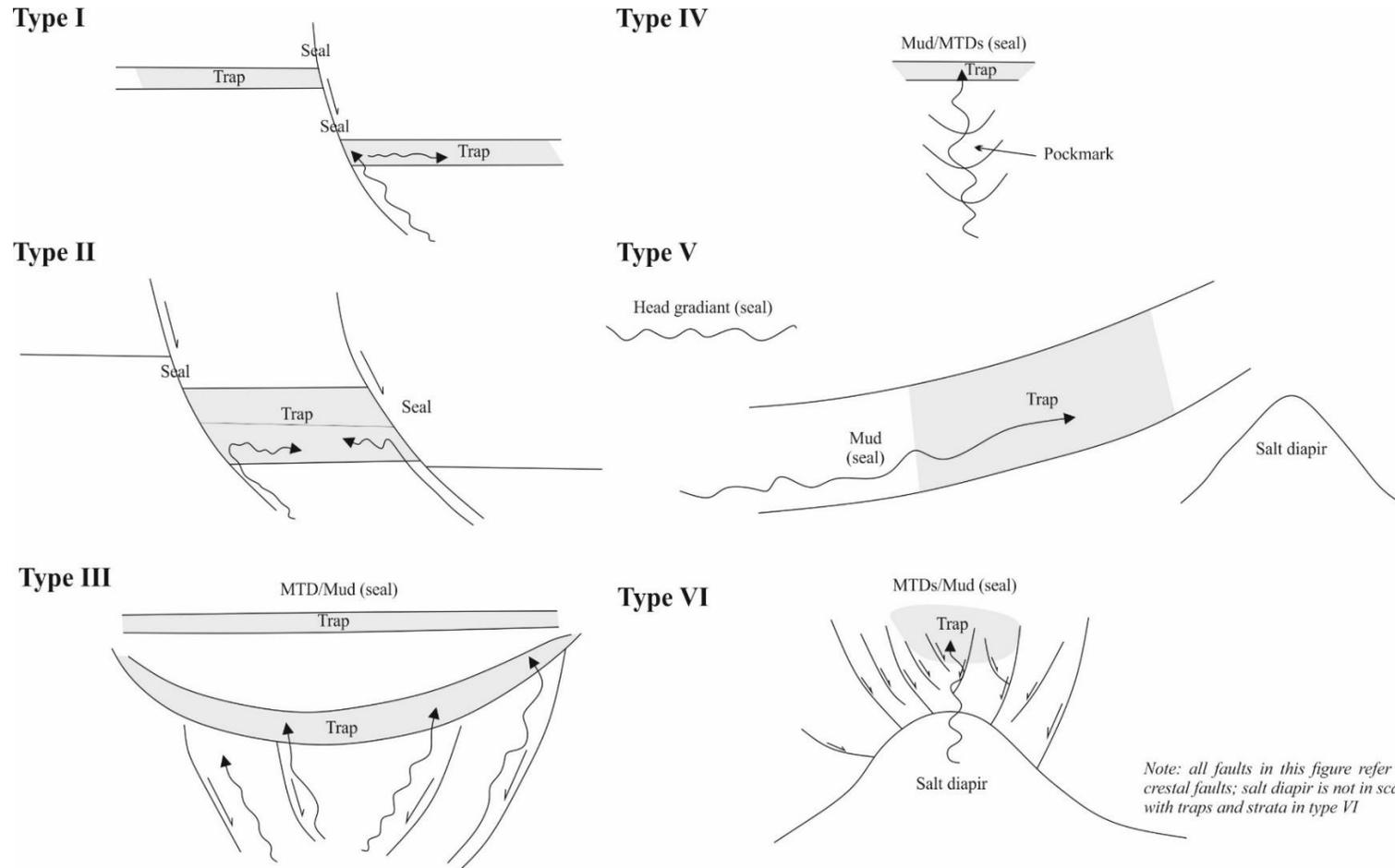
Fig. 7-10 Types of traps identified in the study area (offshore Espírito Santo Basin, SE Brazil). Six main types of traps are identified as closely associated with crestal faults and fluid flow features in supra-salt successions.

223

Fig. 7-11 Examples of type I traps in supra-salt successions.

Fig. 7-12 Examples of type II traps in supra-salt successions.

Type VI traps comprise a type of combination trap. These traps are located directly on top of rising salt diapirs, and fluids are sourced from the salt body or pre-salt successions (see section 7.3 for detail discussion). Developed fault systems act as fluid pathways while soft sediment act as seals (Fig. 7-16).

7.4.2 Petroleum potential of structural traps in supra-salt successions

Petroleum exploration in areas dominated by salt tectonics is largely focused in understanding the potential pre-salt successions, with salt being regarded as the perfect seal for hydrocarbon trapped under giant salt deposits. However, as indicated by this research, salt seal failure, and fluid sourcing from pre-salt successions account for the formation of important fluid flow features in supra-salt successions (section 7.3). With the types of traps in supra-salt successions classified as in Figures 7-11 to 7-16, sufficient evidence is provided in this thesis that supra-salt traps can form significant petroleum fields. Examples given in this study are located in shallow sub-surface areas. These traps can be identified clearly for their geometries and their relationships with associated structural and stratigraphic elements. As for deeper-seated salt structures, or thicker supra-salt successions, it is hard to have the same resolution as in this case study, this research work offers important insights into future strategies for petroleum exploration in supra-salt successions around the world.

Fig. 7-13 Examples of type III traps in supra-salt successions.

227

Fig. 7-14 Examples of type IV traps in supra-salt successions.

Fig. 7-15 Examples of type V traps in supra-salt successions.

Fig. 7-16 Examples of type VI traps in supra-salt successions.

7.5 Limitations of the research

Three-dimensional seismic data contribute to most of the research outcomes in the thesis. As previously noted, data resolution has always a strong impact on fault analyses. Limitations of the three distinct result chapters are summarised in the following aspects.

7.5.1   Seismic data related limitations

Eocene volcaniclastic deposits comprise the most apparent seismic unit when interpreting the seismic stratigraphy of the Espírito Santo Basin. Apart from the accurate identification of this unit, due to the lack of well constraints, the thesis was only capable of roughly construct a stratigraphic framework based on the published literature. As a result, specific (absolute) timings for fault nucleation, linkage and reactivation, fluid flow events and episodic salt activity are not mentioned in this thesis. Rather, the thesis focus more on a broader understanding of these latter aspects.

The seismic volume used in this study is truncated below -5000 ms (twt). A greater depth range would have provided a full extent of the Aptian evaporites, correlating the pre-salt units with the regional stratigraphy, to allow the accurate mapping of fault families in pre-salt units. More importantly, salt seal failure will be better understood with pre-salt structures and compartmentalisation being better revealed. Further research on whether distinct crestal fault families are associated with pre-salt structures will be conducted in the future to better understand the dynamics of crestal faults'.

7.5.2   Limitations of stress analyses

When conducting stress analyses, important constraints such as regional stresses will greatly influence the results. Most of the published work developing stress analyses at a regional scale uses data from the World Stress Map (Heidback et al., 2008). However, the closest stress data available near the study area is located onshore (Heidback et al., 2008), and is likely to underrepresent the regional stress field in the compressional

domain of the Espírito Santo Basin. Lacking regional and pore-pressure constraints, the results of stress analyses cannot quantitatively reveal the current status of fault slip possibility and leakage properties. Rather, the stress analysis only reflects the likelihood of fault slip events and the potential for fluid leakage in a small study area.

Another key limitation is the calculation capability of the software used in the stress analyses. When performing stress inversions, it is beyond the capability of the software to have original fault information over a size of 20 MB. As the results in Chapter 6 indicate, it is important that interpreted faults are exported reaching data resolution so to produce accurate fault slip tendency and leakage analysis results. However, when all exported fault surfaces approach the resolution limits of the seismic data one can only perform stress analysis using part of the faults, rather than all interpreted faults, causing uncertainties in stress analysis.

7.5.3 Sample related limitations

A new method to constrain the usage of throw analysis is introduced in the thesis. Quantitative suggestions are proposed as suggestions for future structural interpretation for structural geologists. Fifty-eight (58) faults interpreted on seismic data, thirteen (13) sub-seismic faults and two (2) rift faults are used to produce the results. Even though the results are sufficient enough for the purpose of the research, the author reckon that the number of fault samples has an important influence on the quantitative analysis undertaken in this work. It is suggested future research will added up to improve the result for this new method.

7.6 Future work

The thesis documents for the first-time crestal fault systems associated with a transverse accommodation zone. It also analyses strata-bounded domino style faults (TBFs) associated with episodic fluid flow in supra-salt successions, and new quantitative

methods to constrain the accuracy of throw analyses when interpreting fault growth histories.

The thesis provides two good examples of a transverse accommodation zone and an oblique transfer zone over a salt diapir, how these structures are associated with crestal fault evolution. The chronology of fault growth over salt structures is seldom addressed in the literature. This is a theme worthy of future research as these structures are not negligible in supra-salt tectonics.

A valid model for salt seal failure is postulated in the thesis, but further effort is needed to build more reliable information on the modes of seal failure in salt-dominated basins. Research in this thesis indicates that fluid flow though salt played a vital role between pre- and supra-salt compartments. Future research on the physical properties of heterogeneous salt structures, faulting/folding mechanisms of salt structures under geological conditions, and pre-salt, intra-salt, and supra-salt fault systems should be attained for a better understanding of fluid flow in areas with important salt tectonics.

It is noted that fault-related traps are prevalent in areas with salt tectonics, and fault sealing behaviours (and seal competence) comprise essential aspects to investigate in oil and gas exploration. Thus, whether there is any significant difference in fault sealing behaviours between areas with salt and salt-poor sedimentary basins, is a theme that needs to be further investigated with borehole and seismic data.

The new method to quality control fault growth analysis proposed in this thesis uses a relatively small number of fault samples, especially when considering large-scale rift faults. Future research work should compile more data to perfect the method. Future mathematical modifications to the method and the calculation of a degree of confidence should be undertaken in the future.

Chapter 8

Conclusions

8.1 Conclusions from Chapter 4

In Chapter 4, high-resolution seismic data from the Espírito Santo Basin, SE Brazil, documented distinct fault families on a salt ridge. Detailed structural maps, throw-depth plots and statistical analyses of fault distributions provided us with important insights into the geometry and evolution of crestal fault systems on top of salt structures. The work undertaken in this thesis resulted in the following conclusions:

- A swarm of listric, moderately–highly curved faults is developed on top of the salt ridge, showing resolvable fault densities that reach as much as eighteen (18) faults per kilometre.

- Crestal fault families are controlled by listric border faults, i.e. border faults have larger maximum throws than the remainder of crestal faults, accommodating most the strain and stress on the crest of the salt structure. Faults closer to border faults are less active during the geological time. Border faults are also in a preferential position to be reactivated.

- Erosional surfaces are robust markers to date fault reactivation, particularly when used together with T-Z plots.

- Segment linkage is predominant in the interpreted crestal fault families and controlled their growth. The interpreted crestal faults propagated both vertically and horizontally. Over the salt ridge, horizontal propagation was hindered by an accommodation zone, onto which faults terminate. Vertical propagation stops either when the fault meets the sea floor, or when vertical propagation is accommodated by either blind faults, or by adjacent faults with larger displacements.

- Fault propagation does not follow a 'Coherent model' sensu Jackson and Rotevatn (2013). The geometry and history of propagation of faults segments are not comparable with this later model. In particular, large fault segments propagated to emerge with non-reactivated small fault segments on the crest of the salt ridge, and show later 'blind' propagation towards the surface.

- The transverse accommodation zone (TAZ) developed on a salt ridge had paramount influence on the evolution of the interpreted crestal faults. Two opposite-dipping fault families, reflecting distinct mechanisms for their formation, terminate into the accommodation zone. After its establishment, the development of the crestal fault system became controlled by the accommodation zone per se.

8.2 Conclusions from Chapter 5

High-resolution 3D seismic data from the Espírito Santo Basin, SE Brazil documented in Chapter 5 a strata-bound domino fault set generated on a salt ridge. The detailed mapping of the structural elements and fluid flow features in this area, combined with throw and stress analyses of crestal faults, provided vital insights on the formation of strata-bound domino faults and associated fluid flow features. The main conclusions of this work can be summarised as follows:

- Strata-bound domino faults are important markers for fluid flow in areas with salt tectonics. Mechanisms of formation of strata-bound domino faults include the sudden release of overpressure in adjacent regions to salt diapirs. A dipping detachment surface at their base, and localised fluid conduits, are key elements to the formation of a strata-bound domino set.

- Three episodes of fluid flow are identified in the study area. Vertically stacked and horizontally migrated pockmarks in salt-withdrawal basin are possible indicators of episodic salt activity.

- Crestal faults in salt tectonics can play as both conduits and seals, however, considering crestal faults as a whole system, seal capability of crestal fault system is negative.

- Crestal fault reactivation is a possible indicator of fluid flow in salt tectonics and a possible marker of locating reservoirs in supra-salt tectonics.

8.3 Conclusions from Chapter 6

T-D and T-Z plots are widely used in fault analyses, especially to postulate fault segmentation to assist the interpretation of fault propagation histories. In parallel, fault slip tendency and leakage factors are often modeled to understand fault sealing properties. Chapter 6 presented the first quantitative method to critically evaluate the effect of data sampling on the accuracies of T-D and T-Z plots. Outcropping faults of distinct scales, and faults imaged on 3D seismic data, were analysed to introduce two new parameters: the *Sampling Interval/Fault Length Ratio* (δ) and the *Module Error* (ε_i) to be used as quantitative methods to assess the accuracy of fault analyses. As a corollary, this study reaches the following conclusions:

- Sampling intervals have significant influence on the analysis of fault growth histories in multiple ways. With variable sampling intervals: 1) fault geometry is significantly changed; 2) maximum fault throw values are underestimated; 3) fault segments are unrepresented; 4) the geometry of fault linkage zones is changed; 5) the width of fault linkage zone is underestimated; 6) fault interaction zones are lost. This means, in effect, that methods based on EI and isochron mapping are unreliable beyond certain scales of analysis, i.e. beyond horizon-by-horizon (maximum seismic resolution) interpretation scales (e.g. Alves, 2012).

- Using the SE Brazil seismic data, the accuracy of T-D plots is quantitatively lost when sampling intervals are larger than 37.5 m (every 3 shot-points). This sampling intervals adopted by interpreters, however, should be different depending on the resolution of seismic data used and on the total length of structures.

- Module error (ε_t) decreases rapidly with longer average fault-segment lengths. This ε_t value should be well under 0.06 to avoid any of the caveats summarised in section 4.1.1.

- A δ value of 0.05 is recommended for fault displacement analyses undertaken without prior knowledge of fault segmentation, and for fault lengths are under 3500 m. This signifies sampling throws at distances of <5% the total length of faults.

- The threshold δ values can be as high as 0.1 for faults that comprise only one fault segment. This means a threshold sampling space of <10% the total length of faults.

- The threshold δ value of 0.03 is suggested for faults longer than 3500 m. This signifies, in practice, the acquisition of throw data at distances that are <3% of the total length of the fault.

- For detailed fault slip tendency and leakage factor analysis, a δ value reaching maximum data resolution is strongly suggested to interpreters so to avoid systematic misinterpretations of fault sealing properties. This means T-Z picks at every single seismic reflection, fault sticks at every shot point, and the use of Lidar data (or very small sampling distances) in field-based analyses.

References

ALSOP, G., BROWN, J., DAVISON, I. & GIBLING, M. 2000. The geometry of drag zones adjacent to salt diapirs. Journal of the Geological Society, 157, 1019-1029.

ALSOP, G. I., WEINBERGER, R., LEVI, T. & MARCO, S. 2015. Deformation within an exposed salt wall: Recumbent folding and extrusion of evaporites in the Dead Sea Basin. Journal of Structural Geology, 70, 95-118.

ALSOUKI, M., RIAHI, M. A. & YASSAGHI, A. 2011. Seismic Imaging of Sub-Circular Salt-Related Structures: Evidence for Passive Diapirism in the Straits of Hormuz, Persian Gulf. Petroleum Geoscience, 17, 101-107.

ALVES, T. M. 2012. Scale-relationships and geometry of normal faults reactivated during gravitational gliding of Albian rafts (Espírito Santo Basin, SE Brazil). Earth and Planetary Science Letters, 331-332, 80-96.

ALVES, T. M. 2015. Submarine slide blocks and associated soft-sediment deformation in deep-water basins: A review. Marine and Petroleum Geology, 67, 262-285.

ALVES, T. M., CARTWRIGHT, J. & DAVIES, R. J. 2009. Faulting of salt-withdrawal basins during early halokinesis: Effects on the Paleogene Rio Doce Canyon system (Espírito Santo Basin, Brazil). AAPG Bulletin, 93, 617-652.

ALVES, T. M. & CARTWRIGHT, J. A. 2009. Volume balance of a submarine landslide in the Espírito Santo Basin, offshore Brazil: Quantifying seafloor erosion, sediment accumulation and depletion. Earth and Planetary Science Letters, 288, 572-580.

ALVES, T. M., FETTER, M., LIMA, C., CARTWRIGHT, J. A., COSGROVE, J., GANGÁ, A., QUEIROZ, C. L. & STRUGALE, M. 2017. An incomplete correlation between pre-salt topography, top reservoir erosion, and salt deformation in deep-water Santos Basin (SE Brazil). Marine and Petroleum Geology, 79, 300-320.

ANDERSON, E. M. 1942. The dynamics of faulting and dyke formation with applications to Britain, Oliver and Boyd.

ANDRESEN, K. J. 2012. Fluid flow features in hydrocarbon plumbing systems: What do they tell us about the basin evolution? Marine Geology, 332, 89-108.

ANDRESEN, K. J. & HUUSE, M. 2011. 'Bulls-eye' pockmarks and polygonal faulting in the Lower Congo Basin: relative timing and implications for fluid expulsion during shallow burial. Marine Geology, 279, 111-127.

ANDRESEN, K. J., HUUSE, M., SCHODT, N. H., CLAUSEN, L. F. & SEIDLER, L. 2011. Hydrocarbon plumbing systems of salt minibasins offshore Angola revealed by three-dimensional seismic analysis. AAPG Bulletin, 95, 1039-1065.

ANGELIER, J. 1990. Inversion of field data in fault tectonics to obtain the regional stress—III. A new rapid direct inversion method by analytical means. Geophysical Journal International, 103, 363-376.

ATHMER, W. & LUTHI, S. M. 2011. The effect of relay ramps on sediment routes and deposition: A review. Sedimentary Geology, 242, 1-17.

AVILES, C., SCHOLZ, C. & BOATWRIGHT, J. 1987. Fractal analysis applied to characteristic segments of the San Andreas Fault. Journal of Geophysical Research: Solid Earth, 92, 331-344.

AXEN, G. J. 1986. Superposed normal faults in the Ely Springs Range, Nevada: Estimates of extension. Journal of structural geology, 8, 711-713.

AXEN, G. J. 1988. The geometry of planar domino-style normal faults above a dipping basal detachment. Journal of Structural Geology, 10, 405-411.

BAARS, D. & STEVENSON, G. 1982. Subtle stratigraphic traps in Paleozoic rocks of Paradox basin. AAPG Memoir, 131 - 158.

BAHORICH, M. & FARMER, S. 1995. 3-D seismic discontinuity for faults and stratigraphic features: The coherence cube. The leading edge, 14, 1053-1058.

BARNETT, J. A., MORTIMER, J., RIPPON, J. H., WALSH, J. J. & WATTERSON, J. 1987. Displacement geometry in the volume containing a single normal fault. AAPG Bulletin, 71, 925-937.

BARTON, D. C. 1933. Mechanics of formation of salt domes with special reference to Gulf Coast salt domes of Texas and Louisiana. AAPG Bulletin, 17, 1025-1083.

BAUDON, C. & CARTWRIGHT, J. 2008a. 3D seismic characterisation of an array of blind normal faults in the Levant Basin, Eastern Mediterranean. Journal of Structural Geology, 30, 746-760.

BAUDON, C. & CARTWRIGHT, J. 2008b. Early stage evolution of growth faults: 3D seismic insights from the Levant Basin, Eastern Mediterranean. Journal of Structural Geology, 30, 888-898.

BAUDON, C. & CARTWRIGHT, J. 2008c. The kinematics of reactivation of normal faults using high resolution throw mapping. Journal of Structural Geology, 30, 1072-1084.

BELLAHSEN, N. & DANIEL, J. M. 2005. Fault reactivation control on normal fault growth: an experimental study. Journal of Structural Geology, 27, 769-780.

BERNDT, C., BUNZ, S. & MIENERT, J. 2003. Fluid expulsion from polygonally faulted clays, Norwegian margin. Subsurface sediment mobilisation: Geological Society (London) Special Publication, 216, 223-243.

BERNDT, C. & GAY, A. 2007. Cessation-reactivation of polygonal faulting and effects on fluid flow in the Vøring Basin, Norwegian Margin. Journal of the Geological Society, 164, 129-142.

BERTONI, C. & CARTWRIGHT, J. 2005. 3D seismic analysis of circular evaporite dissolution structures, Eastern Mediterranean. Journal of the Geological Society, 162, 909-926.

BERTONI, C. & CARTWRIGHT, J. 2015. Messinian evaporites and fluid flow. Marine and Petroleum Geology, 66, 165-176.

BLENKINSOP, T. G. & RUTTER, E. 1986. Cataclastic deformation of quartzite in the Moine thrust zone. Journal of Structural Geology, 8, 669-681.

BOOTH-REA, G., AZAÑÓN, J.-M., AZOR, A. & GARCÍA-DUEÑAS, V. C. 2004. Influence of strike-slip fault segmentation on drainage evolution and topography. A case study: the Palomares Fault Zone (southeastern Betics, Spain). Journal of Structural Geology, 26, 1615-1632.

BOSE, S. & MITRA, S. 2010. Analog modeling of divergent and convergent transfer zones in listric normal fault systems. AAPG Bulletin, 94, 1425-1452.

BOSWORTH, W. 1985. Geometry of propagating continental rifts. Nature, 316, 625-627.

BOTT, M. H. P. 1959. The mechanics of oblique slip faulting. Geological Magazine, 96, 109-117.

BOUROULLEC, R., CARTWRIGHT, J. A., JOHNSON, H. D., LANSIGU, C., QUÉMENER, J.-M. & SAVANIER, D. 2004. Syndepositional faulting in the Grès d'Annot Formation, SE France: High-resolution kinematic analysis and stratigraphic response to growth faulting. Geological Society, London, Special Publications, 221, 241-265.

BOWKER, K. A. 2007. Barnett Shale gas production, Fort Worth Basin: issues and discussion. AAPG bulletin, 91, 523-533.

BROWN, A. R., BROWN, A. R., BROWN, A. R. & BROWN, A. R. 2004. Interpretation of three-dimensional seismic data.

BRUHN, C. H. & WALKER, R. G. 1997. Internal architecture and sedimentary evolution of coarse‐grained, turbidite channel‐levee complexes, Early Eocene Regência Canyon, Espírito Santo Basin, Brazil. Sedimentology, 44, 17-46.

BRUN, J.-P. & FORT, X. 2011. Salt tectonics at passive margins: Geology versus models. Marine and Petroleum Geology, 28, 1123-1145.

BUCHANAN, P. G. & MCCLAY, K. R. 1992. Experiments on basin inversion above reactivated domino faults. Marine and Petroleum Geology, 9, 486-500.

BÜRGMANN, R., POLLARD, D. D. & MARTEL, S. J. 1994. Slip distributions on faults: effects of stress gradients, inelastic deformation, heterogeneous host-rock stiffness, and fault interaction. Journal of Structural Geology, 16, 1675-1690.

CAMERON, T. D. J. 1992. The geology of the southern North Sea, London: HMSO.

CARTWRIGHT, J. 2007. The impact of 3D seismic data on the understanding of compaction, fluid flow and diagenesis in sedimentary basins. Journal of the Geological Society, 164, 881-893.

CARTWRIGHT, J. 2011. Diagenetically induced shear failure of fine-grained sediments and the development of polygonal fault systems. Marine and Petroleum Geology, 28, 1593-1610.

CARTWRIGHT, J., BOUROULLEC, R., JAMES, D. & JOHNSON, H. 1998. Polycyclic motion history of some Gulf Coast growth faults from high-resolution displacement analysis. Geology, 26, 819-822.

CARTWRIGHT, J., HUUSE, M. & APLIN, A. 2007. Seal bypass systems. AAPG bulletin, 91, 1141-1166.

CARTWRIGHT, J. & MANSFIELD, C. 1998. Lateral displacement variation and lateral tip geometry of normal faults in the Canyonlands National Park, Utah. Journal of Structural Geology, 20, 3-19.

CARTWRIGHT, J., STEWART, S. & CLARK, J. 2001. Salt dissolution and salt-related deformation of the Forth Approaches Basin, UK North Sea. Marine and Petroleum Geology, 18, 757-778.

CARTWRIGHT, J., TRUDGILL, B. & MANSFIELD, C. 2000. Fault growth by segment linkage: An explanation for scatter in maximum displacement and trace length data from the Canyonlands grabens of SE Utah: Reply. Journal of Structural Geology, 22, 141-143.

CARTWRIGHT, J. A. 1994. Episodic basin-wide fluid expulsion from geopressured shale sequences in the North Sea basin. Geology, 22, 447-450.

CARTWRIGHT, J. A., TRUDGILL, B. D. & MANSFIELD, C. S. 1995. Fault growth by segment linkage: an explanation for scatter in maximum displacement and trace length data from the Canyonlands Grabens of SE Utah. Journal of Structural Geology, 17, 1319-1326.

CATER, F. W. & CRAIG, L. C. 1970. Geology of the salt anticline region in southwestern Colorado.

CHANG, H., KOWSMANN, R. & DEFIGUEIREDO, A. 1988. New concepts on the development of east Brazilian marginal basins. Episodes, 11, 194-202.

CHANG, R. O., KOWSMANN, A., BENDER, A. M. F. & FIGUEIREDO, A. M. F. 1992. Tectonics and stratigraphy of the East Brazil Rift system: an overview. Tectonophysics, 213, 97-138.

CHAPMAN, T. J. & WILLIAMS, G. D. 1984. Displacement-distance methods in the analysis of fold-thrust structures and linked-fault systems. Journal of the Geological Society, 141, 121-128.

CHILDS, C., MANZOCCHI, T., WALSH, J., BONSON, C. G., NICOL, A. & SCHOPFER, M. 2009. A geometric model of fault zone and fault rock thickness variations. Journal of Structural Geology, 31, 117-127.

CHILDS, C., NICOL, A., WALSH, J. & WATTERSON, J. 1996. Growth of vertically segmented normal faults. Journal of Structural Geology, 18, 1389-1397.

CHILDS, C., NICOL, A., WALSH, J. & WATTERSON, J. 2003. The growth and propagation of synsedimentary faults. Journal of Structural Geology, 25, 633-648.

CHILDS, C., WATTERSON, J. & WALSH, J. 1995. Fault overlap zones within developing normal fault systems. Journal of the Geological Society, 152, 535-549.

CHOI, J. H., YANG, S. J., HAN, S. R. & KIM, Y. S. 2015. Fault zone evolution during Cenozoic tectonic inversion in SE Korea. Journal of Asian Earth Sciences, 98, 167-177.

CLARK, R. & COX, S. 1996. A modern regression approach to determining fault displacement-length scaling relationships. Journal of Structural Geology, 18, 147-152.

CLAUSEN, O. R., EGHOLM, D. L., ANDRESEN, K. J. & WESENBERG, R. 2014. Fault patterns within sediment layers overlying rising salt structures: A numerical modelling approach. Journal of Structural Geology, 58, 69-78.

COBBOLD, P. R. & SZATMARI, P. 1991. Radial gravitational gliding on passive margins. Tectonophysics, 188, 249-289.

COFFIELD, D. Q. 1987. Surface expression and internal structure of an accommodation zone, Gulf of Suez, Egypt. AAPG Bulletin, 71, 540-540.

COLLETTA, B., LE QUELLEC, P., LETOUZEY, J. & MORETTI, I. 1988. Longitudinal evolution of the Suez rift structure (Egypt). Tectonophysics, 153, 221-233.

COWIE, P., GUPTA, S. & DAWERS, N. 2000. Implications of fault array evolution for synrift depocentre development: insights from a numerical fault growth model. Basin Research, 12, 241-261.

COWIE, P. A. & SCHOLZ, C. H. 1992a. Displacement-length scaling relationship for faults: data synthesis and discussion. Journal of Structural Geology, 14, 1149-1156.

COWIE, P. A. & SCHOLZ, C. H. 1992b. Growth of faults by accumulation of seismic slip. Journal of Geophysical Research: Solid Earth, 97, 11085-11095.

COWIE, P. A. & SCHOLZ, C. H. 1992c. Physical explanation for the displacement-length relationship of faults using a post-yield fracture mechanics model. Journal of Structural Geology, 14, 1133-1148.

CRISTESCU, N., HUNSCHE, U., CRISTESCU, N. D. & CRISTESCU, N. D. 1998. Time effects in rock mechanics, Wiley New York.

CROSSLEY, R. & CROW, M. 1980. The Malawi rift. Geodynamic Evolution of the Afro-Arabian rift system, 78-87.

CRUTCHLEY, G. J., BERNDT, C., GEIGER, S., KLAESCHEN, D., PAPENBERG, C., KLAUCKE, I., HORNBACH, M. J., BANGS, N. L. & MAIER, C. 2013. Drivers of focused fluid flow and methane seepage at south Hydrate Ridge, offshore Oregon, USA. Geology, 41, 551-554.

DAVISON, I. 1995. Fault slip evolution determined from crack-seal veins in pull-aparts and their implications for general slip models. Journal of Structural Geology, 17, 1025-1034.

DAVISON, I. 2007. Geology and tectonics of the South Atlantic Brazilian salt basins. Geological Society, London, Special Publications, 272, 345-359.

DAVISON, I. 2009. Faulting and fluid flow through salt. Journal of the Geological Society, 166, 205-216.

DAVISON, I., ALSOP, G. I., EVANS, N. G. & SAFARICZ, M. 2000a. Overburden deformation patterns and mechanisms of salt diapir penetration in the Central Graben, North Sea. Marine and Petroleum Geology, 17, 601-618.

DAVISON, I., ALSOP, I., BIRCH, P., ELDERS, C., EVANS, N., NICHOLSON, H., RORISON, P., WADE, D., WOODWARD, J. & YOUNG, M. 2000b. Geometry and late-stage structural evolution of Central Graben salt diapirs, North Sea. Marine and Petroleum Geology, 17, 499-522.

DAVISON, I., BOSENCE, D., ALSOP, G. I. & AL-AAWAH, M. H. 1996. Deformation and sedimentation around active Miocene salt diapirs on the Tihama Plain, northwest Yemen. Geological Society, London, Special Publications, 100, 23-39.

DAWERS, N. H. & ANDERS, M. H. 1995. Displacement-length scaling and fault linkage. Journal of Structural Geology, 17, 607-614.

DAWERS, N. H., ANDERS, M. H. & SCHOLZ, C. H. 1993. Growth of normal faults: Displacement-length scaling. Geology, 21, 1107-1110.

DEMERCIAN, S., SZATMARI, P. & COBBOLD, P. 1993. Style and pattern of salt diapirs due to thin-skinned gravitational gliding, Campos and Santos basins, offshore Brazil. Tectonophysics, 228, 393-433.

DOOLEY, T. P., JACKSON, M. P. & HUDEC, M. R. 2009. Inflation and deflation of deeply buried salt stocks during lateral shortening. Journal of Structural Geology, 31, 582-600.

DOOLEY, T. P., JACKSON, M. P. A., JACKSON, C. A. L., HUDEC, M. R. & RODRIGUEZ, C. R. 2015. Enigmatic structures within salt walls of the Santos Basin—Part 2: Mechanical explanation from physical modelling. Journal of Structural Geology, 75, 163-187.

DUGAN, B. & FLEMINGS, P. B. 2000. Overpressure and fluid flow in the New Jersey continental slope: Implications for slope failure and cold seeps. Science, 289, 288-291.

DUROGBITAN, A. A. 2016. Investigating fault propagation and segment linkage using throw distribution analysis within the Agbada formation of Ewan and Oloye fields, northwestern Niger delta. Journal of African Earth Sciences, 120, 248-265.

EBINGER, C. J. 1989. Geometric and kinematic development of border faults and accommodation zones, Kivu-Rusizi Rift, Africa. Tectonics, 8, 117-133.

EBINGER, C. J., ROSENDAHL, B. & REYNOLDS, D. 1987. Tectonic model of the Malaŵi rift, Africa. Tectonophysics, 141, 215-235.

ELLIS, M. A. & DUNLAP, W. J. 1988. Displacement variation along thrust faults: Implications for the development of large faults. Journal of Structural Geology, 10, 183-192.

EVANS, J. P. 1990. Thickness-displacement relationships for fault zones. Journal of structural geology, 12, 1061-1065.

EVANS, N., MACLEOD, J., MACMILLAN, N., RORISON, P. & SALVADOR, P. 2003. The Banff Field, Blocks 22/27a, 29/2a, UK North Sea. Geological Society, London, Memoirs, 20, 497-507.

FARHOUD, K. 2009. Accommodation zones and tectono-stratigraphy of the Gulf of Suez, Egypt: A contribution from aeromagnetic analysis. Geoarabia, 14, 139-162.

FAULDS, J. E., GEISSMAN, J. W. & MAWER, C. K. 1990. Structural development of a major extensional accommodation zone in the Basin and Range Province, northwestern Arizona and southern Nevada; Implications for kinematic models of continental extension. Geological Society of America Memoirs, 176, 37-76.

FAULDS, J. E. & VARGA, R. J. 1998. The role of accommodation zones and transfer zones in the regional segmentation of extended terranes. Special papers-Geological Society of America, 323, 1-46.

FEJERSKOV, M. & LINDHOLM, C. 2000. Crustal stress in and around Norway: an evaluation of stress-generating mechanisms. Geological Society, London, Special Publications, 167, 451-467.

FIDUK, J. C., BRUSH, E. R., ANDERSON, L. E., GIBBS, P. B. & ROWAN, M. G. Salt deformation, magmatism, and hydrocarbon prospectivity in the Espírito Santo Basin, offshore Brazil. Salt-sediment interactions and hydrocarbon prospectivity: Concepts, applications, and case studies for the 21st century: Proceedings of Gulf Coast Section SEPM Foundation Bob F. Perkins Research Conference, 2004. SEPM, 370-392.

FLEMINGS, P. B. 1998. Generation of overpressure and compaction‐driven fluid flow in a Plio‐Pleistocene growth‐faulted basin, Eugene Island 330, offshore Louisiana. Basin Research, 10, 177-196.

FONSECA, J. 1988. The Sou Hills: A barrier to faulting in the central Nevada seismic belt. Journal of Geophysical Research: Solid Earth (1978–2012), 93, 475-489.

FOSSEN, H. & HESTHAMMER, J. 1997. Geometric analysis and scaling relations of deformation bands in porous sandstone. Journal of Structural Geology, 19, 1479-1493.

FOSSEN, H. & ROTEVATN, A. 2016. Fault linkage and relay structures in extensional settings—A review. Earth-Science Reviews, 154, 14-28.

FRANÇA, R. L., DEL REY, A. C., TAGLIARI, C. V., BRANDÃO, J. R. & FONTANELLI, P. D. R. 2007. Bacia do Espírito Santo. Boletim de Geociencias da PETROBRAS, 15, 501-509.

FRERY, E., GRATIER, J.-P., ELLOUZ-ZIMMERMAN, N., LOISELET, C., BRAUN, J., DESCHAMPS, P., BLAMART, D., HAMELIN, B. & SWENNEN, R. 2015. Evolution of fault permeability during episodic fluid circulation: Evidence for the effects of fluid–rock interactions from travertine studies (Utah–USA). Tectonophysics, 651-652, 121-137.

FURUYA, M., MUELLER, K. & WAHR, J. 2007. Active salt tectonics in the Needles District, Canyonlands (Utah) as detected by interferometric synthetic aperture radar and point target analysis: 1992–2002. Journal of Geophysical Research: Solid Earth (1978–2012), 112.

GAKI-PAPANASTASSIOU, K., KARYMBALIS, E., PAPANASTASSIOU, D., & MAROUKIAN, H. 2009. Quaternary marine terraces as indicators of neotectonic activity of the Ierapetra normal fault SE Crete (Greece). *Geomorphology*, *104*(1-2), 38-46.

GAMBOA, D., ALVES, T., CARTWRIGHT, J. & TERRINHA, P. 2010. MTD distribution on a 'passive' continental margin: The Espírito Santo Basin (SE Brazil) during the Palaeogene. Marine and Petroleum Geology, 27, 1311-1324.

GAMBOA, D. & ALVES, T. M. 2015. Spatial and dimensional relationships of submarine slope architectural elements: A seismic-scale analysis from the Espírito Santo Basin (SE Brazil). Marine and Petroleum Geology, 64, 43-57.

GAMBOA, D. & ALVES, T. M. 2016. Bi-modal deformation styles in confined mass-transport deposits: Examples from a salt minibasin in SE Brazil. Marine Geology, 379, 176-193.

GARCIA, S. F. D., LETOUZEY, J., RUDKIEWICZ, J. L., DANDERFER, A. & DE LAMOTTE, D. F. 2012. Structural modeling based on sequential restoration of gravitational salt deformation in the Santos Basin (Brazil). Marine and Petroleum Geology, 35, 337-353.

GAY, A., LOPEZ, M., BERNDT, C. & SERANNE, M. 2007. Geological controls on focused fluid flow associated with seafloor seeps in the Lower Congo Basin. Marine Geology, 244, 68-92.

GE, H., JACKSON, M. & VENDEVILLE, B. 1997. Kinematics and dynamics of salt tectonics driven by progradation. AAPG Bulletin, 81, 398-423.

GE, H. & JACKSON, M. P. 1998. Physical modeling of structures formed by salt withdrawal: Implications for deformation caused by salt dissolution. AAPG bulletin, 82, 228-250.

GEE, M. & GAWTHORPE, R. 2006. Submarine channels controlled by salt tectonics: Examples from 3D seismic data offshore Angola. Marine and Petroleum Geology, 23, 443-458.

GHALAYINI, R., HOMBERG, C., DANIEL, J. & NADER, F. 2017. Growth of layer-bound normal faults under a regional anisotropic stress field. Geological Society, London, Special Publications, 439, 57-78.

GHANBARZADEH, S., HESSE, M. A., PRODANOVIĆ, M. & GARDNER, J. E. 2015. Deformation-assisted fluid percolation in rock salt. Science, 350, 1069-1072.

GIBA, M., WALSH, J. J. & NICOL, A. 2012. Segmentation and growth of an obliquely reactivated normal fault. Journal of Structural Geology, 39, 253-267.

GILLARD, M., AUTIN, J. & MANATSCHAL, G. 2016. Fault systems at hyper-extended rifted margins and embryonic oceanic crust: Structural style, evolution and relation to magma. Marine and Petroleum Geology, 76, 51-67.

GILLESPIE, P., WALSH, J. T. & WATTERSON, J. 1992. Limitations of dimension and displacement data from single faults and the consequences for data analysis and interpretation. Journal of Structural Geology, 14, 1157-1172.

Glen, R. A., Hancock, P. L., & Whittaker, A. 2005. Basin inversion by distributed deformation: the southern margin of the Bristol Channel Basin, England. *Journal of Structural Geology*, *27*(12), 2113-2134.

GRANIER, T. 1985. Origin, damping, and pattern of development of faults in granite. Tectonics, 4, 721-737.

GRAULS, D. & BALEIX, J. 1994. Role of overpressures and in situ stresses in fault-controlled hydrocarbon migration: A case study. Marine and Petroleum Geology, 11, 734-742.

GUDMUNDSSON, A. 1987. Geometry, formation and development of tectonic fractures on the Reykjanes Peninsula, southwest Iceland. Tectonophysics, 139, 295-308.

GUDMUNDSSON, A. 1992. Formation and growth of normal faults at the divergent plate boundary in Iceland. Terra Nova, 4, 464-471.

GUO, X., HE, S., LIU, K., SONG, G., WANG, X. & SHI, Z. 2010. Oil generation as the dominant overpressure mechanism in the Cenozoic Dongying depression, Bohai Bay Basin, China. AAPG bulletin, 94, 1859-1881.

GUO, X., HE, S., LIU, K. & ZHENG, L. 2011. Quantitative estimation of overpressure caused by oil generation in petroliferous basins. Organic Geochemistry, 42, 1343-1350.

GUO, X., LIU, K., JIA, C., SONG, Y., ZHAO, M. & LU, X. 2016. Effects of early petroleum charge and overpressure on reservoir porosity preservation in the giant Kela-2 gas field, Kuqa depression, Tarim Basin, northwest China. AAPG Bulletin, 100, 191-212.

GUTIÉRREZ, F. 2004. Origin of the salt valleys in the Canyonlands section of the Colorado Plateau: Evaporite-dissolution collapse versus tectonic subsidence. Geomorphology, 57, 423-435.

HEIDBACH, O., TINGAY, M., BARTH, A., REINECKER, J., KURFEß, D. & MÜLLER, B. 2008b. The world stress map database release 2008, doi: 10.1594/GFZ. WSM. Rel2008.

HEMELSDAËL, R. & FORD, M. 2016. Relay zone evolution: a history of repeated fault propagation and linkage, central Corinth rift, Greece. Basin Research, 28, 34-56.

HIPPOLYTE, J.-C., ANGELIER, J. & ROURE, F. 1994. A major geodynamic change revealed by Quaternary stress patterns in the Southern Apennines (Italy). Tectonophysics, 230, 199-210.

HOLDSWORTH, R., BUTLER, C. & ROBERTS, A. 1997. The recognition of reactivation during continental deformation. Journal of the Geological Society, 154, 73-78.

HOVLAND, M. & JUDD, A. 1988. Seabed pockmarks and seepages: impact on geology, biology, and the marine environment, Springer.

HOVLAND, M., RUESLÅTTEN, H., JOHNSEN, H., KVAMME, B. & KUZNETSOVA, T. 2006. Salt formation associated with sub-surface boiling and supercritical water. Marine and Petroleum Geology, 23, 855-869.

HUBBERT, M. K. & RUBEY, W. W. 1959. Role of fluid pressure in mechanics of overthrust faulting I. Mechanics of fluid-filled porous solids and its application to overthrust faulting. Geological Society of America Bulletin, 70, 115-166.

HUDEC, M. R. & JACKSON, M. P. A. 2007. Terra infirma: Understanding salt tectonics. Earth-Science Reviews, 82, 1-28.

HUDEC, M. R. & JACKSON, M. P. A. 2009. Interaction between spreading salt canopies and their peripheral thrust systems. Journal of Structural Geology, 31, 1114-1129.

HULL, J. 1988. Thickness-displacement relationships for deformation zones. Journal of Structural Geology, 10, 431-435.

HUNG KIANG CHANG, R. O., KOWSMANN, A., BENDER, A. M. F. & FIGUEIREDO, A. M. F. 1992. Tectonics and stratigraphy of the East Brazil Rift system: an overview. Tectonophysics, 213, 97-138.

HUNT, J. M. 1990. Generation and Migration of Petroleum from Abnormally Pressured Fluid Compartments. AAPG bulletin, 74, 1-12.

HÜBSCHER, C., CARTWRIGHT, J., CYPIONKA, H., DELANGE, G. J., ROBERTSON, A., SUC, J. P. & URAI, J. L. 2007. Global look at salt giants. Eos, Transactions American Geophysical Union, 88, 177-179.

IMBER, J., CHILDS, C., NELL, P. A. R., WALSH, J. J., IMBER, D., CHILDS, S., WALSH, S., NELL, S., HODGETTS, S. & FLINT, S. 2002. Hanging wall fault

kinematics and footwall collapse in listric growth fault systems. Journal of Structural Geology, 25, 197-208.

JACKSON, C. & LEWIS, M. M. 2012. Origin of an anhydrite sheath encircling a salt diapir and implications for the seismic imaging of steep-sided salt structures, Egersund Basin, Northern North Sea. Journal of the Geological Society, 169, 593-599.

JACKSON, C. & ROTEVATN, A. 2013. 3D seismic analysis of the structure and evolution of a salt-influenced normal fault zone: A test of competing fault growth models. Journal of Structural Geology, 56, 172-172.

JACKSON, C. A.-L., BELL, R. E., ROTEVATN, A. & TVEDT, A. B. 2017. Techniques to determine the kinematics of synsedimentary normal faults and implications for fault growth models. Geological Society, London, Special Publications, 439, SP439. 22.

JACKSON, C. A. L., JACKSON, M. P. A., HUDEC, M. R. & RODRIGUEZ, C. 2014. Internal structure, kinematics, and growth of a salt wall: Insights from 3-D seismic data. Geology, 42, 307-310.

JACKSON, C. A. L., JACKSON, M. P. A., HUDEC, M. R. & RODRIGUEZ, C. R. 2015. Enigmatic structures within salt walls of the Santos Basin—Part 1: Geometry and kinematics from 3D seismic reflection and well data. Journal of Structural Geology, 75, 135-162.

JACKSON, C. A. L. & LARSEN, E. 2009. Temporal and spatial development of a gravity-driven normal fault array: Middle–Upper Jurassic, South Viking Graben, northern North Sea. Journal of Structural Geology, 31, 388-402.

JACKSON, M., VENDEVILLE, B. & SCHULTZ-ELA, D. 1994. Structural dynamics of salt systems: Annual Reviews of Earth and Planetary Sciences, 22, 117.

JACKSON, M. P. A. & VENDEVILLE, B. C. 1994. Regional extension as a geologic trigger for diapirism. Geological Society of America Bulletin, 106, 57-73.

JACQUES, J. M. 2003. A tectonostratigraphic synthesis of the Sub-Andean basins: inferences on the position of South American intraplate accommodation zones and

their control on South Atlantic opening. Journal of the Geological Society, 160, 703-717.

JACQUES, J. M. 2004. The influence of intraplate structural accommodation zones on delineating petroleum provinces of the Sub-Andean foreland basins. Petroleum Geoscience, 10, 1-19.

JAIN, A., VERMA, A., VISHAL, V. & SINGH, T. 2013. Numerical simulation of fault reactivation phenomenon. Arabian Journal of Geosciences, 6, 3293-3302.

JAMISON, W. R. & STEARNS, D. W. 1982. Tectonic deformation of Wingate Sandstone, Colorado National Monument. AAPG Bulletin, 66, 2584-2608.

JENYON, M. K. 1988. Overburden deformation related to the pre-piercement development of salt structures in the North-Sea. Journal of the Geological Society, 145, 445-454.

JUDD, A. & HOVLAND, M. 2007. Seabed fluid flow: the impact on geology, biology and the marine environment, Cambridge University Press.

JUNG, N., HAN, W., WATSON, Z., GRAHAM, J. P. & KIM, K. 2014. Fault-controlled CO_2 leakage from natural reservoirs in the Colorado Plateau, East-Central Utah. Earth Planet. Sci. Lett., 403, 358-367.

KEHLE, R. O. 1988. The origin of salt structures.

KIM, Y.-S., ANDREWS, J. R. & SANDERSON, D. J. 2001. Reactivated strike–slip faults: examples from north Cornwall, UK. Tectonophysics, 340, 173-194.

KIM, Y.-S. & SANDERSON, D. J. 2005. The relationship between displacement and length of faults: a review. Earth Science Reviews, 68, 317-334.

KING, G. 1986. Speculations on the geometry of the initiation and termination processes of earthquake rupture and its relation to morphology and geological structure. Pure and Applied Geophysics, 124, 567-585.

KONG, D. Y., SHEN, H., LIU, J. Y. & YIN, W. 2005. Origin of the transverse accommodation zone of the Shulu subbasin in the Jizhong depression. Geology in China, 32, 694-695.

KOYI, H. 1991. Mushroom diapirs penetrating overburdens with high effective viscosities. Geology, 19, 1229-1232.

KRUEGER, S. W. & GRANT, N. T. Evolution of fault-related folds in the contractional toe of the deepwater Niger Delta. AAPG Annual Convention, 2006. 12.

LANGHI, L. & BOREL, G. D. 2008. Reverse structures in accommodation zone and early compartmentalization of extensional system, Laminaria High (NW shelf, Australia). Marine and Petroleum Geology, 25, 791-803.

LEWIS, M. M., JACKSON, C. A. L. & GAWTHORPE, R. L. 2013. Salt-influenced normal fault growth and forced folding: The Stavanger Fault System, North Sea. Journal of Structural Geology, 54, 156-173.

LEWIS, S. & HOLNESS, M. 1996. Equilibrium halite-H2O dihedral angles: High rock-salt permeability in the shallow crust? Geology, 24, 431-434.

LINDHOLM, C., BUNGUM, H., BRATLI, R., AADNØY, B., DAHL, N., TØRUDBAKKEN, B. & ATAKAN, K. 1995. Crustal stress in the northern North Sea as inferred from borehole breakouts and earthquake focal mechanisms. Terra Nova, 7, 51-59.

LISLE, R. J. & SRIVASTAVA, D. C. 2004. Test of the frictional reactivation theory for faults and validity of fault-slip analysis. Geology, 32, 569-572.

LIU, E., WANG, H., LI, Y., LEONARD, N. D., FENG, Y., PAN, S. & XIA, C. 2015. Relative role of accommodation zones in controlling stratal architectural variability and facies distribution: Insights from the Fushan Depression, South China Sea. Marine and Petroleum Geology, 68, Part A, 219-239.

LOHR, T., KRAWCZYK, C. M., ONCKEN, O. & TANNER, D. C. 2008. Evolution of a fault surface from 3D attribute analysis and displacement measurements. Journal of Structural Geology, 30, 690-700.

LONERGAN, L., CARTWRIGHT, J. & JOLLY, R. 1998. The geometry of polygonal fault systems in Tertiary mudrocks of the North Sea. Journal of Structural Geology, 20, 529-548.

LOPEZ, J. A. 1990. Structural styles of growth faults in the US Gulf Coast Basin. Geological Society, London, Special Publications, 50, 203-219.

LUO, G., FLEMINGS, P. B., HUDEC, M. R. & NIKOLINAKOU, M. A. 2015. The role of pore fluid overpressure in the substrates of advancing salt sheets, ice glaciers, and critical-state wedges. Journal of Geophysical Research: Solid Earth, 120, 87-105.

LØSETH, H., GADING, M. & WENSAAS, L. 2009. Hydrocarbon leakage interpreted on seismic data. Marine and Petroleum Geology, 26, 1304-1319.

MAIONE, S. J. 2001. Discovery of ring faults associated with salt withdrawal basins, Early Cretaceous age, in the East Texas Basin. The Leading Edge, 20, 818-829.

MALONEY, D., DAVIES, R., IMBER, J. & KING, S. 2012. Structure of the footwall of a listric fault system revealed by 3D seismic data from the Niger Delta. Basin Research, 24, 107-123.

MANDL, G. 1987. Tectonic deformation by rotating parallel faults: the "bookshelf" mechanism. Tectonophysics, 141, 277-316.

MANSFIELD, C. & CARTWRIGHT, J. 2001. Fault growth by linkage: Observations and implications from analogue models. Journal of Structural Geology, 23, 745-763.

MANSFIELD, C. S. & CARTWRIGHT, J. A. 1996. High resolution fault displacement mapping from three-dimensional seismic data: evidence for dip linkage during fault growth. Journal of Structural Geology, 18, 249-263.

MANZOCCHI, T., CHILDS, C. & WALSH, J. J. 2010. Faults and fault properties in hydrocarbon flow models. Geofluids, 10, 94-113.

MARRETT, R. & ALLMENDINGER, R. W. 1991. Estimates of strain due to brittle faulting: sampling of fault populations. Journal of Structural Geology, 13, 735-738.

MASON, J., SCHNEIDERWIND, S., PALLIKARAKIS, A., WIATR, T., MECHERNICH, S., PAPANIKOLAOU, I. & REICHERTER, K. 2016. Fault structure and deformation rates at the Lastros-Sfaka Graben, Crete. Tectonophysics, 683, 216-232.

MATTOS, N. H., ALVES, T. M. & OMOSANYA, K. O. 2016. Crestal fault geometries reveal late halokinesis and collapse of the Samson Dome, Northern Norway: Implications for petroleum systems in the Barents Sea. Tectonophysics, 690, 76-96.

Mattos, N. H., & Alves, T. M. 2018. Corridors of crestal and radial faults linking salt diapirs in the Espírito Santo Basin, SE Brazil. *Tectonophysics*, *728*, 55-74.

MAUDUIT, T. & BRUN, J. P. 1998. Growth fault/rollover systems: birth, growth, and decay. Journal of Geophysical Research: Solid Earth, 103, 18119-18136.

MCBRIDE, B. C., WEIMER, P. & ROWAN, M. G. 1998. The effect of allochthonous salt on the petroleum systems of northern Green Canyon and Ewing Bank (offshore Louisiana), northern Gulf of Mexico. AAPG bulletin, 82, 1083-1112.

MCCLAY, K. 1990. Extensional fault systems in sedimentary basins: a review of analogue model studies. Marine and petroleum Geology, 7, 206-233.

MCCLAY, K. 1995. The geometries and kinematics of inverted fault systems: a review of analogue model studies. Geological Society, London, Special Publications, 88, 97-118.

MCFARLAND, J. M., MORRIS, A. P. & FERRILL, D. A. 2012. Stress inversion using slip tendency. Computers & Geosciences, 41, 40-46.

MCLEOD, A. E., DAWERS, N. H. & UNDERHILL, J. R. 2000. The propagation and linkage of normal faults: insights from the Strathspey-Brent-Statfjord fault array, northern North Sea. Basin Research, 12, 263-284.

MEYER, V., NICOL, A., CHILDS, C., WALSH, J. & WATTERSON, J. 2002. Progressive localisation of strain during the evolution of a normal fault population. Journal of Structural Geology, 24, 1215-1231.

MOHAMMEDYASIN, S., LIPPARD, S., OMOSANYA, K., JOHANSEN, S. & HARISHIDAYAT, D. 2016. Deep-seated faults and hydrocarbon leakage in the Snøhvit Gas Field, Hammerfest Basin, Southwestern Barents Sea. Marine and Petroleum Geology, 77, 160-178.

MOHR, M., WARREN, J. K., KUKLA, P. A., URAI, J. L. & IRMEN, A. 2007. Subsurface seismic record of salt glaciers in an extensional intracontinental setting (Late Triassic of northwestern Germany). Geology, 35, 963-966.

MOHRIAK, W., NEMCOK, M. & ENCISO, G. 2008. South Atlantic divergent margin evolution: rift-border uplift and salt tectonics in the basins of SE Brazil. Geological Society, London, Special Publications, 294, 365-398.

MOHRIAK, W. U., SZATMARI, P. & ANJOS, S. 2012. Salt: geology and tectonics of selected Brazilian basins in their global context. Geological Society, London, Special Publications, 363, 131-158.

MORLEY, C., GABDI, S. & SEUSUTTHIYA, K. 2007. Fault superimposition and linkage resulting from stress changes during rifting: Examples from 3D seismic data, Phitsanulok Basin, Thailand. Journal of Structural Geology, 29, 646-663.

MORLEY, C., NELSON, R., PATTON, T. & MUNN, S. 1990. Transfer zones in the East African rift system and their relevance to hydrocarbon exploration in rifts (1). AAPG Bulletin, 74, 1234-1253.

MORLEY, C. K. 1999. Patterns of displacement along large normal faults: implications for basin evolution and fault propagation, based on examples from east Africa. AAPG bulletin, 83, 613-634.

MORLEY, C. K. 2007. Development of crestal normal faults associated with deepwater fold growth. Journal of Structural Geology, 29, 1148-1163.

MORRIS, A., FERRILL, D. A. & HENDERSON, D. B. 1996. Slip-tendency analysis and fault reactivation. Geology, 24, 275-278.

MOURGUES, R. & COBBOLD, P. R. 2003. Some tectonic consequences of fluid overpressures and seepage forces as demonstrated by sandbox modelling. Tectonophysics, 376, 75-97.

MUKHERJEE, S., TALBOT, C. J. & KOYI, H. A. 2010. Viscosity estimates of salt in the Hormuz and Namakdan salt diapirs, Persian Gulf. Geological Magazine, 147, 497-507.

MURAOKA, H. & KAMATA, H. 1983. Displacement distribution along minor fault traces. Journal of Structural Geology, 5, 483-495.

NELSON, T. H. & FAIRCHILD, L. 1989. Emplacement and evolution of salt sills in the northern Gulf of Mexico. Houston Geological Society Bulletin, 32, 6-7.

NUR, A., RON, H. & SCOTTI, O. 1986. Fault mechanics and the kinematics of block rotations. Geology, 14, 746-749.

O'BRIEN, J. & LERCHE, I. 1988. Impact of heat flux anomalies around salt diapirs and salt sheets in the Gulf Coast on hydrocarbon maturity: models and observations. Gulf Coast Association of Geological Societies Transactions, 38, 231-242.

OJEDA, H. 1982. Structural framework, stratigraphy, and evolution of Brazilian marginal basins. AAPG Bulletin, 66, 732-749.

OMOSANYA, K. D. O. & ALVES, T. M. 2013a. Ramps and flats of mass-transport deposits (MTDs) as markers of seafloor strain on the flanks of rising diapirs (Espírito Santo Basin, SE Brazil). Marine Geology, 340, 82-97.

OMOSANYA, K. D. O. & ALVES, T. M. 2014. Mass-transport deposits controlling fault propagation, reactivation and structural decoupling on continental margins (Espírito Santo Basin, SE Brazil). Tectonophysics, 628, 158-171.

OMOSANYA, K. O. & ALVES, T. M. 2013b. A 3-dimensional seismic method to assess the provenance of Mass-Transport Deposits (MTDs) on salt-rich continental slopes (Espírito Santo Basin, SE Brazil). Marine and Petroleum Geology, 44, 223-239.

OMOSANYA, K. O., JOHANSEN, S. E. & HARISHIDAYAT, D. 2015. Evolution and character of supra-salt faults in the Easternmost Hammerfest Basin, SW Barents Sea. Marine and Petroleum Geology, 66, Part 4, 1013-1028.

OSAGIEDE, E. E., DUFFY, O. B., JACKSON, C. A.-L. & WRONA, T. 2014. Quantifying the growth history of seismically imaged normal faults. Journal of Structural Geology, 66, 382-399.

OSBORNE, M. J. & SWARBRICK, R. E. 1997. Mechanisms for generating overpressure in sedimentary basins: a reevaluation. AAPG bulletin, 81, 1023-1041.

PATON, D. A., VAN DER SPUY, D., DI PRIMIO, R. & HORSFIELD, B. 2008. Tectonically induced adjustment of passive-margin accommodation space; influence on the hydrocarbon potential of the Orange Basin, South Africa. AAPG Bulletin, 92, 589-609.

PEACOCK, D., ANDERSON, M., ROTEVATN, A., SANDERSON, D. & TAVARNELLI, E. 2017. The interdisciplinary use of "overpressure". Journal of Volcanology and Geothermal Research, 341, 1-5.

PEACOCK, D. & SANDERSON, D. 1991. Displacements, segment linkage and relay ramps in normal fault zones. Journal of Structural Geology, 13, 721-733.

PEACOCK, D. C. P., NIXON, C. W., ROTEVATN, A., SANDERSON, D. J. & ZULUAGA, L. F. 2017b. Interacting faults. Journal of Structural Geology, 97, 1-22.

PEI, Y., PATON, D. A., KNIPE, R. J. & WU, K. 2015. A review of fault sealing behaviour and its evaluation in siliciclastic rocks. Earth-Science Reviews, 150, 121-138.

PETRI, S. 1987. Cretaceous paleogeographic maps of Brazil. Palaeogeography, Palaeoclimatology, Palaeoecology, 59, 117-168.

PILCHER, R. & ARGENT, J. 2007. Mega-pockmarks and linear pockmark trains on the West African continental margin. Marine Geology, 244, 15-32.

PINHEIRO, R. & HOLDSWORTH, R. 1997. Reactivation of Archaean strike-slip fault systems, Amazon region, Brazil. Journal of the Geological Society, 154, 99-103.

PIZZI, A. & GALADINI, F. 2009. Pre-existing cross-structures and active fault segmentation in the northern-central Apennines (Italy). Tectonophysics, 476, 304-319.

POCHAT, S., CASTELLTORT, S., CHOBLET, G. & VAN DEN DRIESSCHE, J. 2009. High-resolution record of tectonic and sedimentary processes in growth strata. Marine and Petroleum Geology, 26, 1350-1364.

POLLARD, D. D. & AYDIN, A. 1984. Propagation and linkage of oceanic ridge segments. Journal of Geophysical Research: Solid Earth, 89, 10017-10028.

POPP, T., KERN, H. & SCHULZE, O. 2001. Evolution of dilatancy and permeability in rock salt during hydrostatic compaction and triaxial deformation. Journal of Geophysical Research: Solid Earth, 106, 4061-4078.

POWER, W., TULLIS, T., BROWN, S., BOITNOTT, G. & SCHOLZ, C. 1987. Roughness of natural fault surfaces. Geophysical Research Letters, 14, 29-32.

RANDLES, T. A. 2014. Structure and geometry of accommodation zones in host and suprajacent sediments associated with the collapse of salt anticlines. PhD thesis.

RECHES, Z. E. & LOCKNER, D. A. 1994. Nucleation and growth of faults in brittle rocks. Journal of Geophysical Research: Solid Earth, 99, 18159-18173.

REIS, Á. F. C., BEZERRA, F. H. R., FERREIRA, J. M., DO NASCIMENTO, A. F. & LIMA, C. C. 2013. Stress magnitude and orientation in the Potiguar Basin, Brazil: Implications on faulting style and reactivation. Journal of Geophysical Research: Solid Earth, 118, 2012JB009953.

RIBOULOT, V., CATTANEO, A., SULTAN, N., GARZIGLIA, S., KER, S., IMBERT, P. & VOISSET, M. 2013. Sea-level change and free gas occurrence influencing a submarine landslide and pockmark formation and distribution in deepwater Nigeria. Earth and Planetary Science Letters, 375, 78-91.

RIPPON, J. 1984. Contoured patterns of the throw and hade of normal faults in the Coal Measures (Westphalian) of north-east Derbyshire. Proceedings of the Yorkshire Geological Society, 45, 147-161.

ROBERTS, A. 2001. Curvature attributes and their application to 3D interpreted horizons. First break, 19, 85-100.

ROUBY, D., GUILLOCHEAU, F., ROBIN, C., BOUROULLEC, R., RAILLARD, S., CASTELLTORT, S. & NALPAS, T. 2003. Rates of deformation of an extensional growth fault/raft system (offshore Congo, West African margin) from combined accommodation measurements and 3-D restoration. Basin Research, 15, 183-200.

ROWAN, M. G. 2002. Salt-related accommodation in the Gulf of Mexico deepwater: Withdrawal or inflation, autochthonous or allochthonous? Gulf Coast Association of Geological Societies Transactions, 52, 861-869.

ROWAN, M. G. 2014. Passive-margin salt basins: hyperextension, evaporite deposition, and salt tectonics. Basin Research, 26, 154-182.

ROWAN, M. G., JACKSON, M. P. A. & TRUDGILL, B. D. 1999. Salt-related fault families and fault welds in the northern Gulf of Mexico. AAPG Bulletin, 83, 1454-1484.

ROWAN, M. G., LAWTON, T. F., GILES, K. A. & RATLIFF, R. A. 2003. Near-salt deformation in La Popa basin, Mexico, and the northern Gulf of Mexico: A general model for passive diapirism. AAPG bulletin, 87, 733-756.

RYAN, L., MAGEE, C. & JACKSON, C. A.-L. 2017. The kinematics of normal faults in the Ceduna Subbasin, offshore southern Australia: Implications for hydrocarbon trapping in a frontier basin. AAPG Bulletin, 101, 321-341.

SCHLISCHE, R. W. & WITHJACK, M. O. 2009. Origin of fault domains and fault-domain boundaries (transfer zones and accommodation zones) in extensional provinces: Result of random nucleation and self-organized fault growth. Journal of Structural Geology, 31, 910-925.

SCHLISCHE, R. W., YOUNG, S. S., ACKERMANN, R. V. & GUPTA, A. 1996. Geometry and scaling relations of a population of very small rift-related normal faults. Geology, 24, 683-686.

SCHLÉDER, Z. & URAI, J. L. 2007. Deformation and recrystallization mechanisms in mylonitic shear zones in naturally deformed extrusive Eocene–Oligocene rocksalt from Eyvanekey plateau and Garmsar hills (central Iran). Journal of Structural Geology, 29, 241-255.

SCHLÉDER, Z., URAI, J. L., NOLLET, S. & HILGERS, C. 2008. Solution-precipitation creep and fluid flow in halite: a case study of Zechstein (Z1) rocksalt from Neuhof salt mine (Germany). International Journal of Earth Sciences, 97, 1045-1056.

SCHOENHERR, J., URAI, J. L., KUKLA, P. A., LITTKE, R., SCHLEDER, Z., LARROQUE, J.-M., NEWALL, M. J., AL-ABRY, N., AL-SIYABI, H. A. & RAWAHI, Z. 2007. Limits to the sealing capacity of rock salt: A case study of the infra-Cambrian Ara Salt from the South Oman salt basin. AAPG bulletin, 91, 1541-1557.

SCHOLZ, C., DAWERS, N., YU, J. Z., ANDERS, M. & COWIE, P. 1993. Fault growth and fault scaling laws: preliminary results. Journal of Geophysical Research: Solid Earth (1978–2012), 98, 21951-21961.

SCHULTZ, R. A. & FOSSEN, H. 2002. Displacement–length scaling in three dimensions: the importance of aspect ratio and application to deformation bands. Journal of Structural Geology, 24, 1389-1411.

SCHULTZ-ELA, D. D., JACKSON, M. P. A. & VENDEVILLE, B. C. 1993. Mechanics of active salt diapirism. Tectonophysics, 228, 275-312.

SCHULZE, O., POPP, T. & KERN, H. 2001. Development of damage and permeability in deforming rock salt. Engineering Geology, 61, 163-180.

SEEBECK, H., NICOL, A., BEETHAM, J. J., SEEBECK, C., PETTINGA, R. D., WALSH, J. & CHILDS, J. 2014. Fluid flow in fault zones from an active rift. Journal of Structural Geology, 62, 52-64.

SEGALL, P. & POLLARD, D. 1980. Mechanics of discontinuous faults. Journal of Geophysical Research: Solid Earth, 85, 4337-4350.

SEGALL, P. & POLLARD, D. D. 1983. Nucleation and growth of strike slip faults in granite. Journal of Geophysical Research: Solid Earth, 88, 555-568.

SIBSON, R. H. 1985. A note on fault reactivation. Journal of Structural Geology, 7, 751-754.

SIPPEL, J., SAINTOT, A., HEEREMANS, M. & SCHECK-WENDEROTH, M. 2010. Paleostress field reconstruction in the Oslo region. Marine and Petroleum Geology, 27, 682-708.

SIRAT, M., SHINDE, A. L., AL NAEIMI, R. & PERUMALLA, S. V. Fault Seal Assessment of a Fractured Carbonate Reservoir Using 3D Geomechanical Characterisation, Abu Dhabi. International Petroleum Technology Conference, 2014. International Petroleum Technology Conference.

SMIT, J., BRUN, J.-P., FORT, X., CLOETINGH, S. & BEN-AVRAHAM, Z. 2008. Salt tectonics in pull-apart basins with application to the Dead Sea Basin. Tectonophysics, 449, 1-16.

SMITH, G. A., MCINTOSH, W. & KUHLE, A. J. 2001. Sedimentologic and geomorphic evidence for seesaw subsidence of the Santo Domingo accommodation-zone basin, Rio Grande rift, New Mexico. Geological Society of America Bulletin, 113, 561-574.

SPANG, J. H. 1972. Numerical method for dynamic analysis of calcite twin lamellae. Geological Society of America Bulletin, 83, 467-472.

SPERNER, B., RATSCHBACHER, L. & OTT, R. 1993. Fault-striae analysis: a Turbo Pascal program package for graphical presentation and reduced stress tensor calculation. Computers & Geosciences, 19, 1361-1388.

STEWART, S. & ARGENT, J. 2000. Relationship between polarity of extensional fault arrays and presence of detachments. Journal of Structural Geology, 22, 693-711.

STEWART, S., RUFFELL, A. & HARVEY, M. 1997. Relationship between basement-linked and gravity-driven fault systems in the UKCS salt basins. Marine and Petroleum Geology, 14, 581-604.

STEWART, S. A. 2006. Implications of passive salt diapir kinematics for reservoir segmentation by radial and concentric faults. Marine and Petroleum Geology, 23, 843-853.

STEWART, S. A. & COWARD, M. P. 1995. Synthesis of salt tectonics in the southern North Sea, UK. Marine and Petroleum Geology, 12, 457-475.

STROZYK, F., VAN GENT, H., URAI, J. & KUKLA, P. A. 2012. 3D seismic study of complex intra-salt deformation: An example from the Upper Permian Zechstein 3 stringer, western Dutch offshore. Geological Society, London, Special Publications, 363, 489-501.

SUN, Q., WU, S., CARTWRIGHT, J. & DONG, D. 2012. Shallow gas and focused fluid flow systems in the Pearl River Mouth Basin, northern South China Sea. Marine Geology, 315–318, 1-14.

SWARBRICK, R. E. & OSBORNE, M. J. 1998. Memoir 70, Chapter 2: Mechanisms that Generate Abnormal Pressures: an Overview.

TALBOT, C. J. & JACKSON, M. P. 1987. Salt tectonics. Scientific American, 257, 70-79.

TALBOT, C. J. & ROGERS, E. A. 1980. Seasonal movements in a salt glacier in Iran. Science, 208, 395-397.

TERZAGHI, K. 1925. Principles of soil mechanics, IV—Settlement and consolidation of clay. Engineering News-Record, 95, 874-878.

TESFAYE, S., ROWAN, M. G., MUELLER, K., TRUDGILL, B. D. & HARDING, D. J. 2008. Relay and accommodation zones in the Dobe and Hanle grabens, central Afar, Ethiopia and Djibouti. Journal of the Geological Society, 165, 535-547.

THENHAUS, P. C. & BARNHARD, T. P. 1989. Regional termination and segmentation of quaternary fault belts in the Great Basin, Nevada and Utah. Bulletin of the Seismological Society of America, 79, 1426-1438.

THORSEN, C. E. 1963. Age of growth faulting in southeast Louisiana.

TINGAY, M. R., HILLIS, R. R., SWARBRICK, R. E., MORLEY, C. K. & DAMIT, A. R. 2007. 'Vertically transferred' overpressures in Brunei: Evidence for a new mechanism for the formation of high-magnitude overpressure. Geology, 35, 1023-1026.

TINGAY, M. R., HILLIS, R. R., SWARBRICK, R. E., MORLEY, C. K. & DAMIT, A. R. 2009. Origin of overpressure and pore-pressure prediction in the Baram province, Brunei. AAPG Bulletin, 93, 51-74.

TOM RANDLES, S. C., PHIL RICHARDS 2012. Development of Crestal Collapse Structures above Dissolving Salt Anticlines: Application to Seismic Interpretation within Salt-Controlled Basins. AAPG Annual Convention and Exhibition Long Beach, California.

TORABI, A. & BERG, S. S. 2011. Scaling of fault attributes: A review. Marine and Petroleum Geology, 28, 1444-1460.

TRINCARDI, F., CATTANEO, A., CORREGGIARI, A. & RIDENTE, D. 2004. Evidence of soft sediment deformation, fluid escape, sediment failure and regional weak layers within the late Quaternary mud deposits of the Adriatic Sea. Marine Geology, 213, 91-119.

TRUSHEIM, F. 1960. Mechanism of salt migration in northern Germany. AAPG Bulletin, 44, 1519-1540.

TURKO, J. M. & KNUEPFER, P. L. 1991. Late Quaternary fault segmentation from analysis of scarp morphology. Geology, 19, 718-721.

TVEDT, A. B. M., ROTEVATN, A. & JACKSON, C. A. L. 2016. Supra-salt normal fault growth during the rise and fall of a diapir: Perspectives from 3D seismic reflection data, Norwegian North Sea. Journal of Structural Geology, 91, 1-26.

UNDERHILL, J. R. 2009. Role of intrusion-induced salt mobility in controlling the formation of the enigmatic 'Silverpit Crater', UK Southern North Sea. Petroleum Geoscience, 15, 197-216.

VADAKKEPULIYAMBATTA, S., BÜNZ, S., MIENERT, J. & CHAND, S. 2013. Distribution of subsurface fluid-flow systems in the SW Barents Sea. Marine and Petroleum Geology, 43, 208-221.

VAN DER VEER, E. 2013. Induced seismicity in CO2 storage systems; A modeling study into the effect of thermally-induced stress changes on fault reactivation. Master thesis.

VAN GENT, H., BACK, S., URAI, J. L. & KUKLA, P. 2010. Small-scale faulting in the Upper Cretaceous of the Groningen block (The Netherlands): 3D seismic interpretation, fault plane analysis and regional paleostress. Journal of Structural Geology, 32, 537-553.

VAN KEKEN, P., SPIERS, C., VAN DEN BERG, A. & MUYZERT, E. 1993. The effective viscosity of rocksalt: implementation of steady-state creep laws in numerical models of salt diapirism. Tectonophysics, 225, 457-476.

VENDEVILLE, B., GE, H. & JACKSON, M. 1995. Scale models of salt tectonics during basement-involved extension. Petroleum Geoscience, 1, 179-183.

VENDEVILLE, B. C. 2005. Salt tectonics driven by sediment progradation: Part I— Mechanics and kinematics. AAPG Bulletin, 89, 1071-1079.

VENDEVILLE, B. C. & JACKSON, M. P. A. 1992a. The fall of diapirs during thin-skinned extension. Marine and Petroleum Geology, 9, 354-371.

VENDEVILLE, B. C. & JACKSON, M. P. A. 1992b. The rise of diapirs during thin-skinned extension. Marine and Petroleum Geology, 9, 331-354.

WALLACE, R. E. 1951. Geometry of shearing stress and relation to faulting. The Journal of Geology, 59, 118-130.

WALSH, J., BAILEY, W., CHILDS, C., NICOL, A. & BONSON, C. 2003. Formation of segmented normal faults: a 3-D perspective. Journal of Structural Geology, 25, 1251-1262.

WALSH, J., NICOL, A. & CHILDS, C. 2002. An alternative model for the growth of faults. Journal of Structural Geology, 24, 1669-1675.

WALSH, J. & WATTERSON, J. 1987. Distributions of cumulative displacement and seismic slip on a single normal fault surface. Journal of Structural Geology, 9, 1039-1046.

WALSH, J. J. & WATTERSON, J. 1988. Analysis of the relationship between displacements and dimensions of faults. Journal of Structural geology, 10, 239-247.

WALSH, J. J. & WATTERSON, J. 1991. Geometric and kinematic coherence and scale effects in normal fault systems. Geological Society, London, Special Publications, 56, 193-203.

WARD, N. I. P., ALVES, T. M. & BLENKINSOP, T. G. 2016. Reservoir leakage along concentric faults in the Southern North Sea: Implications for the deployment of CCS and EOR techniques. Tectonophysics, 690, 97-116.

WARREN, J. K. 2006. Evaporites: Sediments, Resources and Hydrocarbons: Sediments, Resources, and Hydrocarbons, Springer.

WARREN, J. K. 2016. Salt usually seals, but sometimes leaks: Implications for mine and cavern stability in the short and long term. Earth-Science Reviews, 165, 302-341.

WATTERSON, J. 1986. Fault dimensions, displacements and growth. Pure and Applied Geophysics, 124, 365-373.

WHITTAKER, A. C. & WALKER, A. S. 2015. Geomorphic constraints on fault throw rates and linkage times: Examples from the Northern Gulf of Evia, Greece. Journal of Geophysical Research-Earth Surface, 120, 137-158.

WILLEMSE, E. J., POLLARD, D. D. & AYDIN, A. 1996. Three-dimensional analyses of slip distributions on normal fault arrays with consequences for fault scaling. Journal of Structural Geology, 18, 295-309.

WILLIAMS, G. & CHAPMAN, T. 1983. Strains developed in the hangingwalls of thrusts due to their slip/propagation rate: a dislocation model. Journal of Structural Geology, 5, 563-571.

WILSON, P., ELLIOTT, G. M., GAWTHORPE, R. L., JACKSON, C. A. L., MICHELSEN, L. & SHARP, I. R. 2013. Geometry and segmentation of an

evaporite-detached normal fault array: 3D seismic analysis of the southern Bremstein Fault Complex, offshore mid-Norway. Journal of Structural Geology, 51, 74-91.

WIPRUT, D. & ZOBACK, M. D. 2000. Fault reactivation and fluid flow along a previously dormant normal fault in the northern North Sea. Geology, 28, 595-598.

WOJTAL, S. F. 1994. Fault scaling laws and the temporal evolution of fault systems. Journal of Structural Geology, 16, 603-612.

WOJTAL, S. F. 1996. Changes in fault displacement populations correlated to linkage between faults. Journal of Structural Geology, 18, 265-279.

WOODCOCK, N. H. 1991. N. J. Price & J. W. Cosgrove 1990. Analysis of Geological Structures. xiii + 502 pp. Cambridge, New York, Port Chester, Melbourne, Sydney: Cambridge University Press.

WORUM, G., VAN WEES, J. D., BADA, G., VAN BALEN, R. T., CLOETINGH, S. & PAGNIER, H. 2004. Slip tendency analysis as a tool to constrain fault reactivation- A numerical approach applied to three-dimensional fault models in the Roer Valley rift system (southeast Netherlands). Journal of Geophysical Research: Solid Earth (1978–2012), 109.

YIN, H. & GROSHONG, R. H. 2007. A three-dimensional kinematic model for the deformation above an active diapir. AAPG Bulletin, 91, 343-363.

YU, Y., TANG, L., YANG, W., HUANG, T., QIU, N. & LI, W. 2014. Salt structures and hydrocarbon accumulations in the Tarim Basin, northwest China. AAPG Bulletin, 98, 135-159.

YUKUTAKE, Y., TAKEDA, T. & YOSHIDA, A. 2014. The applicability of frictional reactivation theory to active faults in Japan based on slip tendency analysis. Earth and Planetary Science Letters, 411, 188-198.

ZE, T. & ALVES, T. M. 2016. The role of gravitational collapse in controlling the evolution of crestal fault systems (Espírito Santo Basin, SE Brazil). Journal of Structural Geology, 92, 79-98.

ZE, T. & ALVES, T. M. 2017. The role of gravitational collapse in controlling the evolution of crestal fault systems (Espírito Santo Basin, SE Brazil)–Reply. Journal of Structural Geology, 98, 12-14.

ZHANG, P., SLEMMONS, D. & MAO, F. 1991. Geometric pattern, rupture termination and fault segmentation of the Dixie Valley—Pleasant Valley active normal fault system, Nevada, USA. Journal of Structural Geology, 13, 165-176.

ZOBACK, M. D. 2010. Reservoir geomechanics, Cambridge University Press.

ŽALOHAR, J. & VRABEC, M. 2007. Paleostress analysis of heterogeneous fault-slip data: the Gauss method. Journal of Structural Geology, 29, 1798-1810.